

UNCLASSIFIED

AD NUMBER

ADB029329

LIMITATION CHANGES

TO:

Approved for public release; distribution is unlimited.

FROM:

Distribution authorized to U.S. Gov't. agencies only; Test and Evaluation; MAR 1978. Other requests shall be referred to Air Force Wright Aeronautical Labs., Wright-Patterson AFB, OH 45433.

AUTHORITY

WRDC/IST ltr 16 Oct 1980

THIS PAGE IS UNCLASSIFIED

✓

LEVEL

②

AFFDL-TR-78-37

AD B 0 2 9 3 2 9

SUPERCritical WING FLUTTER

DOUGLAS AIRCRAFT COMPANY
~~McDONNELL DOUGLAS CORPORATION~~
LONG BEACH, CALIFORNIA 90846

MARCH 1978

FINAL REPORT FOR PERIOD AUGUST 1977 - ~~APRIL 1978~~

REC'D
AUG 21 1978
A

DDC FILE COPY

Distribution limited to U.S. Government agencies only; test and evaluation; statement applied in March 1978. Other requests for this document must be referred to AF Flight Dynamics Laboratory (AFFDL/FBR) Wright-Patterson AFB, Ohio 45433.

AIR FORCE FLIGHT DYNAMICS LABORATORY
AIR FORCE WRIGHT AERONAUTICAL LABORATORIES
AIR FORCE SYSTEMS COMMAND
WRIGHT-PATTERSON AIR FORCE BASE, OHIO 45433

78 08 18 002

NOTICE

When Government drawings, specifications, or other data are used for any purpose other than in connection with a definitely related Government procurement operation, the United States Government thereby incurs no responsibility nor any obligation whatsoever; and the fact that the government may have formulated, furnished, or in any way supplied the said drawings, specifications, or other data, is not to be regarded by implication or otherwise as in any manner licensing the holder or any other person or corporation, or conveying any rights or permission to manufacture, use, or sell any patented invention that may in any way be related thereto.

This technical report has been reviewed and is approved for publication.

Lawrence J. Huttzell

LAWRENCE J. HUTTSELL
Project Engineer
Aeroelastic Group
Analysis and Optimization Branch

Charles A. Bair, Jr.

CHARLES A. BAIR, Jr, Major, USAF
Chief, Analysis & Optimization Branch
Structural Analysis Division

FOR THE COMMANDER

Ralph L. Kuster, Jr.

RALPH L. KUSTER, JR., Colonel, USAF
Chief, Structural Mechanics Division

Copies of this report should not be returned unless return is required by security considerations, contractual obligations, or notice on a specific document.

Unclassified

SECURITY CLASSIFICATION OF THIS PAGE (When Data Entered)

REPORT DOCUMENTATION PAGE		READ INSTRUCTIONS BEFORE COMPLETING FORM	
1. REPORT NUMBER AFFDL-TR-78-37	2. GOVT ACCESSION NO.	3. RECIPIENT'S CATALOG NUMBER	
4. TITLE (and Subtitle) SUPERCRITICAL WING FLUTTER,	5. TYPE OF REPORT & PERIOD COVERED Final Technical Report. Aug-1977-April 1978		
7. AUTHOR(s) J. A./McGrew, J. P./Giesing, R. M./Pearson,	K./Zuhuruddin M. E./Schmidt T. P. Kalman	6. PERFORMING ORG. REPORT NUMBER 2 Aug 77-1 Mar 78	8. CONTRACT OR GRANT NUMBER(s) F33615-77-C-3101
9. PERFORMING ORGANIZATION NAME AND ADDRESS McDonnell Douglas Corporation Douglas Aircraft Company Long Beach, California 90846	10. PROGRAM ELEMENT, PROJECT, TASK AREA & WORK UNIT NUMBERS Project 2401 Task 240102		
11. CONTROLLING OFFICE NAME AND ADDRESS Air Force Flight Dynamics Laboratory (FBRC) Wright-Patterson AFB, Ohio 45433	12. REPORT DATE March 1978		
14. MONITORING AGENCY NAME & ADDRESS (if different from Controlling Office) 12 238p.	13. NUMBER OF PAGES 221		
	15. SECURITY CLASS. (of this report) Unclassified		
	15a. DECLASSIFICATION/DOWNGRADING SCHEDULE		
16. DISTRIBUTION STATEMENT (of this Report) Distribution limited to U. S. Government agencies only; test and evaluation; statement applied in March 1978. Other requests for this document must be referred to Air Force Flight Dynamics Laboratory, (AFFDL/FBR), Wright-Patterson AFB, Ohio 45433			
17. DISTRIBUTION STATEMENT (of the abstract entered in Block 20, if different from Report)			
18. SUPPLEMENTARY NOTES			
19. KEY WORDS (Continue on reverse side if necessary and identify by block number) Weight Factors Nonplanar Lifting Surface Theory Transonic Lifting Surface Theory Vortex Lattice Supercritical Airfoils Doublet Lattice Reynolds Number Effects Aircraft Flutter Aeroelastic Effects Oscillatory Aerodynamics Dynamic Loads Analysis Generalized Forces Unsteady Aerodynamic Loads			
20. ABSTRACT (Continue on reverse side if necessary and identify by block number) Transonic methods for correcting subsonic oscillatory aerodynamic influence coefficients (AIC's) based on the Doublet Lattice Method for use in flutter and dynamic response analyses of supercritical wings are developed and applied to a TF-8A flutter model and the YC-15II prototype aircraft. The effects of static aeroelasticity are included and evaluated. Reynolds number effects on test results are discussed. Correlation of improved methods showed good agreement with test results. For the two applications included, the			

DD FORM 1 JAN 73 1473

EDITION OF 1 NOV 65 IS OBSOLETE
S/N 0102-014-6601

Unclassified

SECURITY CLASSIFICATION OF THIS PAGE (When Data Entered)

116 410 78 08 18 002 LB

Unclassified

SECURITY CLASSIFICATION OF THIS PAGE(When Data Entered)

Block 20 Abstract Continued:

steady corrections dominated the unsteady corrections. In the process of developing transonic corrections a new transonic lifting surface theory (currently two-dimensional) is presented, explored and correlated using the NLR 7301 airfoil. The effects of shock wave motion are included in the theory.

SECURITY CLASSIFICATION OF THIS PAGE(When Data Entered)

TABLE OF CONTENTS

SECTION	Page
I INTRODUCTION	1
II TECHNICAL DISCUSSION	3
2.1 Basic Aerodynamic Data	3
2.2 Vibration Modal Data.	7
2.3 Static Aeroelastic Analysis Procedures	8
2.4 Aerodynamic Weighting Factors	10
2.4.1 Effects of Twist and Reynolds Number on the Steady Weight Factors	13
2.5 Transonic Two-Dimensional Lifting Surface Theory	22
2.5.1 Basic Theory Without Shock Wave Effects	23
2.5.1.1 The Transonic Source	23
2.5.1.2 Equivalent Sending Point Location	28
2.5.1.3 The Two-Dimensional Transonic Source.	34
2.5.1.4 Acoustic Pulse Generator.	36
2.5.1.5 Application to Lifting Surface Theory	48
2.5.2 Effects of Shock Wave Motion	72
2.5.2.1 Interference Flow Due to Shock Motion	72
2.5.2.2 Pressures Due to Shock Wave Motion Interaction with Steady Flow	77
2.5.2.3 Investigation of a Simple Method for Accounting for Transonic Effects	83
2.5.2.4 Shock Wave Compatibility Relations	88
2.6 Flutter Analysis Procedures	95
2.7 Flutter Model Procedures	95
III RESULTS OF ANALYSES	97
3.1 Phase I Results	97
3.1.1 TF-8A Vibration Modal Data	97
3.1.2 TF-8A Static Aeroelastic Solutions	117
3.1.3 Aerodynamic Data and Weighting Factors for the TF-8A Wing	117
3.1.4 TF-8A Flutter Analysis Results - Steady Weighting	146
3.2 Phase II Results	149
3.2.1 TF-8A Flutter Analysis Results - Unsteady Corrections.	149

TABLE OF CONTENTS (Contd)

SECTION	Page
3.3	Phase III Results 150
3.4	Phase IV Results 175
3.4.1	YC-15II Basic Data 175
3.4.2	YC-15II Static Aeroelastic Solution 175
3.4.3	Aerodynamic Data and Weighting Factors for the YC-15II Wing 175
3.4.4	YC-15II Flutter Analysis Results 177
3.5	Flutter Model Test Plan 189
IV	CONCLUSIONS 192
4.1	Conclusions Related to Flutter Analysis 192
4.2	Conclusions Related to Transonic Aerodynamics 195
V	RECOMMENDATIONS 196
5.1	Recommendations Related to Flutter Analysis 196
5.2	Recommendations Related to Transonic Aerodynamics 197
	Appendix A: Source in a Nonuniform Flow Field 199
	Appendix B: Flow Field Calculations Using Two-Dimensional, Steady, Transonic Jameson Procedure 205
	Appendix C: Supersonic Two-Dimensional Doublet Lattice Method . 210
	Appendix D: The Garabedian Transonic Inverse Procedure 218
	REFERENCES 220

ILLUSTRATIONS

Figure		Page
2.1-1	TF-8A Idealization	4
2.1-2	YC-15II Idealization	5
2.4-1	Strip Theory Approximation for a High Aspect Ratio Wing . .	12
2.4-2	Steady and Quasi-Steady Pressure Distributions on the NLR 7301 Airfoil in Transonic Flow (Taken from Reference 4).	14
2.4-3	Experimental Lift and Moment Coefficient for the TF-8A Wing.	15
2.4-4	Elastic Twist of the TF-8A Pressure Model	17
2.4-5	The Effects of Boundary Layer Displacement Thickness on a Section of the TF-8A Wing ($y/(b/2) = 0.933$, $M_{3D} = 0.90$, $M_{2D} = 0.72$, $\alpha_s = -3^\circ$)	19
2.4-6	The Effect of Reynolds Number on the Lift Curve of an Outboard Wing Station of the TF-8A Wing	20
2.5-1	Time Histories of a Series of Acoustic Pulses Emmitted from a Moving Point Source	25
2.5-2	Pulse Surface Velocity Vectors	26
2.5-3	Matching a Circular Pulse to the Actual Pulse at the Receiving Point (x,y,z)	29
2.5-4	Pulse Surface at Time = t and $t+\Delta t$ and Associated Vector Quantities	31
2.5-5	Result of Assuming that the Equivalent Geometry ($\bar{\xi}_0, \bar{\zeta}_0$) Applies Directly to a Point Pressure Doublet	36
2.5-6	Quantities Associated with the Trajectories of Points Lying on a Pulse Surface	37
2.5-7	Grid Used for The Interpolation of the Transonic Flow Velocity Field	38
2.5-8	Nonuniform Flow Field Increment Over the NLR 7301 Airfoil as Calculated by the Jameson Transonic Flow Method	41
2.5-9	Time History of An Acoustic Pulse Whose Origin is At $x/c = 0.55$ for the Nonuniform Flow (above axis) and Uniform Flow (below axis) Cases. Nonuniform Flow is that for the NLR 7301 Airfoil ($M_\infty = 0.7$, $\alpha = 1.75^\circ$) on the Upper Surface .	44
2.5-10(a)	Time History of an Acoustic Pulse Whose Origin is at $x/c = 0.70$ for the Nonuniform Flow (above axis) and Uniform Flow (below axis) Cases. Nonuniform Flow is that for the NLR 7301 Airfoil ($M_\infty = 0.745$, $\alpha_{2D} = -0.2$) On the Upper Surface	45
2.5-10(b)	Time History of an Acoustic Pulse Whose Origin is at $x/c = 0.4$ for the Nonuniform Flow (above axis) and Uniform Flow (below axis) Case. Nonuniform Flow is that for the NLR 7301 Airfoil ($M_\infty = 0.745$, $\alpha = -0.2^\circ$) on the Upper Surface	46

ILLUSTRATIONS (Contd)

Figure	Page	
2.5-11	Time History of an Acoustic Pulse Whose Origin is at $x/c = 0.55$ for the Nonuniform Flow (above axis) and Uniform Flow (below axis) Cases. Nonuniform Flow is that for the TF-8A Wing Section at $y/(b/2) = 0.657$ ($M_{2D} = 0.711$ $\alpha_{2D} = 4.2^\circ$) on the Upper Surface	47
2.5-12	Comparison of the Present Method with the Analytic Solution for the Oscillatory Supersonic Case. Airfoil Pitching About Mid-Chord at $k_r = 0.99$ and $M_\infty = 1.2$	49
2.5-13	Comparison of Transonic and Classical Acoustic Pulse Time-of-Arrival for a Source at $x/c = 0.7$ on an NLR 7301 Airfoil	52
2.5-14	Time-of-Arrival versus Chordwise Position for Acoustic Pulses at Various Sending Point Locations	53
2.5-15(a)	Effective Local Mach Number, \bar{M} , Along the Airfoil for Various Sending Points on the Upper Surface of the NLR 7301 Airfoil. (a) $M_\infty = 0.745$ $\alpha = 0.2^\circ$ Note: M is the Local Surface Mach Number	54
2.5-15(b)	Effective Local Mach Number, \bar{M} , Along the Airfoil for Various Sending Points on the Upper Surface of the NLR 7301 Airfoil. (b) $M_\infty = 0.70$ $\alpha = 1.75^\circ$	55
2.5-16	Pulse Wave Patterns for Various Flow Conditions	57
2.5-17	Comparison of Actual and Approximate Values of Acoustic Pulse Time-of-Arrival for a Source at $x/c = 0.4$ on an NLR 7301 Airfoil	58
2.5-18	Time of Arrival, Along the Airfoil Surface, of an Acoustic Pulse Emitted at Time $t = \tau$ and Located on the Surface of the NLR 7301 Airfoil ($M_\infty = 0.745$, $\alpha = 0.2^\circ$)	61
2.5-19	Comparison of the Present Method and the Classical Theory with the Jameson Transonic Method for Two Average Angles for the Case of Shock Free Flow	65
2.5-20	Comparison of the Present Method (Without Shock Wave Effects) and the Classic Theory with the Jameson Transonic Method.	67
2.5-21	Comparison of the Jameson Transonic Flow Method with Data for the NLR 7301 Airfoil ($M_\infty = 0.745$, $\alpha = 0.2^\circ$). Angle of Attack for Theory Adjusted for Best Correlation	68
2.5-22	Comparison of the Jameson Transonic Flow Method with Data for the NLR 7301 Airfoil ($M_\infty = 0.7$, $\alpha = 1.75^\circ$). Angle of Attack for Theory Adjusted for Best Correlation	69
2.5-23	Comparison of the Jameson Transonic Method with Wind Tunnel Data for the NLR 7301 Airfoil. Jameson Method Used at Two Angles of Attack	70

ILLUSTRATIONS (Contd)

Figure		Page
2.5-24	Comparison of the Jameson Transonic Method with Wind Tunnel Data for the NLR 7301 Airfoil	71
2.5-25	Analytic Continuation of Flow Variable due to Shock Wave Motion	74
2.5-26	Shock Vorticity Interference Flow	75
2.5-27	Shock Vortex Interference Flow Downwash for the NLR 7301 Airfoil Operating at $M_\infty = 0.7$ and $\alpha = 1.75^\circ$	76
2.5-28	Pressure Distribution on the NLR 7301 Airfoil Operating at $M_\infty = 0.7$, $\alpha = 1.75^\circ$ due to the Shock Vortex Interference Flow	78
2.5-29	Comparison of the Present Method (with Shock Wave Effects) with the Jameson Transonic Method for the NLR 7301 Airfoil	81
2.5-30	Comparison of the Jameson Method with the Simplified Transonic Method	84
2.5-31	Comparison of the Simple Transonic Method with Experimental Data. Simple Method Uses Steady Data from Two Sources. . .	85
2.5-32	Time of Arrival of an Acoustic Wave, Whose Origin is at the Airfoil Trailing Edge, as it Passes Upstream Over the NLR 7301 Airfoil ($M_\infty = 0.7$, $\alpha = 1.75^\circ$)	87
2.5-33	Ratio of Oscillatory to Steady Shock Wave Amplitude for The NLR 7301 ($M = 0.7$, $\alpha = 3^\circ$).	89
3.1-1	TF-8A Modal Deflection Measurement Grid	99
3.1-2	TF-8A Transformed Aerodynamic Deflection Idealization . . .	107
3.1-3	TF-8A Flutter Model Wing Rigidity Distribution	114
3.1-4	TF-8A Flutter Model Wing Mass and Inertia	115
3.1-5	TF-8A Flutter Model Wing C.G. Distribution	116
3.1-6	TF-8A Static Twist Distribution $M_\infty = 0.60$, $M_\infty = 0.90$. . .	120
3.1-7	TF-8A Static Twist Distribution, $M_\infty = 0.99$, $M_\infty = 0.95$, $M_\infty = 0.80$	121
3.1-8	TF-8A Elastic Correlation with NASA Data	122
3.1-9	TF-8A C_l vs α_{eff} ; $M_\infty = .99$; $y/(b/2) = .133, .307, .480$. . .	123
3.1-10	TF-8A C_l vs α_{eff} ; $M_\infty = .99$; $y/(b/2) = .653, .804, .933$. . .	124
3.1-11	TF-8A C_m vs α_{eff} ; $M_\infty = .99$; $y/(b/2) = .133, .307, .48$. . .	125
3.1-12	TF-8A C_m vs α_{eff} ; $M_\infty = .99$; $y/(b/2) = .653, .804, .933$. . .	126
3.1-13	TF-8A C_l , $x_{a.c}$ vs $y/(b/2)$, $M_\infty = .50$	127
3.1-14	TF-8A C_l^α , $x_{a.c}$ vs $y/(b/2)$; $M_\infty = .80$	128

ILLUSTRATIONS (Contd)

Figure		Page
3.1-15	TF-8A C_{l_α} , $x_{a.c}$ vs $y/(b/2)$; $M_\infty = .90$	129
3.1-16	TF-8A C_{l_α} , $x_{a.c}$ vs $y/(b/2)$; $M_\infty = .95$	130
3.1-17	TF-8A C_{l_α} , $x_{a.c}$ vs $y/(b/2)$; $M_\infty = .99$	131
3.1-18	TF-8A Flutter Results	148
3.3-1	The Association of Aerodynamic Bays with Selected Wing Sections for the TF-8A Wing	154
3.3-2	The Association of Aerodynamic Bays with Selected Wing Sections for the YC-15II Wing	155
3.3-3	Comparison of Original Pressure - Model Airfoil Section Shapes with those Required to Match Experimental Data for the TF-8A Wing. Required Airfoil Generated by Garabedian Inverse Process	158
3.3-4	Steady Pressure Distribution Near the Shock Wave for Angles of Attack Near the Required Value (1.5°) for the TF-8A Wing ($y/(b/2) = 0.657$, $M_\infty = M_{3D} = 0.99$, $M_{2D} = .80$). Illustration of the Calculation $\partial \lambda / \partial \alpha$ ($C_{PS_2} = C_{PS_1}$)	161
3.3-5	Unsteady Weight Factors for the TF-8A Wing ($y/(b/2) = 0.657$, $M_{3D} = 0.90$, $M_{2D} = 0.711$)	165
3.3-6	Unsteady Weight Factors for the TF-8A Wing ($y/(b/2) = 0.933$, $M_{3D} = 0.9$, $M_{2D} = 0.72$)	166
3.3-7	Unsteady Weight Factors for the TF-8A Wing ($y/(b/2) = 0.657$, $M_{3D} = 0.95$, $M_{2D} = 0.75$)	167
3.3-8	Unsteady Weight Factors for the TF-8A Wing ($y/(b/2) = 0.933$, $M_{3D} = 0.95$, $M_{2D} = 0.75$)	168
3.3-9	Unsteady Weight Factors for the TF-8A Wing ($y/(b/2) = 0.657$, $M_{3D} = 0.99$, $M_{2D} = 0.80$)	169
3.3-10	Unsteady Weight Factors for the TF-8A Wing ($y/(b/2) = 0.933$, $M_{3D} = 0.99$, $M_{2D} = 0.77$)	170
3.3-11	Unsteady Weight Factors for the YC-15II ($y/(b/2) = 0.16$, $M_{2D} = 0.759$)	171
3.3-12	Unsteady Weight Factors for the YC-15II ($y/(b/2) = 0.42$, $M_{2D} = 0.759$), Upper Surface	172
3.3-13	Unsteady Weight Factors for the YC-15II ($y/(b/2) = 0.42$, $M_{2D} = 0.759$), Lower Surface	173
3.3-14	Unsteady Weight Factors for the YC-15II ($y/(b/2) = 0.85$, $M_{2D} = 0.761$)	174

ILLUSTRATIONS (Contd)

Figure		Page
3.4-1	YC-15II Static Twist Distribution, $M_\infty = .76$	178
3.4-2	YC-15II C_ℓ vs α , $M_\infty = .76$	179
3.4-3	YC-15II C_m vs α , $M_\infty = .76$	180
3.4-4	YC-15II C_{ℓ_α} , $x_{a.c}$ vs $y/(b/2)$	181
3.5-1	Proposed Cantilevered Wing Flutter Model	191
4.1-1	Comparison of Theoretical Aircraft Lift Curve Slope with Experimental Data for Conventional and Supercritical Wings	192
4.1-2	Nonlinear Character of the Transonic Lift-Curve	193
A-1	Acoustic Source Pulse Surface at Time $t - \tau$ For the Uniform and Nonuniform Flow Cases	199
B-1	Physical Plane	206
B-2	Scaled and Shifted Plane	206
B-3	Unwrapped Plane	207
B-4	Vertical Shear Plane	207
B-5	Computational Plane	208
C-1	Potential Jump Due to a Point Pressure Doublet	214

TABLES

Table		Page
3.1-1	TF-8A Mode Shape Measurement Stations	100
3.1-2	TF-8A Measured Modal Deflections 1st Wing Bending	101
3.1-3	TF-8A Measured Modal Deflections 2nd Wing Bending	102
3.1-4	TF-8A Measured Modal Deflections 1st Wing Torsion	103
3.1-5	TF-8A Measured Modal Deflections 3rd Wing Bending	104
3.1-6	TF-8A Measured Modal Deflections 4th Wing Bending	105
3.1-7	TF-8A Measured Modal Deflections 2nd Wing Torsion	106
3.1-8	TF-8A Transformed Modal Deflections 1st Wing Bending	108
3.1-9	TF-8A Transformed Modal Deflections 2nd Wing Bending	109
3.1-10	TF-8A Transformed Modal Deflections 1st Wing Torsion	110
3.1-11	TF-8A Transformed Modal Deflections 3rd Wing Bending	111
3.1-12	TF-8A Transformed Modal Deflections 4th Wing Bending	112
3.1-13	TF-8A Transformed Modal Deflections 2nd Wing Torsion	113
3.1-14	TF-8A Steady Weight Factors	132
3.1-15	TF-8A Unsteady Weight Factors $M_\infty = .90$	134
3.1-16	TF-8A Unsteady Weight Factors $M_\infty = .95$	138
3.1-17	TF-8A Unsteady Weight Factors $M_\infty = .99$	142
3.3-1	Elastic Axis Locations	156
3.3-2	TF-8A Incremental Angles of Attack Between the Elastic Flutter Model and Pressure Model	156
3.3-3	YC-15II Incremental Angles of Attack Between the Elastic Aircraft and Pressure Model	156
3.3-4	(TF-8A) Corrections to Jameson Transonic Theory to Give Best Match to Data	160
3.3-5	(YC-15II) Differences Between Data and Garabedian Theory for α and M	160

TABLES (Contd)

Table	Page
3.3-6 Shock Location & Motion Variables for the TF-8A Wing Section	162
3.3-7 Shock Location & Motion Variables for the YC-15II Wing Sections	162
3.4-1 YC-15II Steady Weight Factors	182
3.4-2 YC-15II Unsteady Weight Factors $M_\infty = .759$, $M_\infty = .761$	183

LIST OF SYMBOLS

[AIC]	Aerodynamic influence coefficients relating sectional forces and sectional pitching and plunging
a	Speed of sound
B	$\sqrt{M^2 - 1}$
b	Wing reference span
C_L	Lift coefficient
C_p	Pressure coefficient
c, \bar{c}	Local chord, reference chord
c_l, c_m	Section lift and moment coefficients
[D]	Aerodynamic influence matrix relating pressure to downwash
F	Force
f	Ratio of pulse surface strength in nonuniform flow to that which exists for uniform flow
G	Shock amplitude for the oscillatory case normalized by that for steady case for the NLR 7301 airfoil at $M_\infty = 0.7$
g	Equation of the acoustic pulse surface, $g = 0$
H	Step function
h	Modal deflection normal to surface, + down
$H_n^{(2)}$ (ARG)	Hankle function of the second kind
Im	Imaginary part
J_n (ARG)	Bessel function
k_r	Reduced frequency $\omega \bar{c} / 2U_\infty$
M	Mach Number; M_∞ (free stream), \bar{M} (equivalent), M (local)
\bar{n}	Normal vector to acoustic pulse surface
p	$\lambda(x - x_0)$
q	Dynamic pressure

R	Hyperbolic radius; $R^2 = (x - \xi_0)^2 + \beta^2 r^2$
\bar{R}	Equivalent hyperbolic radius; $\bar{R}^2 = (x - \bar{\xi}_0)^2 + \beta^2 \bar{r}^2$
\tilde{R}	Inverse of acoustic pulse surface strength for the nonuniform flow case
r	$\sqrt{(y - \eta_0)^2 + (z - \zeta_0)^2}$
Re	Reynolds Number or Real part
t	Time
U_∞	Freestream velocity at infinity
u, v	Perturbation velocity in x- and y direction
\vec{V}	Nonuniform steady flow field velocity vector
[WT]	Diagonal matrix of weight factors
WTSCCL WTUSCL WTSCM WTUSCM	Steady (S) and unsteady (US) weight factors (WT) for lift (CL) and moment (CM)
w	Downwash velocity at the airfoil surface
x, y, z	Receiving point or general field point coordinates
α	Angle of attack, α_s (section angle of attack)
β	$\sqrt{1 - M^2}$
Γ_s	Point vortex strength due to shock perturbations
γ	Vorticity per unit length on the shock wave
ΔARG	Increment in ARG where ARG stands for any parameter
ΔC_p	Lifting pressure across a surface
$\Delta \phi$	Difference in potential across a surface
ϵ	Twist, ϵ_e (elastic twist), ϵ_j (built in twist)
ξ, η, ζ	Coordinates of a sending, or source, or doublet point
Λ	Wing sweep airfoil quarter chord (if not otherwise specified)

λ	$\omega M/U_\infty \beta^2$ or $k_r M^2/c \beta^2$
ρ	Radius of an acoustic pulse
σ	Source strength
τ	Time at which the acoustic pulse was created
ϕ	Velocity potential
ω	Frequency, rad/sec

Superscripts

a	Aircraft
exp	Experimental
f	Flutter model
p	Pressure model
2D	Classical two-dimensional value
2DTRANS	Transonic two-dimensional value
-	Equivalent

Subscripts

ac	Aerodynamic center
eff	Corrected back to an effective rigid body state
ea	Elastic axis
j	Jig or built in conditions
o	Location of point source, or shock free conditions
r	Reference conditions
s	Steady conditions or, at the shock wave location
T	Total
TO	Tail off conditions

2D	Pertaining to two-dimensions
3D	Pertaining to three-dimensions
r	Pertaining to the shock vortex
∞	Conditions at infinity

SECTION I INTRODUCTION

Modern aircraft wing designs are increasingly taking advantage of recently developed supercritical airfoil sections which are more aerodynamically efficient than conventional airfoil sections. This increased efficiency is achieved by delaying the drag rise, thus allowing the aircraft to cruise at higher Mach numbers with less sweep. Also, higher lift coefficients are obtainable with wings using these advanced airfoil sections. The YC-15 and YC-15II prototype aircraft are recent examples using supercritical wings.

There has been concern that the flutter characteristics of supercritical wings may be significantly different from wings with conventional airfoils. Recent NASA test data on a TF-8A flutter model showed a substantially larger decrease of flutter speed near the Mach number of maximum lift curve slope than predicted by theoretical subsonic oscillatory aerodynamic theory. Further studies were needed to determine the aerodynamic mechanisms which contribute to this large decrease in flutter speed.

The objective of this study was to develop and evaluate transonic flutter prediction methods for supercritical wings. The study was divided into five phases:

- a. Phase I - TF-8A Flutter Analysis (Steady Corrections) -
Conduct a flutter analysis of the TF-8A flutter model using correction factors to the aerodynamic influence coefficients (AIC's) based upon steady aerodynamic data from the pressure model and correlate with test results.
- b. Phase II - TF-8A Flutter Analysis (Unsteady Correction) -
Apply an improved unsteady correction factor technique (see Phase III) to the flutter analysis of the TF-8A flutter model and correlate with test results.
- c. Phase III - Transonic Method Improvement
Improve the time lag representation and include shock wave motion in the transonic method.

- d. Phase IV - YC-15II Flutter Analysis -
Use the final, proven methods of Phases I, II and III to perform a flutter analyses of the YC-15II.

- e. Phase V - Flutter Test Plan -
Use the results of the analytical effort to define an economical flutter model test plan.

SECTION II TECHNICAL DISCUSSION

2.1 BASIC AERODYNAMIC DATA

The basic theory used for the flutter and static aeroelastic analyses reported herein was the Doublet Lattice Method (DLM) described in Reference 1. This method is applicable to general configurations and is well proven and correlated. The DLM requires that the lifting surfaces (wings, tails, etc.) be broken up into boxes and the bodies (fuselage, nacelles, etc.) be idealized with both slender body and interference elements. Figures 2.1-1 and 2.1-2 present the idealizations for the two configurations considered in this report, i.e., the TF-8A wing-body and the YC-15II.

Experimental wind-tunnel data are available for both of these configurations. The YC-15II data were taken from unpublished McDonnell Douglas sources while the TF-8A data were taken from Reference 2. The TF-8A wind tunnel model was found to be quite elastic considering that it was to be a nominally 'rigid' model. Aeroelastic corrections were applied to the data in an attempt to remove the effects of flexibility. These corrections were essential to obtain the correct section lift curve slopes across the span and consisted of determining the actual or 'effective' angle-of-attack, α_{eff} , of each section and using these in the distributions of c_l and c_m . The aeroelastic correction was based on a bending curve found in Reference 2 for one particular loading. This curve was generalized for all cases by normalization with respect to the angle-of-attack and dynamic pressure. The twist for the reference condition was obtained from the bending curve by taking the slope and scaling it with the sine of the sweep angle.

$$\epsilon_{e_r} = (dz / d\tilde{y}) \sin \Lambda,$$

where z is the local bending deflection and \tilde{y} is distance along the elastic axis.

The resulting normalized elastic twist, T_α , is given as:

$$T_\alpha = \epsilon_{e_r} / \alpha_r q_r$$

and is plotted in Figure 2.4-4. Subsection 2.4 presents additional details

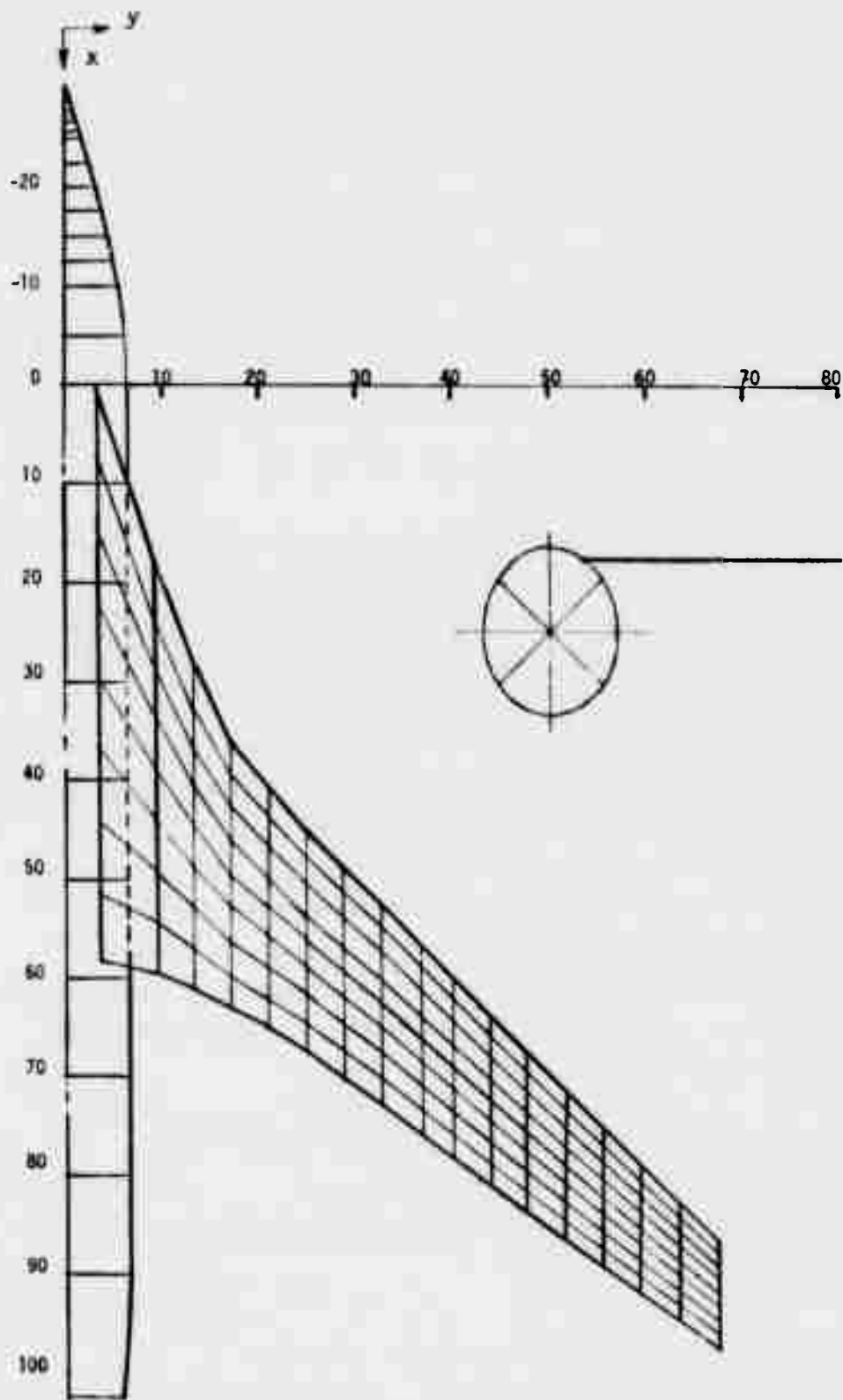


Figure 2.1-1 TF-8A Idealization

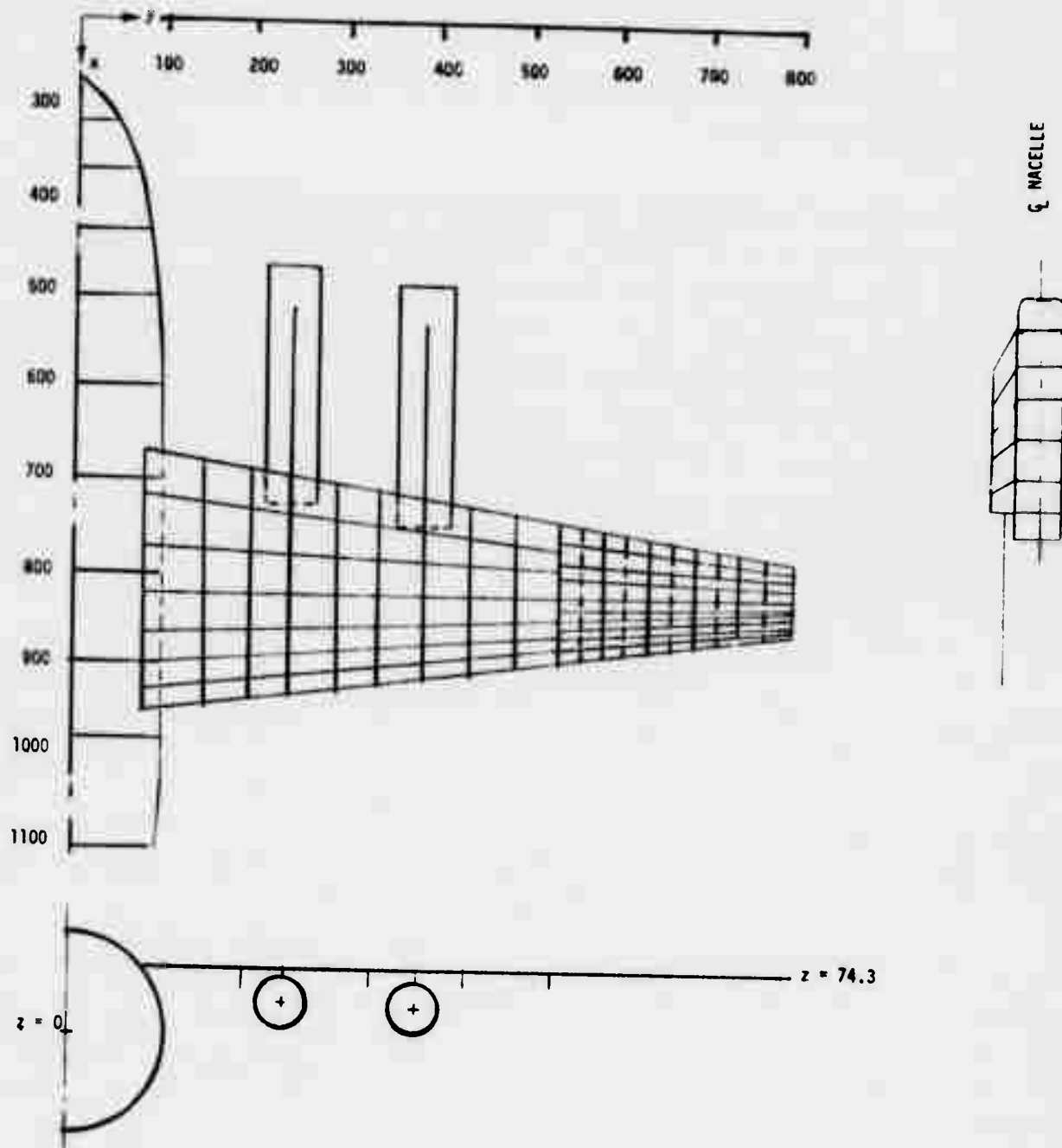


Figure 2.1-2 YC-15II Idealization

of the aeroelastic correction procedure including the corrected or effective angle-of-attack, α_{eff} , at each spanwise section which is given by:

$$\alpha_{eff} = \alpha(1 - T_{\alpha} q)$$

Subsection 3.1.3 presents plots of section c_l and c_m data versus α_{eff} for various conditions.

The data of Reference 2 were obtained for a low Reynolds Number, specifically 1.96×10^6 , based on the chord at the three-quarter span location. Thus, the data is not considered reliable for predicting the stall or near stall conditions. Because of this, only lift curve and moment curve slopes in the low angle-of-attack range were used, i.e., where c_l was a near-linear function of α_{eff} . The moment curves were not linear anywhere but the non-linearity in the small angle-of-attack range was due to transonic effects and thus were considered more reliable. The points on the lift and moment curves where the slopes were taken are given in the results section (Section 3).

2.2 VIBRATION MODAL DATA

Normal modes of vibration of the TF-8A wing and the YC-15II wing were used as the basis for flutter and static aeroelastic calculations. For the YC-15II modes were available from the design analyses process and were used directly. These modal data had been correlated with past aircraft vibration test data and good agreement shown.

NASA (Langley) provided measured mode shapes and generalized mass for six elastic modes of the TF-8A model wing in the form of normal modal deflections at 81 wing locations. Spanwise sectional plots of these deflections showed relatively small camber deformations in the modes of concern and therefore the modal amplitudes were transformed into sectional pitch and plunge degrees of freedom in order to simplify the subsequent aerodynamic weighting processes.

A sectional least squares fit was used to determine pitch and plunge amplitudes for a sixteen spanwise section mathematical model. The measured modal data and transformed modes are shown in Section 3.1.

As a check against the transformation process, vibration modes for the same (sectional) model were calculated with distributed stiffness and inertial data which become available later in the study program. The resulting mode shapes, frequencies and generalized mass agreed well with the transformed test data except for the torsion mode, in which the discrepancy is due to a probable misinterpretation of torsional stiffness magnitude. Factoring the torsional stiffness levels led to good agreement in modal deflections and generalized mass.

2.3 STATIC AEROELASTIC ANALYSIS PROCEDURES

The analysis procedures used for all static aeroelastic analyses procedures used herein consist of a subset of the generalized equations used to solve for the linear elastic trim conditions and deformation of a free flying aircraft. It is assumed that total balance force of the model is specified and the wind tunnel model is then pitched until that specified total lift is achieved. Drag forces are not accounted for herein although the procedure is simply extended for these forces if required. The number of equations to be solved for is $n + 1$, where n is the number of normal elastic modes of the system used. Lift and weight are taken as positive down and moments are positive nose up in the following. The generalized equations are formed by a similarity transform with the normal modes upon the mass and aerodynamic equations for the model. The total force on the model support is given by

$$\bar{q} (D_{h\alpha} \alpha + [D_{hE}] \{q\}) + \bar{q} \bar{L}_j + W = F_T \quad (2.3-1)$$

The elastic equations are:

$$[K_{EE}] \{q\} - \bar{q} (\{D_{E\alpha}\} \alpha + [D_{EE}] \{q\}) - g \{m_{EH}\} - \bar{q} \{L_j\} = 0 \quad (2.3-2)$$

where

- \bar{q} = dynamic pressure, psi
- α = model reference angle of attack
- q = generalized modal amplitudes (an $n \times 1$ vector)
- \bar{L}_j = total jig (reference integrated basic lift), lift/ \bar{q}
- W = total weight
- F_T = total specified force on the modal balance
- K_{EE} = generalized stiffness ($m_{EE} : \omega_{EE}^2$)
- $g \cdot m_{EH}$ = generalized weight forces
- L_j = generalized jig (reference basic lift and moment), forces/ \bar{q}
- $D_{h\alpha}$ = total lift due to α/\bar{q}

$$\begin{aligned}
D_{E\alpha} &= \text{elastic aerodynamic force}/\alpha \cdot \bar{q} \\
D_{hE} &= \text{total lift}/q \cdot \bar{q} \\
D_{EE} &= \text{elastic aerodynamic force}/q \cdot \bar{q}
\end{aligned}$$

The model reference angle of attack is split into two parts for convenience:

$$\alpha = \alpha_0 + \alpha_T$$

where

$$\alpha_0 = \text{model insertion angle}$$

$$\alpha_T = \text{model trim angle}$$

Equation (2.3-1) may be solved for α_T in terms of α_0 , q , jig forces and balance force and substituted into Equation (2.3-2) leaving n equations with n unknowns (q). Post multiplication of the vector q into the modal set used to obtain the equations leads to the deformed surface

$$\{h\} = [\phi] \{q\} \quad (2.3-3)$$

where h are the deflections (and rotations) of the surface and ϕ is the set of normal mode shapes of the surface. The spanwise local angle of attack distribution then is given by the sum of the model insertion angle, the model trim angle, the local elastic twist angles and the effective jig or built in twist distribution.

2.4 AERODYNAMIC WEIGHTING FACTORS

The concept of modifying the matrix of theoretical Aerodynamic Influence Coefficients [AIC's] with a correction factor or weight factor matrix [WT] has been investigated in many reports one of which is Reference 3. One of the methods of Reference 3 is to premultiply the theoretical AIC matrix with the weight factor matrix as follows:

$$[AIC]_{WT} = [WT] [AIC]$$

This technique is the one used in the present report.

The type of AIC matrix used is that for an elastic axis representation. Thus, the elements of the AIC are proportional to the sectional values of lift and moment coefficients. In what is to follow the sectional lift coefficient is discussed primarily; however, the concept applies equally to the section moment coefficient.

The weight factor for a particular section lift coefficient (at a particular wing spanwise location) is given in two parts: a steady part, WTS and an unsteady part, WTUS. The total weighted value for lift is:

$$c_{l_{\alpha}}^{(wt)}(k_r) = WTUSCL \text{ WTSCL } c_{l_{\alpha}}(k_r)$$

where WTSCL and WTUSCL are WTS and WTUS for the $c_{l_{\alpha}}$ term.

The steady weight factor, WTS, is usually obtained from wind tunnel section lift coefficient data. The idea is to correct the theoretical lift coefficient so that it gives the experimental values when the frequency is zero. This term is obtained from the ratio of experimental to theoretical lift curve slope at $k_r = 0$. Thus:

$$WTSCL = c_{l_{\alpha}}^{(exp)}(k_r = 0) / c_{l_{\alpha}}(k_r = 0)$$

Where $c_{l_{\alpha}}$ is the theoretical result and $c_{l_{\alpha}}^{(exp)}$ is that obtained experimentally.

Similarly for the moment

$$WTSCM = c_{m_\alpha}^{(exp)}(k_r = 0) / c_{m_\alpha}(k_r = 0)$$

Or, in terms of aerodynamic center, x_{ac} , and lift coefficient:

$$WTSCM = c_{l_\alpha}^{(exp)}(x_{ea} - x_{ac}^{(exp)}) / c_{l_\alpha}(x_{ea} - x_{ac})$$

where x_{ea} is the axis about which the moment is taken.

The aerodynamic theory used to obtain the AIC and, consequently, the $c_{l_\alpha}(k_r)$ is a subsonic lifting surface theory containing no transonic effects. Thus, the effects of shock motion, etc., are not contained in this theory. Transonic effects can be included into the analysis by using an unsteady weight factor based on other theories which contain transonic effects. For instance, if a two-dimensional transonic theory is available, then it can be used as a basis for the weight factor, WTUS, on a strip theory basis as follows:

$$WTUSCL(k_r) = \frac{c_{l_\alpha}^{(2DTRANS)}(k_r) / c_{l_\alpha}^{(2D)}(k_r)}{c_{l_\alpha}^{(2DTRANS)}(k_r = 0) / c_{l_\alpha}^{(2D)}(k_r = 0)}$$

where $c_{l_\alpha}^{(2DTRANS)}$ is the result obtained from the two-dimensional transonic theory and $c_{l_\alpha}^{(2D)}$ is the result obtained from the two-dimensional subsonic theory (the two-dimensional equivalent of the AIC). The reason for the division by the values of c_{l_α} at $k_r = 0$ (steady values) is so that the weight factor WTUS will reduce to unity for the steady case. This is required since WTS has already taken care of the steady weighting.

The formula above for WTUSCL holds equally well for the moment; simply replace WTUSCL with WTUSCM and c_{l_α} with c_{m_α} .

The application of two-dimensional theory to the three-dimensional swept wing case requires further analysis. Consider Figure 2.4-1.

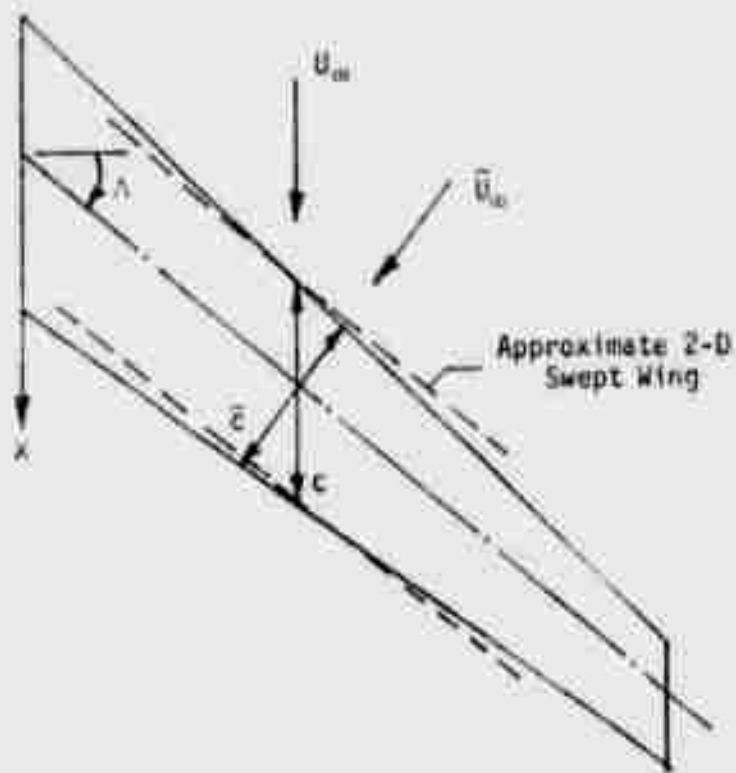


Figure 2.4 - 1 Strip Theory Approximation For a High Aspect Ratio Wing

The constant chord two-dimensional swept wing, that approximates the strip on the wing whose chord length is c , is shown as dashed lines. The flow is two-dimensional, in a plane normal to the axis of sweep. If we designate all values given in this reference system with a superscript tilda, then the section lift, moment and frequency are:

$$c_{\tilde{l}} = \frac{1}{c} \int_0^c \Delta C_p dx = \frac{1}{\tilde{c}} \int_0^{\tilde{c}} \Delta C_p d\tilde{x} = \tilde{c}_{\tilde{l}}$$

$$c_{\tilde{m}} = \frac{1}{c^2} \int_0^c \Delta C_p (x - x_m) dx = \frac{1}{\tilde{c}^2} \int_0^{\tilde{c}} \Delta C_p (\tilde{x} - \tilde{x}_m) dx = \tilde{c}_{\tilde{m}}$$

$$k_{r2D} = \frac{\omega \tilde{c}}{2\tilde{U}_\infty} = \frac{\omega c \cos \Lambda}{2U_\infty \cos \Lambda}$$

where $k_{r_{2D}}$ is the frequency to use in the two-dimensional theory. The two-dimensional frequency is related to the three-dimensional theory as follows:

$$k_{r_{2D}} = \frac{\omega \bar{c}}{2U_{\infty}} \frac{c}{c} = k_{r_{3D}} \frac{c}{c}$$

The two-dimensional transonic theory used as a basis for this strip theory is presented in subsections 2.5 and 3.3. The Mach Number used in the two-dimensional theories is related to the free stream Mach Number as follows:

$$M_{2D} = M_{\infty} \cos \Lambda$$

In the strip theory approach the chord line of the airfoil section considered is foreshortened as Figure 2.4-1 shows. The thickness and camber distributions however are not changed thus the effective thickness and camber of the airfoil section, as a percent of local chord, increases as $1/\cos\Lambda$. Also the angle of attack increases in the same way.

2.4.1 Effects of Twist and Reynolds Number on the Steady Weight Factors

The steady weight factors, WTS, are usually determined from wind tunnel data taken on semi rigid models. It has been found that the steady incidence angle of each wing section has an important bearing on both the steady and unsteady lift curve slopes especially for supercritical wings. Since the shock moves as the section angle of attack, α , is changed, there appears a large increase in perturbation pressure, $C_{p\alpha}$, at the steady shock location which is proportional to the jump in steady pressure. Figure 2.4-2 which was taken from Reference 4, illustrates this effect. The effect of the peak in pressure is very noticeable in the moment coefficient especially for supercritical type wing sections.

Figure 2.4-3 presents the lift and moment coefficient for the TF-8A wing ($y/(b/2) = .804$) operating at a free stream Mach Number of 0.99. Notice especially the nonlinearity in the moment coefficient. Figure 2.4-3 also shows nonlinearities caused by viscous or separation effects. These are easily seen in the plot of c_l versus α .

The slopes of these curves, $c_{l\alpha}$, $c_{m\alpha}$, are the parameters required for the weight factor calculation. It is obvious that the slopes vary along the curves. Sometimes this variation is very large. Thus, the values of $c_{l\alpha}$ and $c_{m\alpha}$

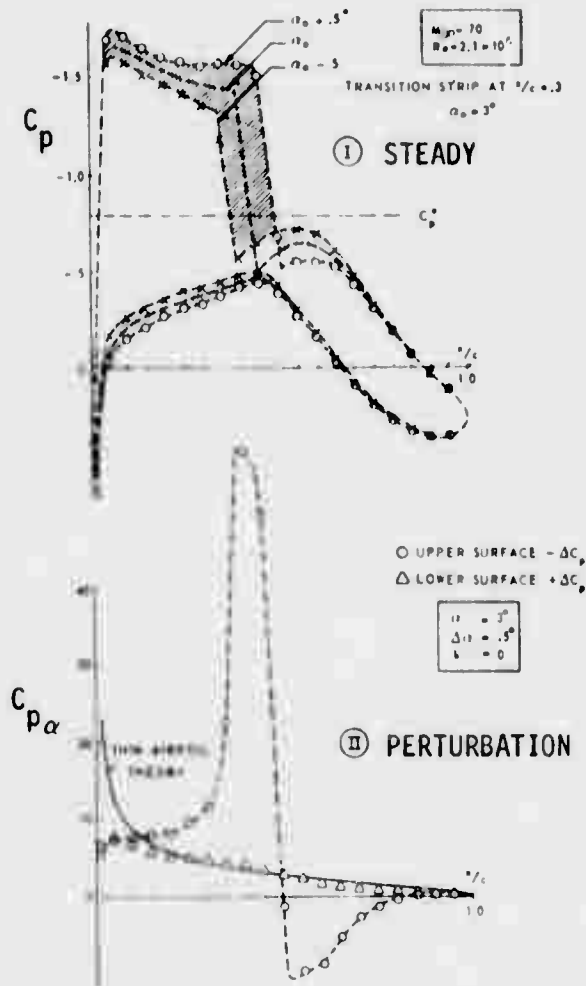


Figure 2.4-2 Steady and Quasi-Steady Pressure Distributions on the NLR 7301 Airfoil in Transonic Flow (Taken from Reference 4)

$M_\infty = 0.99$
 $q = 600 \text{ PSF}$
 $Re = 1.96 \times 10^6$
 $y/(b/2) = 0.804$

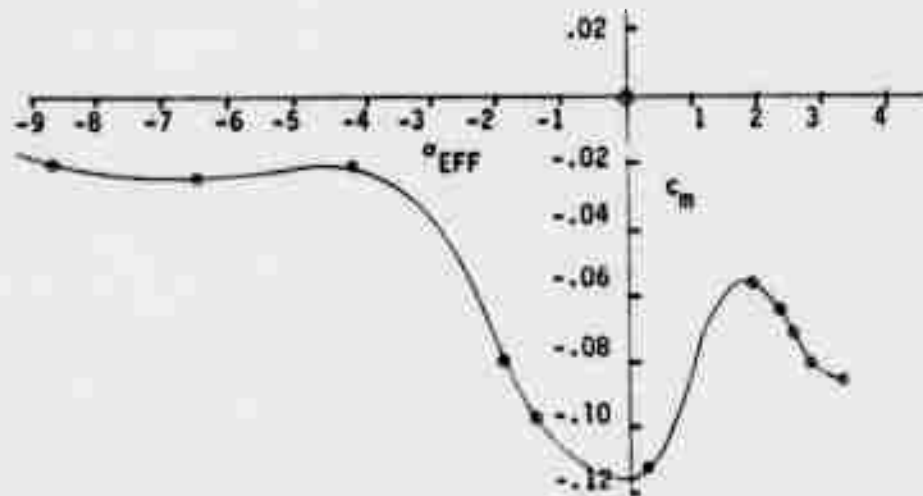
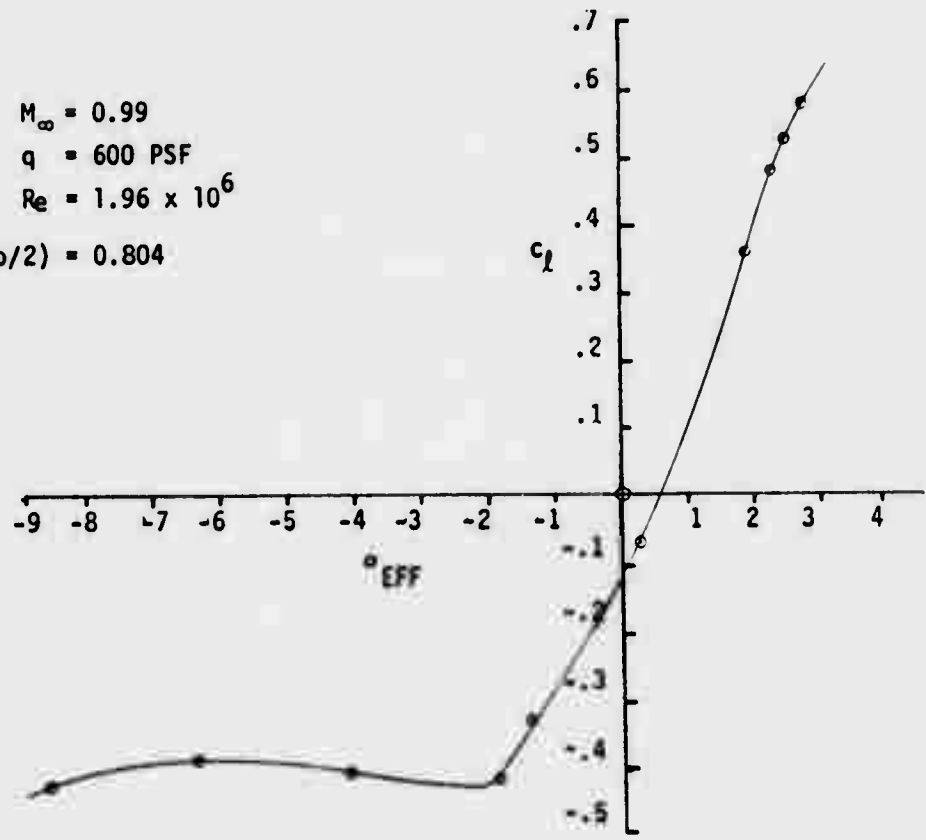


Figure 2.4-3 Experimental Lift and Moment Coefficient for the TF-8A Wing

used depend to a large degree on the section angle of attack. The section angle of attack, α_s , is made up of the following parts:

$$\alpha_s = \alpha + \epsilon_j + \epsilon_e$$

which consist of the aircraft angle of attack α (which is a function of weight, etc.), the built-in twist, ϵ_j , and the elastic twist, ϵ_e , (which is proportioned to loading, dynamic pressure, etc.). Once the section twist is known, the values of $c_{l\alpha}$ and $c_{m\alpha}$ can be determined from the curves obtained from the wind tunnel.

This procedure is slightly different from the usual procedure of reading $c_{l\alpha}$ and $c_{m\alpha}$ on the linear part of the curve. The usual procedure is considered conservative because the linear value of $c_{l\alpha}$ is most often the maximum value, resulting, usually, in the lowest flutter speed.

Some caution must be exercised when using α_s to find the lift and moment curve slope. The reason for this is that the experimental curves of c_l and c_m , versus α may be inaccurate or inappropriate for several reasons. First, the pressure model is not entirely rigid and model bending and twisting induce elastic twist in the model. For instance, the elastic twist, ϵ_e , induced by the bending of the swept TF-8A wing can be calculated from bending data given in Reference 2. Figure 2.4-4 presents a plot of normalized elastic twist $\epsilon_e/q\alpha$ versus span for the one condition ($\epsilon_{er}, q_r, \alpha_r$) at which the bending was determined. This curve was used to correct the section angle-of-attack to an effective angle of attack, α_{eff} , for all cases as follows:

$$\alpha_{eff} = \alpha + \epsilon_e$$

where

$$\epsilon_e = -T_\alpha \alpha q$$

or

$$\alpha_{eff} = \alpha (1 - T_\alpha q)$$

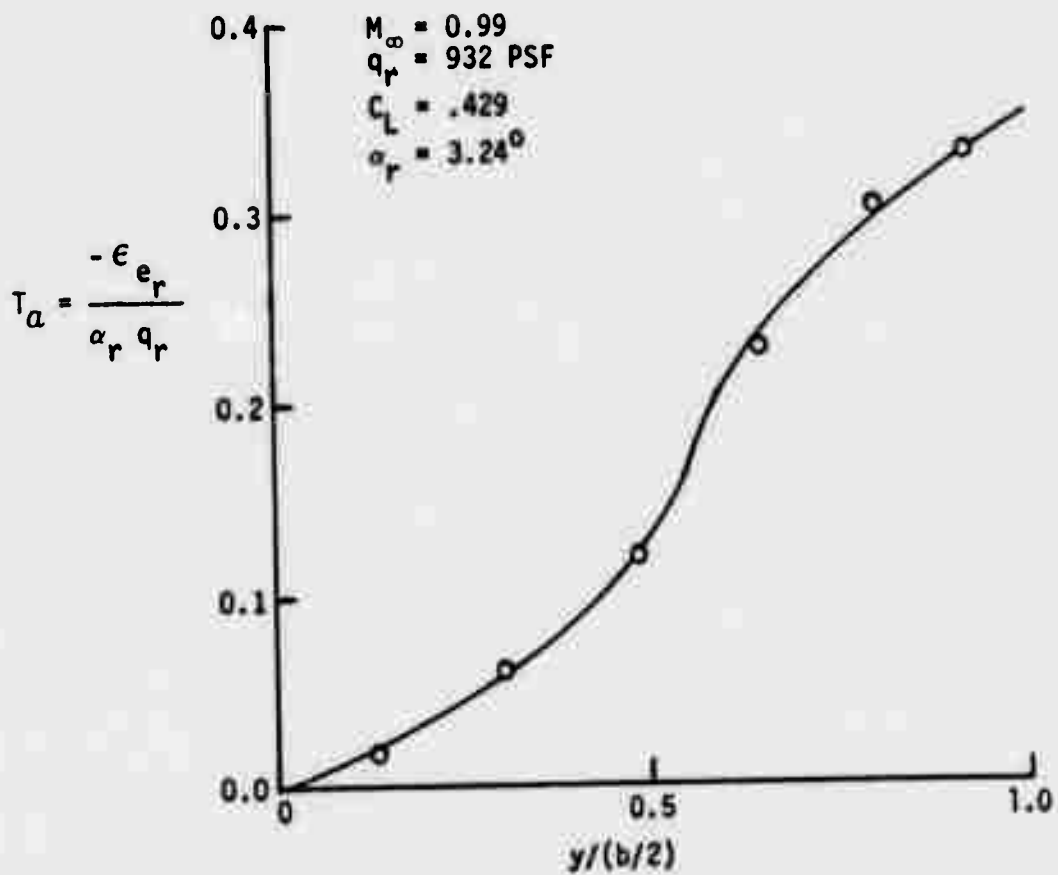


Figure 2.4-4 Elastic Twist of the TF-8A Pressure Model

where

$$T_{\alpha} = -c_{e_r} / \alpha_r q_r$$

and where the reference condition is given by $\alpha_r = 3.24^\circ$ $q_r = 932$ PSF, and the free stream Mach Number, $M_\infty = 0.99$.

Just as small changes in steady section mean angle of attack, α_s , change the loading on the flutter model, small changes in α_s on the pressure model have the same effect. Thus, elastic twist, although usually assumed small for the pressure model, wall induced angle of attack, etc. are important considerations when using the pressure model data.

Another important consideration, especially for supercritical wing sections, is the camber change due to boundary layer thickness. Shock location and the loading on the aft part of the supercritical wing section are sometimes very critically affected by the boundary layer as Figure 2.4-5 shows. This indicates that the boundary layer must be modeled accurately in the wind tunnel. Therefore, among other things, the test Reynolds Number must be sufficiently large.

Another reason for requiring that the test Reynolds Numbers be large is that the proper stall characteristics may need to be simulated. Flutter models are usually highly flexible so that flutter speeds can be reached in the wind tunnel. These models are dynamically modeled but are not statically modeled. This flexibility can cause large negative twist values for swept wings. Figure 2.4-3 shows that, at $y/(b/2) = 0.804$ for the TF-8A wing operating at $M_\infty = 0.99$, any twist of the flutter model (beyond that built-in to the pressure model) of greater than a -2 degrees will put the flutter model into an apparent stall condition. At other sections, which do not stall quite so easily, the slope of the lift curve at a negative twist angle may change drastically from its untwisted position. Reynolds Number plays a part here since the nonlinear shape of the curve is a function of it. Thus, for insufficient Reynolds Number, the lift and moment curve slopes are not to be trusted except in the linear range. Figure 2.4-6 presents the effect

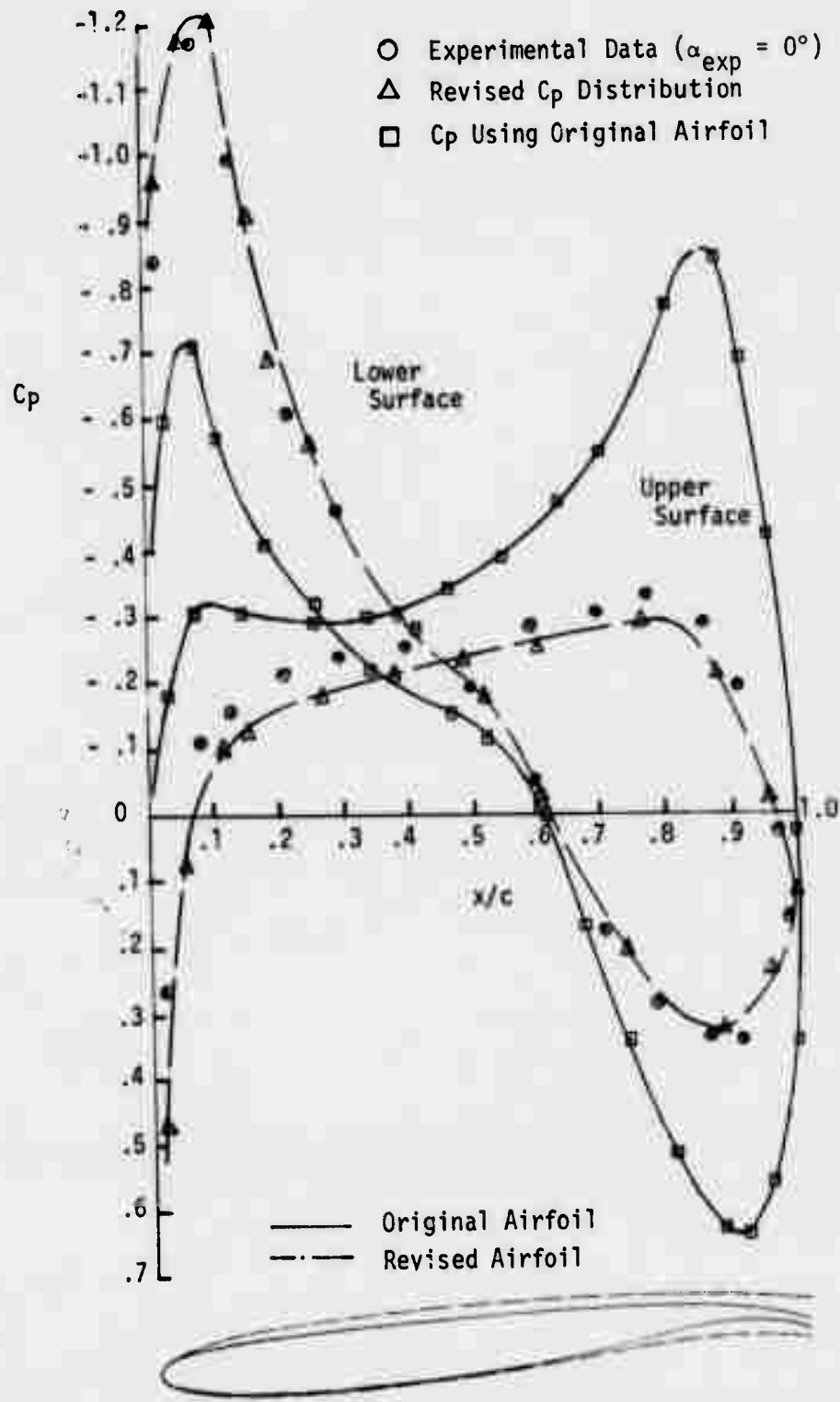


Figure 2.4-5 The Effects of Boundary Layer Displacement Thickness on a Section of the TF-8A Wing ($y/(b/2) = 0.933$, $M_{3D} = 0.90$, $M_{2D} = 0.72$, $\alpha_s = -3^\circ$)

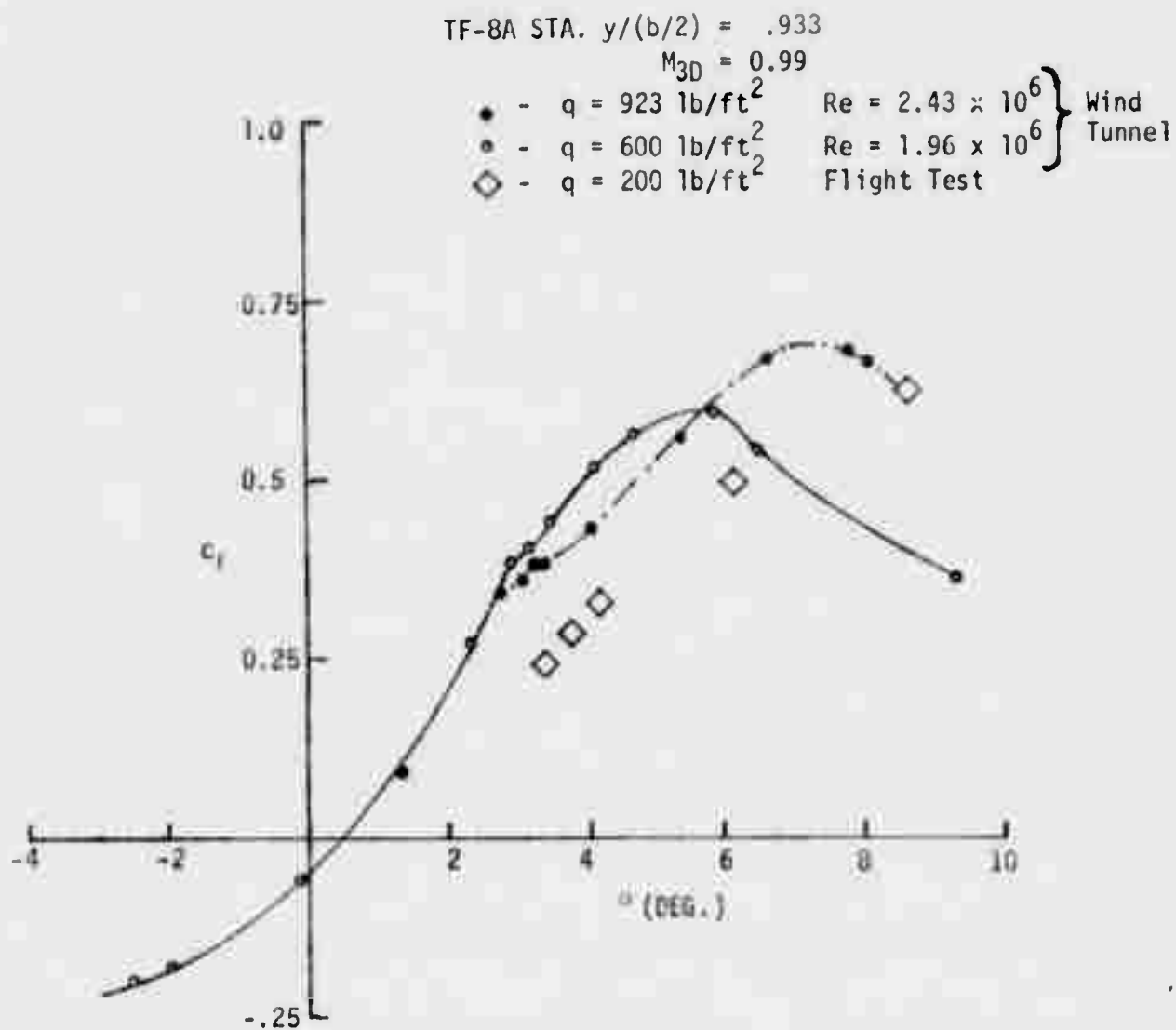


Figure 2.4-6 The Effect of Reynolds Number on the Lift Curve of an Outboard Wing Station of the TF-8A Wing

of Reynolds Number on the lift curve slope for positive angles of attack. There are noticeable changes in $c_{l, \max}$ for small changes in Reynolds Number. Thus, if the Reynolds Number for the pressure model test is insufficient (it should be approximately 10^7) then the results for lift and moment curve slopes may be inaccurate for angles of attack in the nonlinear range.

For the case of the TF-8A wing, the pressure test was run at a Reynolds Number of 1.96×10^6 (based on the chord at $y/(b/2) = 0.75$) where as the flutter model was run at a Reynolds Number ranging from 3.0 to 9.0×10^6 .

Thus, it must be concluded that the nonlinear portions of the lift and moment curves, as obtained from the pressure model, probably do not apply to the flutter model.

The shock location also has a large effect on the unsteady and steady weight factors. Thus, the twist and angle of attack of the flutter model, or aircraft, must be known at the flutter speed if these weight factors are to be calculated properly.

2.5 TRANSONIC TWO-DIMENSIONAL LIFTING SURFACE THEORY

Three approaches to the unsteady transonic flow problem are: (1) direct numerical solution of the time dependent differential equations step-by-step in time using finite difference techniques (see References 5 and 6); (2) direct numerical solution of the oscillatory transonic differential equations using finite difference or finite element techniques (see References 7, 8, and 9); and, (3) solution of the transonic problem using lifting surface theory (see References 3 and 10).

The first approach, which is currently operational in two-dimensional analyses, accounts for transient shock motion. The cost of this type of approach is prohibitive in production flutter and PSD gust analysis, at least with current generation computers.

The second approach shows promise even though shock motions are currently not accounted for and even though it is restricted to low reduced frequencies. The dependence of the oscillatory transonic solution on the steady state solution multiplies the number of cases that must be done in a routine flutter investigation, thus, also multiplying the cost.

Classical subsonic lifting surface theory has gone a long way in predicting flutter speeds even in the transonic region, especially when steady weight factors are applied. It seems logical that modifications of lifting surface theory, to account for transonic effects, is a profitable avenue to investigate. The third approach deals with this area. The approach of Cunningham (Reference 10) is encouraging. This approach uses a local application of classic subsonic and supersonic lifting surface theories coupled with an appropriate shock motion analysis.

The method of Reference 3 addresses the problem of modifying the classic lifting surface theories themselves to account for transonic effects. The lifting surface theory approach to the problem is economically the most desirable if it produces sufficient accuracy.

In this section of the report, an investigation into a two-dimensional

transonic lifting surface theory is presented which is an extension of the initial work of Reference 3. The theory is split up into a part which is independent of shock wave motion and one part that deals strictly with the effects of the shock wave motion. The method is correlated using the NLR 7301 airfoil.

2.5.1 Basic Theory Without Shock Wave Motion Effects

In this section, the basic differential equation for the potential, ϕ , is solved using Green's theory which results in a surface singularity approach. The nonuniformity of the flow field is accounted for in the expression for the point singularities used. The airfoil boundary conditions are satisfied by adjusting the singularity strength. The basic singularity used in lifting surface theory is the doublet; however, the doublet can be obtained from an even more basic singularity, i.e., the source. The derivation of the expression for a transonic source is given in the following and in Appendix A.

The shock boundary conditions are dealt with in Section 2.5.2.

2.5.1.1 The Transonic Source

Lifting surface theory is based on the assumption that the disturbances to the fluid caused by a surface moving through it are small. These small disturbances travel through the fluid at the speed of sound as acoustic waves. Classic lifting surface theory makes the further assumption that the medium through which the waves travel is uniform. It is felt that one of the major transonic effects arises due to the fact that acoustic waves encounter nonuniform flow fields. This is especially important for forward traveling waves in a near sonic stream. Small changes in fluid speed can change the direction of motion of these waves thereby changing the character of the flow. A derivation of an expression for the potential, ϕ , due to a source in a nonuniform stream is presented in Appendix A. The result is:

$$\phi(x,y,z,t) = \sum_{i=1}^N \frac{\sigma(\tau_i)}{4\pi R_i}$$

The term σ is the source strength which is a function of time. To understand this expression, it must be noted that a source in a fluid stream is actually an infinite string of acoustic pulses; one born at each instant, traveling downstream. Figure 2.5-1 shows a source in a uniform flow located at (ξ_0, η_0, ζ_0) with an illustration of the trailing acoustic pulses. Notice the two pulses that reach the receiving point (x, y, z) at the particular time in question. These pulses were generated previously one at $t = \tau_1$ and one at $t = \tau_2$, at the sending or source point (ξ_0, η_0, ζ_0) .

Once an acoustic pulse is generated, its total strength remains unchanged. Of course, the local wave strength on the pulse perimeter varies with time as the wave expands and distributes its strength along an ever-lengthening perimeter. Thus, the total strengths of the waves that have reached the receiving point (x, y, z) are a function of the time at which they were generated at the point (ξ_0, η_0, ζ_0) . The strengths of the waves reaching (x, y, z) are the strengths of the source at (ξ_0, η_0, ζ_0) at the previous times $t = \tau_1$ and τ_2 . This idea is written as $\sigma(\tau_1)$ and $\sigma(\tau_2)$.

For the uniform flow supersonic case, these times τ_1, τ_2 , or phase lags, are expressed as:

$$\left. \begin{aligned} \tau_1 &= \frac{1}{a\beta_\infty^2} \{M_\infty (x - \xi_0) + R\} + t & i = 1 \\ \tau_2 &= \frac{1}{a\beta_\infty^2} \{M_\infty (x - \xi_0) - R\} + t & i = 2 \end{aligned} \right\} \text{Uniform super-sonic case}$$

For the uniform flow subsonic case, only one wave passes the receiving point, thus

$$\tau_1 = \frac{1}{a\beta_\infty^2} \{M_\infty (x - \xi_0) - R\} + t \quad i = 1 \text{ Uniform Subsonic Case}$$

where

$$R^2 = (x - \xi_0)^2 + \beta^2 r^2$$

$$r^2 = (y - \eta_0)^2 + (z - \zeta_0)^2$$

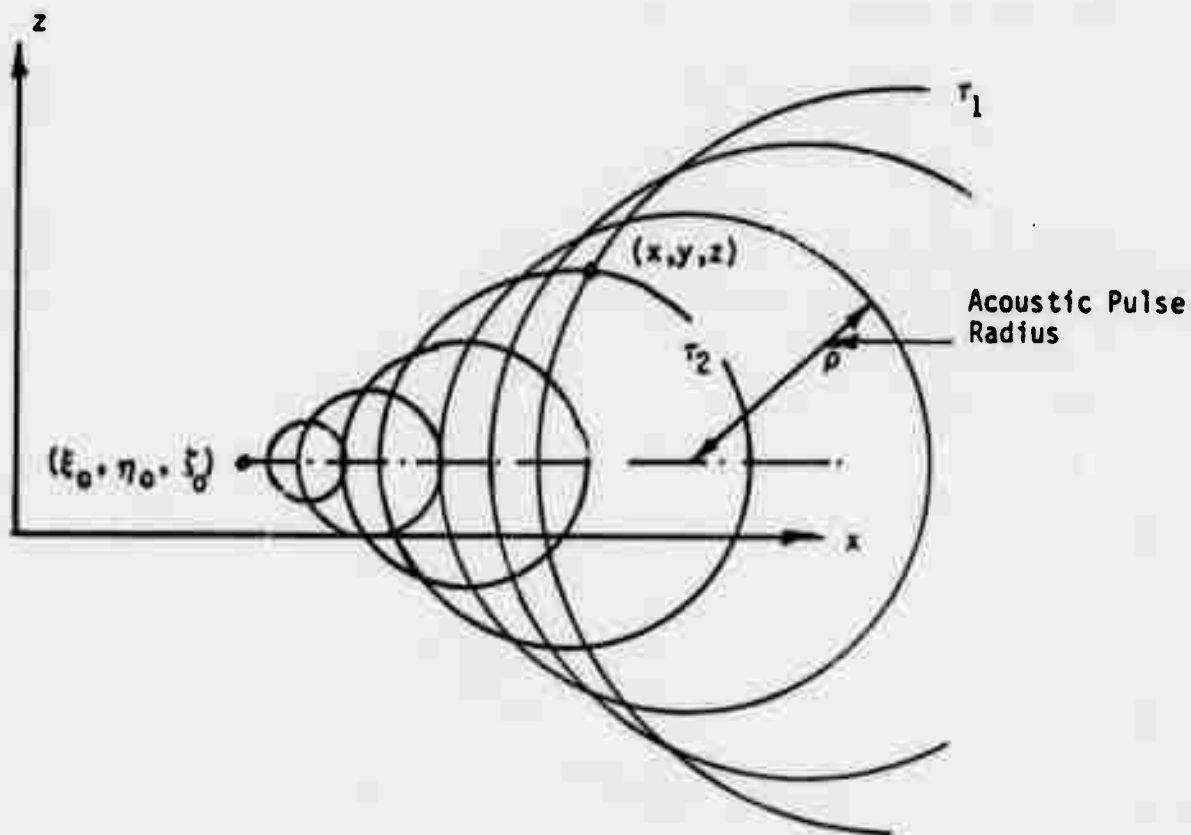


Figure 2.5-1 Time Histories of a Series of Acoustic Pulses Emittted From a Moving Point Source

$$\beta_{\infty}^2 = 1 - M_{\infty}^2$$

a = Speed of sound

In general, there are N such waves passing the receiving point for the nonuniform flow case. For this case, a special acoustic pulse generator is required to determine the time histories of the shapes and locations of the generated acoustic pulses in a nonuniform flow. Such an acoustic pulse generator is described in subsection 2.5.1.4.

In the expression for the source potential, ϕ , the term \tilde{R}_i is expressed in terms of acoustic pulse parameters as follows:

$$\tilde{R} = \tilde{\rho} \frac{|\vec{V}_T \cdot \vec{n}|}{\bar{a}}$$

where \vec{V}_T is the total velocity of a point on the acoustic pulse surface, \vec{n} its surface normal vector in the direction of travel (see Figure 2.5-2), \bar{a} , an equivalent speed of sound and $\tilde{\rho}$ an equivalent acoustic pulse radius. The acoustic pulse generator is used to determine \vec{V}_T and \vec{n} . The equivalent speed

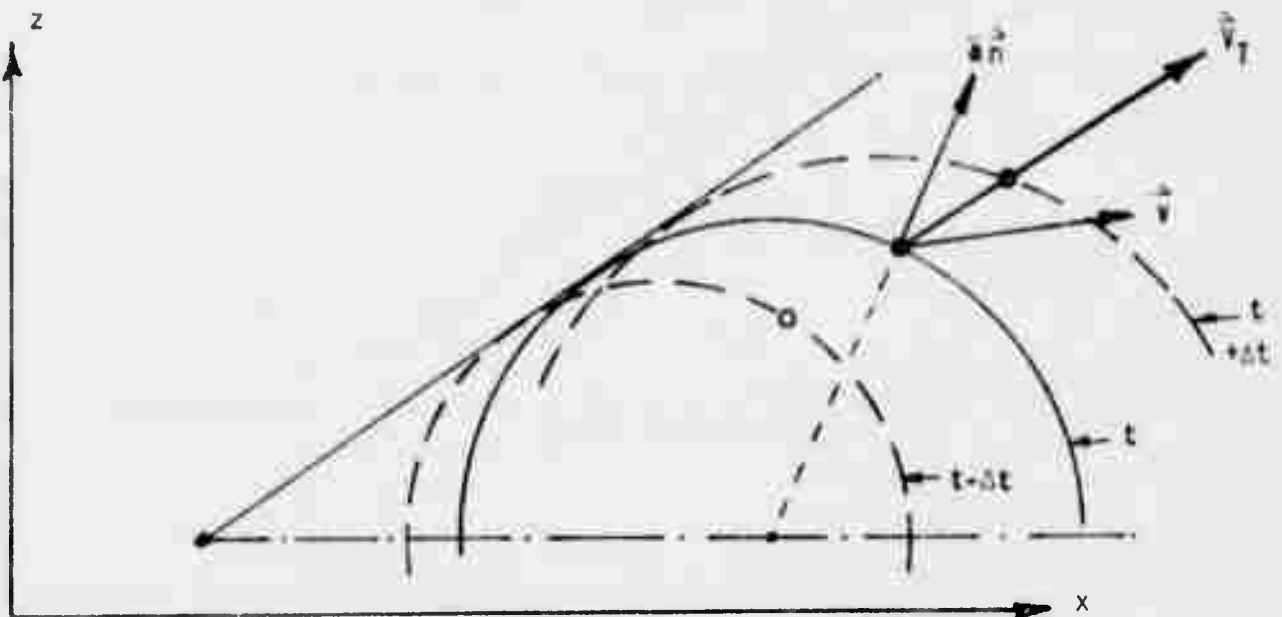


Figure 2.5-2 Pulse Surface Velocity Vectors

of sound \bar{a} is determined implicitly from the following formula

$$\vec{V}_T = \vec{V} + \bar{a} \vec{n}$$

This formula simply says that the total velocity, \vec{V}_T , of the wave front is a vector combination of the fluid velocity \vec{V} and the acoustic velocity of the pulse, $\bar{a} \vec{n}$. This is observed graphically in Figure 2.5-2. The nonuniform flow field \vec{V} must be known from a suitable steady transonic flow solution; in this case the Jameson Method (see section 2.5.1.4). Since the total, \vec{V}_T , is known from the acoustic pulse generator the equivalent speed of sound, \bar{a} , may be solved for. When no approximations for \vec{n} are used $\bar{a} = a$ and the formula for \bar{a} is not needed. The expression for \bar{a} is kept, however, for later reference as approximations for \vec{n} are introduced.

$$\bar{a} = (\vec{V}_T - \vec{V}) \cdot \vec{n}$$

The effective local Mach Number, \bar{M} , is then

$$\bar{M} = \frac{|\vec{V}|}{\bar{a}} = \frac{|\vec{V}|}{\vec{V}_T \cdot \vec{n} - \vec{V} \cdot \vec{n}}$$

The inverse of the term $\tilde{\rho}$ is a measure of the local wave strength along the wave parameter. For the uniform flow case this term reduces to the acoustic pulse radius, ρ , (see Figure 2.5-1) where:

$$\rho(t) = a(t - \tau_i)$$

and where a is the speed of sound in a uniform flow. A factor f is introduced to account for the fact that the wave strength, in a nonuniform flow, is not exactly proportional to the inverse of the acoustic pulse radius.

$$\tilde{\rho} = f\rho = fa(t - \tau_i)$$

For uniform flow, Appendix A shows that \tilde{R}_i simply becomes the hyperbolic radius for both the subsonic and supersonic cases. That is,

$$\tilde{R}_i \rightarrow R = \frac{r^2}{(x - \xi_0)^2 + \beta_\infty^2 r^2} \quad i = 1, 2 \quad \text{Uniform Flow Case}$$

If, further, the oscillatory case is considered for uniform flow, i.e., $\sigma(\tau) = \bar{\sigma} \exp(i\omega\tau)$, then the expression for the potential becomes:

$$\phi = \frac{1}{4\pi} \frac{\bar{\sigma}}{R} \sum_{j=1}^N e^{i\omega\tau_j}$$

For the supersonic case $N = 2$, and using the expressions for τ_1, τ_2 gives

$$\phi(t) = \frac{\bar{\sigma}}{2\pi R} \cos\left(\frac{\omega R}{a\beta^2}\right) \exp[i\omega M_\infty(x - \xi_0) / a\beta_\infty^2] e^{i\omega t}$$

For the subsonic case $N = 1$, and using the expression for τ_1 gives

$$\phi(t) = \frac{\bar{\sigma}}{4\pi R} \exp[i\omega M_\infty(x - \xi_0) / a\beta_\infty^2] \exp[-i\omega R/a\beta_\infty^2] e^{i\omega t}$$

These are the classic results for the potential of the supersonic and subsonic source.

2.5.1.2 Equivalent Sending Point Location

The acoustic pulse generator, to be described in subsection 2.5.1.4, provides a means of calculating the time history of an acoustic pulse emitted from a sending point (ξ_0, η_0, ζ_0) moving in a nonuniform steady transonic flow field. When the pulse has arrived at the receiving point, it has distorted from the classic circular shape and its wave strength has deviated from the classic value of σ/ρ where ρ is the pulse radius. However, locally at the receiving point (x, y, z) an equivalent circular pulse can be matched to the actual pulse (see Figure 2.5-3).

The quantities to be matched are the terms τ_j and \tilde{R}_j appearing in the expression for the source in a nonuniform flow potential:

$$\phi = \sum_{i=1}^N \frac{\sigma(\tau_i)}{4\pi\tilde{R}_i}$$

that is, the terms τ_i and \tilde{R}_i , for the equivalent circular pulse, are to be

matched to the actual pulse at the receiving point (x, y, z) . Once the match is made an equivalent sending point location $(\bar{\xi}_0, \bar{\eta}_0, \bar{\zeta}_0)$, flow field speed \bar{V} , speed of sound \bar{a} and pulse radius $\bar{\rho}$ can be found. The bar over the terms indicates equivalent terms and not actual ones. The derivation of these equivalent terms is given as follows.

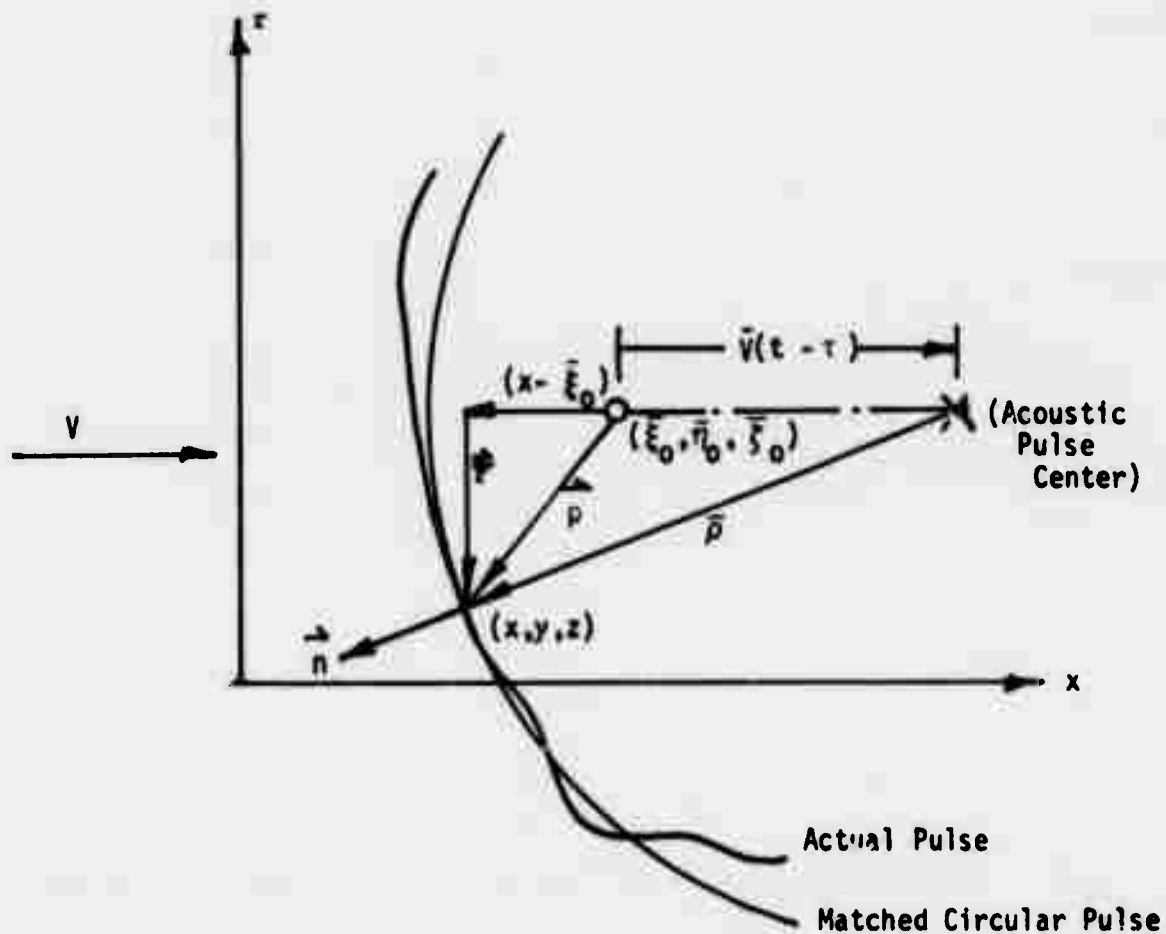


Figure 2.5-3 Matching a Circular Pulse to the Actual Pulse at the Receiving Point (x, y, z)

From Figure 2.5-3, the following vector identity is easily observed:

$$\vec{\rho} = (x - \bar{\xi}_0) \vec{i} + \vec{r} = \bar{V} (t - \tau) + \bar{\rho} \vec{n}$$

or by components:

$$(x - \bar{\xi}_0) = \bar{V} (t - \tau) + \bar{\rho} n_x$$

and

$$r = \bar{\rho} n_r$$

where $n_r = \hat{n} \cdot \frac{\vec{r}}{r}$

Using these quantities in the expression for the equivalent hyperbolic radius, \bar{R} , gives:

$$\begin{aligned} \bar{R}^2 &= (\bar{V} (t - \tau) + \bar{\rho} n_x)^2 + \bar{\beta}^2 \bar{\rho}^2 n_r^2 \\ &= \frac{\bar{\rho}^2}{\bar{a}^2} \left\{ \bar{a}^2 + 2n_x \bar{V} \bar{a} + \bar{V}^2 n_x^2 + L \right\} \end{aligned}$$

where

$$L = n_r^2 (\bar{V}^2 - \bar{M}^2 \bar{a}^2)$$

Now if we require that

$$\bar{M} = \frac{\bar{V}}{\bar{a}}$$

then $L = 0$ and \bar{R} becomes

$$R = \bar{\rho} \left| 1 + \frac{\bar{V} n_x}{\bar{a}} \right|$$

It can be shown that this expression reduces to the expression for \tilde{R}/f as follows:

$$\tilde{R} = \tilde{\rho} \left| \frac{\vec{V}_T \cdot \vec{n}}{\bar{a}} \right| = f \bar{R}$$

when it is assumed that the equivalent velocity is parallel to the x-axis, i.e., $\vec{V} = \bar{V} \hat{i}$ and when we take note of the expressions

$$\vec{V}_T = \vec{V} + \bar{a} \vec{n}$$

$$\tilde{\rho} = f \bar{\rho}$$

which were given in subsection 2.5.1. Thus, the equivalent hyperbolic radius is \bar{r} and the expression for the potential becomes:

$$\phi_e = \sum_{i=1}^N \frac{\sigma(\tau_i)}{f_i} \frac{1}{\bar{R}_i}$$

The quantities \bar{V} , $\bar{\rho}$, f and \bar{a} are yet to be determined. First, assume that \bar{V} is the local flow field velocity at the receiving point (x, y, z) . Secondly, the pulse radius $\bar{\rho}$ can be selected by fitting the best radius to the actual pulse or simply by letting it be $\bar{a}(t - \tau)$ where \bar{a} is the equivalent speed of sound. For simplicity, the latter is assumed. The quantity f is then obtained by noting the actual strength of the wave and comparing it to $\bar{a}(t - \tau)$, i.e.,

$$f = \frac{\bar{\rho}}{\bar{a}(t - \tau)}$$

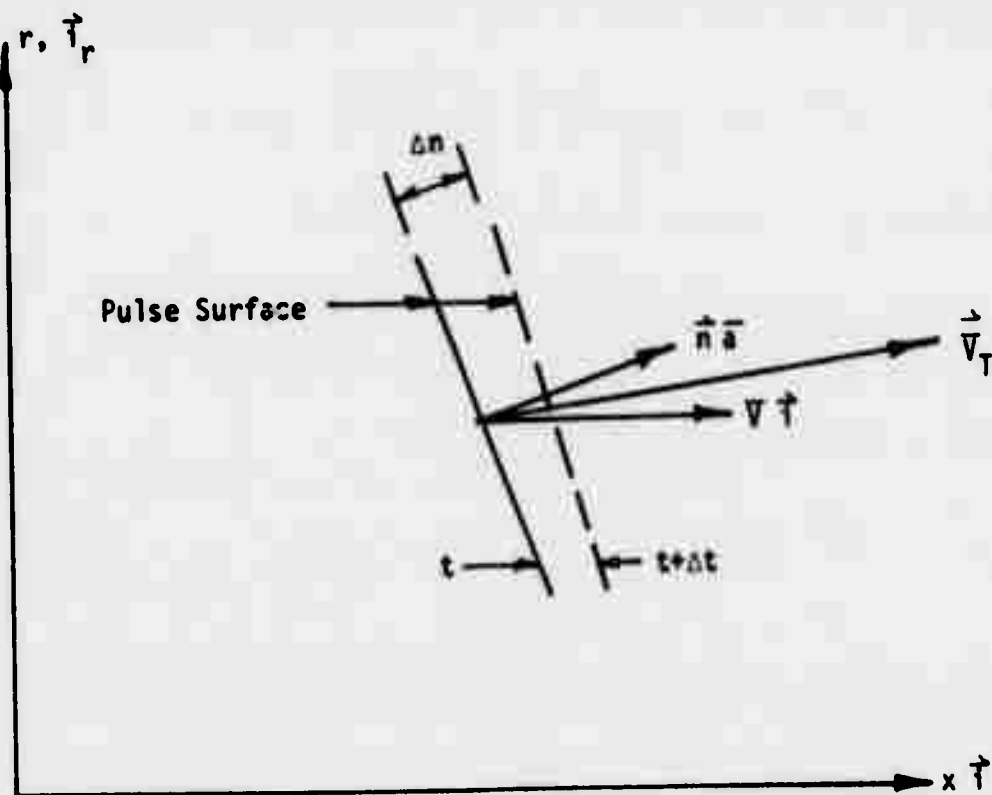


Figure 2.5-4 Pulse Surface at Time = t and $t+\Delta t$ and Associated Vector Quantities

Thirdly, the equivalent local speed of sound can be obtained by referring to Figure 2.5-4. This figure shows the position of a wave at two time intervals Δt apart. Inspection of the figure shows that:

$$\vec{V}_T = \vec{n} \bar{a} + \bar{V} \vec{i} = \frac{\Delta n}{\Delta t} \vec{n}$$

The term $\Delta n/\Delta t$ can be obtained from the acoustic pulse generator in a numerical manner from the pulse shape at two successive times. Lastly, knowing the values of \bar{V} and \vec{n} allows \bar{a} to be solved for as follows:

$$\bar{a} = \left(\frac{\Delta n}{\Delta t} - \bar{V} \vec{i} \cdot \vec{n} \right)$$

All terms in the expression for ϕ_e are now known and it can be used in the form presented. However, the classic potential is usually not used in this form. Usually the more classical one given at the end of subsection 2.5.1.1 is used. In these expressions, the terms τ_1 and τ_2 are given in terms of $(x - \xi_0)$, M_∞ and R as given in Appendix A. According to Figure 2.5.3,

$$\bar{r}^2 + [(x - \bar{\xi}_0) + \bar{V} (t - \tau)]^2 = \bar{a}^2 (t - \tau)^2$$

solving this expression in terms of $(t - \tau)$ gives

$$\pm (t - \tau) = \frac{-(x - \bar{\xi}_0) \bar{V}/\bar{a} \pm \bar{R}}{\bar{a} (1 - \bar{M}^2)}$$

Since $\bar{M} = \bar{V}/\bar{a}$ then

$$\bar{\beta}^2 = 1 - \bar{M}^2$$

$$\bar{R}^2 = (x - \xi_0)^2 + \bar{\beta}^2 \bar{r}^2$$

and

$$\bar{r} \omega(t - \tau) = \left\{ k_r \frac{2\bar{M}}{c\bar{\beta}^2} [(x - \bar{\xi}_0) \bar{M} \pm \bar{R}] \right\} / \bar{V}/U_\infty$$

where $k_r = \omega \bar{c} / 2U_\infty$

Thus, the classic expression for $\omega(t - \tau)$ is modified by simply replacing M_∞ with \bar{M} , and $(x - \xi_0)$ and r with $(x - \bar{\xi}_0)$ and \bar{r} and dividing by \bar{V}/U_∞ . The classic oscillatory subsonic case has one root, i.e., $i = 1$ and the result, taken from the end of subsection 2.5.1.1, is:

$$\phi = e^{i\omega t} \frac{\bar{\sigma}}{4\pi R} \exp [(M_\infty (x - \xi_0) - R) (ik_r 2M_\infty / \bar{c} \beta_\infty^2)]$$

If we introduce the equivalent quantities, i.e.,

$$(x - \xi_0) \rightarrow (x - \bar{\xi}_0) = \bar{V}(t - \tau) + \bar{\rho} \eta_x$$

$$r \rightarrow \bar{r} = \bar{\rho} \eta_r$$

$$M_\infty \rightarrow \bar{M} = \bar{V}/\bar{a}$$

where

$$\bar{a} = \left(\frac{\Delta n}{\Delta t} - \bar{V} \hat{i} \cdot \hat{n} \right)$$

$$\bar{\rho} = (t - \tau) \bar{a}$$

and where \bar{V} is the local flow field velocity at the receiving point and $(t - \tau)$ is the time required for the acoustic pulse to move from the sending point to the receiving point; then the equivalent potential ϕ_e for a source in a nonuniform flow is

$$\phi_e = e^{i\omega t} \frac{\bar{\sigma}}{4\pi \bar{R} \bar{f}} \exp [(\bar{M} (x - \bar{\xi}_0) - \bar{R}) (ik_r 2\bar{M} U_\infty / \bar{c} \bar{\beta}^2 \bar{V})]$$

where

$$\bar{R}^2 = (x - \bar{\xi}_0)^2 + \bar{\beta}^2 \bar{r}^2$$

Here the quantities $(t - \tau)$, $\Delta n/\Delta t$ and \hat{n} are obtained from the acoustic

pulse generator and, \bar{V} , from the steady transonic flow generator.

2.5.1.3 The Two Dimensional Transonic Source

The three-dimensional source can be written as:

$$\begin{aligned}\phi_e &= \bar{\phi}_e e^{i\omega t} \\ \bar{\phi}_e &= \frac{\bar{\sigma}}{4\pi f} e^{i\bar{M}\bar{\lambda}(x-\bar{\xi}_0)} \frac{e^{-i\bar{\lambda}\bar{R}}}{\bar{R}}\end{aligned}$$

where $\bar{\lambda} = \lambda/\bar{V}/U_\infty$

where $\lambda = k_r \frac{\bar{M}}{\bar{\beta}^2} \frac{2}{c}$

The two-dimensional source can be obtained from the three-dimensional one by integrating the sending point in the η_0 -direction from plus to minus infinity.

$$\bar{\phi}_{2D} = \int_{-\infty}^{\infty} \bar{\phi}_e d\eta_0$$

If we assume f is independent of η then

$$\bar{\phi}_{2D} = \frac{\bar{\sigma}}{4\pi f} e^{i\bar{M}\bar{\lambda}(x-\bar{\xi}_0)} \int_{-\infty}^{\infty} e^{-i\bar{\lambda}\bar{R}} d\eta_0$$

but

$$\int_{-\infty}^{\infty} \frac{e^{-i\bar{\lambda}\bar{R}}}{\bar{R}} d\eta_0 = 2 \int_{R_{2D}}^{\infty} \frac{e^{-i\bar{\lambda}\bar{R}} d\bar{R}}{-\bar{\beta}^2(y-\eta_0)} = \frac{2}{-\bar{\beta}} \int_{R_{2D}}^{\infty} \frac{e^{-i\bar{\lambda}\bar{R}} d\bar{R}}{\sqrt{\bar{R}^2 - R_{2D}^2}}$$

where

$$R_{2D}^2 = (x - \bar{\xi}_0)^2 - \bar{\beta}^2 (z - \bar{\zeta}_0)^2$$

Introducing $\theta = \bar{R}/R_{2D}$ gives

$$\frac{2}{-\bar{\beta}} \int_{-\infty}^{\infty} \frac{e^{-i\lambda R}}{\sqrt{\bar{R}^2 - R_{2D}^2}} d\bar{R} = \frac{2}{-\bar{\beta}} \int_1^{\infty} \frac{e^{-i\lambda R_{2D} \theta}}{\sqrt{\theta^2 - 1}} d\theta = \frac{i\pi}{\bar{\beta}} H_0^{(2)}(\lambda R_{2D})$$

Thus the two-dimensional equivalent source is

$$\phi_{2D} = \frac{i\bar{\sigma}}{\bar{\beta}4f} e^{i\bar{M}\lambda(x - \bar{\xi}_0)} H_0^{(2)}(\lambda R_{2D})$$

(See Appendix C for expression for supersonic flow)

The only difference between this source and the classic uniform flow source are the quantities f , \bar{V}/U_{∞} , \bar{M} and $x - \bar{\xi}_0$ and $z - \bar{\zeta}_0$.

The assumption is now made that the source potential, ϕ_{2D} , may be differentiated and integrated to produce the velocity field due to a pressure doublet. This is necessary because the pressure doublet is the basic singularity used in lifting surface theory.

This assumption is probably accurate for differentiation; however, integration requires consideration of a sending point that varies from the origin to downstream infinity. The first step in obtaining the downwash due to a pressure doublet is to obtain the downwash due to a velocity doublet by a double differentiation, i.e., $\partial^2 \phi_e / \partial \xi \partial z$. The second step is to integrate the effects of a distribution of velocity doublets along a line originating at (ξ_0, ζ_0) and passing to downstream infinity parallel to the x-axis. The most accurate way to handle this is to obtain a new $(t - \tau)$, $\Delta n / \Delta t$, etc. for points along the integration path and perform the integration numerically. For now however, the values of $(t - \tau)$, $\Delta n / \Delta t$, etc. will be obtained for the origin only (ξ_0, ζ_0) . In essence, this assumption states that the flow is nonuniform from the sending point $(\bar{\xi}_0, \bar{\zeta}_0)$ to the receiving point (x, z) but that the flow is uniform from a point in the wake of the sending point up to the sending point itself. Figure 2.5-5 gives a graphical illustration.

With these assumptions one simply introduces the equivalent geometry, $(x - \bar{\xi}_0)$ and $(z - \bar{\zeta}_0)$, along with the equivalent Mach Number, \bar{M} , into the

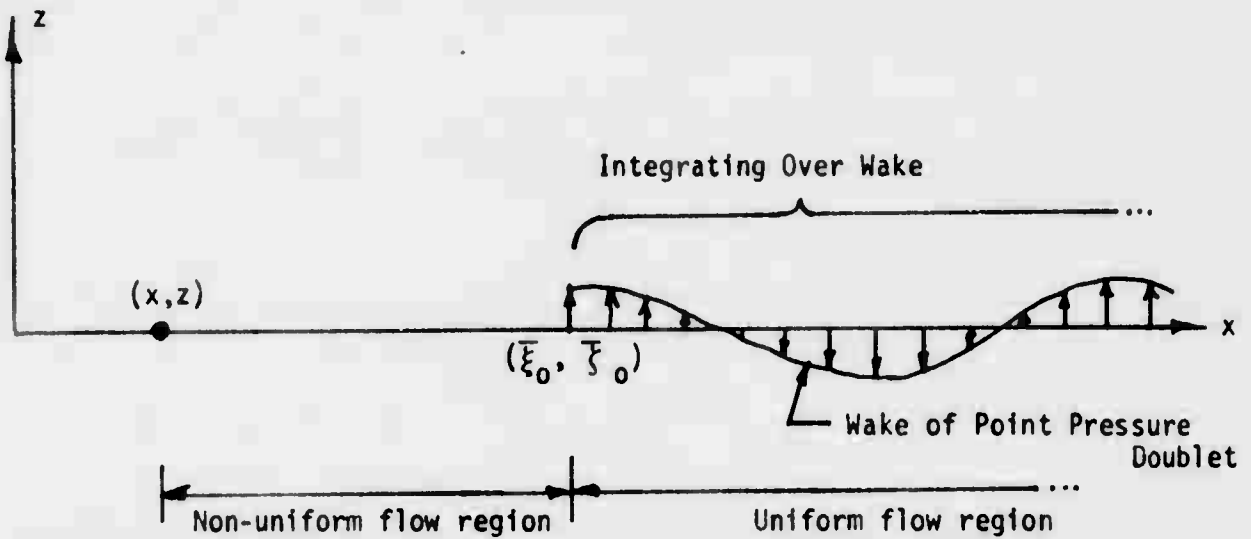


Figure 2.5-5 Result of Assuming that the Equivalent Geometry $(\bar{\xi}_0, \bar{\zeta}_0)$ Applies Directly to a Point Pressure Doublet.

expression for the point pressure doublet (used in lifting surface theory) and then proceeds to solve the resulting equations in the usual manner.

2.5.1.4 Acoustic Pulse Generator

In the previous subsections expressions were derived for equivalent distances and Mach Numbers based on the properties of acoustic pulses traveling in nonuniform flow fields. It was assumed that the following data were obtainable from these acoustic pulses: (1) $(t - \tau)$, the time taken for a pulse to travel from its origin (ξ_0, ζ_0) to a receiving point (x, z) ; (2) \vec{n} , the normal vector of the pulse surface at the receiving point; and (3) f , the dialation of the pulse over and above the usual time dialation. These quantities are known if the time history of the pulse is known. In this subsection, a method of computing the pulse time history in a nonuniform flow field will be presented.

Basically, a pulse surface is made up of a series of points each of which has its own time history or trajectory. The velocity of these surface points depends on the flow field velocity, the speed of sound, and the normal direction of the surface in the direction of motion.

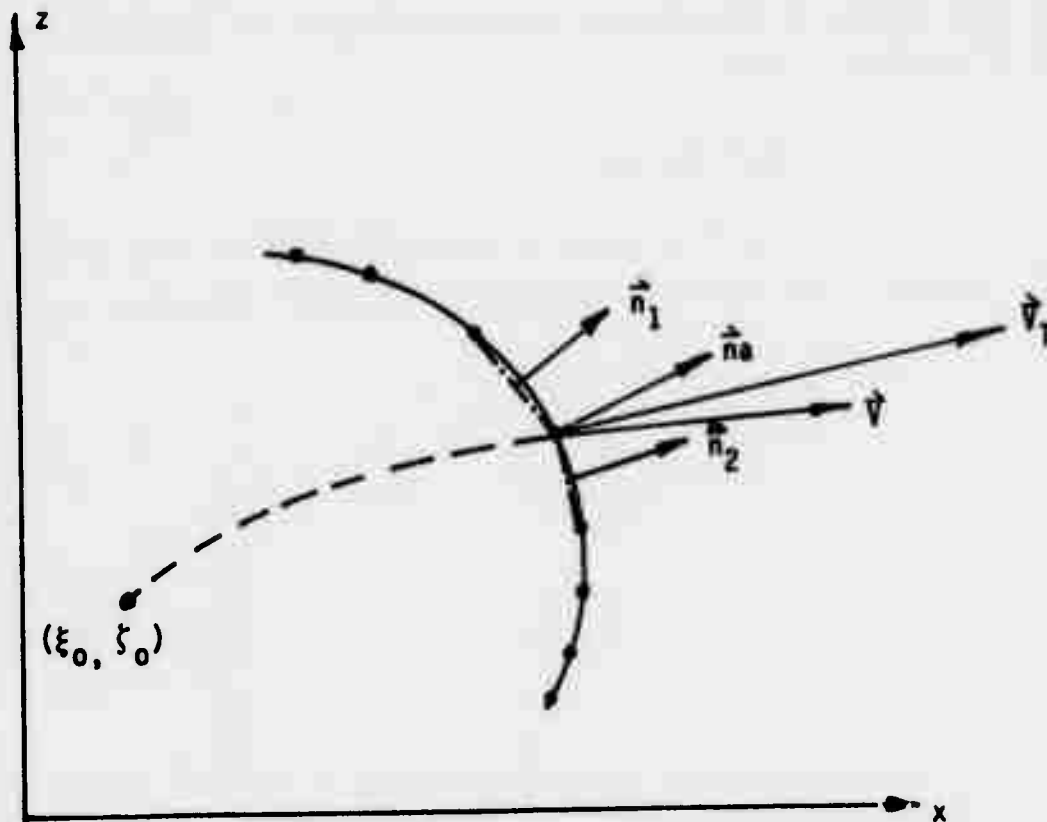


Figure 2.5-6 Quantities Associated With the Trajectories of Points Lying on a Pulse Surface

Specifically, Figure 2.5-6 shows that the total velocity \vec{V}_T of a point in the acoustic pulse surface is the vector addition of the flow field, \vec{V} , and the pulse front velocity, which is the speed of sound in the direction of the surface normal, i.e., a \vec{n} . Thus the total is:

$$\vec{V}_T = \vec{V} + \vec{n}a$$

or in the normalized form,

$$\frac{\vec{V}_T}{U_\infty} = \frac{\vec{V}}{U_\infty} + \frac{\vec{n}a}{M_\infty}$$

where M_∞ is the free stream Mach Number.

The normal vector, n , at a pulse surface point is obtained by averaging the normal vectors of the elements on either side of the point as Figure 2.5-6 illustrates. Thus,

$$\vec{n} = (\vec{n}_1 + \vec{n}_2) / 2$$

More sophisticated curve fitting procedures were tried but they were found to be time consuming and sometimes unstable. This simple procedure has worked best.

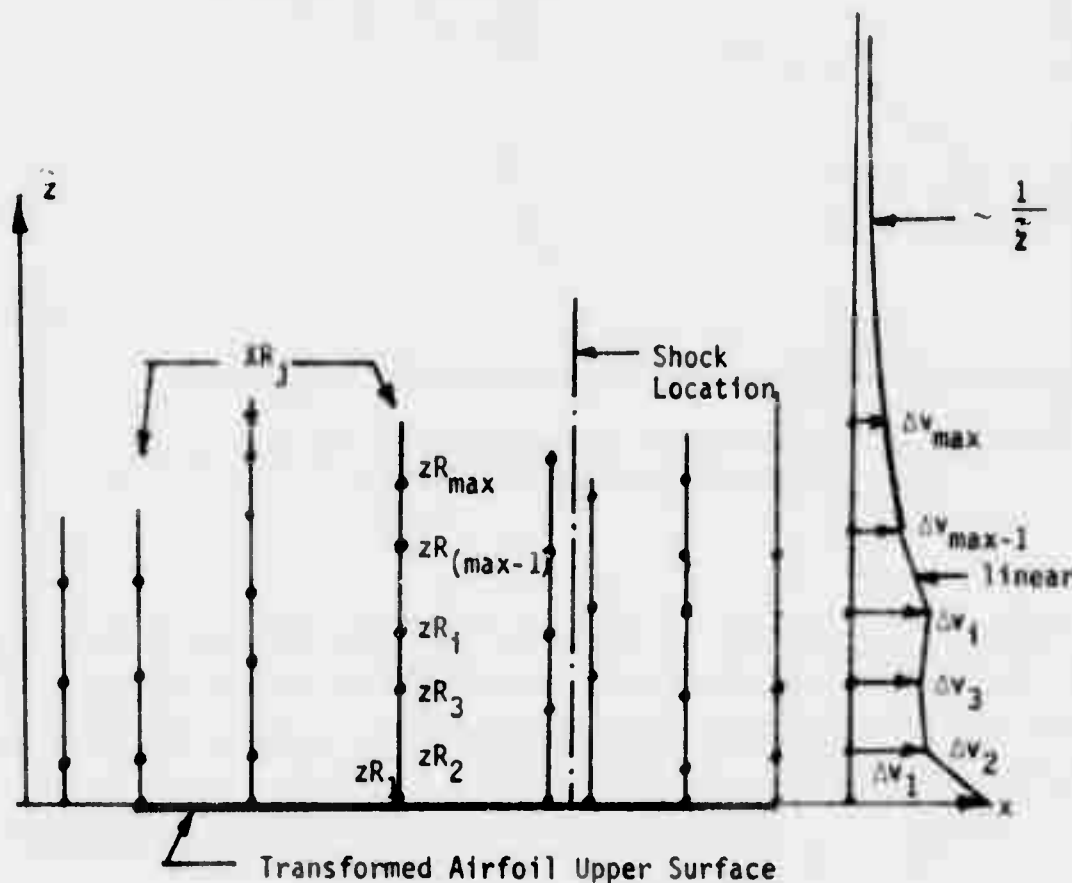


Figure 2.5-7 Grid Used for The Interpolation of The Transonic Flow Velocity Field

The velocity $\vec{V}(x, z)$ was obtained by an interpolation/extrapolation procedure based on a set of velocities obtained from a modified Jameson steady two-dimensional transonic computer program (Reference 11).

The onset velocity field V is broken up into a uniform component $U_{\infty} \vec{i}$ and a nonuniform increment, ΔV . The interpolation/extrapolation is performed on the nonuniform increment, ΔV . The vector notation will be dropped for convenience. Also, with this program, it was assumed that $\Delta V_z k$ was small enough to ignore. The interpolation in the x-direction is linear as follows:

$$\Delta V(x, \tilde{z}) = [\Delta V_{j+1}(\tilde{z}) - \Delta V_j(\tilde{z})] m_x + \Delta V_j(\tilde{z})$$

where

$$m_x = \frac{x - XR_j}{XR_{j+1} - XR_j}$$

and where XR_j are the x-locations of $\Delta V_j(\tilde{z})$, i.e., the values to be interpolated from. Figure 2.5-7 illustrates the grid of points. The tilda over the z indicates a transformed plane where the airfoil surface transforms into the $\tilde{z} = 0$ plane. The upper and lower surfaces are calculated separately and treated independently. The transformation required to render $\tilde{z} = 0$ on the surface is assumed small enough to ignore subsequent to the transformation.

The determination of $\Delta V_j(\tilde{z})$ is either found by linear interpolation, for $\tilde{z} \leq ZR_{(\max-1)}$ or by curve fitting for $\tilde{z} > ZR_{(\max-1)}$. The expression for interpolation is:

$$\Delta V_j(\tilde{z}) = [\Delta V_j(\tilde{z}R_{i+1}) - \Delta V_j(\tilde{z}R_i)] m_{z_i} + \Delta V_j(\tilde{z}R_i) \quad \tilde{z} \leq ZR_{(\max-1)}$$

where

$$m_{z_i} = \frac{\tilde{z} - \tilde{z}R_i}{\tilde{z}R_{i+1} - \tilde{z}R_i}$$

For the case $z > ZR_{(\max-1)}$ the formula to use is:

$$\Delta V_j(\tilde{z}) = \Delta V_j(ZR_{\max}) \frac{(bZR_{\max} + 1)}{(b\tilde{z} + 1)}$$

$$b = \frac{\Delta V_j(ZR_{\max}) - \Delta V_j(ZR_{\max-1})}{ZR_{\max-1} \Delta V_j(ZR_{\max-1}) - ZR_{\max} \Delta V_j(ZR_{\max})}$$

This formula has the property of approaching zero like $1/\tilde{z}$ as \tilde{z} approaches infinity. This formula is fitted through the last two points; ZR_{\max} and $ZR_{\max-1}$. Figure 2.5-7 also illustrates this curve.

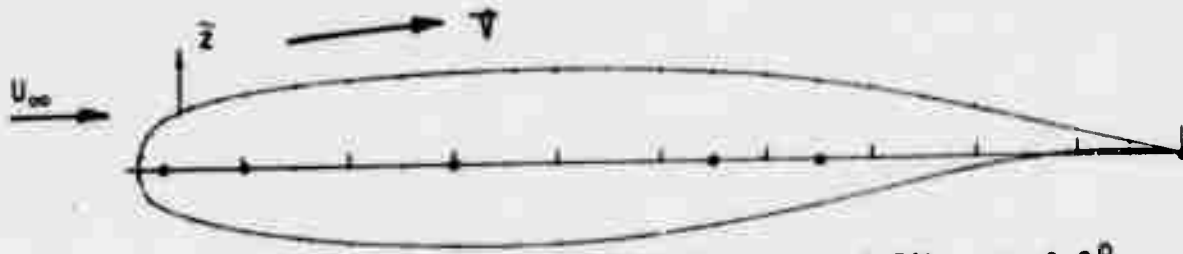
The values of $\Delta V_j(ZR_i)$ are obtained from a modified version of the steady flow two-dimensional transonic method of Jameson (Reference 11). The method had to be modified since only surface values of velocity, pressure and Mach Number were computed. Appendix B presents the method used in modifying the Jameson procedure to produce the flow field velocities off of the body surface. Basically, what was available was the potential at various grid points in a plane transformed so that the space around the airfoil was mapped into a rectangle, one unit high and two units wide. The procedure involves multiple mappings and Appendix B presents the properties of these and their use in obtaining the flow field velocities. Figure 2.5-8 presents an example of the flow field incremental velocity, $V - U_\infty$, as calculated by the modified Jameson procedure for the NLR 7301 airfoil operating at $M_\infty = 0.745$ and $\alpha = -0.20^\circ$.

The acoustic pulse generator is initiated by prescribing an initial set of points, given on the arc of a very small circle. As time passes, the pulse radius, and thus, the distance between adjacent points, becomes large. An automatic procedure for filling points in between these initial points has been implemented. Thus, the character and accuracy of the pulse surface is maintained even if the surface is dialated excessively at various points. Points are filled in at a rate such that the distance, D , between adjacent points does not exceed:

$$D \leq A(t - \tau)a$$

where A is a prescribed parameter.

Example calculations of the acoustic pulse generator are shown in Figure 2.5-9 through 2.5-11. Figure 2.5-9 presents the time history of the surface of an acoustic pulse in a nonuniform flow whose origin is at the 55% point on the NLR 7301 airfoil operating at $M_\infty = 0.7$ and $\alpha = 1.75^\circ$. Below the x-axis is presented, for reference, the time history of the same pulse in



NLR 7301 Airfoil, $M_\infty = 0.745$, $\alpha = -0.2^\circ$

$$\Delta V = |\vec{V}| - U_\infty$$

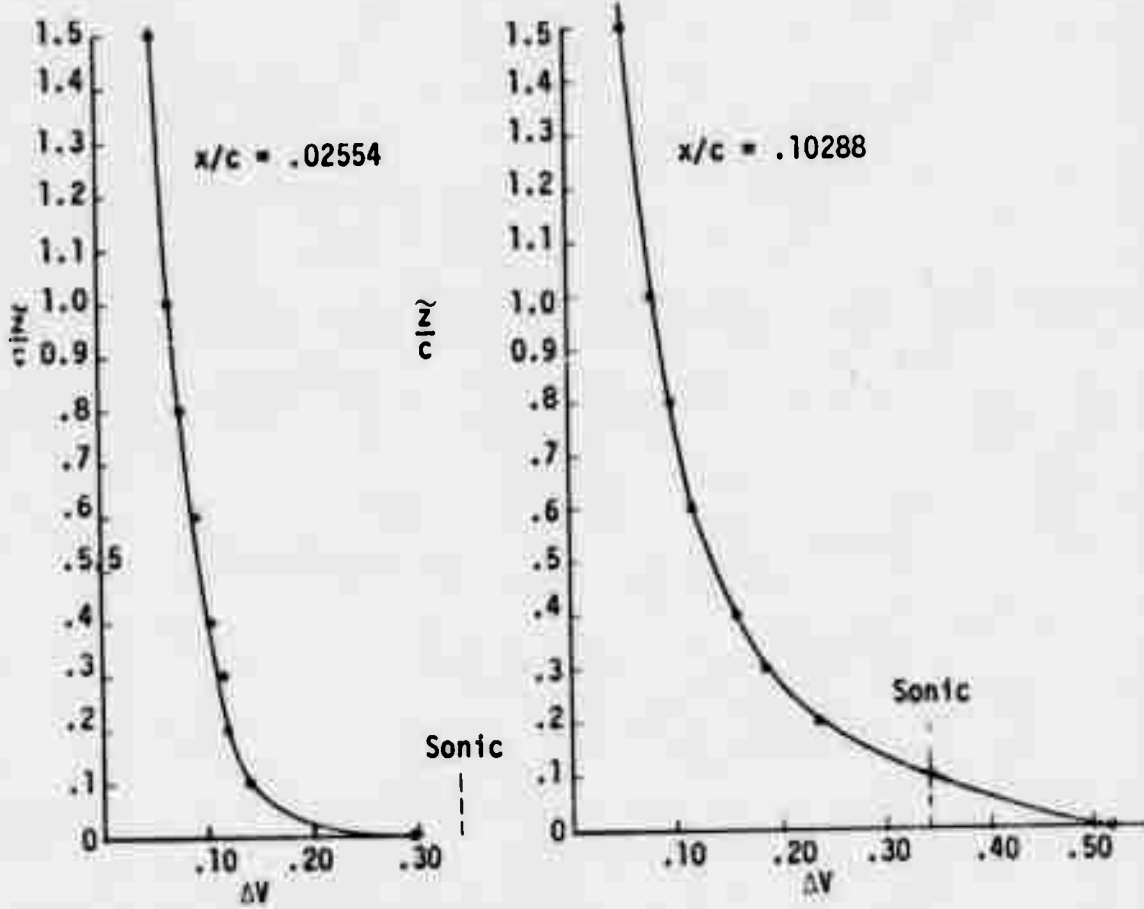


Figure 2.5-8 Non-uniform Flow Field Increment Over the NLR 7301 Airfoil As Calculated by the Jameson Transonic Flow Method

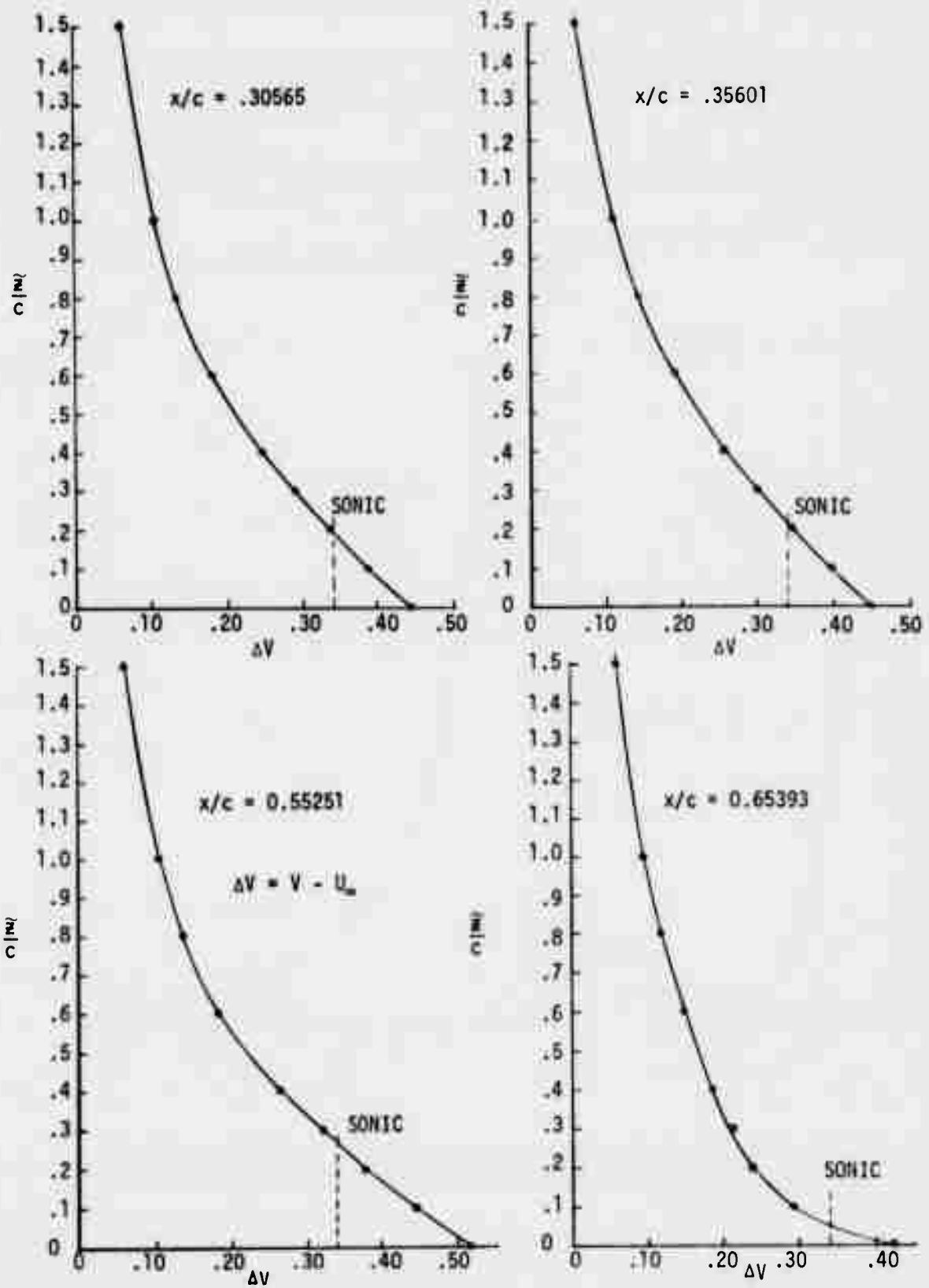


Figure 2.5-8 (Continued)

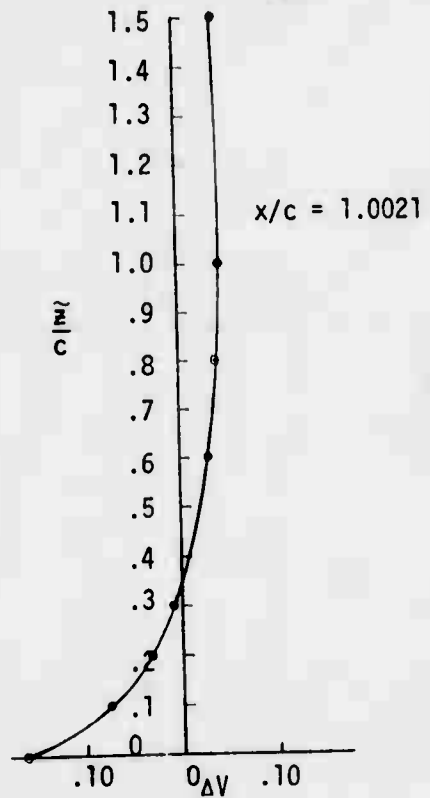
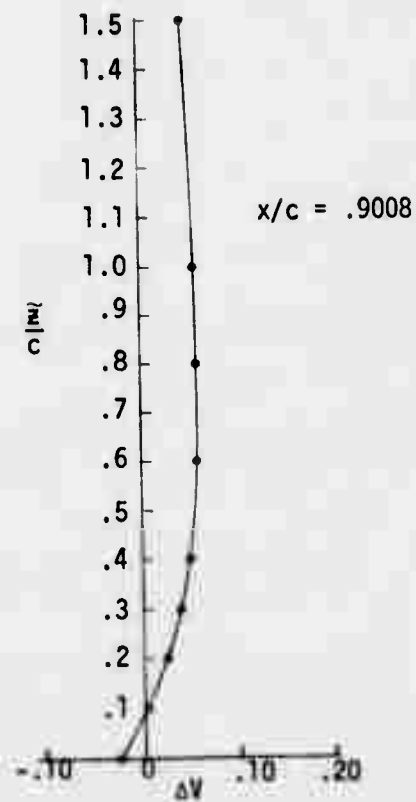
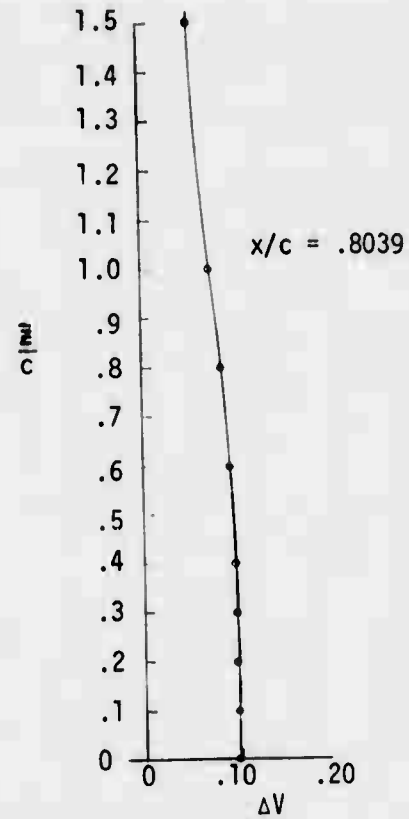
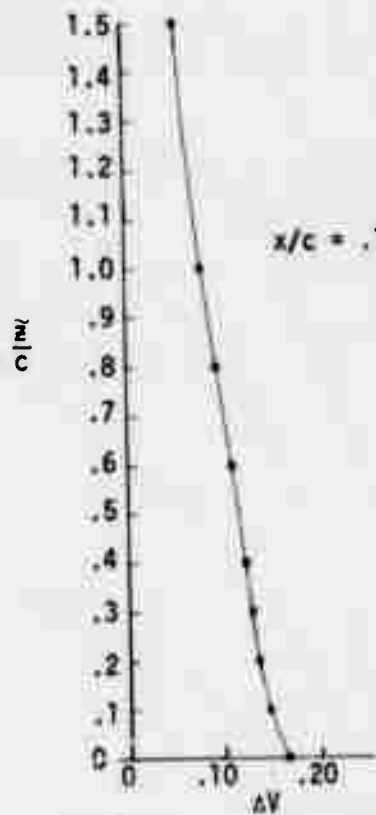


Figure 2.5-8 (Continued)

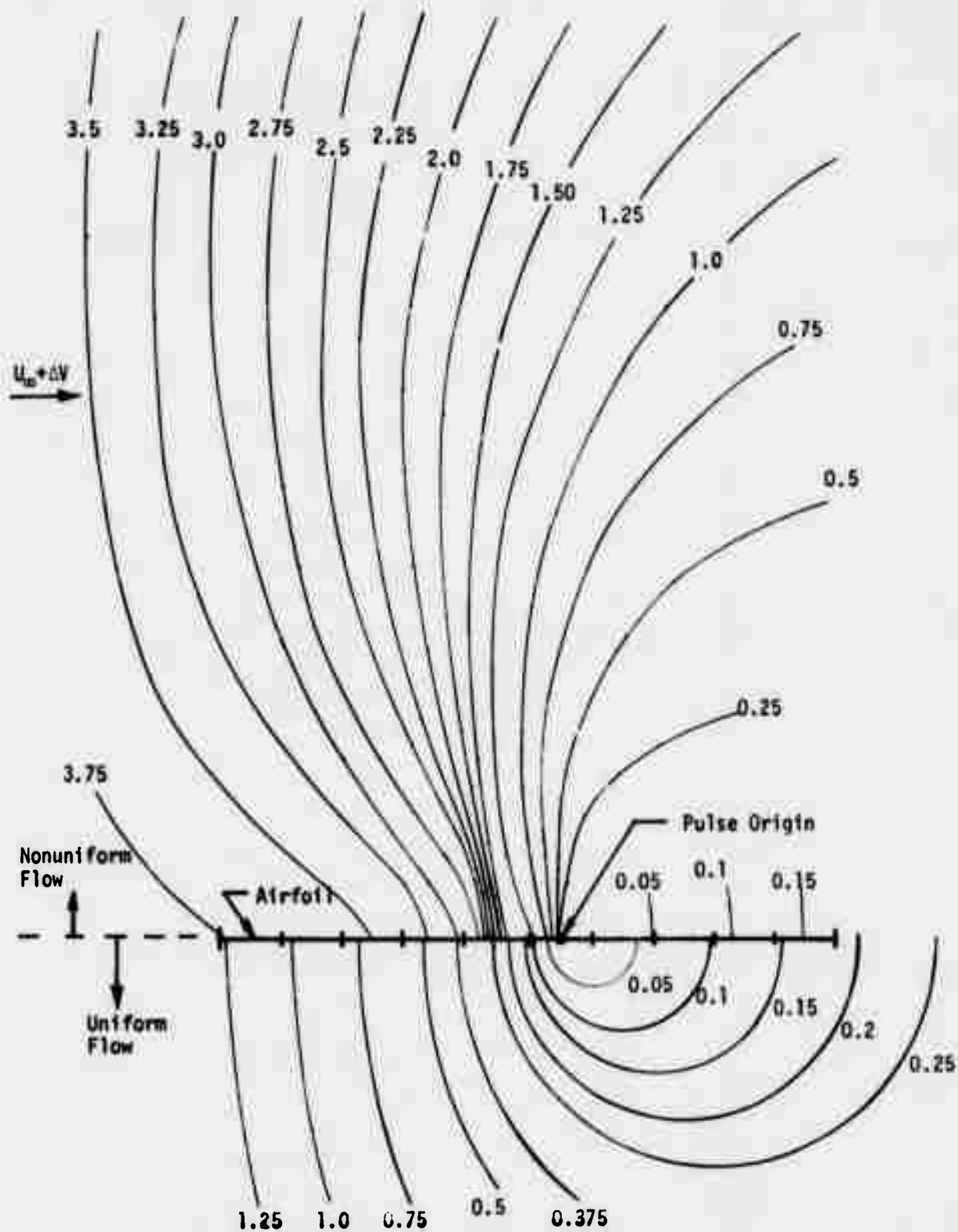


Figure 2.5-9 Time History of An Acoustic Pulse Whose Origin is At $x/c = 0.55$ For The Nonuniform Flow (above axis) and Uniform Flow (below axis) Cases. Nonuniform Flow is That for The NLR 7301 Airfoil ($M_\infty = 0.7, \alpha = 1.75^\circ$) on the Upper Surface

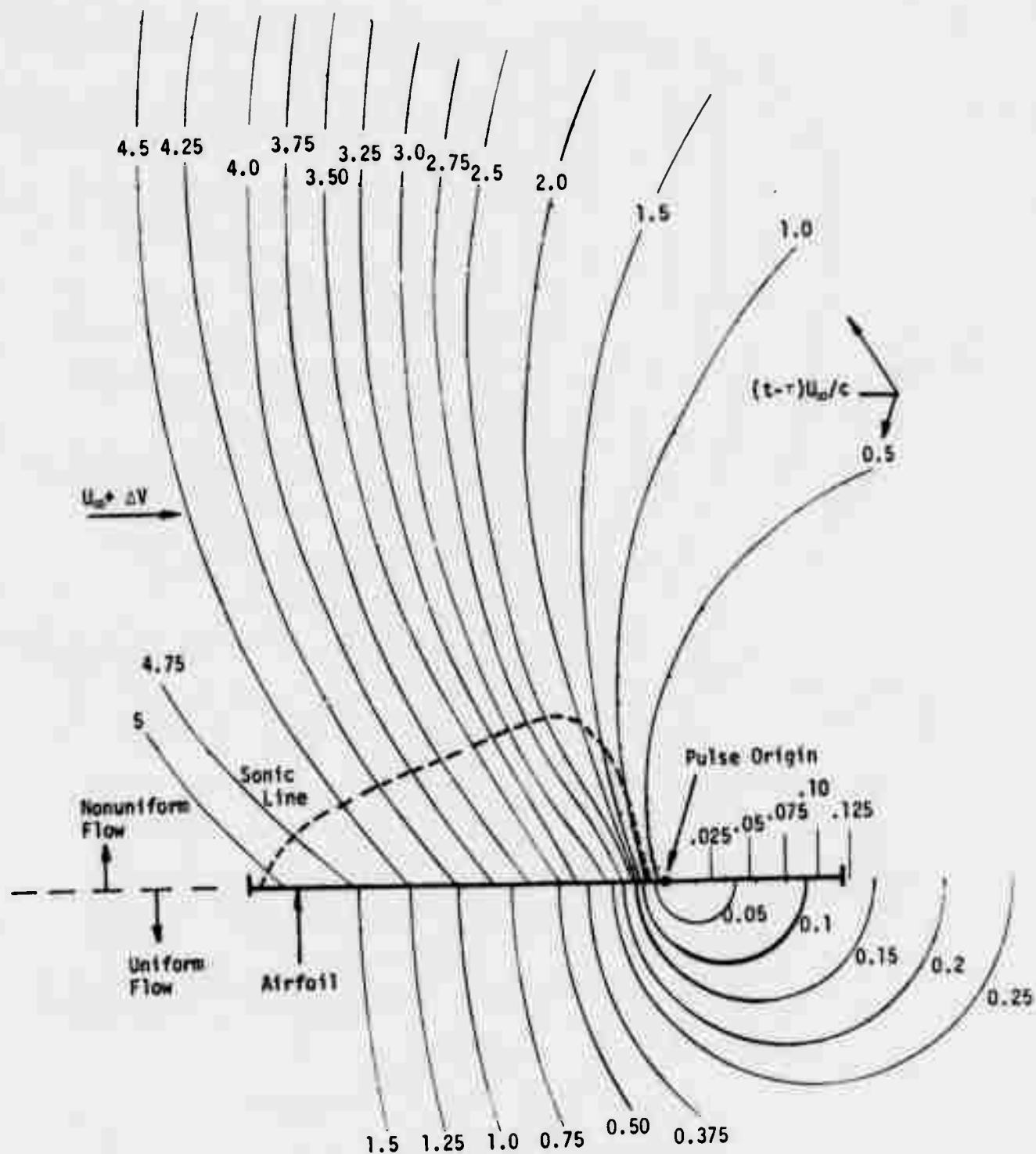


Figure 2.5-10(a) Time History of an Acoustic Pulse Whose Origin is At $x/c = 0.70$ For the Non-Uniform Flow (above axis) And Uniform Flow (below axis) Cases. Non-Uniform Flow is That for the NLR 7301 Airfoil ($M_\infty = 0.745$, $\alpha = -0.2$) On The Upper Surface.

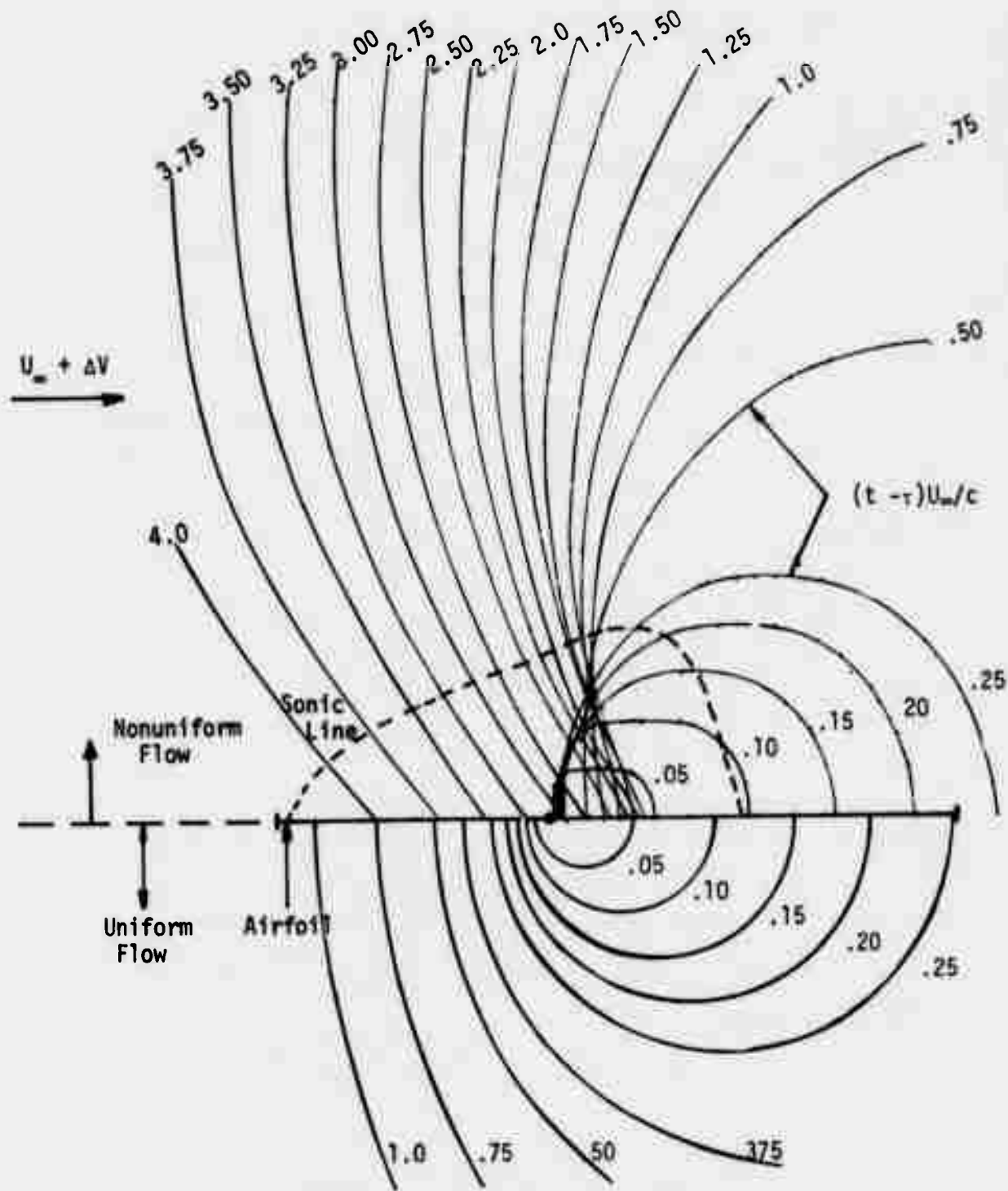


Figure 2.5-10 (b) Time History of an Acoustic Pulse Whose Origin is at $x/c = 0.4$ for the Non-Uniform Flow (Above Axis) and Uniform Flow (below axis) Case. Nonuniform Flow is that for the NLR 7301 Airfoil ($M_\infty = 0.745$, $\alpha = -0.2^\circ$) on the Upper Surface.

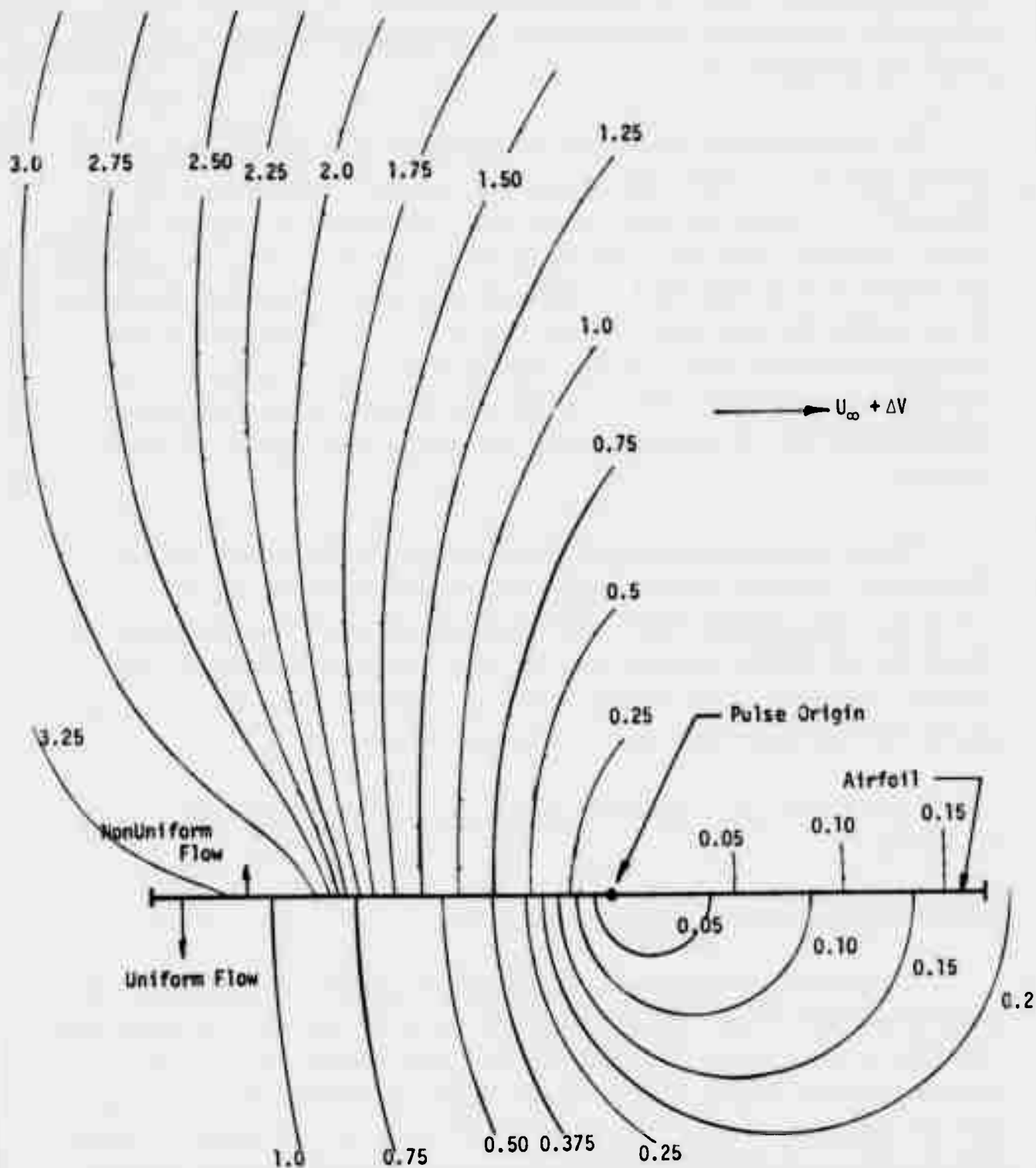


Figure 2.5-11 Time History of An Acoustic Pulse Whose Origin is At $x/c = 0.55$ For The Non-Uniform Flow (above axis) and Uniform Flow (below axis) Cases. Non-Uniform Flow is That for The TF-8A Wing Section at $y/(b/2) = 0.657$ ($M_{2D} = 0.711$ $\alpha_{2D} = 4.2^\circ$) on the Upper Surface.

in a uniform flow. The time history depicted below the x-axis is the type assumed for the classic lifting surface theory, whereas that shown above the x-axis is the actual one.

The nonuniform flow field found on the upper surface of the NLR 7301 airfoil operating as indicated possesses a supersonic zone ahead of the 40% point which is terminated with a shock wave that extends to a height of $0.2c$. A small secondary supersonic zone occurs aft of the shock also. The acoustic pulse surface moves forward very slowly at first slowing down even further as it approaches the shock wave location (40% point). The upper part of the acoustic pulse moves forward of the lower part causing a rotation in the inclination of the wave surface. As the wave rotates counter clockwise it starts moving into the supersonic zone; the greater the rotation the faster it moves.

Figures 2.5-10(a) and (b) presents a similar calculation for the NLR 7301 airfoil operating at the design "shock free" point of $M_\infty = 0.745$ and $\alpha = -0.20$. Even though there is no shock the supersonic zone still acts like a barrier to the advancing acoustic wave. The wave shapes are qualitatively similar to those for the shock wave condition except that the pulse passes into the supersonic zone a little more smoothly.

Figure 2.5-11 presents a third example calculation. This involves the TF-8A wing.

2.5.1.5 Application to Lifting Surface Theory

The transonic approach taken in this report consists of finding equivalent geometry and Mach Number that exist between a sending and receiving points and then placing these equivalent quantities into the classic theory for the desired transonic result. Thus a classic method is required that will cover both the subsonic and supersonic cases. The Doublet Lattice Method is subsonic only and thus, a supersonic extension is needed. Such an extension for the two-dimensional case is derived in Appendix C. As a test case, the supersonic Doublet Lattice Method was compared to the analytic solution for an airfoil pitching about its mid-chord at $M = 1.2$ and $k_\gamma = 0.99$. The result shown in

Figure 2.5-12 is very satisfactory.

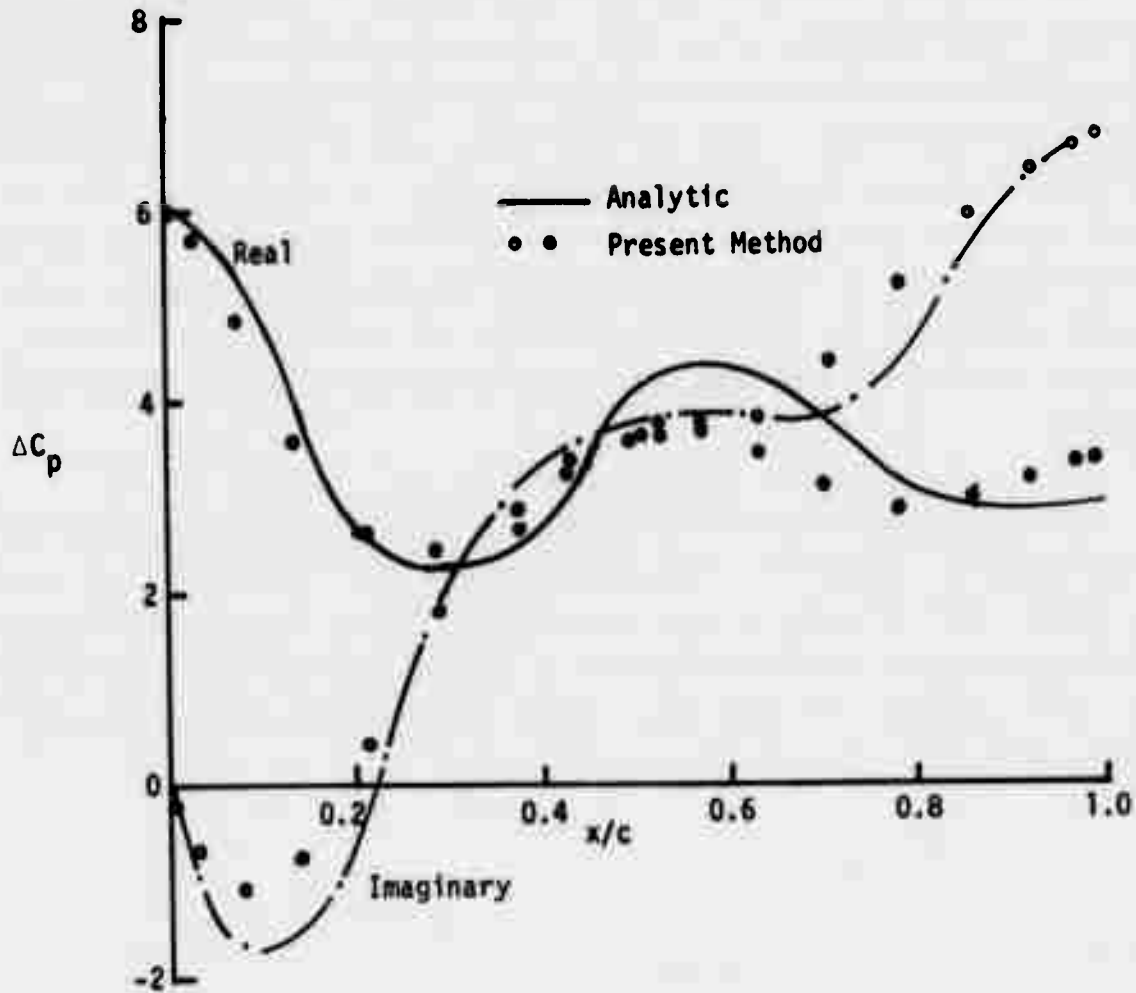


Figure 2.5-12 Comparison of the Present Method With the Analytic Solution for The Oscillatory Supersonic Case. Airfoil Pitching About Mid-Chord at $k_r = 0.99$ and $M_\infty = 1.2$

Cunningham (Reference 10) has shown that the downwash boundary conditions should be modified for the transonic case.

$$\bar{w} = \frac{M}{M_\infty} w$$

Or, the modified downwash, \bar{w} , is the unusual downwash, w , times the ratio of local surface Mach Number, M , to the free stream Mach Number, M_∞ . Cunningham

goes on to modify the reduced frequency in a similar manner.

In the method developed for finding an equivalent geometry (subsection 2.5.1.2) the possibility exists that a planar case (airfoil in $z = 0$ plane) may become nonplanar because of the acoustic pulse matching procedure. That is, the matched circular pulse may have its origin $(\bar{\xi}_0, \bar{\zeta}_0)$ off the airfoil surface even though the actual origin (ξ_0, ζ_0) is on the surface. This is especially true for acoustic pulse waves traveling upstream over the top of supersonic zones. As Figures 2.5-9 through 2.5-11 show, these pulse waves become inclined to the airfoil surface. Such an inclination for matched circular pulse waves indicates a pulse origin that lies off of the airfoil surface.

At this stage of development of the method, such a complication of the calculation is unjustified. Thus, an assumption is introduced at this point. The fitted circular pulse origin is assumed to lie on the airfoil surface. This means that the wave normal vector is not matched but the time of arrival $(t - \tau)$ is matched. The equivalent values of geometry and flow parameters then become:

$$(x - \bar{\xi}_0) \rightarrow \bar{V} (t - \tau) + \delta_m \bar{\rho}$$

where

$$\delta_m = \text{sign} (x - \xi_0)$$

$$\bar{r} \rightarrow 0$$

$$\bar{M} = \bar{V}/\bar{a}$$

where

$$\bar{a} = \left| \frac{\Delta x}{\Delta t} - \bar{V} \right|$$

$$\bar{\rho} = (t - \tau) \bar{a}$$

Where Δx is the incremental distance along the x-axis that the pulse has traveled during time Δt . With these quantities $(x - \bar{\xi}_0)$ and \bar{M} , can be

written as:

$$(x - \bar{x}_0) = (t - \tau) (1 + \delta_m / \bar{M}) \bar{V} / U_\infty$$

$$\bar{M} = 1 / \left| \frac{\Delta x}{\Delta t \bar{V}} - 1 \right|$$

The values of $(t - \tau)$ and \bar{M} are introduced into the subsonic-supersonic two-dimensional Doublet Lattice Method to account for transonic effects. To save computation and input time and expense, the values of $t - \tau$ and \bar{M} are not input for every sending/receiving point combination (which for 10 elements would be 100 values) but are input at a selected set of points. The values needed are then obtained by a double linear interpolation scheme. Figure 2.5-13 presents an example of a typical time-of-arrival plot. Specifically, the time of arrival of an acoustic pulse (whose origin is located at the 70% point) at various locations on the airfoil surface is presented. Notice that the time of arrival of the pulse is large upstream of the pulse origin and small downstream of it. This is because upstream moving acoustic pulses are moving against the flow while downstream moving pulses are moving with the flow. The result for the uniform flow case is also shown. Even though the flow at the airfoil surface is supersonic on the forward portion of the airfoil, the acoustic pulse still moves upstream (see Figures 2.5-9 through 11), even if only very slowly.

Notice that the curve of $(t - \tau)$ vs x/c has a discontinuous slope at the sending point. A special interpolation procedure is used because of this change in slope. This special procedure requires that the curves of $(t - \tau)$ vs x/c be known not only over the airfoil surface but a short distance up and down stream of it. For instance, in Figure 2.5-14, if the desired sending point, XSI_1 , lies between two available sending points, XSI and $XS2$, then an interpolated curve (shown dashed) must be constructed. The right half of the interpolated curve is obtained from the right halves of the known curves conversely the left half of the interpolated curve is obtained from the left halves of the known curves. In this example it is easily seen that the left half of the known curve emanating from XSI must extend forward of the leading edge so that an interpolated left half can be constructed. The converse is

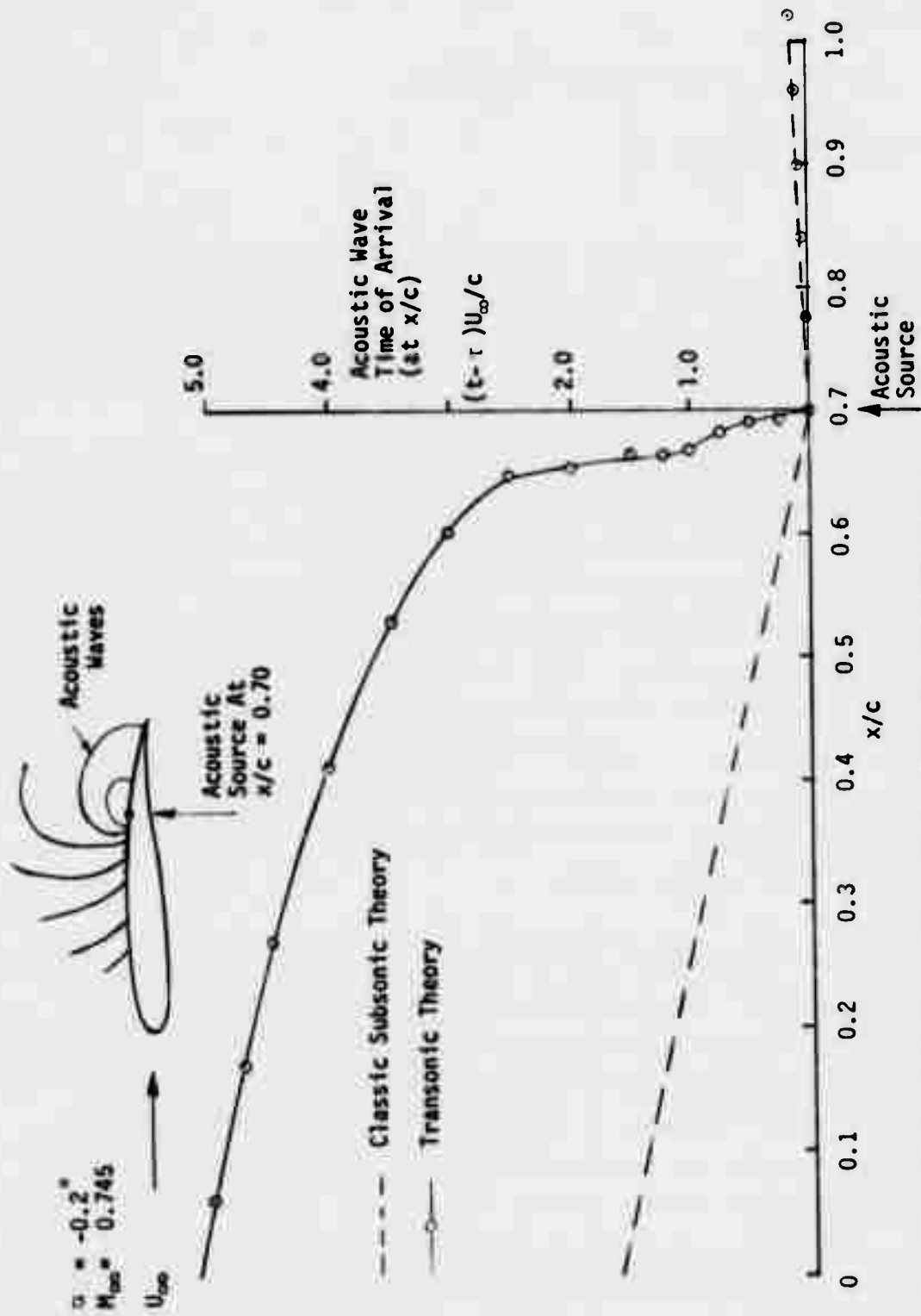


Figure 2.5-13 Comparison of Transonic and Classical Acoustic Pulse Time-of-Arrival for a Source at $x/c = 0.70$ on an NLR 7301 Airfoil

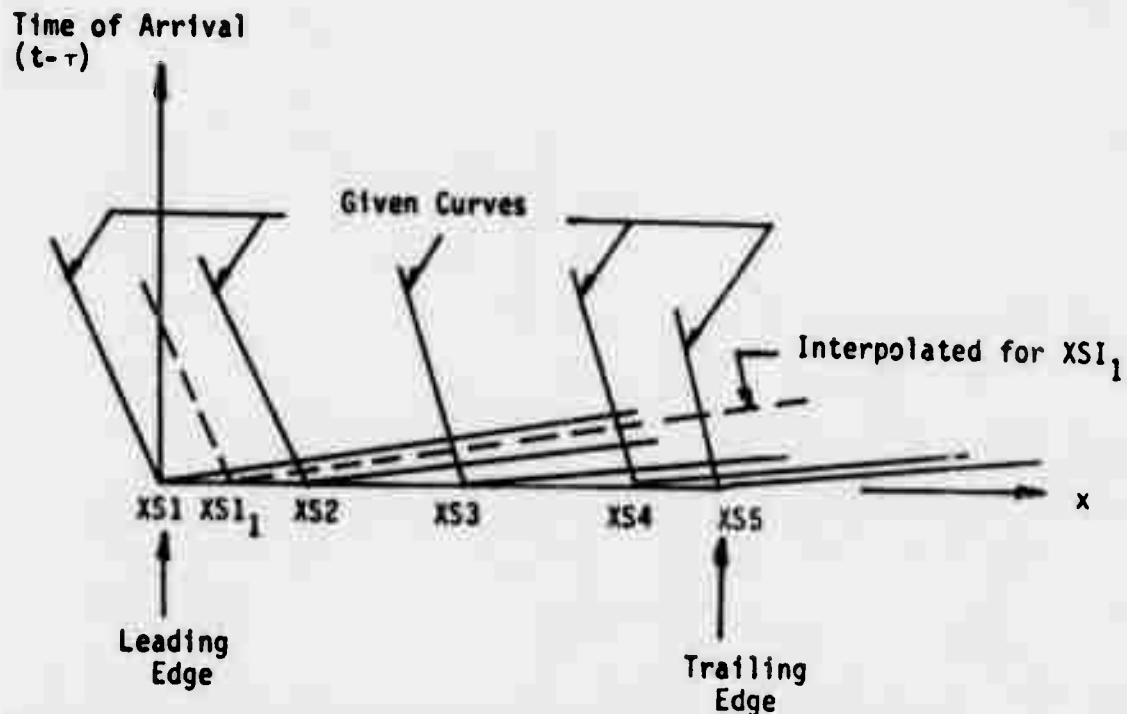


Figure 2.5-14 Time-of-Arrival versus Chordwise Position for Acoustic Pulses at Various Sending Point Locations

true for the trailing edge when dealing with the right half of an interpolated curve whose origin lies between XS4 and XS5.

The local effective Mach Number, \bar{M} , is also a discontinuous function and requires special treatment. It has been found that it is a function mostly of the receiving point location and whether it is up or down stream of the sending point. Figures 2.15(a) and (b) present the local effective Mach Number plotted versus the receiving point location for various sending point locations for two conditions. The following conclusions can be drawn from these figures. First, for receiving points downstream of the sending point, the local effective Mach Number is close to the local surface Mach Number. Second, for receiving points downstream of the supersonic zone the local effective Mach Number is also close to the local surface Mach Number independent of the location of the sending point. Third, for receiving points upstream of sending points (in a supersonic zone) the local effective Mach Number falls on one curve independent of sending point location and the Mach Numbers are subsonic. The reason why the effective Mach Numbers are

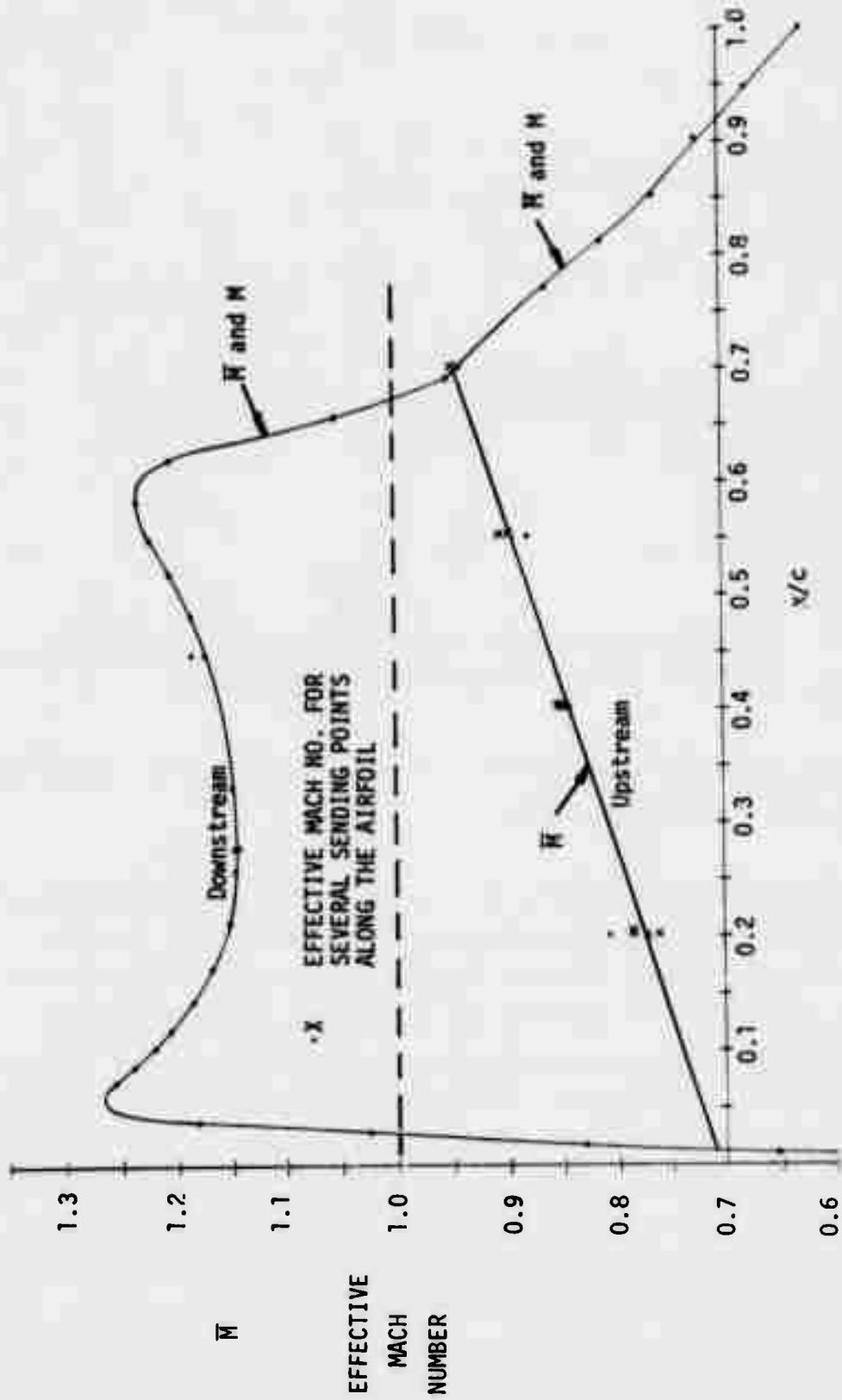


Figure 2.5-15 (a) Effective Local Mach Number, \bar{M} , Along the Airfoil for Various Sending Points on the Upper Surface of the MLR 7301 Airfoil. (a) $M_\infty = 0.745$ $\alpha = 0.2$.

Note: M is the Local Surface Mach Number.

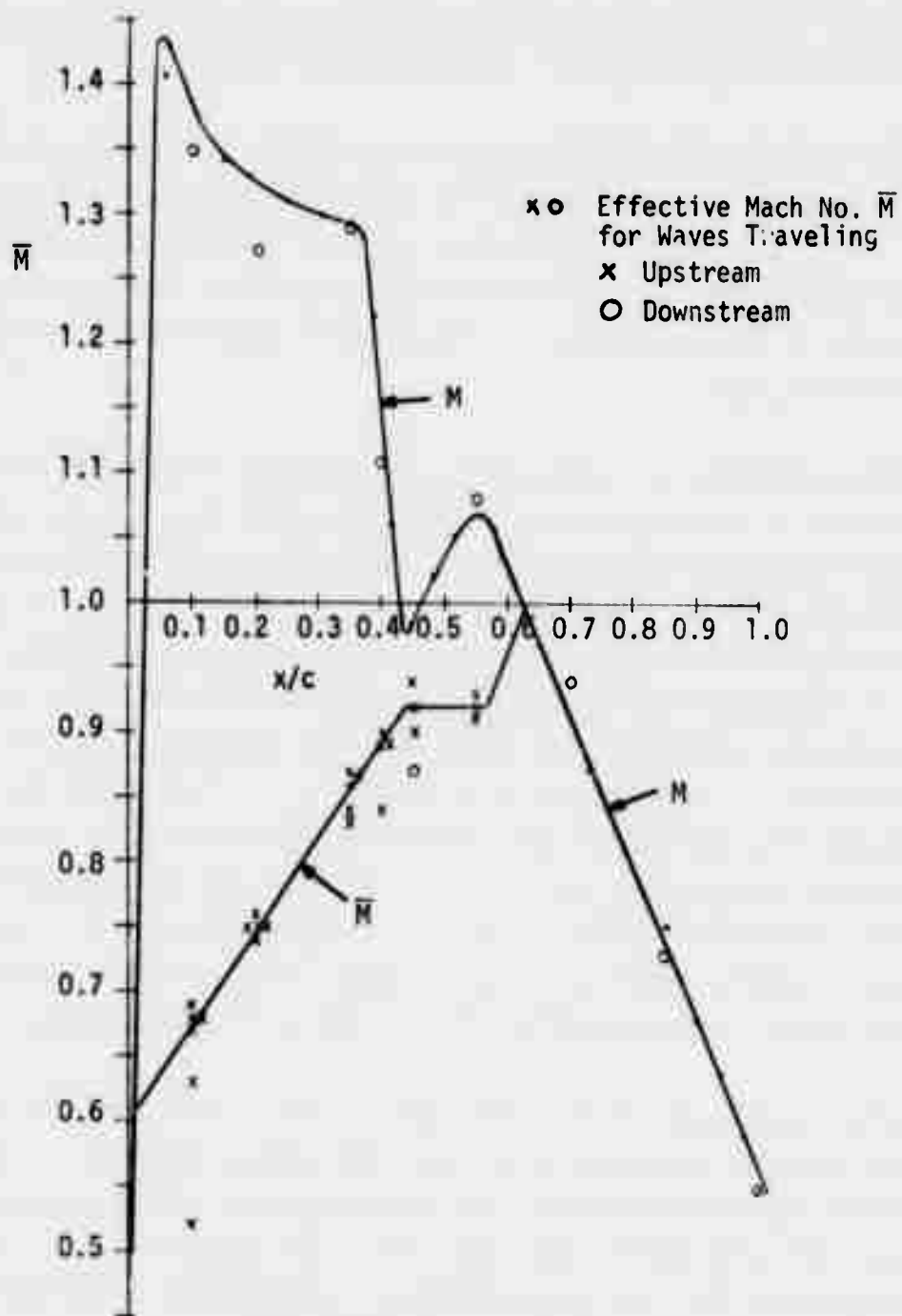


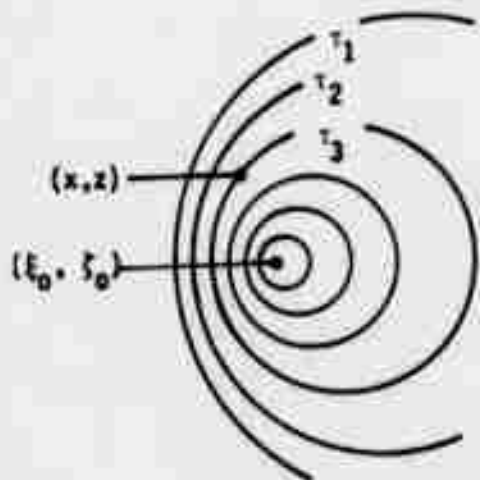
Figure 2.5-15(b) $M_\infty = 0.70$ $\alpha = 1.75^\circ$

subsonic for this condition is that the acoustic pulse wave fronts manage to propagate up into this supersonic zone just as if the Mach Numbers were subsonic. Figures 2.5-9 through 11 illustrate this mechanism.

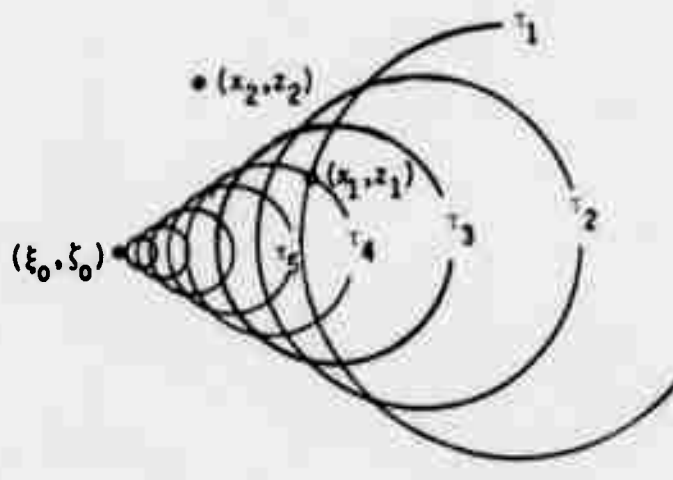
Other assumptions have been made to facilitate the incorporation of the effective geometry and Mach Number into the classic subsonic and supersonic methods. For instance, the application of this technique to pressure doublets, which are used in the Doublet Lattice Method, requires just such an assumption. A discussion of this assumption is presented in subsection 2.5.1.3 but it bears repeating here.

Pressure doublets are made up of a distribution of velocity point doublets along a line starting at the pressure point (ξ_0, ζ_0) and passing to downstream infinity in the x-direction. The effective geometry and Mach Number should, strictly speaking, be applied separately to each of these points in the 'wake' of the pressure doublet. However, to simplify this procedure, it is assumed that the effective geometry and Mach Number for the pressure doublet (with wake) are those based on the leading edge of the pressure doublet, i.e., the sending point (ξ_0, ζ_0) . This means that pulses that elinate from the wake of the pressure doublet (aft of the point (ξ_0, ζ_0)) see a uniform flow between them and the point (ξ_0, ζ_0) and a nonuniform flow from there to the receiving point (x, z) . The effects of this assumption are not easily observed; however, in general they should not be too large. Future refinements may involve the elimination of this assumption.

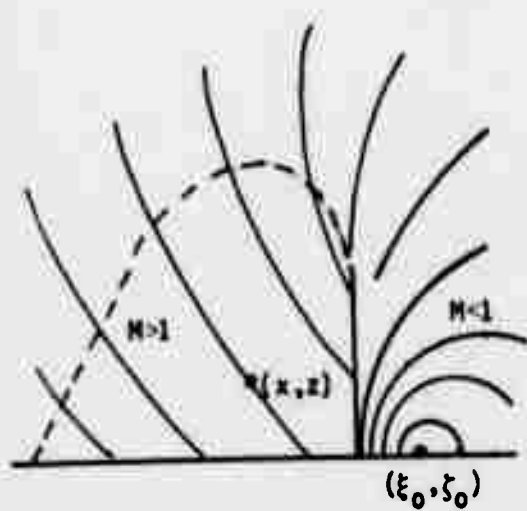
Another assumption involves the basic nature of the transonic pulse. The basic theory of transonic nonuniform flow (subsection 2.5.1.1) shows that the effect of an acoustic source at a receiving point (x, z) depends on how many times the pulse passes over that point. The summation over j from 1 to N in the equation for ϕ in subsection 2.5.11 and Appendix A indicates this fact. In classic subsonic flow, the acoustic pulse passes over a given point only once (see Figure 2.5-16a). The upstream facing part of the pulse moves slowly upstream while the downstream part moves rapidly in the downstream direction. In supersonic flow, such is not the case. The pulse wave either passes over the point twice (for a point lying in the aft Mach cone of the source) or not at all, for points lying outside of the Mach cone. The down-



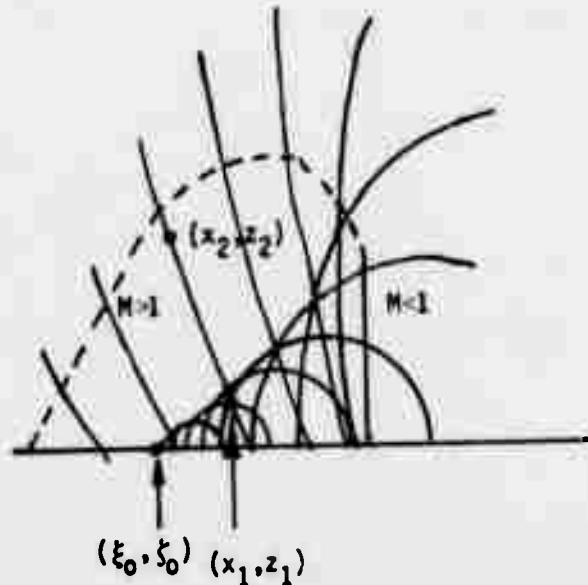
(a) Subsonic



(b) Supersonic



(c) Transonic (Upstream Influence)



(d) Transonic (Downstream Influence)

Figure 2.5-16 Pulse Wave Patterns for Various Flow Conditions

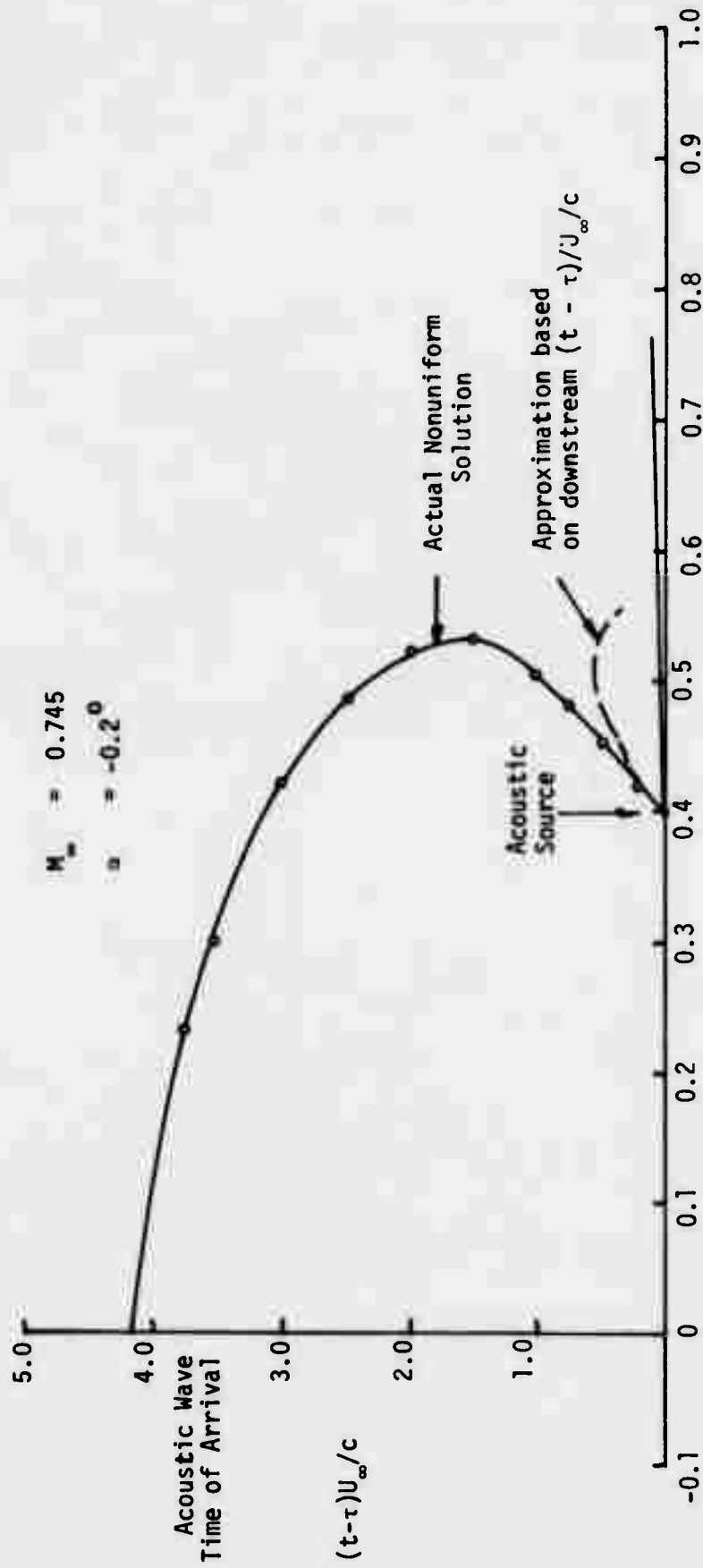


Figure 2.5-17 Comparison of Actual and Approximate Values of Acoustic Pulse Time-of-Arrival for a Source at $x/c = 0.4$ for an NLR 7301 Airfoil

stream facing part of the wave passes first and then the upstream facing part, which is being swept downstream (see Figure 2.5-16b).

For transonic flow, the qualitative characteristics of pulse wave passage can be more complicated than just described and can also act subsonically in a supersonic zone and supersonically in a subsonic zone. For instance, it has been shown that pulses can move upstream up and over a shock wave and down into the supersonic zone (see Figures 2.5-9 through 11 and Figure 2.5-16c). The basic nature of this pulse is subsonic; acting in accordance with the local effective Mach Number \bar{M} and not the local supersonic Mach Number M . For this case, the pulse passes over the receiving point once. Thus, the subsonic Doublet Lattice Method is modified for this case using $(x - \bar{\xi}_0)$ and \bar{M} . Referring to Figure 2.5-16d, it is seen that pulses that start out in a supersonic zone have a dual character: a supersonic character, where the pulse passes over those receiving points twice that are within the Mach cone (x_1, z_1) (not quite a cone for this case) and, a subsonic character, as the pulse breaks out of the Mach cone and moves upstream to pass over points that lie outside of the Mach cone (x_2, z_2) . The receiving point (x_1, z_1) then has the pulse passing over it three times. An assumption currently adopted, which could be eliminated, is that the third passing of the wave is neglected for points lying within the Mach cone. The single passing of the wave at (x_2, z_2) , however, is retained. Figure 2.5-17 illustrates this case by presenting the time-of-arrival versus airfoil location for an acoustic source located at $x/c = 0.4$ for the NLR 7301 airfoil at $M = 0.745$ and $\alpha = -0.20^\circ$. In the area lying between $0.53 \geq \frac{x}{c} \geq 0.4$, there are three values for the time-of-arrival of the acoustic pulse. Currently, in the present method the highest of the values of $(t - \tau)$ is ignored in this area. There is some justification for this since the pulse wave strength weakens as time increases. However, other factors, like the speed with which the wave passes over the receiving point, have a large effect on the magnitude of the pulse contribution. The second highest value for the time of arrival is accounted for implicitly by using the first time of arrival to obtain $(x - \bar{\xi}_0)$ and \bar{M} and assuming supersonic flow. This means that the second time of arrival is legislated using $(x - \bar{\xi}_0)$ and \bar{M} and is not quite equal to the actual value. The relationship between the two times-of-arrival (assuming uniform flow quantities of \bar{V} , \bar{a} , etc.) is

$$(t - \tau)_2 = (t - \tau)_1 \left(\frac{\bar{M} + 1}{\bar{M} - 1} \right)$$

The result is shown in Figure 2.5-17 as the dashed line. This assumption can also be eliminated by breaking up the supersonic evaluation into its two component parts and applying a separate time-of-arrival and local effective Mach Number for each part. Currently, this refinement does not seem warranted but may be in the future.

In summary, the equivalent $(x - \bar{\xi}_0)$ and \bar{M} are used in the classical formulas for either the supersonic ($\bar{M} > 1$) or subsonic ($\bar{M} < 1$) downwash influence coefficients for every sending ($\bar{\xi}_0$) receiving (x) pair of points. The classical method used is the Doublet Lattice Method. This simple way of using the equivalent data, i.e., $(x - \bar{\xi}_0)$ and \bar{M} is approximate in some ways but at this stage of development this seems appropriate. There is no use refining a method before it has been tried.

This method was applied to the NLR 7301 airfoil at its shockfree design point. Figure 2.5-15(a) presents the values of \bar{M} used, while Figure 2.5-18 presents the time-of-arrival data used. Figure 2.5-19 presents a comparison for the steady case of the present method and the Jameson Method. The results for the Jameson method are obtained by taking a numerical derivative of the results at α as follows:

$$C_{p_\alpha} = \left\{ C_p \left(\alpha = \bar{\alpha} + \frac{\Delta\alpha}{2} \right) - C_p \left(\alpha = \bar{\alpha} - \frac{\Delta\alpha}{2} \right) \right\} / \Delta\alpha$$

Figure 2.5-19 presents data for the upper and lower surfaces. On the upper surface the present method is compared to the numerical derivative of the Jameson method ($\Delta\alpha = 0.10^\circ$) for two average angles of attack, $\bar{\alpha}$, that are only slightly different. The difference in the Jameson results for $\bar{\alpha}$ of -0.2° and 0.175° is large. The large response of C_p to small $\bar{\alpha}$ changes is not currently understood. Because of this, the derivative itself may be in doubt. The present method is in better agreement with the Jameson method than is the classical result (which is the negative of the classic result for the lower surface). It is the opinion of the author that the large response of the Jameson method to small changes in $\bar{\alpha}$ can not be duplicated in

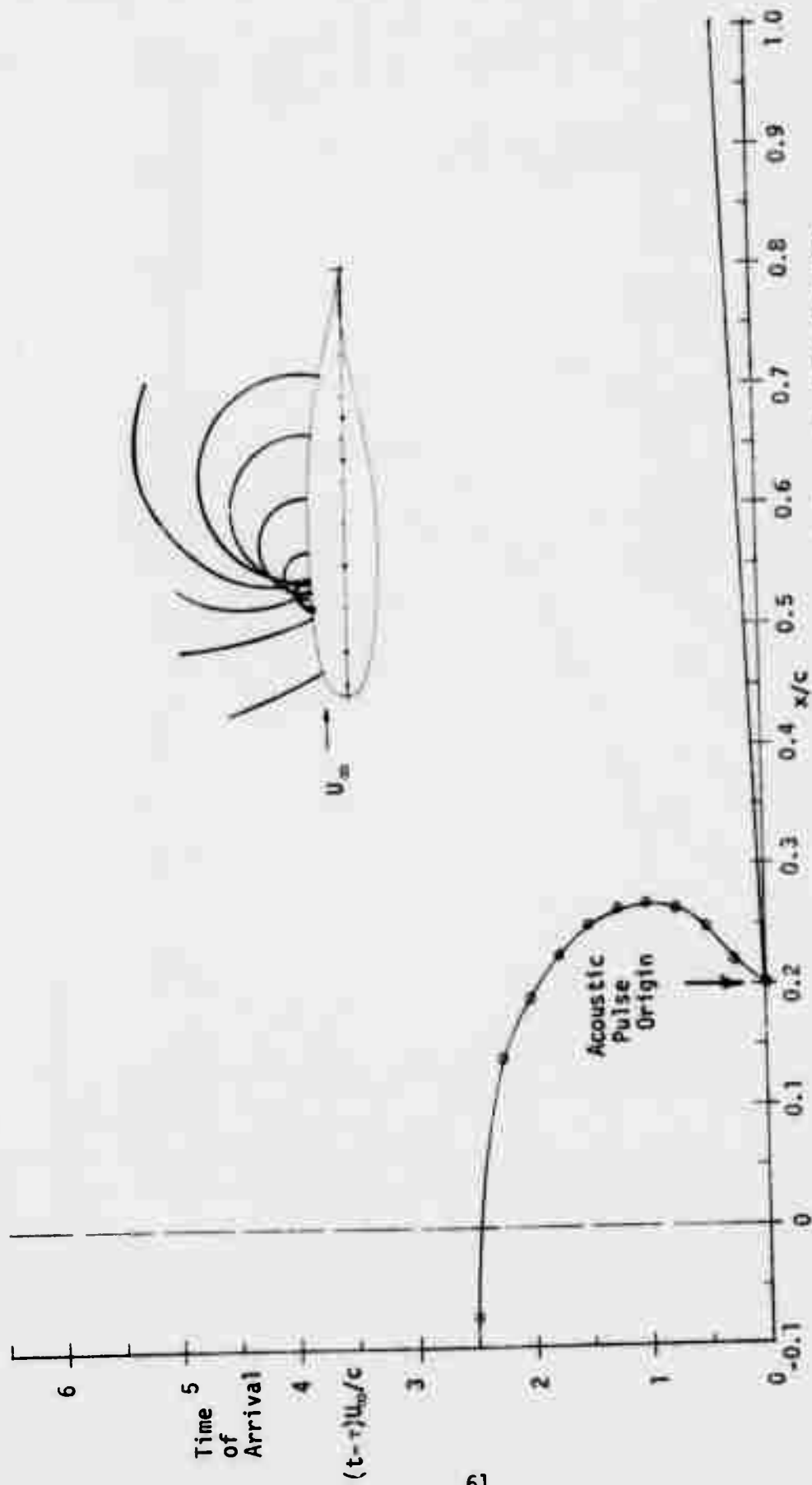


Figure 2.5-18 Time of Arrival, Along the Airfoil Surface, of An Acoustic Pulse Emitted at Time $t = \tau$ and Located on The Surface of The HLR 7301 Airfoil ($M_\infty = 0.745, \alpha = 0.2$)

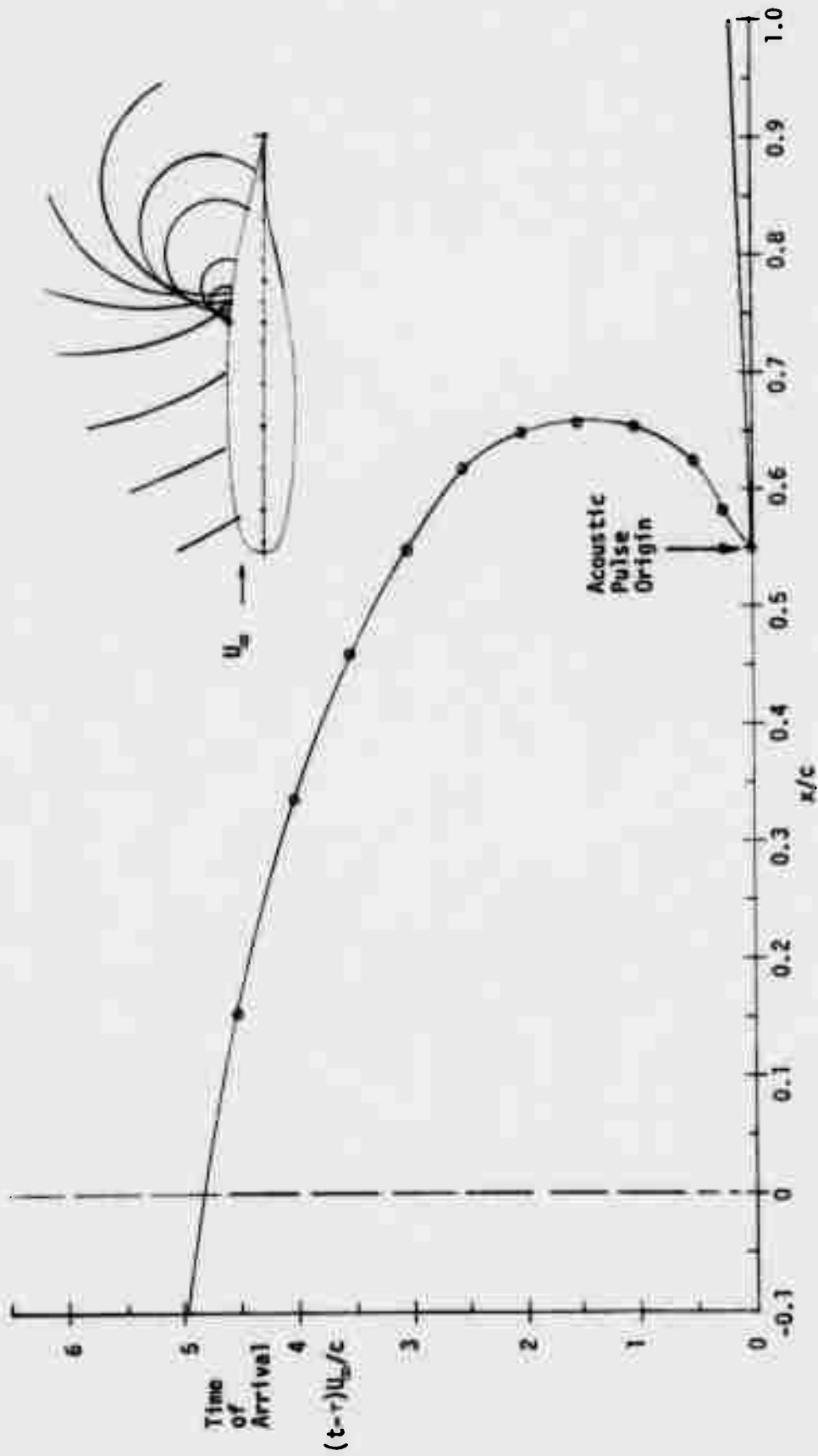


Figure 2.5-18 (Continued)

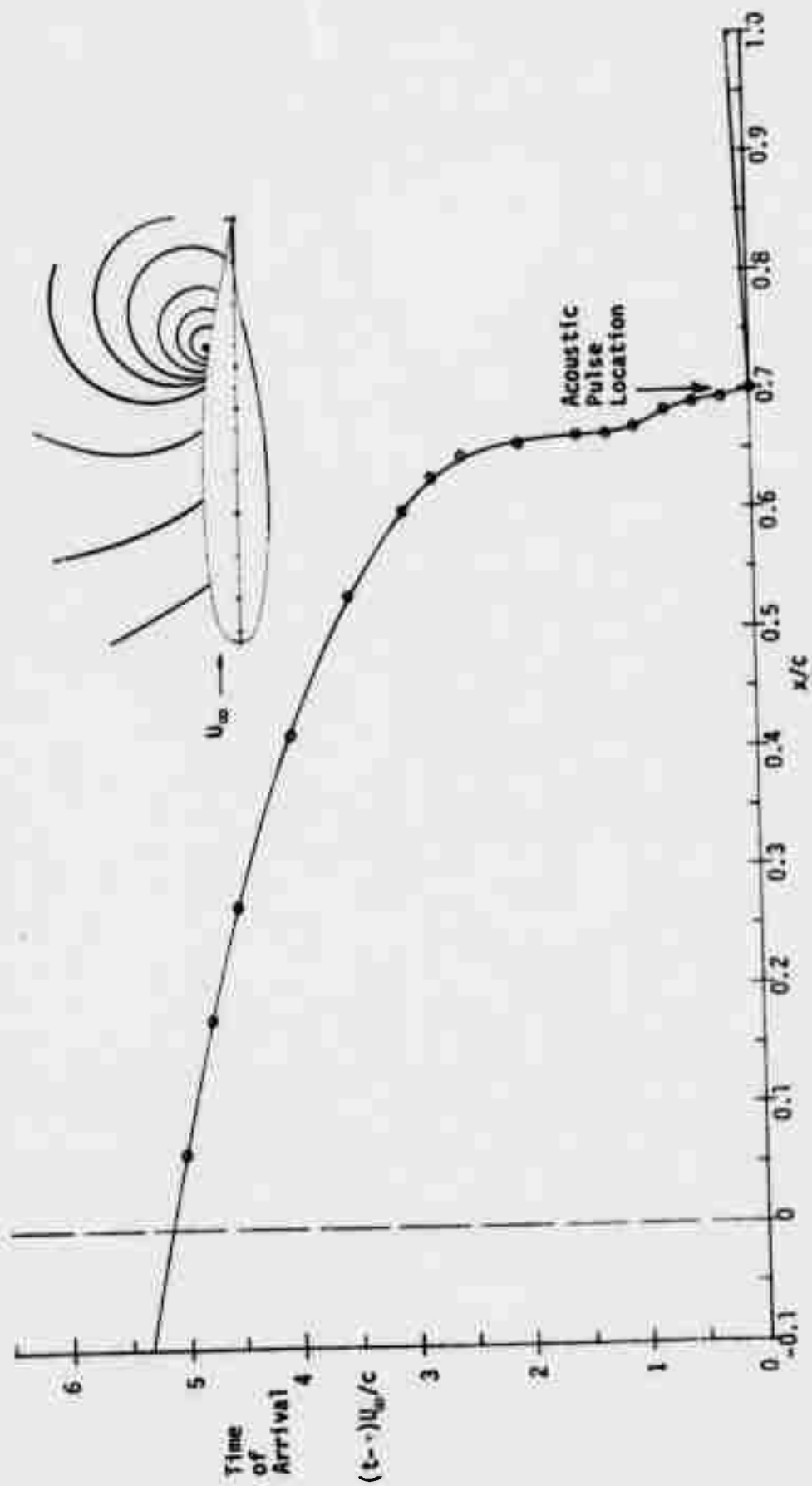


Figure 2.5-18 (Continued)

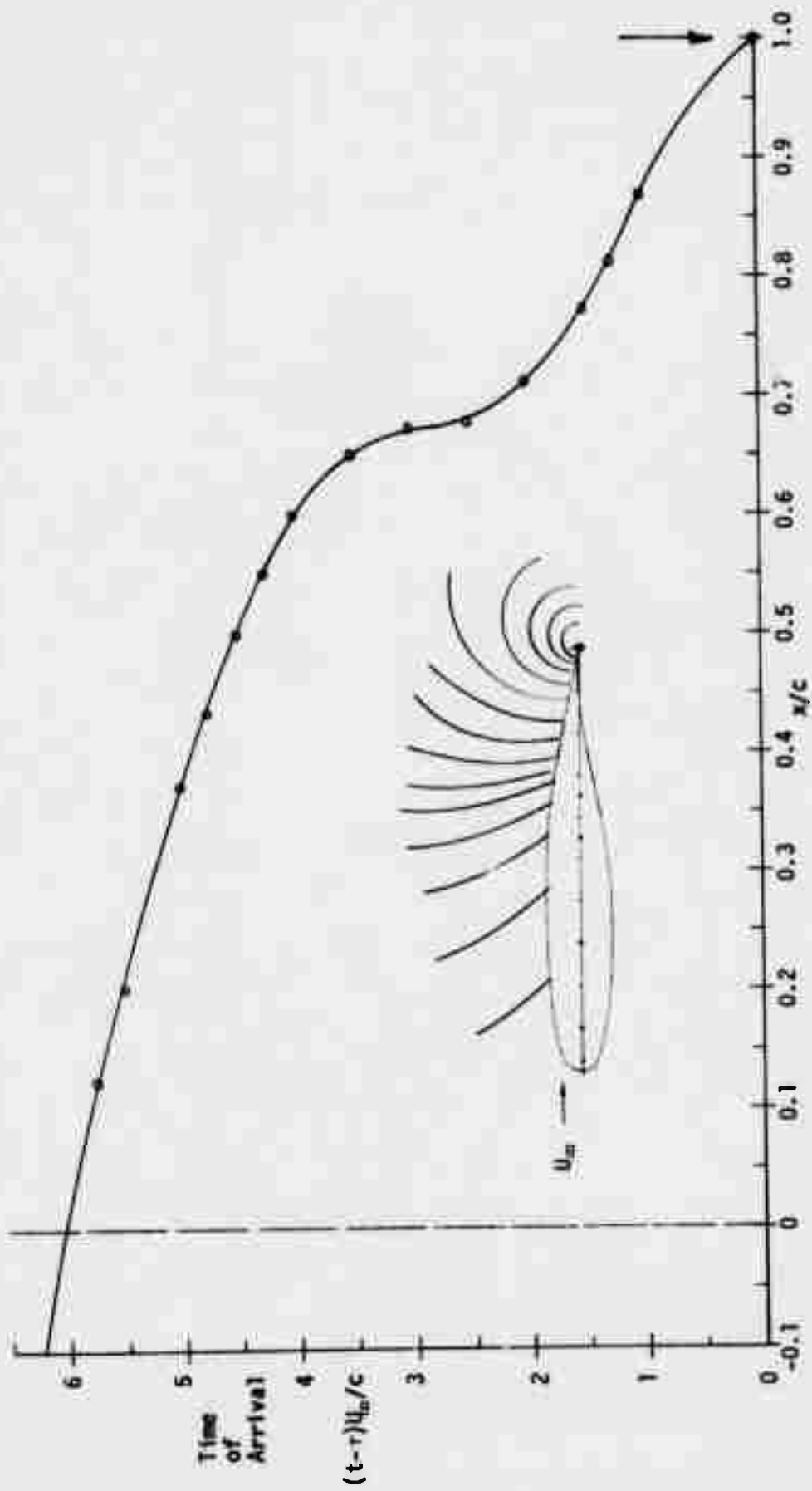


Figure 2.5-18 (Continued)

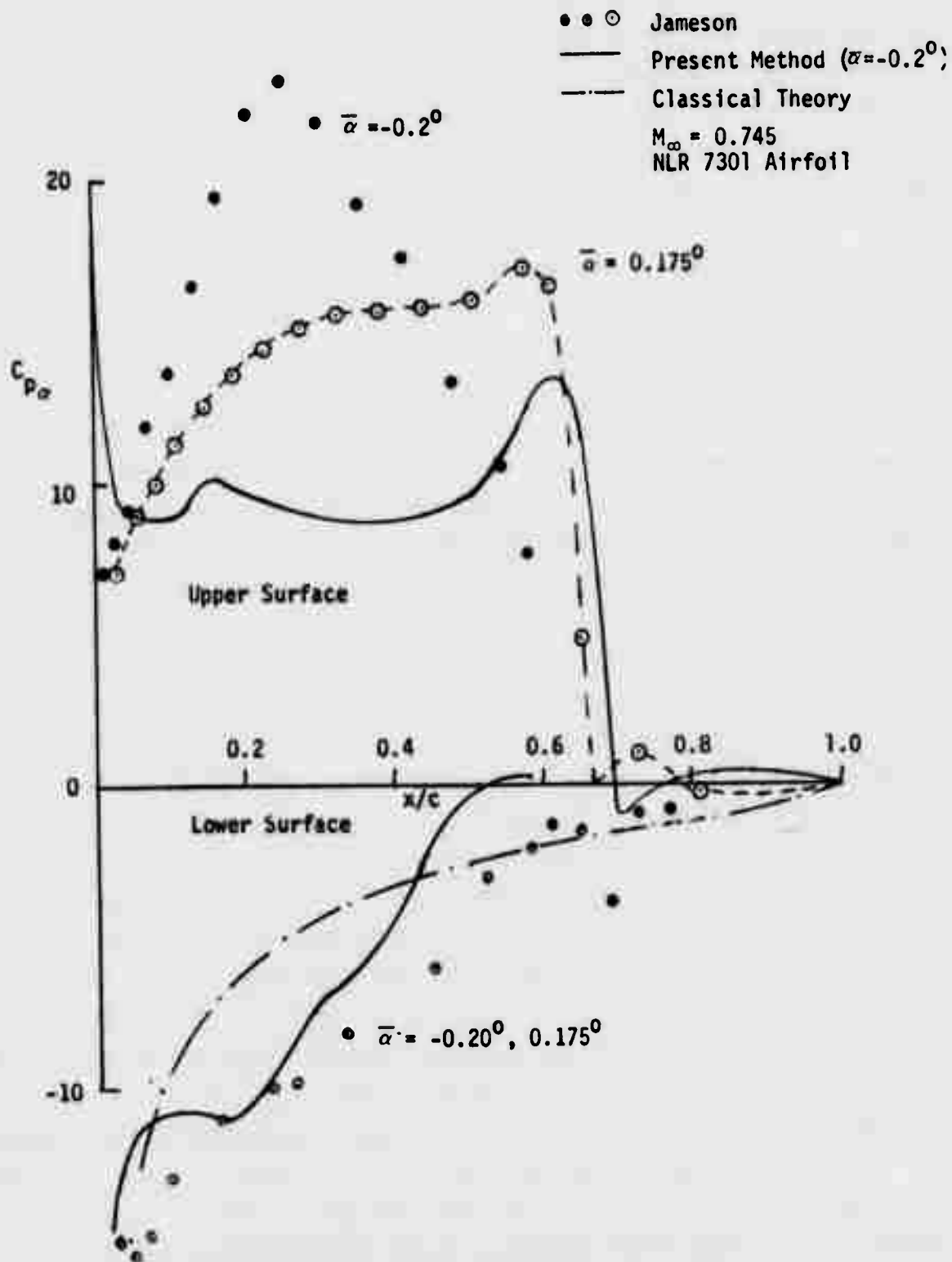


Figure 2.5-19 Comparison of the Present Method and the Classical Theory with the Jameson Transonic Method for Two Average Angles for the Case of Shock Free Flow

practice by the present method with its current set of assumptions. The present method depends on the Jameson method at $\bar{\alpha}$ but it does not seem possible that the flow field would change enough (by changing $\bar{\alpha}$ from -0.2 to $.17$) to change the entire character of the acoustic pulse solutions. If such changes do occur, it seems that a much more accurate representation of the flow field must be used, in the acoustic pulse generator, than the one in use (double linear interpolation). It seems that a fruitful line of investigation would be to try and uncover the mechanism of this rapid change of character with $\bar{\alpha}$ using a finite difference method like the Jameson method or better yet, the Traci-Farr-Albano method (Reference 8).

On the lower surface of the NLR 7301 airfoil, the classic theory and present method are compared with results from the Jameson Method. As expected, this surface exhibits less transonic effects than the upper surface. Also, changing $\bar{\alpha}$ from -0.2° to 0.17° does not effect the result to any noticeable degree. The results for the present method agree fairly well with the Jameson method.

Application of the present method and Jameson method to the NLR 7301 airfoil for an off design case ($M_\infty = 0.7$, $\bar{\alpha} = 1.75^\circ$) is presented in Figure 2.5-20. In this case, a shock wave exists at $x/c = 0.4$ (see Figure 2.5-22). Also, shown in this figure, is the classic uniform flow subsonic result which bears no resemblance to the Jameson result. The results given by the present method do not correlate with the Jameson results especially in the region of the shock wave. Notice especially that the large peak in pressure at the shock location is missing. In addition, the large negative peak in pressure is missing. What does exist is a pressure that peaks at a value that is approximately the average of the two peaks however which lies midway between them. This indicates that shock wave motion effects are missing from the present method. This could easily be the case since no boundary or compatibility conditions were introduced at the shock location. The subject of the next subsection is the inclusion and satisfaction of shock wave motion boundary and compatibility conditions in the present method.

Before proceeding to these subsections, it will be instructive to compare the Jameson method with experimental data gathered for the NLR 7301 airfoil

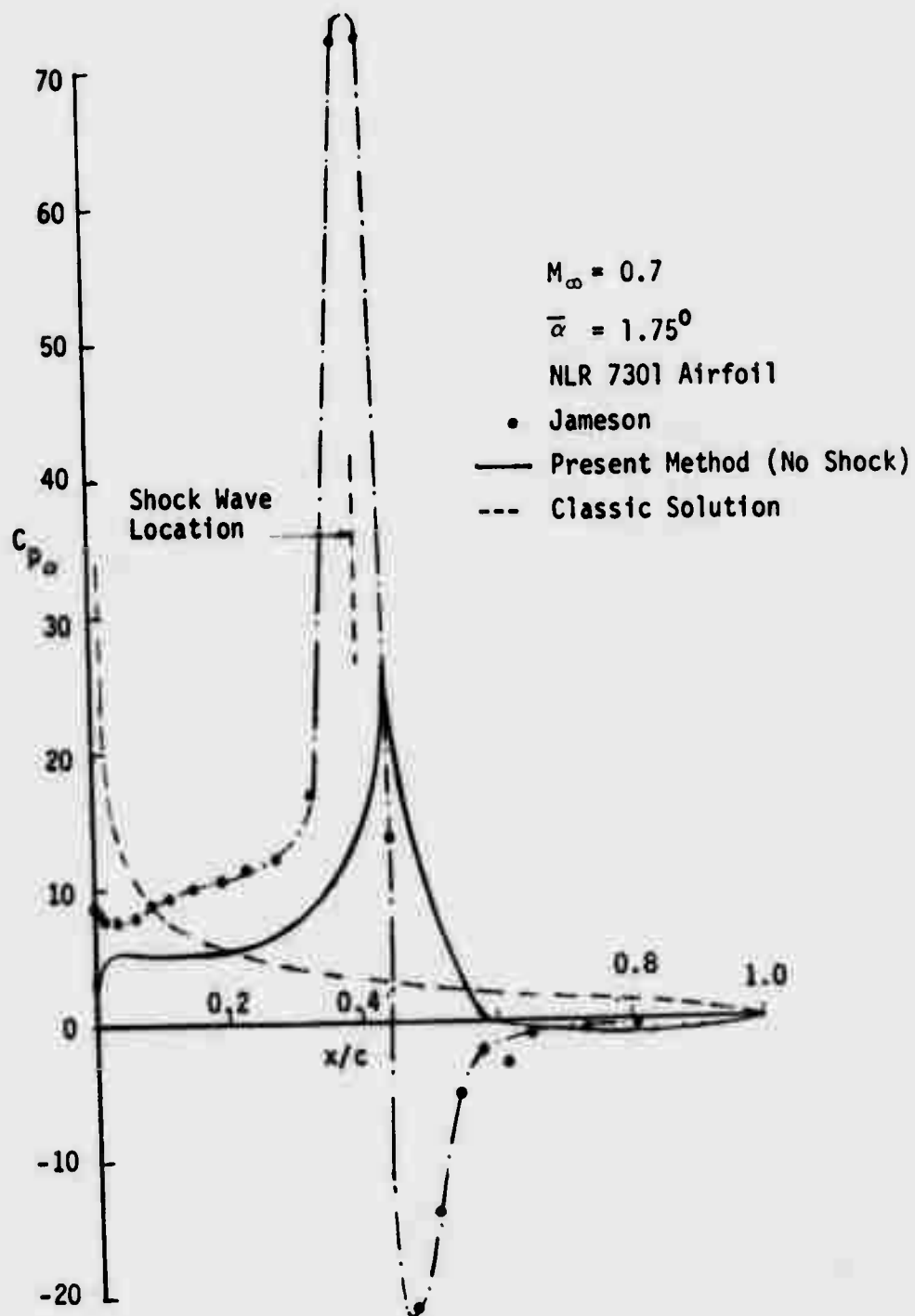


Figure 2.5-20 Comparison of the Present Method (Without Shock Wave Effects) and the Classic Theory With the Jameson Transonic Method

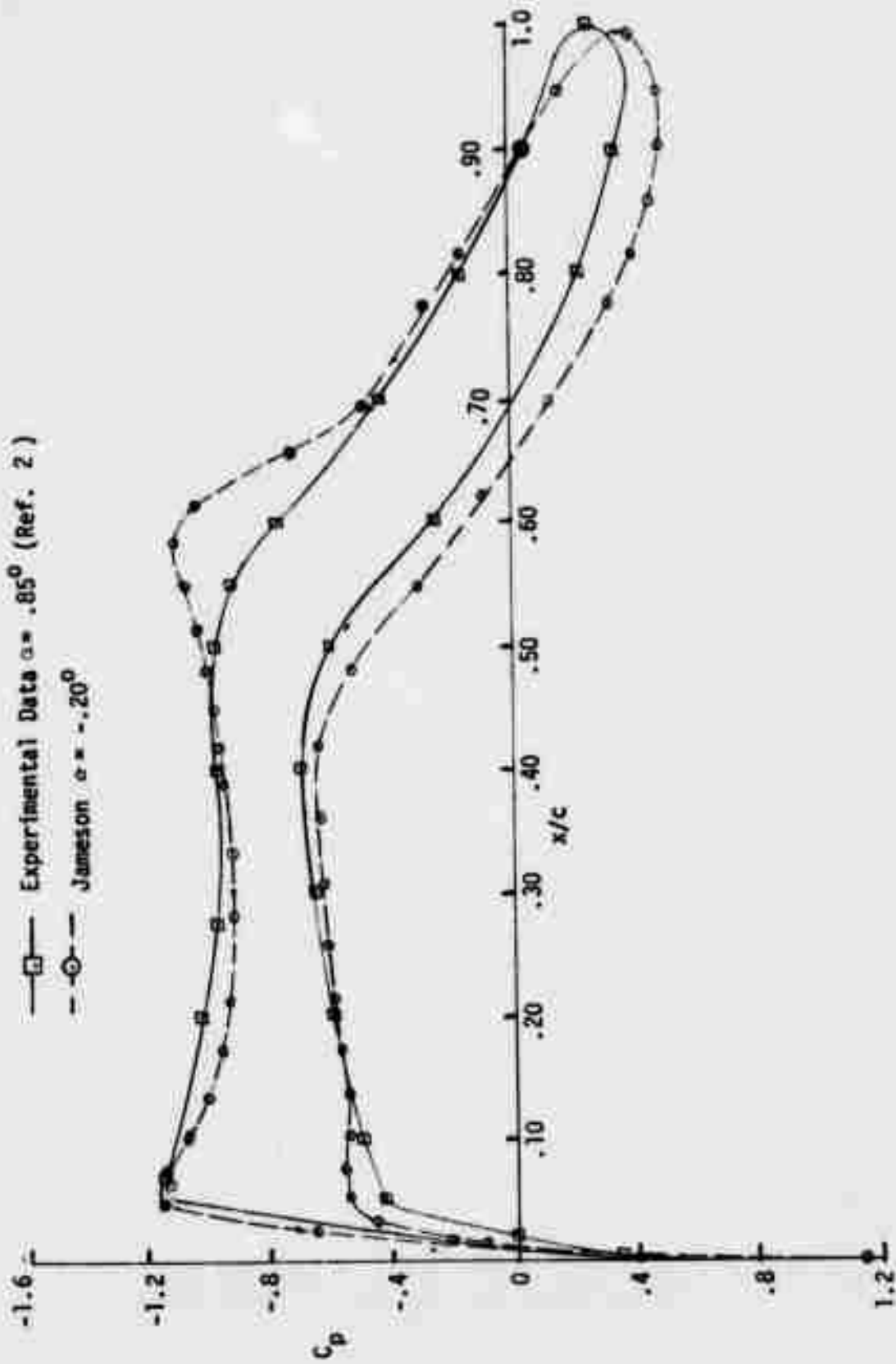


Figure 2.5-21 Comparison of The Jameson Transonic Flow Method With Data for The NLR 7401 Airfoil ($M_\infty = 0.745$, $\alpha = 0.20^\circ$). Angle of Attack for Theory Adjusted for Best Correlation.

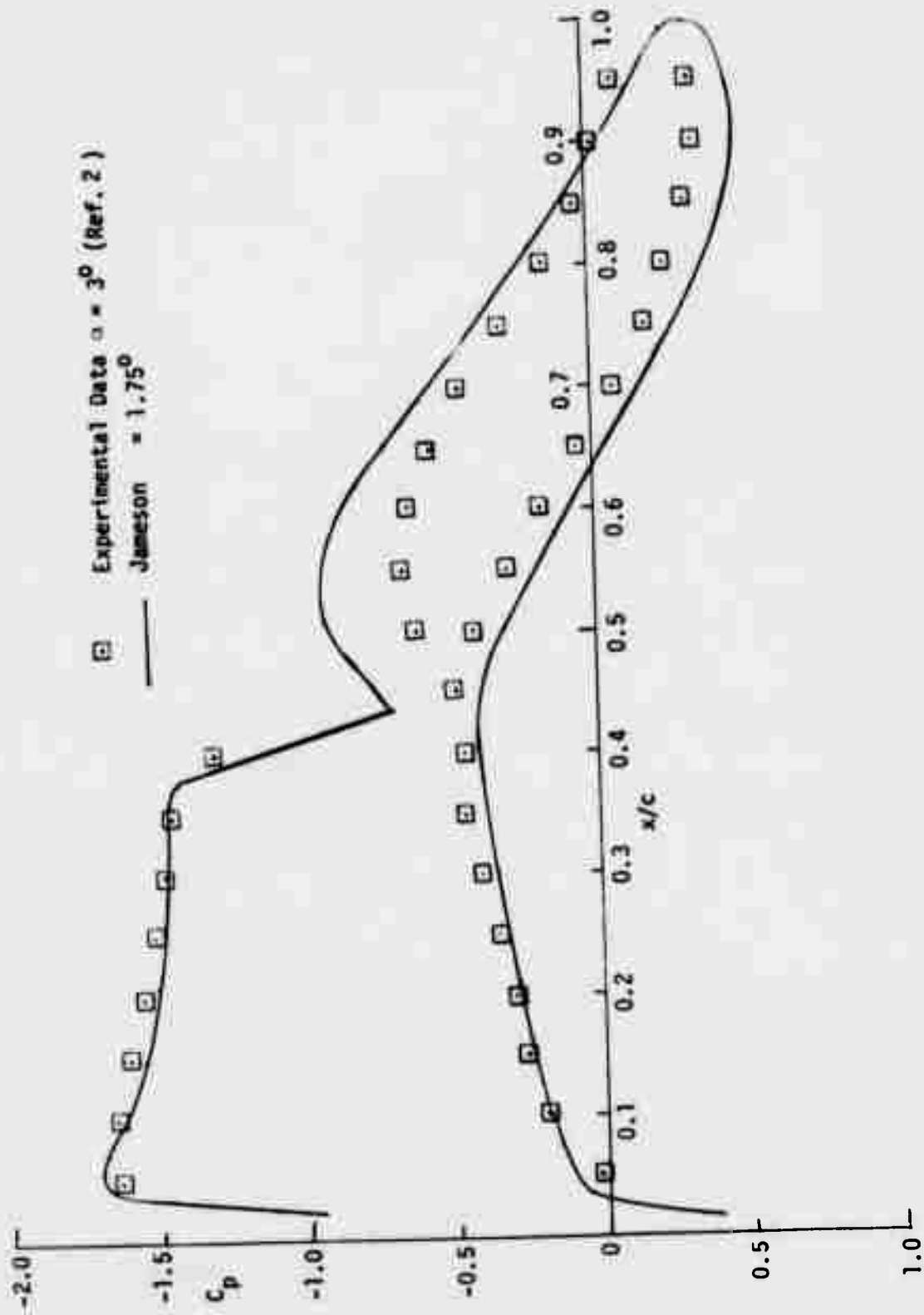


Figure 2.5-22 Comparison of the Jameson Transonic Flow Method With Data for The NLR 7301 Airfoil
 ($M_\infty = 0.7$, $\alpha = 1.75^\circ$). Angle of Attack for Theory Adjusted for Best Correlation.

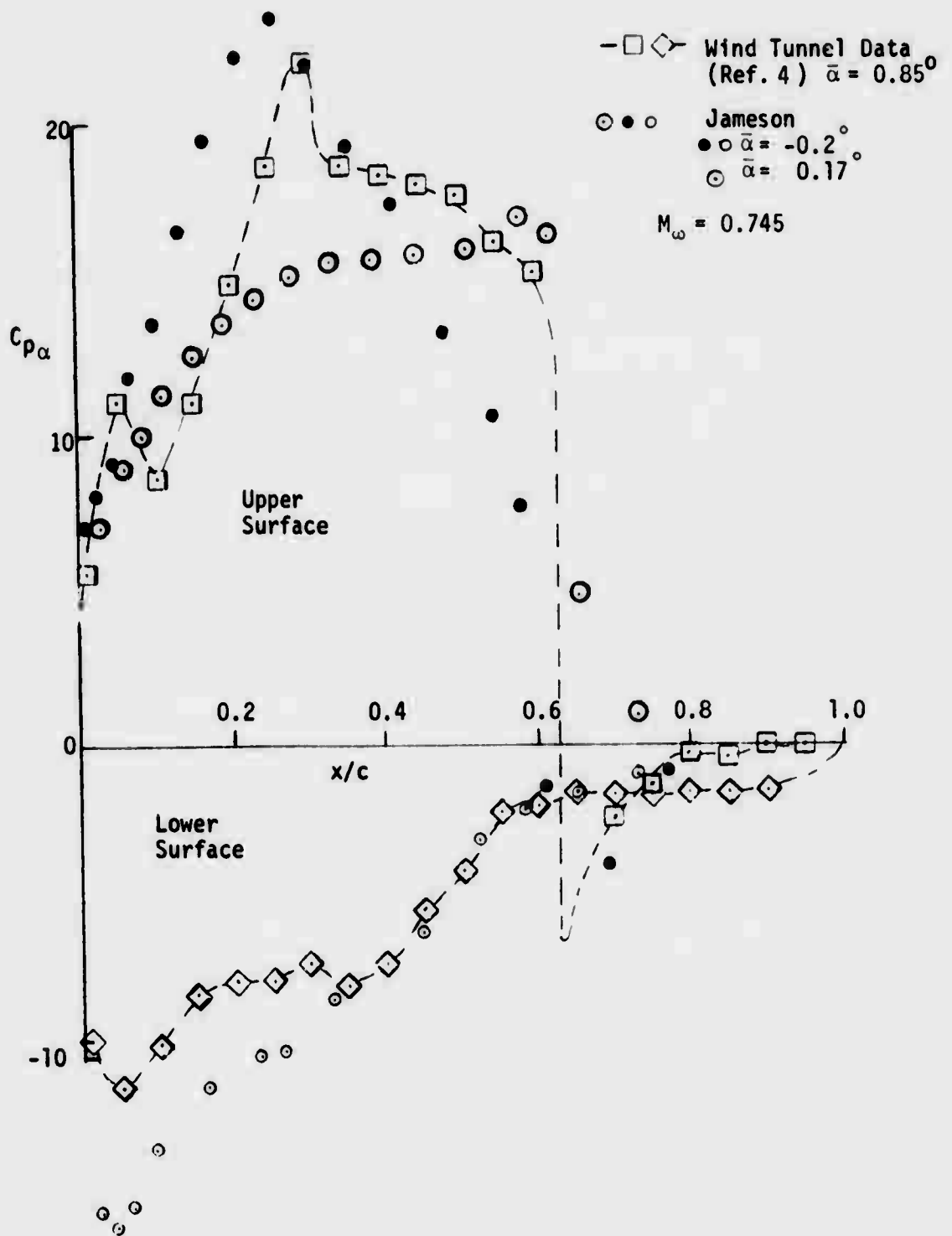


Figure 2.5-23 Comparison of the Jameson Transonic Method With Wind Tunnel Data for The NLR 7301 Airfoil. Jameson Method Used at Two Angles of Attack

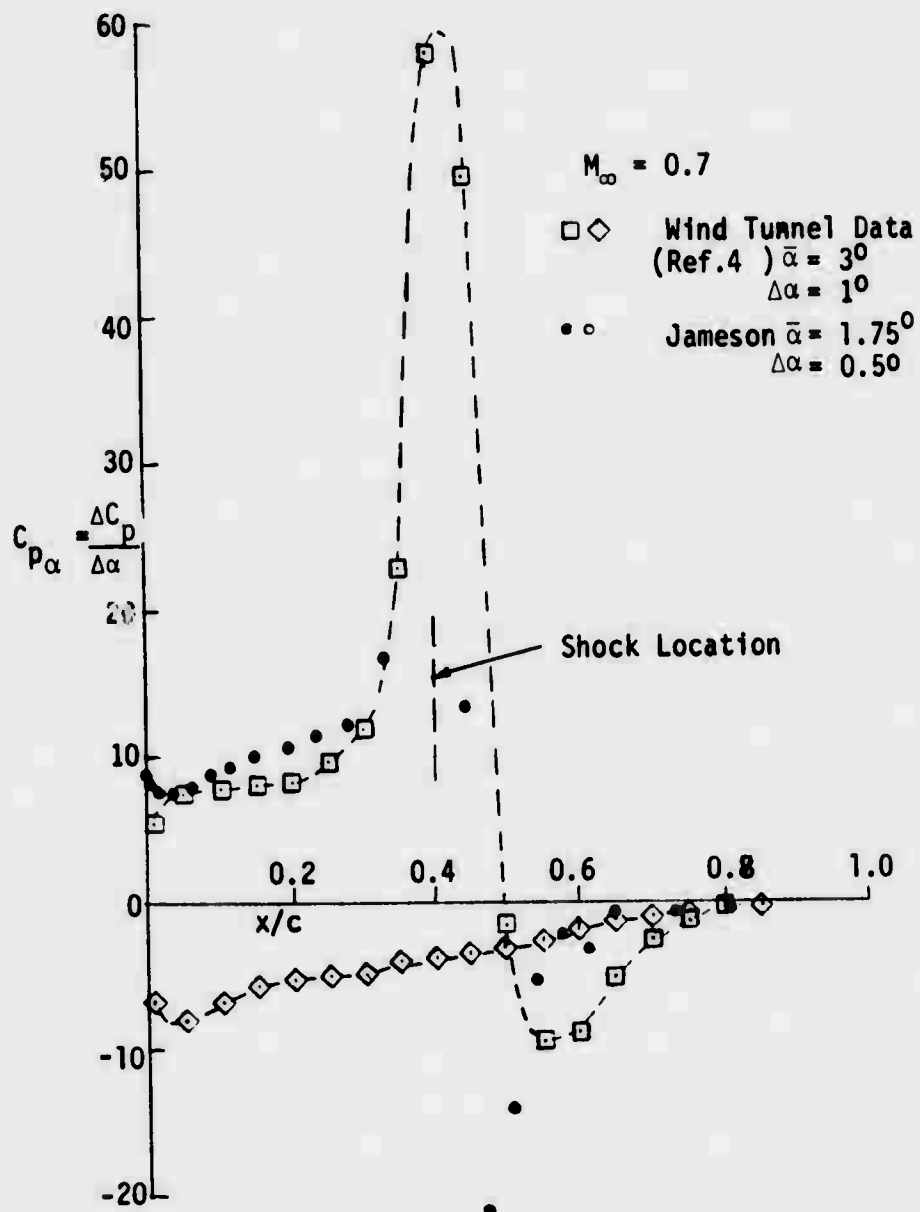


Figure 2.5-24 Comparison of the Jameson Transonic Method With Wind Tunnel Data for The NLR 7301 Airfoil.

and presented in Reference 4. Figures 2.5-21 and -22 present comparisons of wind tunnel data with the Jameson Method for the two conditions previously studied. The angles of attack have been adjusted to reproduce the best comparison. A better method of matching however, is to add the boundary layer thickness to the airfoil and rerun the transonic calculations. A second method is to perform an inverse calculation whereby the required pressure distribution is input and the modified airfoil shape is output. This latter technique was applied in the cases of the TF-8A and YC-15 wing sections (to be discussed later) but was not applied in this case. Figures 2.5-23 and -24 compare data with the Jameson method for $\Delta C_p / \Delta \alpha$. These figures show that the pressure levels output by the Jameson method are approximately correct and can be used as a basis for comparison with the present method. These figures, especially 2.5-23, show that the transonic perturbation pressures are very volatile, varying rapidly with the flow parameters. In Figure 2.5-24 note especially the disagreement between the Jameson method and data aft of the shock.

The question may arise: if the Jameson program predicts the perturbation loads adequately, why not use the Jameson program alone and not worry about the lifting surface method. First, the Jameson program is applicable only to steady flow. Second, the extension of the Jameson method to three-dimensional flows will increase the cost significantly, whereas the lifting surface theory costs are very reasonable.

2.5.2 Effects of Shock Wave Motions

Figure 2.5-20 illustrates that the present method, as developed up to this point, does not account for shock wave motion. Inspection of this figure shows that the shock motion effect plays a dominant role in the prediction of transonic loads. Thus in the next few subsections the theory for the effects of shockwave oscillation will be developed. Along these lines References 10, 12 and 13 are helpful in the following developments.

2.5.2.1 Interference Flow Due to Shock Motion

The following jump conditions across a shock wave can be derived from

Reference 14 (page 59 Eq. 2.47).

$$\tilde{u}_2 - \tilde{u}_1 = -\frac{2}{\gamma+1} \tilde{u}_1 \left(1 - \frac{1}{M_{1,2}}\right)$$

$$\tilde{w}_2 - \tilde{w}_1 = 0$$

where u and w are the x and z components of the velocity, the tilda stands for instantaneous position and the subscripts stand for locations just up and downstream of the shock. Therefore these shock jump conditions hold just up and downstream of the instantaneous shock position. In order to translate these conditions to the steady shock surface an analytic continuation of the steady conditions is necessary. Consider the velocity potential for instance:

$$\tilde{\phi}_{1,2} = \phi_{s_{1,2}} + e^{i\omega t} \left[\lambda \frac{\partial \phi_{s_{1,2}}}{\partial x} + \bar{\phi}_{1,2} \right]$$

where $\phi_{s_{1,2}}$ is the steady potential just up (ϕ_{s_1}) or downstream (ϕ_{s_2}) of the steady shock position, λ is the amplitude of oscillatory motion of the shock, and $\bar{\phi}_{1,2}$ is the oscillatory perturbation potential just up or downstream of the steady shock location (see Figure 2.5-25). Here we have made the assumption that the shock moves in a simple harmonic manner. Since $\tilde{w} = \partial \tilde{\phi} / \partial z$ the tangential flow boundary condition $\tilde{w}_2 - \tilde{w}_1 = 0$ can be written as follows using the above expression for $\tilde{\phi}_{1,2}$:

$$\begin{aligned} w_{s_2} - w_{s_1} &= 0 && \text{steady} \\ \bar{w}_2 - \bar{w}_1 &= -\lambda \left(\frac{\partial w_{s_2}}{\partial x} - \frac{\partial w_{s_1}}{\partial x} \right) && \text{Oscillatory} \end{aligned}$$

But since $\bar{w} = \partial \bar{\phi} / \partial z$ then

$$\partial w_s / \partial x = \partial^2 \phi_s / \partial z \partial x = \partial u_s / \partial z$$

Thus the oscillatory shock jump condition can be rewritten as:

$$\bar{w}_2 - \bar{w}_1 = -\lambda \frac{\partial}{\partial z} (u_{s_2} - u_{s_1})$$

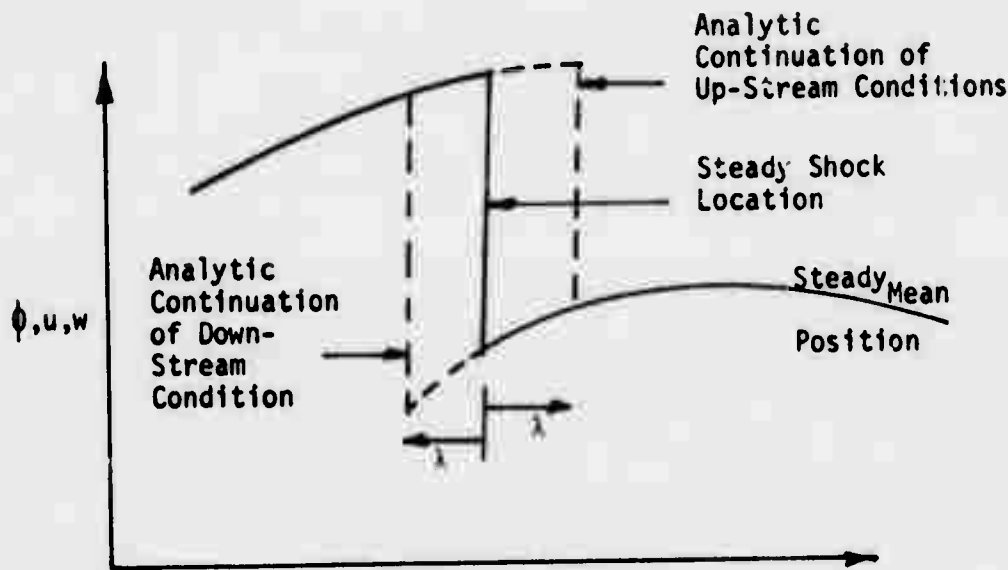


Figure 2.5-25 Analytic Continuation of Flow Variables Due to Shock Wave Motion

This equation shows that vorticity exists on the shock surface because there is a jump in the tangential velocity, \bar{w} , across the shock. Let $\bar{\gamma}$ be this vorticity, then

$$\bar{\gamma} = -(\bar{w}_2 - \bar{w}_1) = \lambda \frac{\partial}{\partial z} \left(\bar{u}_{s_2} - \bar{u}_{s_1} \right)$$

If we use the linear expression for the steady pressure, i.e., $C_{p_s} = -2 u_s / U_\infty$ then the vorticity $\bar{\gamma}$ can be expressed in terms of pressure jump across the steady shock wave.

$$\bar{\gamma} = -\lambda \frac{\partial}{\partial z} \left(C_{p_{s_2}} - C_{p_{s_1}} \right) U_\infty / 2 \quad (2.5.2-1)$$

The quantities $C_{p_{s_2}}(z)$ and $C_{p_{s_1}}(z)$ are known from the steady solution, therefore $\bar{\gamma}/\lambda$ is known.

This vorticity distribution induces a flow field (see Figure 2.5-26) in the vicinity of the airfoil which must be negated by the doublet lattice elements that are on the lifting surface. Cunningham (Reference 12) came to

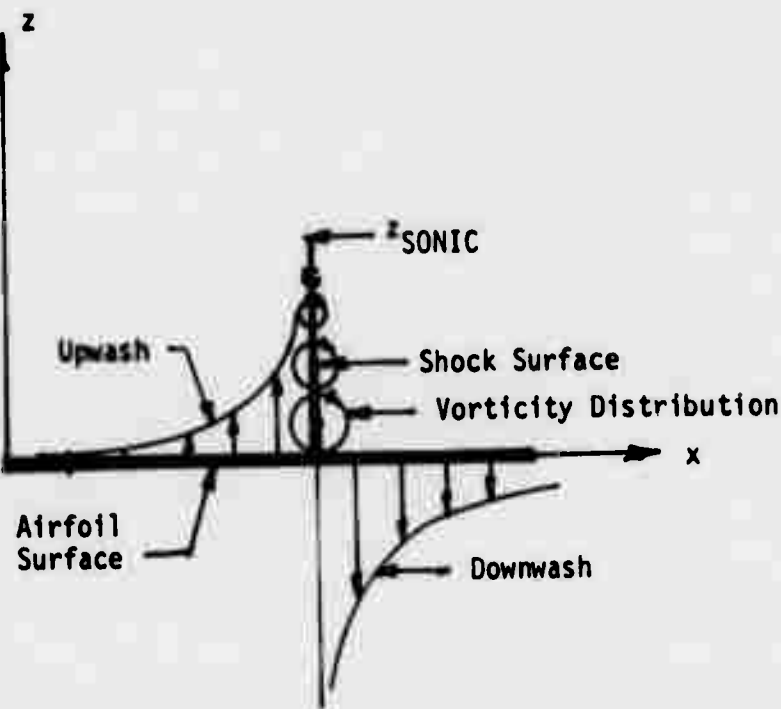


Figure 2.5-26 Shock Vorticity Interference Flow

the conclusion that a concentrated vortex was to be placed at the foot of the shock wave to simulate the shock motion interference. However from the above derivation it is seen that such a concentrated vortex is an approximation of the distributed vorticity that lies on the shock surface. The strength, Γ , of this equivalent concentrated vortex is:

$$\bar{\Gamma} = \int_0^{z_{\text{sonic}}} \bar{\gamma} dz = \lambda \left(C_{p_{s_2}}(0) - C_{p_{s_1}}(0) \right) U_{\infty} / 2 \quad (2.5.2-2)$$

since $C_{p_{s_2}}(z_{\text{sonic}}) - C_{p_{s_1}}(z_{\text{sonic}}) = 0$. This is because the pressure jump across the shock at its upper end, z_{sonic} , is zero. The quantities $C_{p_{s_2}}(0)$,

$C_{p_{s_1}}(0)$ are the steady pressure coefficients on the surface ($z = 0$) in front,

$C_{p_{s_1}}$, and in back of, $C_{p_{s_2}}$, of the steady shock.

For simplicity in the present analysis the point vortex model will be adopted. The onset downwash flow field due to this point vortex can be computed with the aid of the equivalent geometry, $(x - \bar{x}_{0}^{sv})$, and Mach Number \bar{M} where the subscript "sv" stands for "shock vortex". Some question arises, however, as to what values of time delay $(t - \tau)$ should be used in this downwash calculation and if the point vortex is to be placed on or off of the airfoil surface. At present it will be assumed that the point vortex lies on the airfoil surface and that the time delay to be used is that which is associated with this surface point. Figure 2.5.27 presents the downwash due to a unit

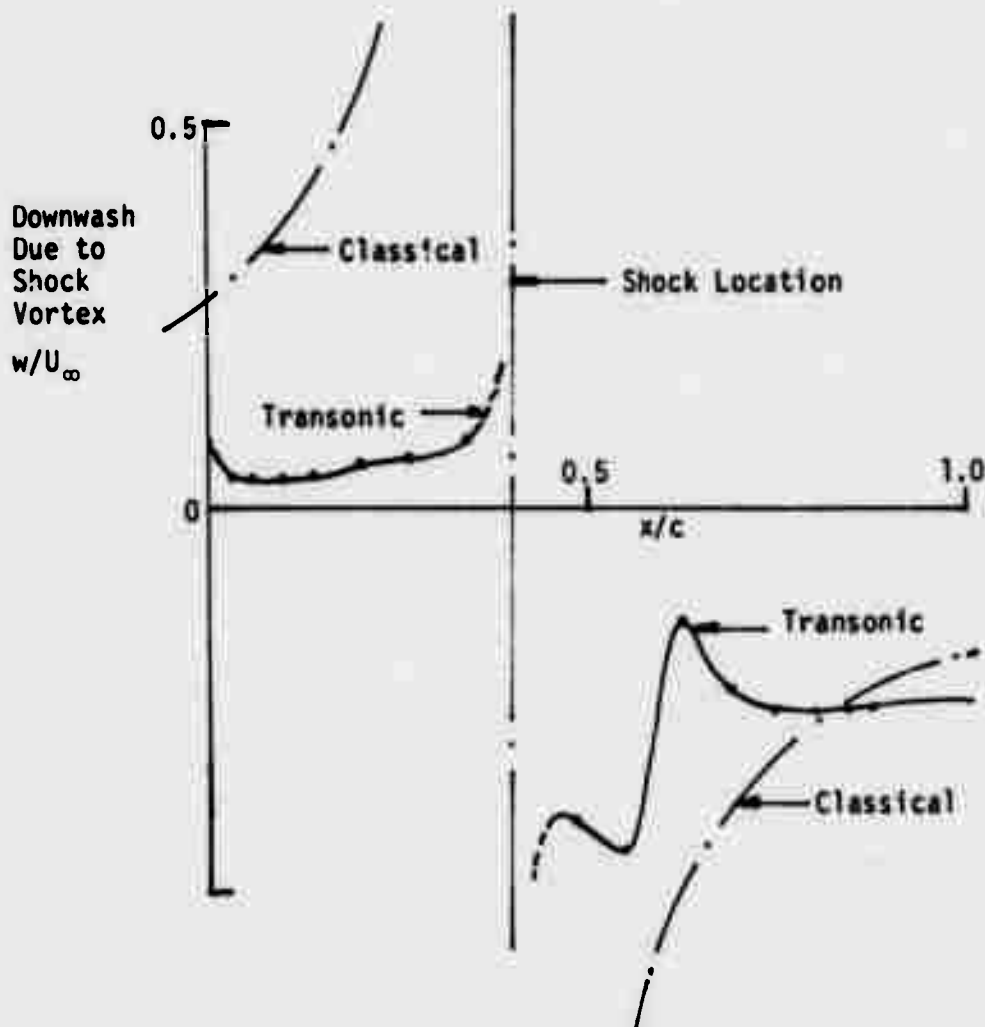


Figure 2.5-27 Shock Vortex Interference Flow Downwash For The NLR 7301 Airfoil Operating at $M_{\infty} = 0.7$ and $\alpha = 1.75^{\circ}$

point vortex on the surface of the NLR 7301 airfoil at the shock location $x/c = 0.4$ for the off-design case of $M_\infty = 0.7$. Shown in this figure are two curves; one representing the downwash due to a transonic vortex and one representing the downwash due to a classic subsonic vortex in a uniform stream (of $M_\infty = 0.7$) for reference. As a check on $t - \tau$ for the shock wave vortex the acoustic pulse generator was rerun for a series of points above the airfoil along the shock surface. The results are that the time delay, $t - \tau$, did not change significantly for points along the length of the shock wave.

For the NLR 7301 airfoil the shock motion λ is known because of experimental data and data from the Jameson method. Thus the vortex strength, $\bar{\Gamma}$, is:

$$\bar{\Gamma} = \lambda/2 \left(C_{p_{s_2}}(0) - C_{p_{s_1}}(0) \right) = \alpha \frac{\partial \lambda/2}{\partial \alpha} \left(C_{p_{s_2}}(0) - C_{p_{s_1}}(0) \right)$$

where $\partial \lambda / \partial \alpha$ is the rate of change of shock motion from its steady position with respect to α . In general this term is time complex but in the steady case to follow it is simply a real number. For the NLR airfoil at $M_\infty = 0.7$, $\alpha = 1.75^\circ$ the Jameson method gives $\partial \lambda / \partial \alpha \left(C_{p_{s_2}}(0) - C_{p_{s_1}}(0) \right) = 6.02$. Thus $\bar{\Gamma}_\alpha = 3.01$ for this airfoil and condition. The resulting interference pressure is presented in Figure 2.5-28. Large variations are observed between the classic subsonic vortex and the transonic one. This volatility indicates that the details of the vorticity on the shock may be important. Future refinements should then include refinements in the modeling of the shock vorticity.

2.5.2.2 Pressures Due to Shock Wave Motion Interaction with Steady Flow

The pressures C_{p_α} caused by the shock vortex interference flow (shown in Figure 2.5.28) is to be added to the pressure calculated in the absence of the shock (shown in Figure 2.5-20). Before this is done however there is one more term that must be considered. This last term in the pressure is caused by the direct action of the shock wave on the surface. As the shock wave

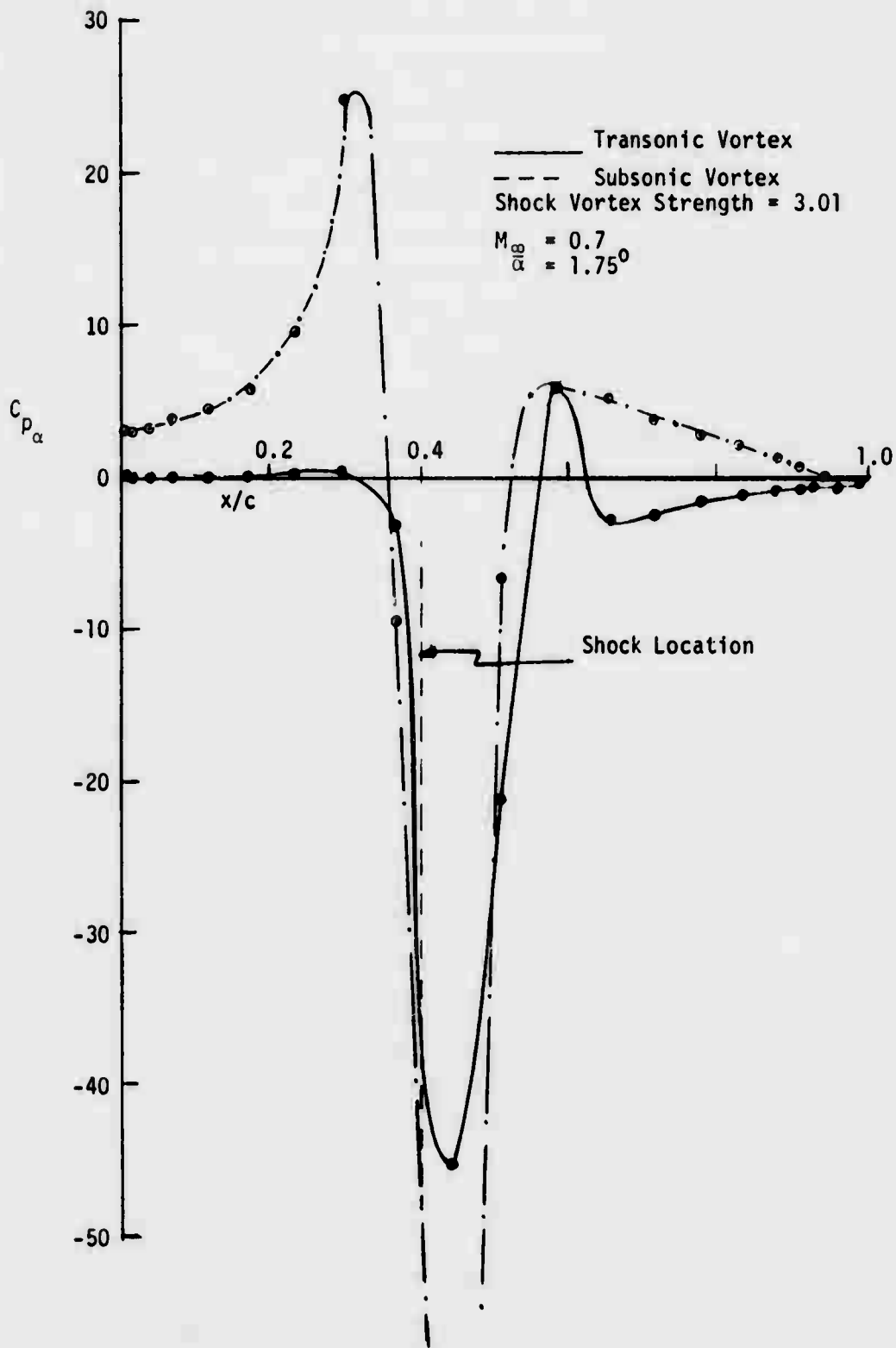


Figure 2.5-28 Pressure Distribution on the NLR 7301 Airfoil Operating at $M_\infty = 0.7$, $\alpha = 1.75^\circ$ Due to the Shock Vortex Interference Flow

THIS REPORT HAS BEEN DELIMITED
AND CLEARED FOR PUBLIC RELEASE
UNDER DOD DIRECTIVE 5200.20 AND
NO RESTRICTIONS ARE IMPOSED UPON
ITS USE AND DISCLOSURE.

DISTRIBUTION STATEMENT A

APPROVED FOR PUBLIC RELEASE;
DISTRIBUTION UNLIMITED.

passes over a particular point the perturbation pressure rises sharply. The region on the airfoil where this occurs is confined to that area over which the shock wave moves.

The pressure coefficient C_p on the airfoil due to the motion of the shock wave is

$$C_p(\alpha, x) = (C_{p_{s_2}} - C_{p_{s_1}}) H\left(\frac{x}{c} - \frac{\tilde{x}_s}{c}(\alpha)\right) + C_{p_{s_1}}$$

where H is the step function at the instantaneous position of the shock $\tilde{x}_s(\alpha)$ and the zeros have been dropped from $C_{p_{s_2}}(0)$ and $C_{p_{s_1}}(0)$ for convenience.

The derivative is:

$$C_{p_\alpha} = (C_{p_{s_2}} - C_{p_{s_1}}) \delta\left(\frac{x}{c} - \frac{\tilde{x}_s}{c}(\alpha)\right) \left(-\frac{\partial \tilde{x}_s}{\partial \alpha} / c\right) \quad (2.5.2-3)$$

where δ is a dirac delta function. In the limit as the amplitude of shock wave travel is reduced to zero then

$$\tilde{x}_s(\alpha) \rightarrow x_s \equiv \text{steady position of the shock}$$

$$\frac{\partial \tilde{x}_s}{\partial \alpha} \rightarrow \frac{\partial \lambda}{\partial \alpha} \Bigg|_{x = x_s}$$

The force, F_α/q , generated by this pressure is then

$$F_\alpha/q = - \int C_{p_\alpha} dx = (C_{p_{s_2}} - C_{p_{s_1}}) \frac{\partial \lambda}{\partial \alpha} \quad (2.5.2-4)$$

For the case of oscillatory motion $\lambda = \lambda_0 \exp(-i\omega\tau)$ and $\alpha = \alpha \exp(i\omega t)$.
If $F/q = \bar{F}/q \exp(i\omega t)$ then:

$$\bar{F}/q = \bar{F}_\alpha/q \bar{\alpha} = \bar{\alpha} (C_{p_{s_2}} - C_{p_{s_1}}) \frac{\partial \lambda_0}{\partial \alpha} \exp(-i\phi_s) \quad (2.5.2-5)$$

where ϕ_s and $\frac{\partial \lambda_0}{\partial \alpha}$ are functions of the reduced frequency k_r . Notice that equation 2.5.2-4 is exactly equal to the force generated by the shock vortex of strength $\bar{\Gamma}_\alpha$. That is:

$$\begin{aligned} \bar{F}_\alpha/q &= \frac{\rho U_\infty \bar{\Gamma}_\alpha}{\frac{1}{2} \rho U_\infty^2} = \frac{2}{U_\infty} \frac{\partial \lambda}{\partial \alpha} (C_{p_{s_2}} - C_{p_{s_1}}) \frac{U_\infty}{2} \\ &= \frac{\partial \lambda}{\partial \alpha} (C_{p_{s_2}} - C_{p_{s_1}}) \end{aligned}$$

The expression for the pressure, C_p , given in equation (2.5.2-3), is not suitable for plotting and applies for infinitesimally small motions. For finite motions, consider the finite form of C_{p_α} :

$$\frac{\Delta C_D}{\Delta \alpha} = \left(\frac{C_{p_{s_2}} - C_{p_{s_1}}}{\Delta \alpha} \right) \left\{ H \left(x - \left(x_s + \frac{\partial \lambda}{\partial \alpha} \right) \right) - H(x - x_s) \right\} \quad (2.5.2-6)$$

This is a rectangular shape of height $(C_{p_{s_2}} - C_{p_{s_1}})/\Delta \alpha$ and width $\Delta \eta = \frac{\partial \lambda}{\partial \alpha} \Delta \alpha$. This equation applies for shock waves that are not defused. However Figure 2.5-22 shows that the shock is not sharp for the NLR 7301 airfoil at $M_\infty = 0.7$ and $\alpha = 1.75^\circ$, but is spread out from $x/c = 0.39$ to $x/c = 0.45$; a total length of $\Delta x_s = 0.06$. An approximate way of accounting for this effect would be to plot $\Delta C_D/\Delta \alpha$ as a trapezoid whose base is $\Delta \lambda + \Delta x_s$, whose top width is $\Delta \lambda$ and whose area is \bar{F}_α/q . For the NLR 7301 airfoil at $M_\infty = 0.7$, $\alpha = 1.75^\circ$ the value of $\Delta \lambda$ is 0.065 for a corresponding $\Delta \alpha$ of 0.0087 rad. The trapezoid base is then 0.125, the top width is 0.065. The total force, $\frac{\partial \lambda}{\partial \alpha} (C_{p_{s_2}} - C_{p_{s_1}})$, = 6.02 thus the height of the trapezoid is $6.02(.065 + .125)/2 = 63.4$.

All of the contributing terms for the final pressure distribution are now known, that is, 1) the shock free pressure distribution derived in subsection 2.5.1, 2) the pressure distribution caused by the interference flow of the shock vortex, and, 3) the pressure distribution just discussed which is a direct result of the moving of the shock wave. Specific application to

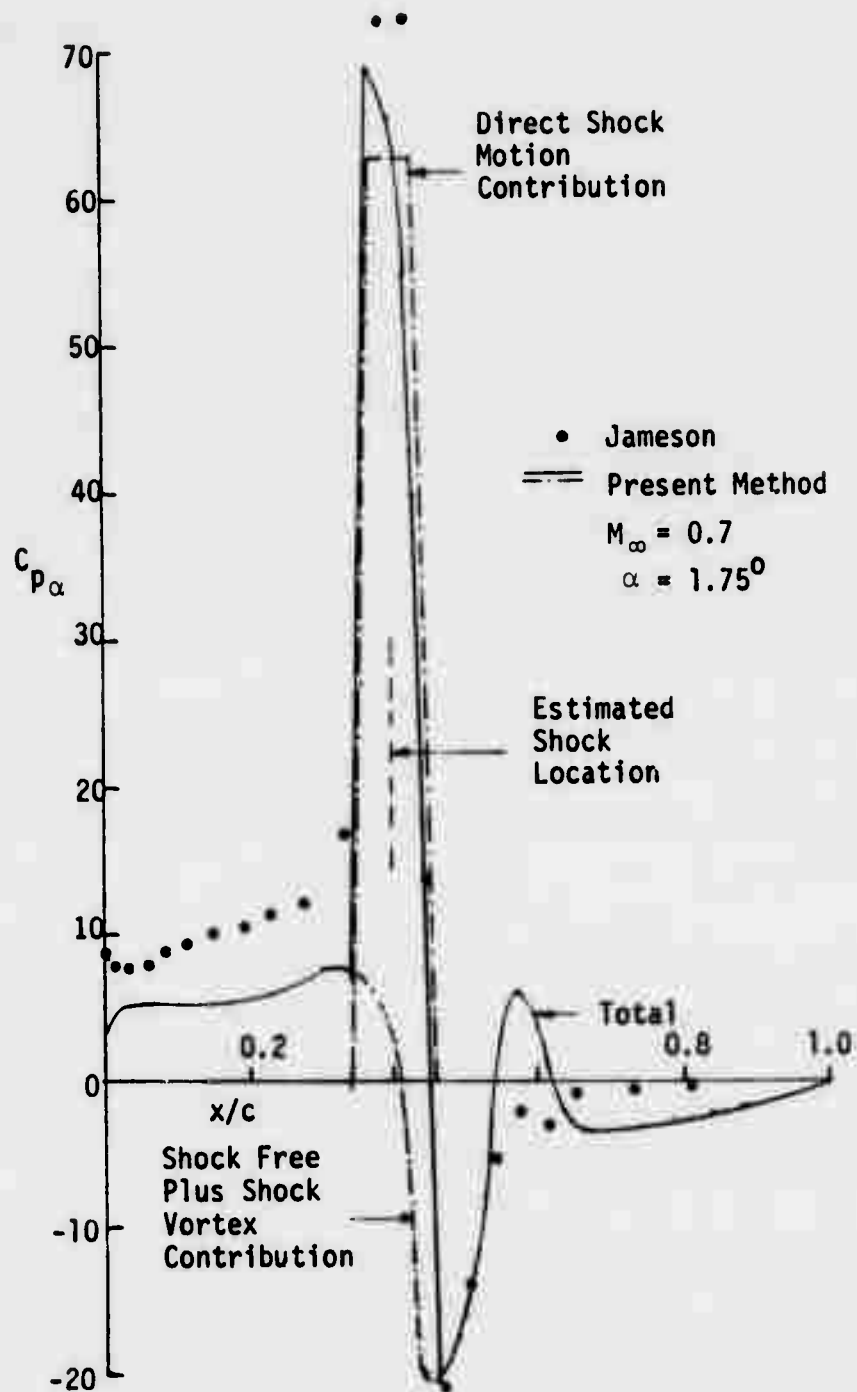


Figure 2.5-29 Comparison of the Present Method (With Shock Wave Effects) With the Jameson Transonic Method For the NLR 7301 Airfoil

the NLR 7301 airfoil at $M_\infty = 0.7$ and $\alpha = 1.75^\circ$ is presented in Figure 2.5-29, where the results of Figure 2.5-20 (shock free flow) are combined with the results of Figure 2.5-28 (transonic shock vortex) and with the trapezoidal distribution discussed above. The agreement is good except in the region forward of the shock wave in the supersonic zone. The good agreement aft of the shock may not be entirely trustworthy since it appears that the shock vortex interference pressures are presently somewhat in doubt and this is the flow that produces this correlation. The correlation with the shock peak is good because the present method has been constrained to reproduce the proper total force \bar{F}_α/q due to steady shock motion. This total force is proportional to shockwave motion, $\partial\lambda/\partial\alpha$, and steady pressure jump ($C_{p_{s_2}} - C_{p_{s_1}}$). Currently the present method uses either experimental data or results from the Jameson steady transonic flow method to obtain the quantities needed, i.e., $\partial\lambda/\partial\alpha$ and $C_{p_{s_2}} - C_{p_{s_1}}$. The next subsections describe a possible method for determining the shock wave amplitude $\partial\lambda/\partial\alpha$ for the general oscillatory case (which includes the steady case). The Jameson method can not be used to obtain shock wave motion data for the oscillatory case although it can be used to aid in its determination.

The object of the present method is to furnish an inexpensive lifting surface theory for transonic flow that can be run for various modes of motion at various frequencies and which is based on steady flow data which is used once and for all. This steady flow data can be from experimental sources or from transonic steady flow methods.

So far in the correlation of the present method only steady flow conditions have been considered. However at this stage of development this seems appropriate since the steady perturbation results must agree before the unsteady results are attempted. In addition the unsteady shock wave amplitude calculation has not yet been tried in the present method and therefore a complete correlation awaits this development.

The correlation illustrated in Figure 2.5-29 shows that the shock wave motion contribution to the pressure is a dominant transonic effect. A

possible method of including transonic effects in a simple way would be to add the shock wave motion effect to the classic theory. This idea is pursued in the next subsection.

2.5.2.3 Investigation of a Simple Method for Accounting for Transonic Effects

In this subsection the results of adding the shock motion pressures to those determined by the classical subsonic theory is investigated for the NLR 7301 airfoil. The pressure distribution is presented in Figure 2.5-30 for reference.

In the analysis of flutter and other dynamic aeroelastic phenomena it is the section lift and moment which are of paramount importance. In Reference 4 the experimental lift and moment are plotted versus the reduced frequency for various Mach Numbers. The results of the classic theory are compared to these experimental values. At low Mach Numbers the data and theory should agree since transonic effects are small. However there is still a difference between theory and data and this difference is attributable to viscous boundary layer effects. This boundary layer effect can be isolated by subtracting the results for the experiment from those of the theory for the low Mach Number case. This effect can then be taken out of the data for transonic Mach Numbers so that viscous effects do not confuse the issue.

Transonic effects can be easily isolated now that the viscous effects are eliminated. This is accomplished by taking the difference between the classical theory and the corrected experimental data in the transonic speed range. This has been done for the NLR 7301 airfoil at $M_\infty = 0.7$, $\alpha = 1.75^\circ$ and the results plotted in Figure 2.5-31. The specific formula for the corrected transonic increment in lift $\tilde{\Delta c}_{l_\alpha}$ is:

$$\tilde{\Delta c}_{l_\alpha} = \tilde{c}_{l_\alpha} \text{ (data)} - c_{l_\alpha} \text{ (classic theory)} \quad \text{at } M_\infty = 0.7$$

where the corrected data, \tilde{c}_{l_α} , is the result of eliminating the viscous loss of lift, Δc_{l_α} , from the data:

$$\tilde{c}_{l_\alpha} \text{ (data)} = c_{l_\alpha} \text{ (data)} + \Delta c_{l_\alpha} \quad \text{at } M_\infty = 0.7$$

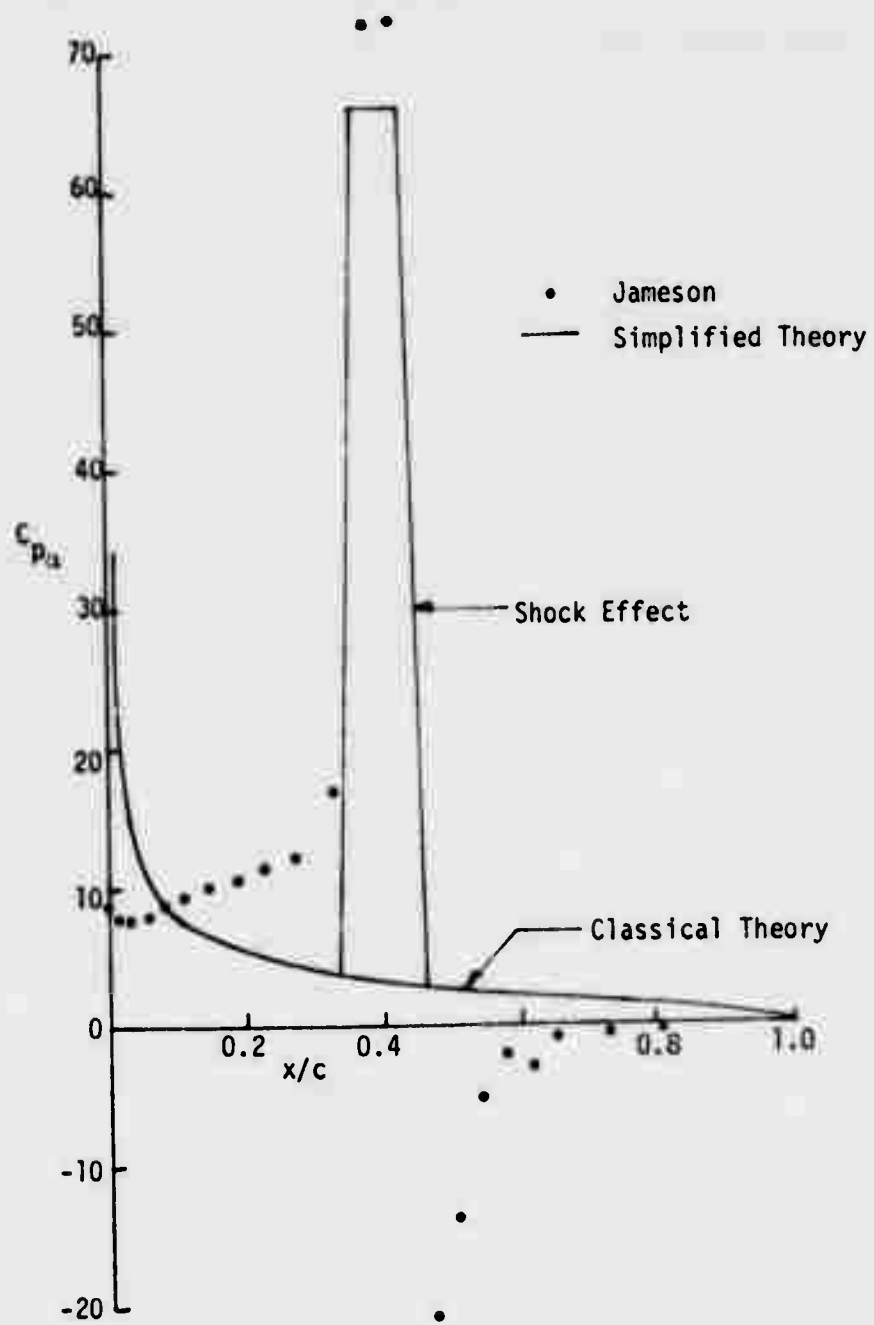


Figure 2.5-30 Comparison of The Jameson Method With The Simplified Transonic Method

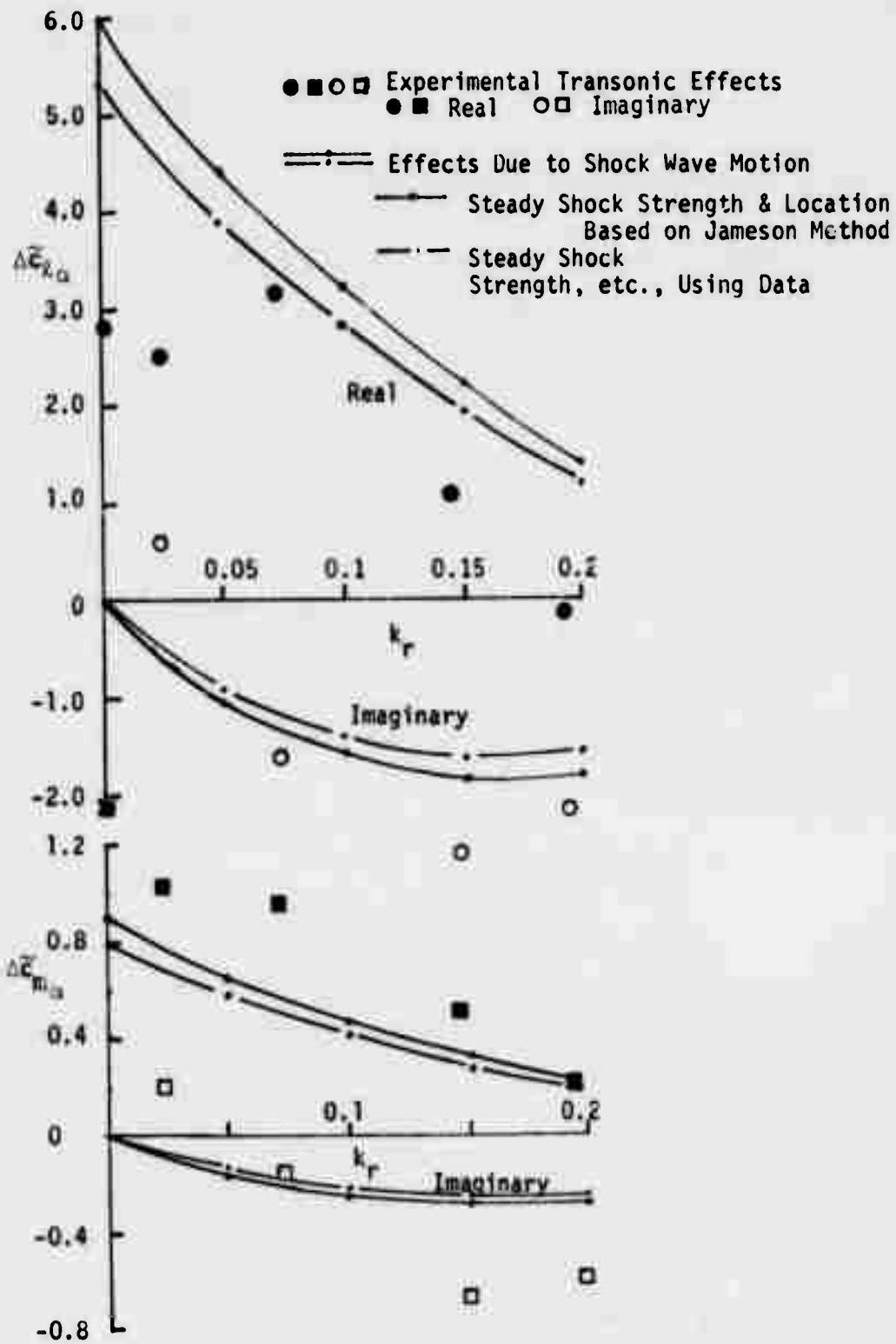


Figure 2.5-31 Comparison of The Simple Transonic Method With Experimental Data. Simple Method Uses Steady Data From Two Sources.

where the viscous loss of lift Δc_{l_α} is determined from theory and data at $M_\infty = 0.5$.

$$\Delta c_{l_\alpha} = c_{l_\alpha}(\text{theory}) - c_{l_\alpha}(\text{data}) \quad \text{at } M_\infty = 0.5.$$

A similar procedure applies to the moment.

This data is compared with the simplified transonic effect consisting of the shock motion pressure alone. Thus

$$\tilde{\Delta c}_{l_\alpha} = \bar{F}_\alpha / qc = \frac{\partial \lambda / c}{\partial \alpha} (c_{p_{s_2}} - c_{p_{s_1}})$$

$$\tilde{\Delta c}_{m_\alpha} = \tilde{\Delta c}_{l_\alpha} x_s / c$$

where \bar{F}_α / qc is the normalized force due to shock wave motion and x_s is the shock location point at which the force \bar{F}_α acts.

The term λ is, in general, a complex number which can be represented as follows (see Equation 2.5.2-5):

$$\lambda = \lambda_0(k_r) \exp(-i\phi_s)$$

where ϕ_s is the phase lag between the shock and airfoil motions. Reference 4 shows that this phase lag is proportional to the frequency. Based on an approximate calculation it was concluded that the constant of proportionality was the time, τ , it takes a "Kutta wave" to reach the shock wave. Reference 4 defines the Kutta wave as an acoustic wave emanating from the trailing edge. Using the acoustic wave generator described in subsection 2.5.1.4 the time history of an acoustic wave emanating from the trailing edge was generated. The results are presented in Figure 2.5-32. The time that the shock first feels this acoustic wave is approximately $\bar{\tau} = \tau U_\infty / c = 3.0$. The experimental data of Reference 4 shows that

$$\phi_s = 4.32 k_r$$

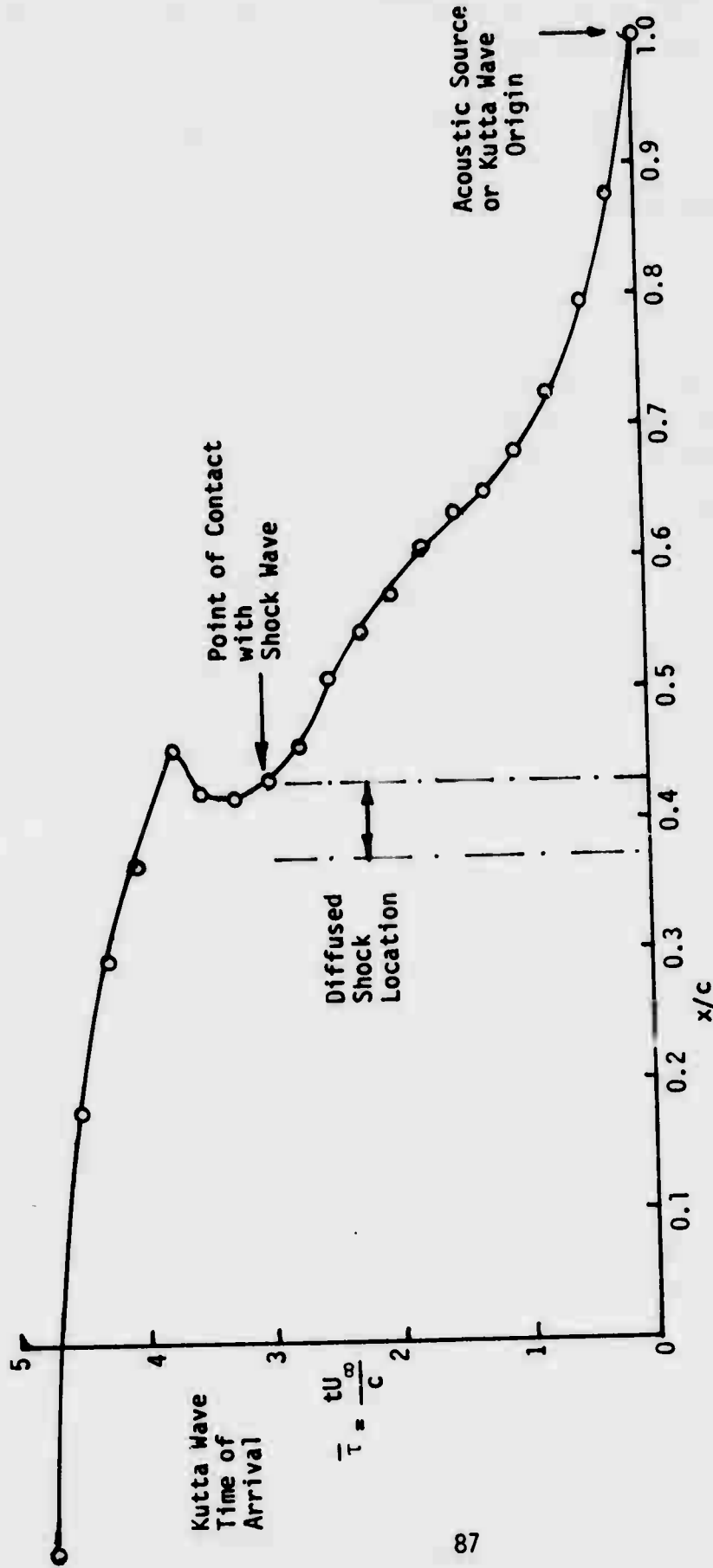


Figure 2.5-32 Time of Arrival of an Acoustic Wave Whose Origin is at The Airfoil Trailing Edge as It Passes Upstream Over the NLR 7301 Airfoil ($M_{\infty} = 0.7, \bar{\alpha} = 1.750$)

If it is assumed that ϕ_s is also proportional to the time $\bar{\tau}$ then the proportionality constant is 1.44 or

$$\phi_s = 1.44 k_r \bar{\tau} \text{ (concluded by present authors)}$$

The authors of Reference 4 concluded that

$$\phi_s = 2 k_r \bar{\tau}$$

because they had only an approximate value for τ . Irrespective of these two formulas the phase lag, ϕ_s , is taken as the experimental value of 4.32. (Actually, for Figure 2.5-31, the value $\phi_s = 4.56$ was used. The difference, 5%, should not cause any significant difference).

Reference 4 also presents experimental data (for the NLR 7301 airfoil) for the amplitude of the shock wave motion, λ_o , as a function of frequency. This data can be generalized by normalizing it with respect to the steady amplitude $\lambda_o(k_r = 0)$. A plot of $\lambda_o(k_r)/\lambda_o(k_r = 0) = G$ shown in Figure 2.5-33. This curve will be used later for the TF-8A and YC-15 wings. The value of $\lambda_o(k_r)$ is obtained from this curve as follows:

$$\lambda_o(k_r) = \lambda_o(k_r = 0) G(k_r)$$

For Figure 2.5-31 two values of $\lambda_o(k_r = 0)$ were used: the experimental value and the value obtained from the Jameson method.

The agreement for the incremental transonic effects is fairly good considering the simplicity of the theory. The percent error due to the differences in the lift increments will be reduced when added to the basic lift. For the moment however the shock movements represent the largest portion of the final result and thus the percent error will not change much. In general it is observed that the theory over predicts the lift and under predicts the moment.

2.5.2.4 Shock Wave Compatibility Relations

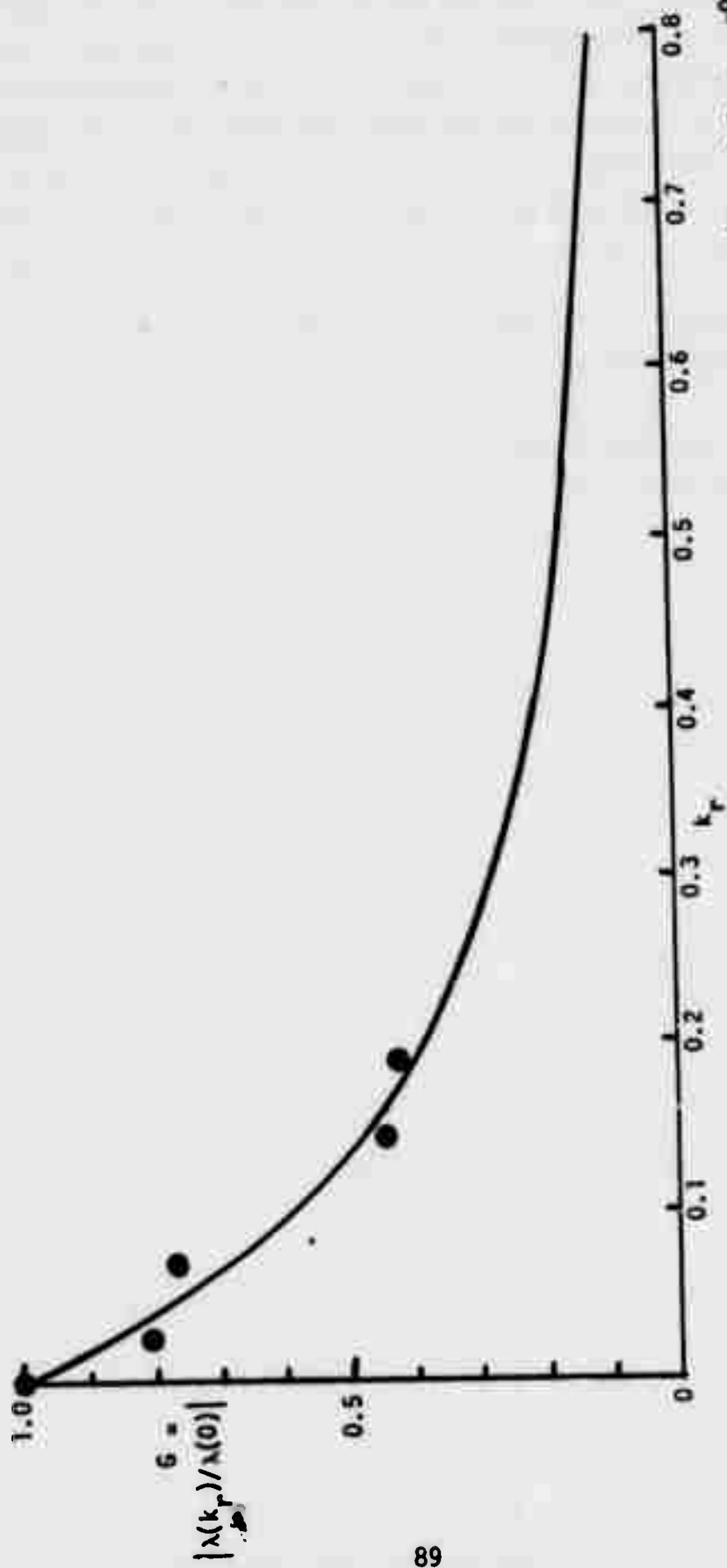


Figure 2.5-33 Ratio of Oscillatory to Steady Shock Wave Amplitude for The MLR 7301 ($M = 0.7$, $\alpha = 3^\circ$)

In subsection 2.5.2.1 the tangential velocity shock jump-condition was used to obtain the interference flow due to the shock motion. It was shown that this interference flow is caused by a vorticity distribution of known shape which is proportional to the shock wave amplitude. The shape of the vorticity was simplified to a point vortex on the surface. The total vorticity is proportional to the steady component of pressure rise across the shock wave, $(C_{p_{s_2}} - C_{p_{s_1}})$, and the amplitude of shock wave motion, $\partial\lambda/\partial\alpha$. The steady pressures are known but the amplitude of unsteady shock motion is not known and it is the object of this section to suggest a procedure for obtaining it.

The first equation of subsection 2.5.2.1 presents the jump conditions for the x-component of velocity at the instantaneous shock position:

$$\tilde{u}_2 - \tilde{u}_1 = \frac{-2}{\gamma+1} \tilde{u}_1 \left(1 - \frac{1}{M_1^2} \right)$$

where, as before, the tilda indicates instantaneous shock position and the subscripts indicate positions just upstream, 1, and just downstream, 2, of the shock. Landahl (Reference 15, Equation 1.17, page 4) gives an expression for \tilde{M}_1

$$\frac{1}{\tilde{M}_1^2} = \frac{1}{M_\infty^2} + (1-\gamma) \left[\tilde{\phi}_x + \tilde{\phi}_t + O(\phi_{x,z}^2) \right] / U_\infty$$

where $O(\quad)$ indicates order of magnitude. The following analytical continuation of $\tilde{\phi}$ is used:

$$\tilde{\phi} = \phi_s + (\lambda \partial\phi/\partial x + \bar{\phi}) \exp(i\omega t)$$

If the proper derivatives are taken of $\tilde{\phi}$ and the nonlinear terms, $O(\phi_{x,z}^2)$ are assumed small enough to ignore then

$$\begin{aligned} \frac{1}{\tilde{M}_1^2} = & \left\{ \frac{1}{M_\infty^2} + (1-\gamma) \partial\phi_{s_1}/\partial x \right\} + (1-\gamma) \left\{ \lambda \left(\partial^2\phi_{s_1}/\partial x^2 + i\omega \partial\phi_{s_1}/\partial x \right) \right. \\ & \left. + \left(\partial\bar{\phi}_1/\partial x + i\omega\bar{\phi}_1 \right) \right\} \exp(i\omega t) \end{aligned}$$

where ϕ_s and $\bar{\phi}$ are the steady and oscillatory components of the potential.

Applying the analytic continuation procedure to \tilde{u}_1 gives

$$\tilde{u}_1 = u_{s_1} + (\lambda \partial u_{s_1} / \partial x + \bar{u}_1) \exp(i\omega t)$$

Introducing the expressions for \tilde{u}_1 , and $1/\tilde{M}_1^2$ into the expression for $\tilde{u}_2 - \tilde{u}_1$ and remembering that $\partial\phi/\partial x = u$ gives:

$$\tilde{u}_2 - \tilde{u}_1 = \frac{-2}{\gamma+1} \left\{ A + [\lambda B + C\bar{u}_1 + D\phi_1] \exp(i\omega t) + O(\exp(i2\omega t)) \right\}$$

where

$$A = -u_{s_1} (\beta_\infty^2 / M_\infty^2 + (1 - \gamma) u_{s_1})$$

$$B = -u_{s_1} (1 - \gamma) (u_{s_1 x} + i\omega u_{s_1}) - u_{s_1 x} (\beta_\infty^2 / M_\infty^2 + (1 - \gamma) u_{s_1})$$

$$C = -u_{s_1} (1 - \gamma) - (\beta_\infty^2 / M_\infty^2 + (1 - \gamma) u_{s_1})$$

$$D = -u_{s_1} (1 - \gamma) i\omega$$

Expanding the left hand side of the equation $\tilde{u}_2 - \tilde{u}_1$ and using the expression for analytic continuation gives:

$$\tilde{u}_2 - \tilde{u}_1 = E + (\lambda F + \bar{u}_2 - \bar{u}_1) \exp(i\omega t)$$

where

$$E = u_{s_2} - u_{s_1}$$

$$F = u_{s_2 x} - u_{s_1 x}$$

Equating the two expressions for $\tilde{u}_2 - \tilde{u}_1$ and separating steady and

oscillatory parts gives:

$$u_{s_2} - u_{s_1} = + \frac{2}{\gamma+1} \left(\beta_\infty^2 / M_\infty^2 + (1 - \gamma) u_{s_1} \right) u_{s_1} \quad \text{steady flow}$$

$$\bar{u}_1 - \bar{u}_2 = \lambda \left(F + \frac{2}{\gamma+1} B \right) + u_1 \left(\frac{2}{\gamma+1} C \right) + \phi_1 \left(\frac{2}{\gamma+1} D \right) \quad (2.5.2.4-1)$$

oscillatory flow

These are the final expressions for the u-component jump conditions across the shock referred to the steady position of the shock.

The jump conditions for the w-component were given in subsection 2.5.2.1 as

$$\bar{w}_2 - \bar{w}_1 = - \lambda \partial(u_{s_2} - u_{s_1}) / \partial z$$

If this expression is integrated clockwise around the shockwave then

$$\begin{aligned} \bar{\phi}_2(z) - \bar{\phi}_1(z) &= \int_z^{z_{\text{sonic}}} \bar{w}_1 \, ds + \int_{z_{\text{sonic}}}^z \bar{w}_2 \, ds \\ &= - \int_z^{z_{\text{sonic}}} (\bar{w}_2 - \bar{w}_1) \, ds = \lambda \int_z^{z_{\text{sonic}}} \partial(u_{s_2} - u_{s_1}) / \partial s \, ds \end{aligned}$$

$$\phi_2(z) - \phi_1(z) = - \lambda (u_{s_2}(z) - u_{s_1}(z)) \quad (2.5.2.4-2)$$

since $u_{s_2} - u_{s_1} = 0$ at the sonic point $z = z_{\text{sonic}}$. Here the assumption has been made that the amplitude does not vary with height above the airfoil.

If this is not the case then this assumption can be eliminated by considering λ to be an assumed function of z of unknown amplitude. Equations (2.5.2.4-1)

and (2.5.2.4-2) can be combined to eliminate the unknown shock wave motion, λ as follows:

$$\bar{u}_1 G - \bar{u}_2 H = \bar{\phi}_1 J - \bar{\phi}_2 K \quad (2.5.2.4-3)$$

where

$$G = [1 - 2c/(\gamma+1)] (u_{s2} - u_{s1})$$

$$H = (u_{s2} - u_{s1})$$

$$J = [F + 2B/(\gamma+1)] + (u_{s2} - u_{s1}) 2D/(\gamma+1)$$

$$K = F + 2B/(\gamma+1)$$

In terms of pressures $C_p = -2 \left(\frac{\phi_x}{U_\infty} + i \frac{\omega \phi}{U_\infty^2} \right)$. Equation (2.5.2.4-3) can be written as:

$$\frac{-U_\infty}{2} G C_{p1} + \frac{U_\infty}{2} H C_{p2} = \bar{\phi}_1 (J + i \frac{\omega}{U_\infty} G) - \bar{\phi}_2 (K + \frac{i\omega}{U_\infty} H) \quad (2.5.2.4-4)$$

Equations (2.5.2.4-3) or (2.5.2.4-4) furnishes a compatibility condition that is to be satisfied by the oscillatory flow across the steady shock position. These equations hold at all positions along the shock from the surface ($z = 0$) to the sonic point ($z = z_{sonic}$). Consistent with the assumption that the shock amplitude of motion does not change along the shock is the assumption that the compatibility equation is not a function of the vertical direction z . These equations can thus be satisfied on the airfoil surface only. In this case the second version of the compatibility equation, i.e. (2.5.2.4-4) is appropriate. This expression furnishes one additional equation in the set of equations for the lifting surface pressures. The wave amplitude, λ , is the one additional unknown in the problem. Thus

the problem is determinent.

The lifting surface theory without a shock wave (but with transonic effects) can be written in matrix form as:

$$\left\{ c_{p_o} \right\} = [D] \left\{ w_o \right\}$$

where the subscript "o" indicates shock free transonic flow. The shock vortex onset flow is given by

$$\left\{ c_{p_T} \right\} = \lambda [D] \left\{ w_T \right\}$$

where $\{w_T\}$ is the downwash due to the shock vortex or vorticity. The strength of the vortex is that associated with shock motion of unit amplitude. The compatibility equation can be written as:

$$a = \{L\}^T \left\{ c_{p_T} \right\}$$

where the term $\{L\}^T$ is the matrix form of Equation (2.5.2.4-4) and where:

$$\left\{ c_{p_T} \right\} = \left\{ c_{p_o} \right\} + \left\{ c_{p_T} \right\}$$

Combining the first two equations with the third produces an equation that can be solved for the shock motion amplitude λ . Placing λ into the expression for $\left\{ c_{p_T} \right\}$ and adding $\left\{ c_{p_o} \right\}$ produces the final total. This total represents the combination of the shock free transonic and shock vortex flows. To this is added the shock motion pressure. It is anticipated that the steady value of λ can be used as an aid in the evaluation of the quantities required in the compatibility equation.

In summary, a procedure has been outlined for determining the shock wave motion amplitude for oscillatory flow. This procedure has not been implemented under the current contract or McDonnell Douglas Company IRAD funds. Future investigations of this procedure are thus recommended.

2.6 FLUTTER ANALYSIS PROCEDURES

All of the flutter analyses performed in this study were carried out using the standard American, or V-g method. The analyses used the measured aerodynamic mode shapes, generalized mass, and frequencies of six elastic modes of the TF-8A flutter model. A few cases were also analyzed using modal deflection data as calculated from basic distributions of inertial and rigidity data. Section 3 below discusses the basic data used in the flutter analysis in detail.

Analyses were run at Mach numbers of .6, .8, .9, .95 and .99 for the TF-8A flutter model and .76 for the YC-15II. In each case the unsteady aerodynamic influence coefficients (AIC's) were generated theoretically by the subsonic Doublet Lattice Method and weighted appropriately.

Two sorts of weighting were applied to each case; they are described in detail in Sections 2.4 and 2.5. Briefly, the first method, loosely described as "steady corrections" assumes that the ratio of the correct data to the theoretical data at all values of reduced frequency, k , is the same as at $k_r = 0$. The correct data at $k_r = 0$ is of course the available static pressure model data, converted to spanwise distribution of sectional lift and moment coefficient. This method does account for the static aeroelastic twist and the non-linear character of the aerodynamic derivatives. The second method, described as "unsteady corrections" theoretically accounts for unsteady transonic effects and results in a multiplicative correction factor which is applied to the "steady corrected" AIC's. This multiplicative correction factor is a complex valued function of k_r and reduces to 1.0 at $k_r = 0$.

The V-g solution was obtained for several values of density for each Mach number so that the calculated flutter speed at each density could be cross-plotted to obtain the flutter speed which matched the Mach number under consideration. Structural damping was assumed to be $g = 0.02$ in all elastic modes.

2.7 FLUTTER MODEL PROCEDURES

The analytical work documented in this report shows the need for further wind tunnel flutter model test confirmation of the analysis methods. Airfoil shape, static twist, reduced frequency at flutter, and Reynolds numbers are some of the parameters that the flutter model should evaluate.

A cantilevered wing (with adjustable root pitch) would be an ideal candidate for the study since it would avoid problems of scaling lift to weight ratio inherent in a free-flying model. The basic planform area should be one for which high speed rigid model steady aerodynamic data already exists, such as the proposed C-15A wing.

Instrumentation should be included to measure the wing spanwise static bending and torsion deformation. Optical methods can confirm the tip twist. The Langley Research Center Transonic Dynamics Tunnel provides the current optimum facility for this study. Reynolds number effects can be evaluated by building models of difference size and/or air/freon mixes. All of the other parameter of interest can be incorporated into a single spar design.

Section 3.5 below discusses some details of a proposed flutter model.

SECTION III RESULTS OF ANALYSIS

3.1 PHASE I RESULTS

3.1.1 TF-8A Vibration Modal Data

The flutter analysis of the TF-8A flutter model was based upon measured vibration deflection data supplied by NASA. Figure 3.1-1 shows the modal deflection measurement grid. Table 3.1-1 lists the coordinates of this grid. Tables 3.1-2 to 3.1-7 show the modal deflections at the deflection control points for the six measured TF-8A modes. The frequency and generalized mass of each mode as supplied by NASA are also shown in Tables 3.1-2 to 3.1-7.

In order to more easily weight the AIC's it was decided to transform the idealization into plunge and pitch deflections along a set of streamwise strips. This proved to be justifiable since an inspection of the original modal data showed the wing to be essentially rigid in a structural chordwise direction. The method used to make this transformation is discussed above in Section 2.2. Figure 3.1-2 shows the transformed idealization. Tables 3.1-8 to 3.1-13 show the transformed modal deflections.

The vibration modes of the TF-8A flutter model were also calculated from NASA supplied rigidity and mass data. Figures 3.1-3 to 3.1-5 show these data. The resulting mode shapes agreed well with the transformed test values. For the bending modes, the calculated values of frequency were within five percent and the generalized masses within four percent of the test value. For the torsion modes a discrepancy between measured and calculated frequency and generalized mass existed. Factoring the torsional stiffness eliminated this discrepancy, and when the calculated aerodynamic mode shapes were used in the flutter analysis along with the measured frequencies and generalized masses, the results were within two percent of those obtained using the transformed measured deflections.

Since, at the time the calculated modes were obtained, the study was already underway, it was decided to continue using the transformed measured modal data as the basis of the flutter analysis instead of switching in mid-stream to the calculated shapes. This was justified in light of the good flutter analysis correlation mentioned above.

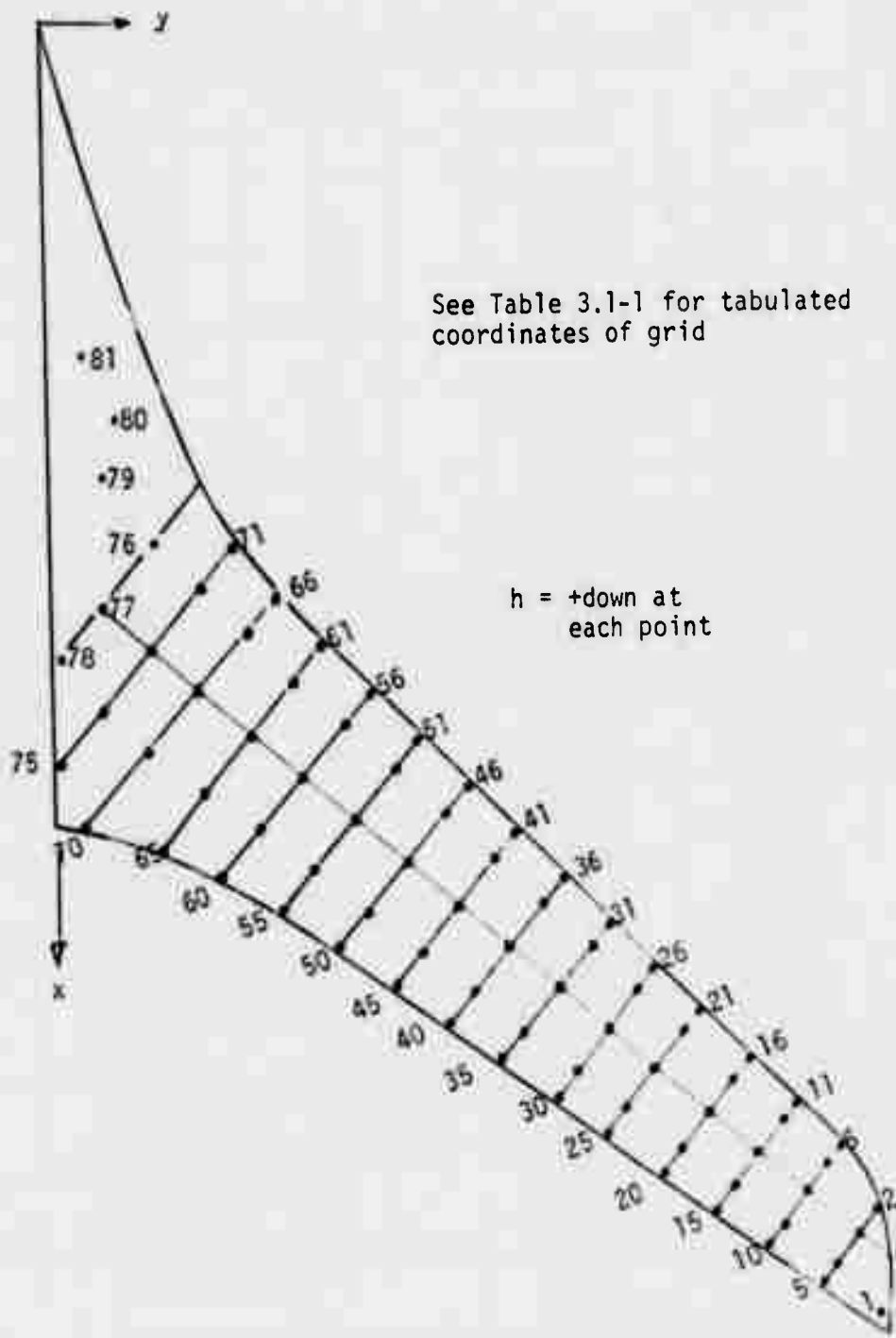


Figure 3.1-1 TF-8A Modal Deflection Measurement Grid

TABLE 3.1-1
TF-8A MODE SHAPE MEASUREMENT STATIONS

STATION	X INCHES	Y INCHES	STATION	X INCHES	Y INCHES
1	96.1993	62.5528	46	55.7806	31.2348
2	88.4250	62.4873	47	57.6151	29.6872
3	90.1830	61.0042	48	61.2075	26.6567
4	92.3614	59.1665	49	65.0292	23.4327
5	93.4315	58.2638	50	67.3987	21.4338
6	84.1375	59.8087	51	52.3291	27.6861
7	85.0929	59.0027	52	54.2399	26.0741
8	87.0802	57.3262	53	58.0235	22.8823
9	89.4497	55.3273	54	61.9981	19.5293
10	90.7491	54.2311	55	64.6160	17.3209
11	80.5271	56.1493	56	48.7943	24.0388
12	81.5972	55.2466	57	50.7434	22.3946
13	83.7756	53.4089	58	54.7563	19.0094
14	86.3362	51.2488	59	58.9602	15.4629
15	87.5209	50.2494	60	61.8265	13.0449
16	77.0373	52.6329	61	45.1149	20.6078
17	78.1839	51.6657	62	47.2933	18.7701
18	80.5916	49.6345	63	51.5355	15.1914
19	83.3432	47.3132	64	55.8540	11.5483
20	84.8337	46.0559	65	59.6376	8.3565
21	73.3547	49.1980	66	41.7422	17.0750
22	74.6923	48.0696	67	44.0353	15.1406
23	77.3676	45.8128	68	48.3920	11.4652
24	80.2874	43.3496	69	52.9017	7.6609
25	81.8772	42.0084	70	58.0993	3.2762
26	69.8996	45.4901	71	37.5245	14.0915
27	71.3137	44.2972	72	40.4902	11.5897
28	74.1036	41.9437	73	45.1680	7.6435
29	77.1992	39.3322	74	49.8688	3.6780
30	78.9572	37.8492	75	53.3466	.7441
31	66.4505	42.0218	76	37.1668	7.8518
32	67.9792	40.7322	77	41.9440	3.8217
33	70.9601	38.2174	78	45.5747	.7589
34	74.2469	35.4448	79	34.1000	4.1000
35	76.1959	33.8005	80	29.9000	5.0000
36	62.9207	39.4580	81	25.1000	2.5000
37	64.5641	37.0716			
38	67.7361	34.3957			
39	71.1757	31.4941			
40	73.2012	29.7854			
41	59.3910	34.8941			
42	61.0725	33.4756			
43	64.5121	30.5740			
44	68.1046	27.5434			
45	70.3212	25.6735			

Table 3.1-2

TF-8A Measured Modal Deflections

MODE NO. 1		1ST WING BENDING		GENERALIZED MASS=
RAY	H	BAY	H	
				.00484
1	0.190E+01	54	0.609E-01	
2	0.876E+00	55	0.582E-01	
3	0.887E+00	56	0.417E-01	
4	0.892E+00	57	0.373E-01	
5	0.904E+00	58	0.353E-01	
6	0.790E+00	59	0.329E-01	
7	0.774E+00	60	0.299E-01	
8	0.766E+00	61	0.187E-01	
9	0.775E+00	62	0.170E-01	
10	0.772E+00	63	0.161E-01	
11	0.693E+00	64	0.134E-01	
12	0.657E+00	65	0.103E-01	
13	0.558E+00	66	0.630E-02	
14	0.667E+00	67	0.550E-02	
15	0.661E+00	68	0.650E-02	
16	0.561E+00	69	0.530E-02	
17	0.551E+00	70	0.570E-02	
18	0.589E+00	71	0.780E-02	
19	0.536E+00	72	0.720E-02	
20	0.574E+00	73	0.670E-02	
21	0.505E+00	74	0.350E-02	
22	0.486E+00	75	0.250E-02	
23	0.488E+00	76	0.850E-02	
24	0.433E+00	77	0.910E-02	
25	0.432E+00	78	0.950E-02	
26	0.411E+00	79	0.970E-02	
27	0.393E+00	80	0.940E-02	
28	0.396E+00	81	0.111E-01	
29	0.416E+00			
30	0.393E+00			
31	0.320E+00			
32	0.304E+00			
33	0.292E+00			
34	0.286E+00			
35	0.288E+00			
36	0.228E+00			
37	0.220E+00			
38	0.220E+00			
39	0.207E+00			
40	0.215E+00			
41	0.170E+00			
42	0.160E+00			
43	0.155E+00			
44	0.151E+00			
45	0.147E+00			
46	0.109E+00			
47	0.104E+00			
48	0.103E+00			
49	0.101E+00			
50	0.462E-01			
51	0.713E-01			
52	0.654E-01			
53	0.651E-01			

THIS PAGE IS BEST QUALITY PRACTICABLE
 FROM COPY FURNISHED TO DDC

Table 3.1-3

TF-8A Measured Modal Deflections

MODE NO.	2	2ND WING BENDING		GENERALIZED MASS =
BAY	H	BAY	H	
				.00268
1	0.100E+01	54	-0.160E+00	
2	0.686E+00	55	-0.154E+00	
3	0.482E+00	56	-0.138E+00	
4	0.743E+00	57	-0.132E+00	
5	0.738E+00	58	-0.124E+00	
6	0.348E+00	59	-0.112E+00	
7	0.393E+00	60	-0.100E+00	
8	0.425E+00	61	-0.354E-01	
9	0.461E+00	62	-0.352E-01	
10	0.478E+00	63	-0.785E-01	
11	0.142E+00	64	-0.672E-01	
12	0.150E+00	65	-0.543E-01	
13	0.180E+00	66	-0.531E-01	
14	0.222E+00	67	-0.497E-01	
15	0.229E+00	68	-0.467E-01	
16	-0.694E-01	69	-0.392E-01	
17	-0.575E-01	70	-0.342E-01	
18	-0.301E-01	71	-0.305E-01	
19	-0.400E-01	72	-0.280E-01	
20	-0.630E-01	73	-0.269E-01	
21	-0.222E+00	74	-0.219E-01	
22	-0.239E+00	75	-0.153E-01	
23	-0.131E+00	76	-0.139E-01	
24	-0.110E+00	77	-0.163E-01	
25	-0.154E+00	78	-0.150E-01	
26	-0.310E+00	79	-0.147E-01	
27	-0.272E+00	80	-0.140E-01	
28	-0.270E+00	81	-0.130E-01	
29	-0.240E+00			
30	-0.241E+00			
31	-0.344E+00			
32	-0.320E+00			
33	-0.308E+00			
34	-0.290E+00			
35	-0.284E+00			
36	-0.280E+00			
37	-0.280E+00			
38	-0.280E+00			
39	-0.280E+00			
40	-0.280E+00			
41	-0.280E+00			
42	-0.280E+00			
43	-0.276E+00			
44	-0.267E+00			
45	-0.247E+00			
46	-0.247E+00			
47	-0.236E+00			
48	-0.222E+00			
49	-0.206E+00			
50	-0.198E+00			
51	-0.184E+00			
52	-0.179E+00			
53	-0.175E+00			

THIS PAGE IS BEST QUALITY PRACTICABLE
FROM COPY FURNISHED TO DDG

Table 3.1-4

TF-8A Measured Modal Deflections

MODE NO.	3	1ST WING TORSION	GENERALIZED MASS =	
BAY	H	FREQ = 37.10	H	
1	0.100E+01	54	0.521E+00	.02735
2	-0.175E+01	55	0.736E+00	
3	-0.576E+00	56	-0.265E+00	
4	-0.771E+00	57	-0.157E+00	
5	0.145E+01	58	0.457E-01	
6	-0.223E+01	59	0.344E+00	
7	-0.164E+01	60	0.508E+00	
8	-0.405E+00	61	-0.179E+00	
9	0.101E+01	62	-0.117E+00	
10	0.179E+01	63	0.337E-01	
11	-0.213E+01	64	0.190E+00	
12	-0.155E+01	65	-0.286E+00	
13	-0.265E+00	66	-0.119E+00	
14	0.118E+01	67	-0.888E-01	
15	0.170E+01	68	0.157E-01	
16	-0.132E+01	69	0.784E-01	
17	-0.131E+01	70	0.580E-01	
18	-0.146E+00	71	-0.940E-01	
19	0.125E+01	72	-0.824E-01	
20	0.191E+01	73	-0.335E-01	
21	-0.166E+01	74	-0.177E-01	
22	-0.111E+01	75	0.275E-01	
23	0.707E+01	76	-0.842E-01	
24	0.134E+01	77	-0.527E-01	
25	0.198E+01	78	-0.320E-01	
26	0.136E+01	79	-0.955E-01	
27	-0.845E+00	80	-0.118E+00	
28	0.179E+00	81	-0.142E+00	
29	0.131E+01			
30	0.135E+01			
31	-0.109E+01			
32	-0.642E+00			
33	0.248E+00			
34	0.123E+01			
35	0.176E+01			
36	-0.338E+00			
37	-0.475E+00			
38	0.276E+00			
39	0.107E+01			
40	0.152E+01			
41	-0.627E+00			
42	-0.360E+00			
43	0.259E+00			
44	0.906E+00			
45	0.127E+01			
46	-0.462E+00			
47	-0.261E+00			
48	0.201E+00			
49	0.709E+00			
50	0.102E+01			
51	-0.371E+00			
52	-0.195E+00			
53	0.146E+00			

THIS PAGE IS BEST QUALITY PRACTICABLE
 FROM COPY FURNISHED TO DDC

Table 3.1-5

TF-8A Measured Modal Deflections

MODE NO.	H	BAY	H	GENERALIZED MASS =
				.00165
1	0.100E+01	54	0.163E+00	
2	0.621E+00	55	0.140E+00	
3	0.589E+00	56	0.241E+00	
4	0.591E+00	57	0.208E+00	
5	0.572E+00	58	0.173E+00	
6	0.267E+00	59	0.138E+00	
7	0.255E+00	60	0.115E+00	
8	0.223E+00	61	0.168E+00	
9	0.185E+00	62	0.141E+00	
10	0.167E+00	63	0.115E+00	
11	-0.190E-01	64	0.915E-01	
12	-0.300E-01	65	0.688E-01	
13	-0.327E-01	66	0.931E-01	
14	-0.148E+00	67	0.339E-01	
15	-0.181E+00	68	0.708E-01	
16	-0.166E+00	69	0.546E-01	
17	-0.139E+00	70	0.500E-01	
18	-0.250E+00	71	0.440E-01	
19	-0.335E+00	72	0.432E-01	
20	-0.376E+00	73	0.365E-01	
21	-0.186E+00	74	0.252E-01	
22	-0.211E+00	75	0.149E-01	
23	-0.292E+00	76	0.171E-01	
24	-0.389E+00	77	0.140E-01	
25	-0.440E+00	78	0.950E-02	
26	-0.108E+00	79	0.500E-02	
27	-0.130E+00	80	0.130E-02	
28	-0.200E+00	81	0.340E-02	
29	-0.294E+00			
30	-0.340E+00			
31	0.309E-01			
32	-0.310E-02			
33	-0.697E-01			
34	-0.149E+00			
35	-0.204E+00			
36	0.163E+00			
37	0.131E+00			
38	0.595E-01			
39	-0.111E-01			
40	-0.497E-01			
41	0.259E+00			
42	0.223E+00			
43	0.159E+00			
44	0.100E+00			
45	0.676E-01			
46	0.298E+00			
47	0.269E+00			
48	0.217E+00			
49	0.158E+00			
50	0.133E+00			
51	0.288E+00			
52	0.249E+00			
53	0.202E+00			

Table 3.1-6

TF-8A Measured Modal Deflections

MODE NO. 5		4TH WING BENDING		GENERALIZED MASS=
BAY	H	BAY	H	.0008
1	0.100E+U1	54	-0.398E-01	
2	0.525E+00	55	-0.100E-02	
3	0.478E+00	56	-0.219E+00	
4	0.444E+00	57	-0.194E+00	
5	0.418E+00	58	-0.131E+00	
6	0.164E+00	59	-0.730E-01	
7	0.123E+00	60	-0.380E-01	
8	0.561E-01	61	-0.188E+00	
9	-0.506E-01	62	-0.164E+00	
10	-0.979E-01	63	-0.117E+00	
11	-0.642E-01	64	-0.727E-01	
12	-0.101E+00	65	-0.397E-01	
13	-0.194E+00	66	-0.128E+00	
14	-0.321E+00	67	-0.114E+00	
15	-0.391E+00	68	-0.854E-01	
16	-0.109E+00	69	-0.559E-01	
17	-0.139E+00	70	-0.500E-01	
18	-0.218E+00	71	-0.715E-01	
19	-0.329E+00	72	-0.649E-01	
20	-0.388E+00	73	-0.508E-01	
21	-0.162E-01	74	-0.307E-01	
22	-0.402E-01	75	-0.250E-01	
23	-0.908E-01	76	-0.308E-01	
24	-0.140E+00	77	-0.308E-01	
25	-0.179E+00	78	-0.240E-01	
26	0.963E-01	79	-0.200E-01	
27	0.816E-01	80	-0.170E-01	
28	0.652E-01	81	-0.146E-01	
29	0.511E-01			
30	0.489E-01			
31	0.146E+00			
32	0.139E+00			
33	0.154E+00			
34	0.131E+00			
35	0.207E+00			
36	0.948E-01			
37	0.100E+00			
38	0.141E+00			
39	0.183E+00			
40	0.232E+00			
41	-0.240E-01			
42	0.140E-02			
43	0.604E-01			
44	0.123E+00			
45	0.167E+00			
46	-0.150E+00			
47	-0.107E+00			
48	-0.384E-01			
49	0.319E-01			
50	0.731E-01			
51	-0.221E+00			
52	-0.173E+00			
53	-0.105E+00			

THIS PAGE IS BEST QUALITY PRACTICABLE
FROM COPY FURNISHED TO DDC

THIS PAGE IS BEST QUALITY PRACTICABLE
 FROM COPY FURNISHED TO DDC

Table 3.1-7

TF-8A Measured Modal Deflections

MODE NO. 6		2ND WING TORSION		GENERALIZED MASS=
BAY	H	BAY	H	
1	0.100E+01	54	-0.499E+00	.0057
2	-0.649E+00	55	-0.704E+00	
3	-0.761E-01	56	0.996E-01	
4	0.580E+00	57	0.181E-01	
5	0.942E+00	58	-0.179E+00	
6	-0.784E+00	59	-0.393E+00	
7	-0.721E+00	60	-0.568E+00	
8	-0.200E+00	61	0.426E-01	
9	0.446E+00	62	-0.120E-01	
10	0.778E+00	63	-0.132E+00	
11	-0.865E+00	64	-0.249E+00	
12	-0.640E+00	65	-0.337E+00	
13	-0.216E+00	66	0.177E-01	
14	0.264E+00	67	0.107E-01	
15	0.476E+00	68	-0.732E-01	
16	-0.451E+00	69	-0.132E+00	
17	-0.356E+00	70	-0.180E+00	
18	-0.131E+00	71	0.113E-01	
19	0.135E+00	72	-0.190E-02	
20	0.233E+00	73	-0.241E-01	
21	-0.283E-01	74	-0.347E-01	
22	-0.168E-01	75	0.910E-02	
23	0.165E-01	76	0.590E-02	
24	0.615E-01	77	0.310E-02	
25	0.300E-01	78	0.210E-02	
26	0.333E+00	79	0.910E-02	
27	0.255E+00	80	0.910E-02	
28	0.117E+00	81	0.0	
29	-0.257E-01			
30	-0.377E-01			
31	0.567E+00			
32	0.403E+00			
33	0.123E+00			
34	-0.169E+00			
35	-0.334E+00			
36	0.602E+00			
37	0.397E+00			
38	0.437E-01			
39	0.319E+00			
40	-0.535E+00			
41	0.438E+00			
42	0.295E+00			
43	-0.721E-01			
44	-0.460E+00			
45	-0.725E+00			
46	0.325E+00			
47	0.172E+00			
48	0.160E+00			
49	-0.525E+00			
50	-0.751E+00			
51	0.194E+00			
52	0.684E-01			
53	-0.199E+00			

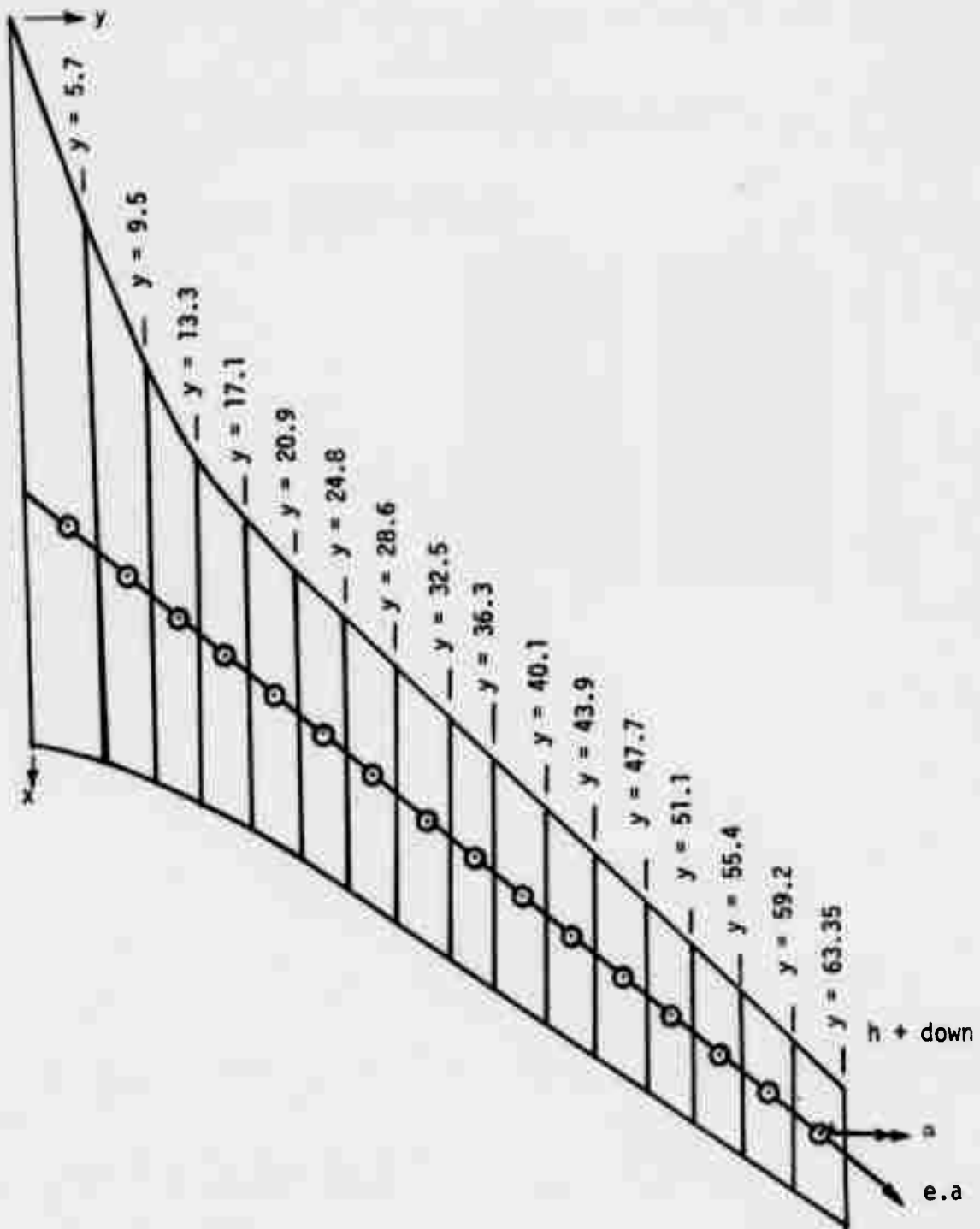


Figure 3.1-2 TF-8A Transformed Aerodynamic Deflection Idealization

Table 3.1-8

TF-8A Transformed Modal Deflections

MODE NO.	H	1	ALPH	GENERALIZED MASS=
BAY				.00484
2	0.8950E+00	0.1537E-01		
3	0.7760E+00	0.1402E-01		
4	0.6690E+00	0.1288E-01		
5	0.5690E+00	0.1180E-01		
6	0.4750E+00	0.1080E-01		
7	0.3850E+00	0.1014E-01		
8	0.3010E+00	0.9070E-02		
9	0.2280E+00	0.7620E-02		
10	0.1650E+00	0.6640E-02		
11	0.1070E+00	0.5780E-02		
12	0.6100E-01	0.4200E-02		
13	0.3000E-01	0.2610E-02		
14	0.1200E-01	0.1170E-02		
15	0.5000E-02	0.1400E-02		
16	0.4000E-02	0.1000E-03		
17	0.3000E-02	0.0		

Table 3.1-9

TF-8A Transformed Modal Deflections

MODE NO. BAY	H	ALPH	2ND WING BENDING FREQ = 18.08	GENERALIZED MASS = .00268
2	0.6500E+00	0.4124E-01		
3	0.4050E+00	0.3890E-01		
4	0.1700E+00	0.3514E-01		
5	-0.3600E-01	0.2932E-01		
6	-0.1900E+00	0.2004E-01		
7	-0.2700E+00	0.1199E-01		
8	-0.3100E+00	0.5930E-02		
9	-0.3070E+00	0.9900E-03		
10	-0.2780E+00	-0.2040E-02		
11	-0.2300E+00	-0.4310E-02		
12	-0.1750E+00	-0.5500E-02		
13	-0.1180E+00	-0.4800E-02		
14	-0.7500E-01	-0.3470E-02		
15	-0.4500E-01	-0.2220E-02		
16	-0.2700E-01	-0.1000E-02		
17	-0.2000E-01	-0.7500E-03		

Table 3.1-10

TF-8A Transformed Modal Deflections

MODE NO.	3		1ST WING TORSION	GENERALIZED MASS=
BAY	H	ALPH	FREQ = 37.10	
2	-0.6000E+00	0.3269E+00		.02735
3	-0.4500E+00	0.3127E+00		
4	-0.2950E+00	0.2893E+00		
5	-0.1220E+00	0.2567E+00		
6	0.6000E-01	0.2234E+00		
7	0.1850E+00	0.1938E+00		
8	0.2420E+00	0.1637E+00		
9	0.2650E+00	0.1341E+00		
10	0.2600E+00	0.1074E+00		
11	0.2230E+00	0.8476E-01		
12	0.1540E+00	0.6260E-01		
13	0.8400E-01	0.4311E-01		
14	0.3000E-01	0.2684E-01		
15	-0.1100E-01	0.1444E-01		
16	-0.3900E-01	0.6590E-02		
17	-0.5400E-01	0.4230E-02		

Table 3.1-11

TF-8A Transformed Modal Deflections

MJDE NO. BAY	H	ALPH	3RD WING BENDING FREQ = 42.80	GENERALIZED MASS =
				.00165
2	0.6000E+00	0.4582E-01		
3	0.2250E+00	0.3556E-01		
4	-0.8000E-01	0.1706E-01		
5	-0.2620E+00	-0.3190E-02		
6	-0.2900E+00	-0.1713E-01		
7	-0.2630E+00	-0.2351E-01		
8	-0.1750E+00	-0.2983E-01		
9	-0.2500E-01	-0.3423E-01		
10	0.1650E+00	-0.2581E-01		
11	0.2170E+00	-0.1157E-01		
12	0.2120E+00	-0.4290E-02		
13	0.1780E+00	0.8400E-03		
14	0.1190E+00	0.3520E-02		
15	0.6800E-01	0.3440E-02		
16	0.3000E-01	0.2310E-02		
17	0.1200E-01	0.1860E-02		

Table 3.1-12

TF-8A Transformed Modal Deflections

MODE NO.	5	4TH WING BENDING		GENERALIZED MASS=
BAY	H	ALPH		FREQ = 73.40
2	0.4850E+00	0.4644E-01		.0008
3	0.5000E-01	0.2150E-01		
4	-0.2080E+00	-0.9580E-02		
5	-0.2240E+00	-0.2909E-01		
6	-0.9300E-01	-0.2967E-01		
7	0.7200E-01	-0.1890E-01		
8	0.1630E+00	-0.1270E-02		
9	0.1500E+00	0.1427E-01		
10	0.6500E-01	0.2306E-01		
11	-0.5000E-01	0.2236E-01		
12	-0.1110E+00	0.1554E-01		
13	-0.1310E+00	0.8980E-02		
14	-0.1200E+00	0.3020E-02		
15	-0.8600E-01	-0.1110E-02		
16	-0.4800E-01	-0.1920E-02		
17	-0.2900E-01	-0.2070E-02		

Table 3.1-13

TF-8A Transformed Modal Deflections

MODE NO.	H	ALPH	GENERALIZED MASS=
2	-0.9000E-01	0.1953E+00	.0057
3	-0.2070E+00	0.1618E+00	
4	-0.2280E+00	0.1054E+00	
5	-0.1220E+00	0.4111E-01	
6	0.2200E-01	-0.8310E-02	
7	0.1270E+00	-0.3421E-01	
8	0.1370E+00	-0.4848E-01	
9	0.5000E-01	-0.5206E-01	
10	-0.7500E-01	-0.5045E-01	
11	-0.1780E+00	-0.4785E-01	
12	-0.2110E+00	-0.4190E-01	
13	-0.1920E+00	-0.3576E-01	
14	-0.1300E+00	-0.2500E-01	
15	-0.5500E-01	-0.1470E-01	
16	-0.1000E-01	-0.4630E-02	
17	0.5000E-02	-0.1930E-02	

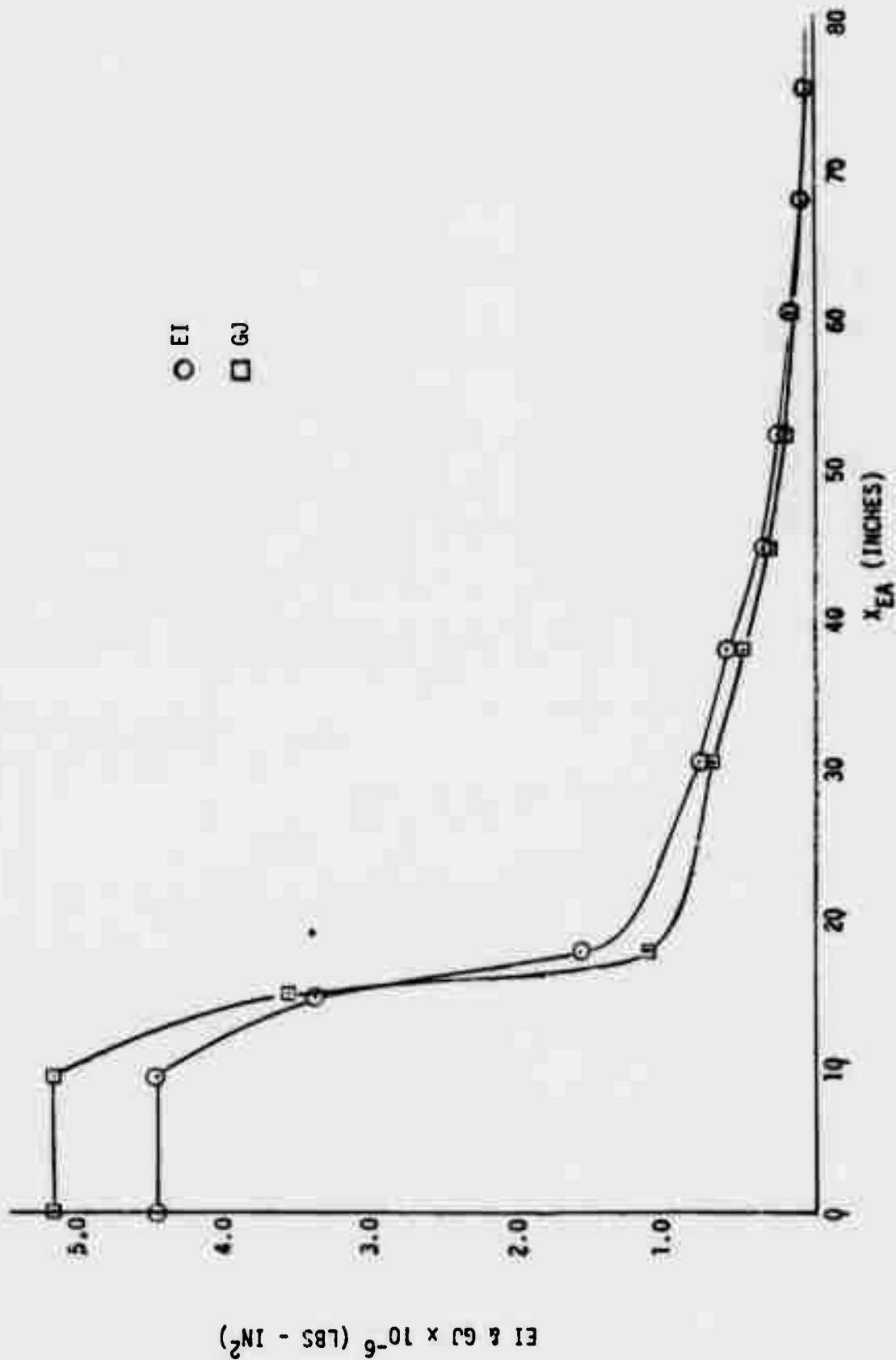


Figure 3.1-3 TF-8A Flutter Model Wing Rigidity Distribution

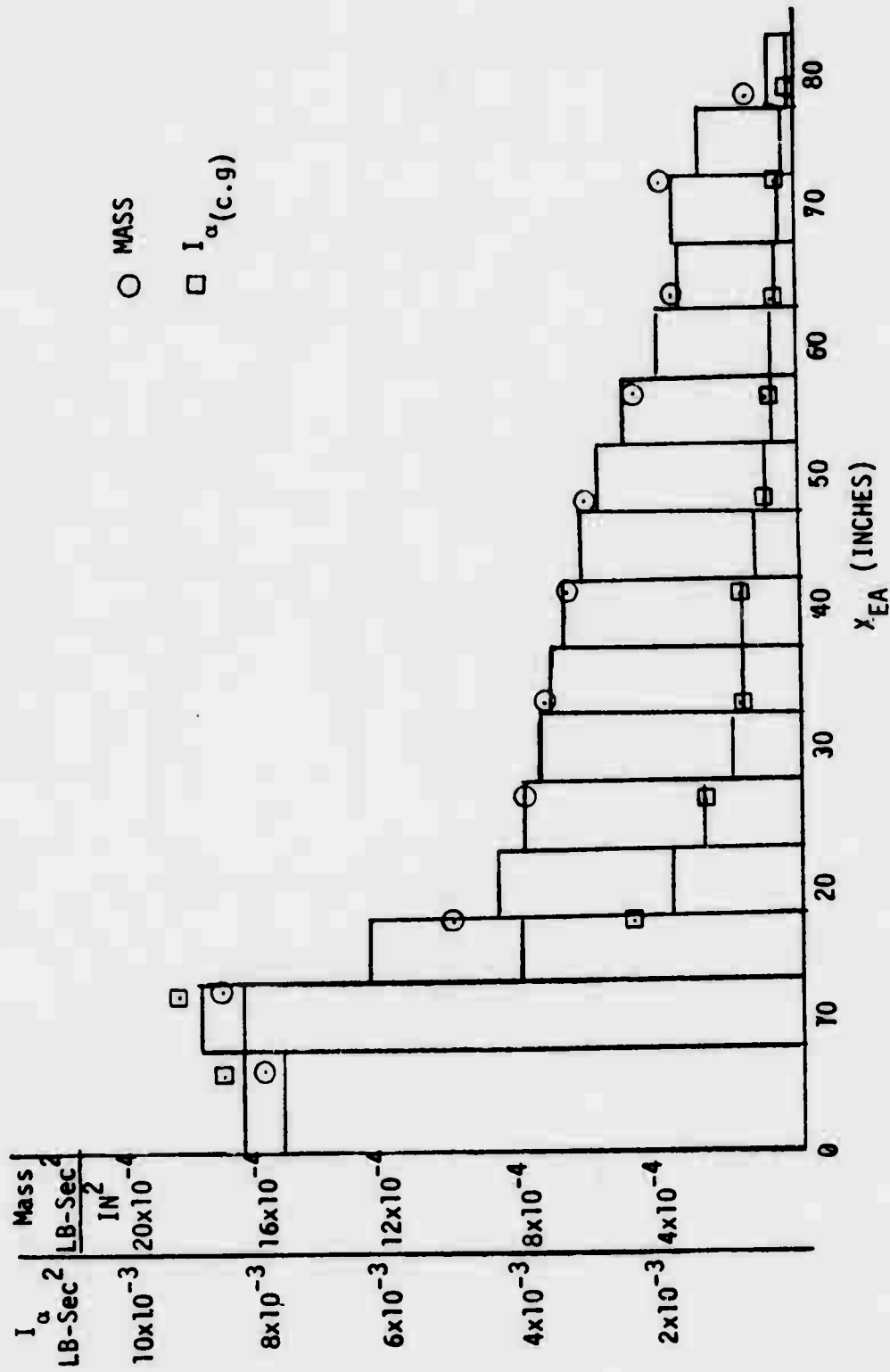


Figure 3.1-4 TF-8A Flutter Model Wing Mass and Inertia

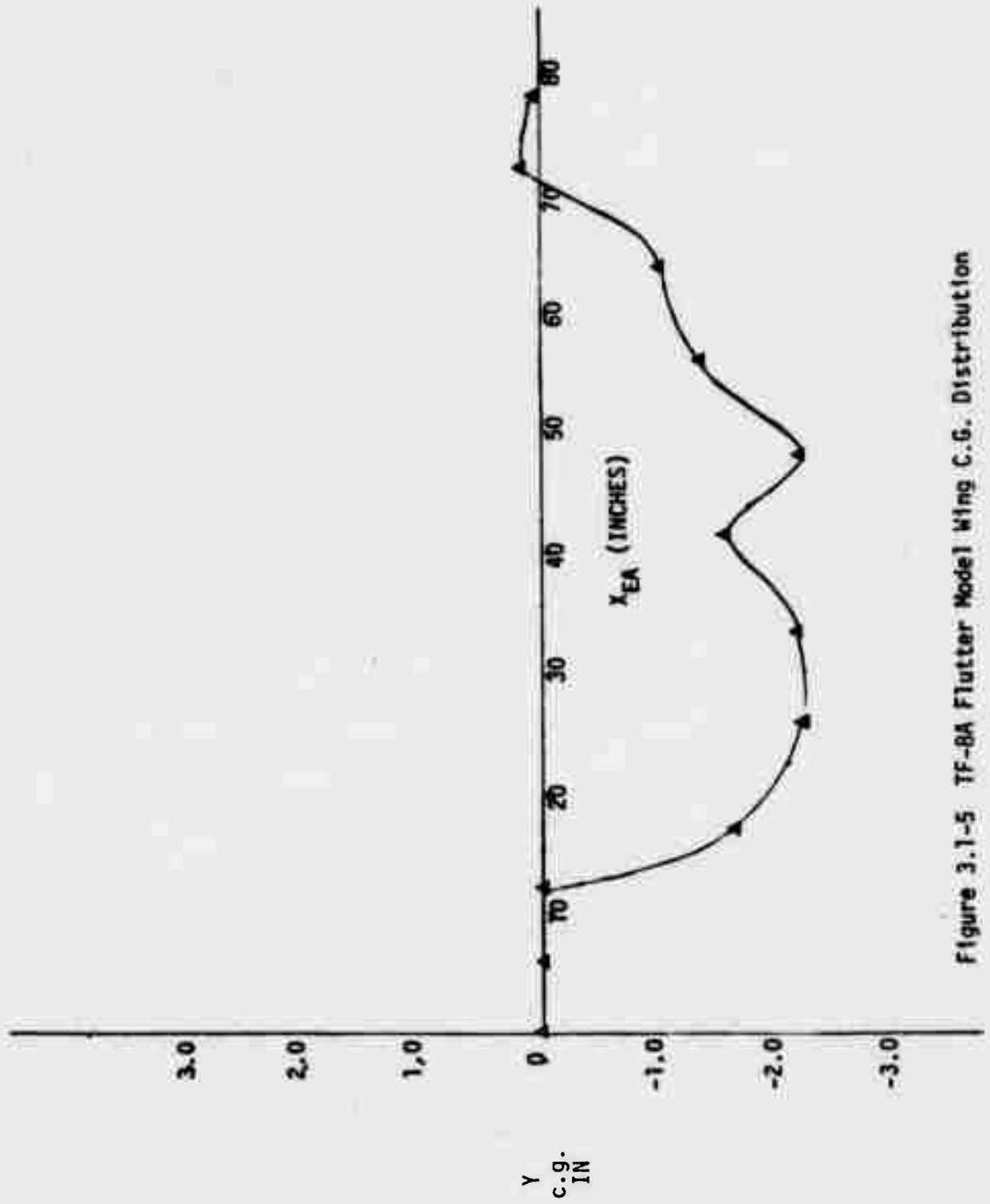


Figure 3.1-5 TF-8A Flutter Model Wing C.G. Distribution

3.1.2 TF-8A Static Aeroelastic Solutions

Section 2.3 above contains the discussion of the method used to generate the TF-8A static aeroelastic solutions. Figures 3.1-6 and 3.1-7 show the resultant twist distribution for the five Mach numbers under consideration. NASA supplied an optically measured static shape for several cases and Figure 3.1-8 shows a comparison of these measurements with a calculated shape for the same lift and Mach number. Good agreement is seen to exist. The use of these static shapes is discussed above in Sections 2.4 and 2.5, and below in Section 3.1.3.

3.1.3 Aerodynamic Data and Weighting Factors for the TF-8A Wing

The Doublet Lattice Idealization of the TF-8A wing is shown in Subsection 2.1. The theoretical results for the spanwise variation of section lift coefficient slope and aerodynamic center are presented in Figures 3.1-13 through 3.1-17 for five freestream Mach Numbers. The experimental data are also shown. As expected, the theory underestimates the lift because several transonic effects are not accounted for.

The data were taken from Reference 2 and corrected for aeroelastic effects as described in Subsections 2.1 and 2.4.1. Limitations of the data due to insufficient Reynolds Numbers were also described in Subsection 2.4.1. It was concluded there that the stall characteristics of the c_l and c_m versus α were not reliable. Thus, the values of c_{l_α} were read only in their 'non-stalled' range and not necessarily at the section angles-of-attack to which the flutter model had deformed statically during the flutter test.

For example, Figures 3.1-9 through -12 present the aeroelastically corrected pressure model data (c_l , c_m vs α_{eff}) for the $M_\infty = 0.99$ case. It is obvious that the values of c_{l_α} and especially c_{m_α} depend on the section angle-of-attack. The section angle-of-attack distribution across the span of the flutter model in turn is the sum of the rigid body angle-of-attack, the built-in twist and the elastic twist as described in Section 2.4. The distribution of section angle-of-attack for the TF-8A wing is given in Subsection 3.1.2. The effective angle-of-attack at which the c_{l_α} and c_{m_α}

are to be read is the difference between the section angle-of-attack of the flutter model, $\alpha_s^{(f)}$, and the built-in twist of the pressure model $\epsilon_j^{(p)}$.

That is,

$$\alpha_{\text{eff}}^{(f)} = \alpha_s^{(f)} - \epsilon_j^{(p)}$$

where $\epsilon_j^{(p)}$ is given in Table 3.3.2. The reason why the elastic twist of the pressure model is not mentioned here is because it has already been accounted for in the term $\alpha_{\text{eff}}^{(f)}$, i.e., the pressure data has already been corrected back to the rigid state.

The values at which the lift and moment curve slopes are to be read, $\alpha_{\text{eff}}^{(f)}$, are also plotted in Figures 3.1-9 through -12. In Figure 3.1-9, the effective section angles-of-attack of the flutter model lie in the non viscous range for the c_l curve and these are the values read. In Figure 3.1-10, the effective angles-of-attack of the flutter model fall in the viscous range only for the section at $y/(b/2) = 0.933$. Since the curve is unreliable there, the value of $c_{l\alpha}$ at $\alpha_{\text{eff}} = 0$ is used.

The curves of moment coefficient versus effective angle-of-attack are nonlinear everywhere due to transonic and viscous effects. For this case the slopes of $c_{m\alpha}$ selected for the $M_\infty = 0.99$ case are shown in 3.1-11 and 3.1-12 as tangent lines to the curves. Due to the lack of data points, the actual shape of the c_m vs α curve is open to various interpretations. This is unfortunate because $c_{m\alpha}$ seems to have a large effect on flutter speed.

In Figure 3.1-12, three separate interpretations of the c_m versus α , curve have been drawn for Stations $y/(b/2) = 0.653$ and 0.804 . The tangent lines or slopes of these curves are also indicated. The solid line indicates our best guess to the slope; however, the other slopes are also retained and used in the flutter analysis to show the effect of flutter speed on the slope $c_{m\alpha}$. Two separate interpretations have been drawn for the curve at $y/(b/2) = 0.48$. The final three curves of aerodynamic center resulting from these various interpretations are given in Figure 3.1-17.

Special consideration is given to the curve of c_m versus α for the wing tip Station $y/(b/2) = 0.933$. As indicated previously, the point at which

$c_{l\alpha}$ and $c_{m\alpha}$ are to be measured lies in the viscous region for the pressure model. Due to the Reynolds Number difference between the pressure and flutter models, (1.96×10^6 for the pressure model and $3.0 - 9.0 \times 10^6$ for the flutter model), the pressure model curves can not really be trusted in the viscous region.

The handling of this difficulty posed a problem since the c_m versus α curve is very nonlinear, even in the non-viscous regions. The motions of shock waves tend to change the character of the c_m curves drastically as α passes from negative to positive values. One possible solution is to extrapolate the c_m versus α curve, based on its shape close to α of zero, to the point in question ignoring the break in the curve at $\alpha = -1.5$ degrees. When this is done, it is found that the aerodynamic center lay very far aft on the airfoil, specifically, at $x_{a.c.}/c \approx 0.70$. This result is considered unreasonable since the aerodynamic center usually moves forward at the wing tip, not aft. If this result ($x_{a.c.}/c = 0.7$) is used in the flutter analysis, the resulting flutter speed is also unreasonable; lying well above the results for the unweighted theory. A two-dimensional transonic solution was applied to the airfoil section (plus boundary layer) at $y/(b/2) = 0.933$. The section data gave a moment curve with a minimum point at $\alpha = 0$ similar to the data. However, the slopes were much less resulting in an aerodynamic center, at $\alpha = -1.82$, of $x_{a.c.}/c = 0.3966$. Three-dimensional effects will move this point forward. It is felt, then, that the aerodynamic center selected for this station, shown in Figure 3.1-17, is correct.

A similar problem was encountered for the case of $M_\infty = 0.95$. Figure 3.1-16 presents the unreasonable aerodynamic center distribution as a dashed line. This curve was flattened to the solid line. Again, if the unreasonable curve of aerodynamic center is used, the flutter speed is well above the unweighted theory result.

The final values of $c_{l\alpha}$ and $x_{a.c.}$ used for all Mach Numbers considered are presented in Figures 3.1-13 through -17 where they are compared with the theory. The ratios of experimental to theoretical $c_{l\alpha}$ and $c_{m\alpha}$ are the steady weight factors, as described in Subsection 2.4. The curves presented in Figures 3.1-13 through -17 were interpolated for $c_{l\alpha}$ and $x_{a.c.}$ at the bay positions for the theoretical as well as experimental data. The weight factors for the five Mach Numbers considered are given in Table 3.1-14.

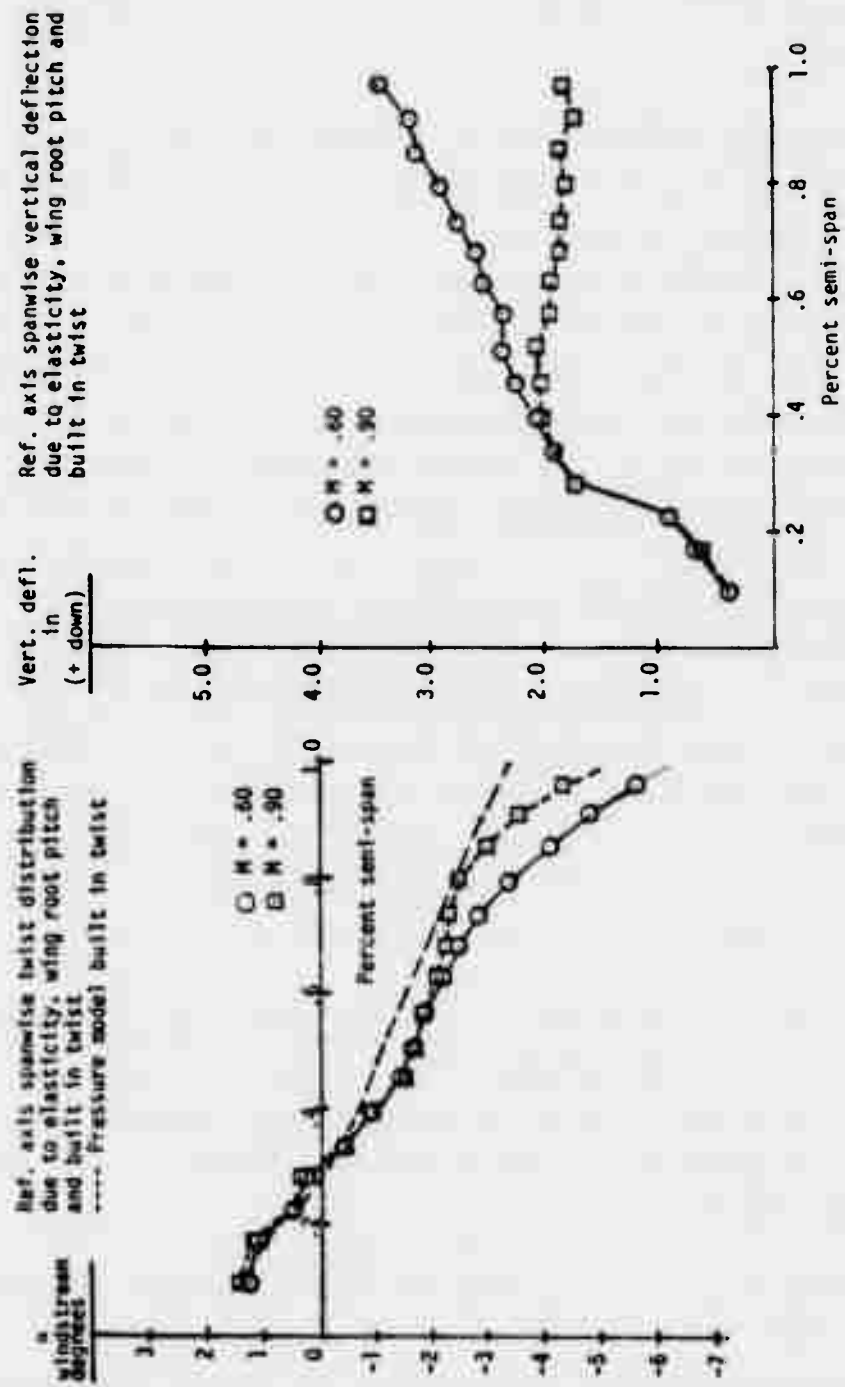


Figure 3.1-6 TF-8A Static Twist Distribution $M_{\infty} = 0.60$, $M_{\infty} = 0.90$

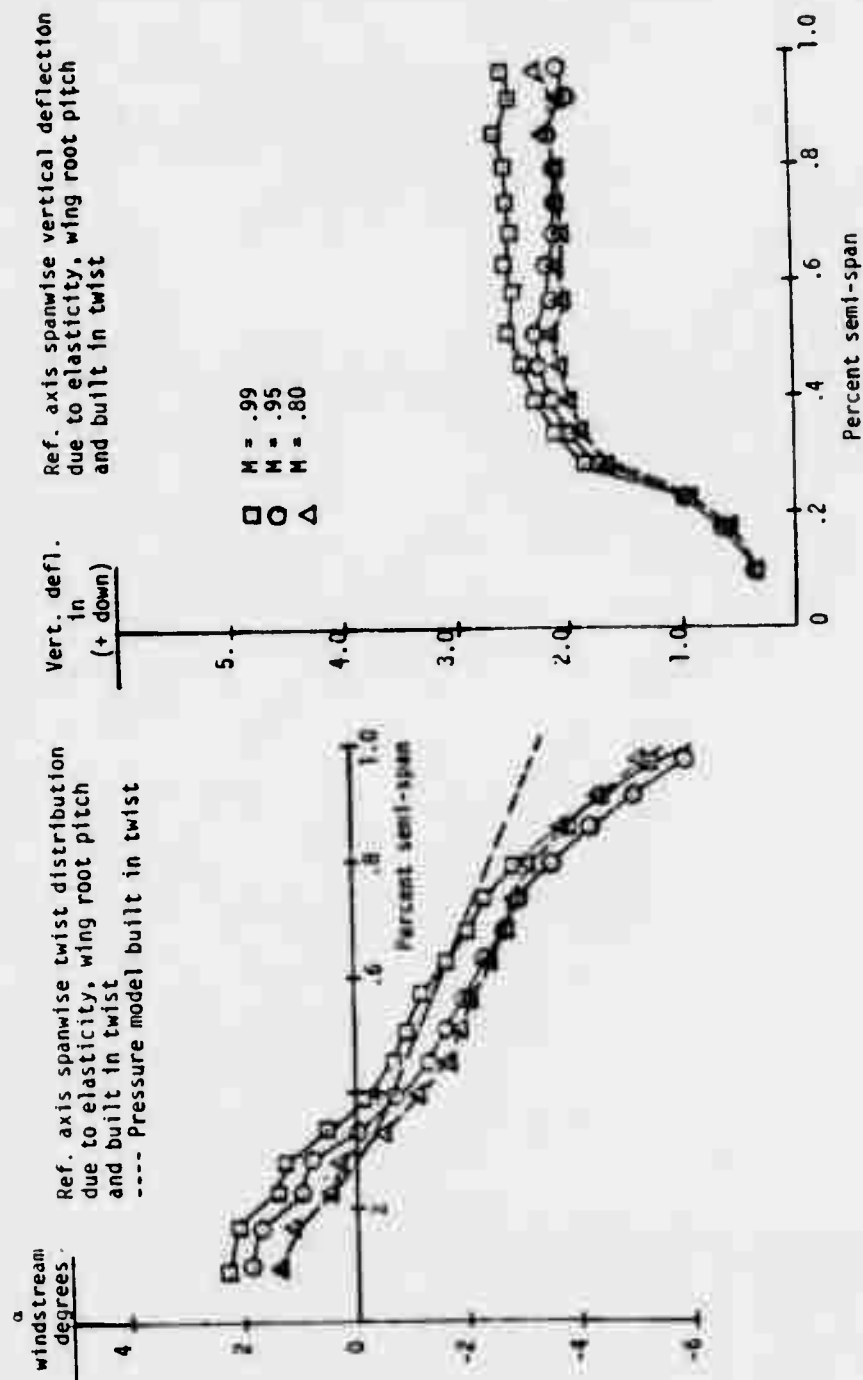


Figure 3.1-7 TF-8A Static Twist Distribution, $M_{\infty} = 0.99$, $M_{\infty} = 0.95$, $M_{\infty} = 0.80$

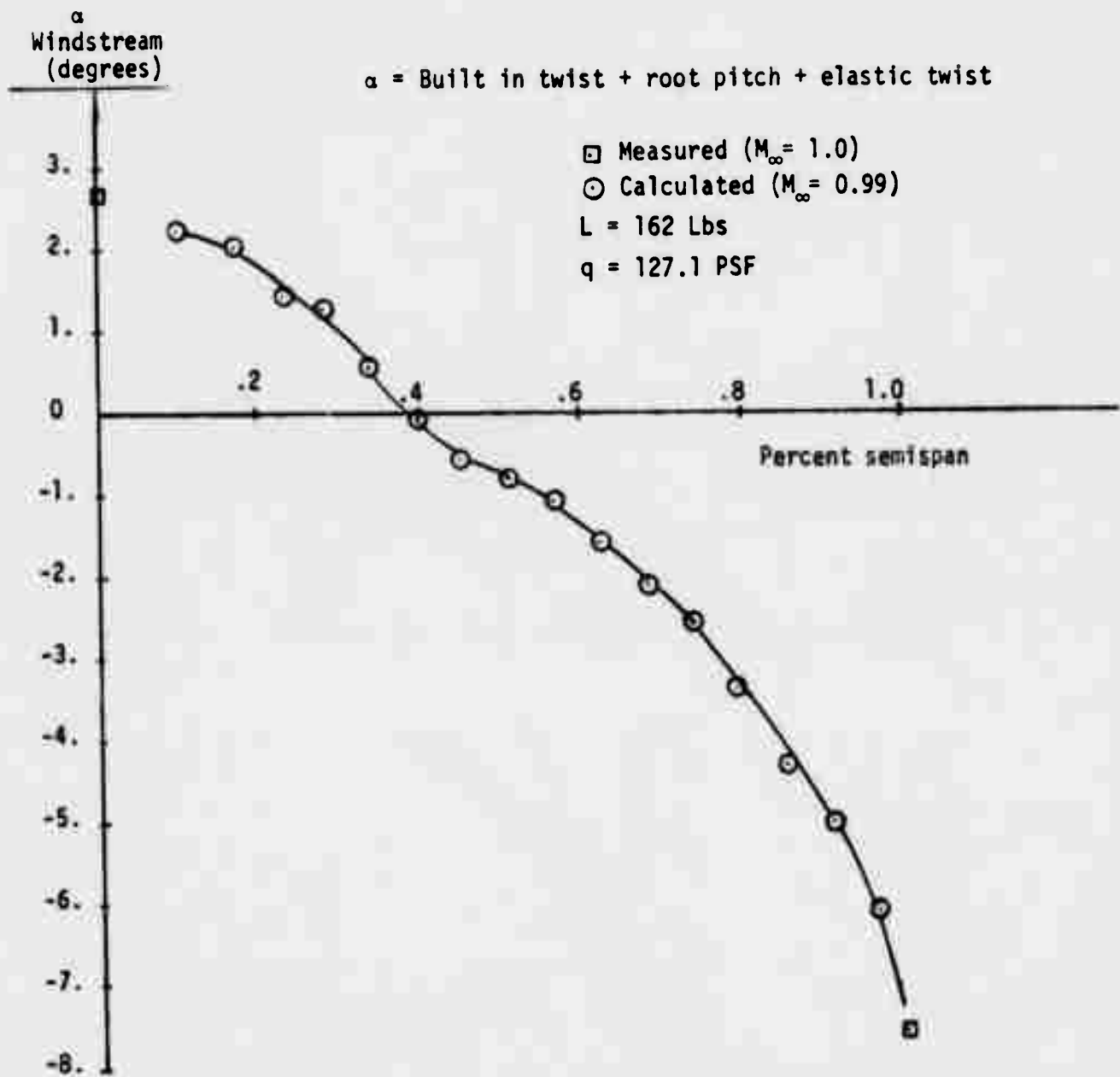


Figure 3.1-8 TF-8A Elastic Correlation with NASA Data

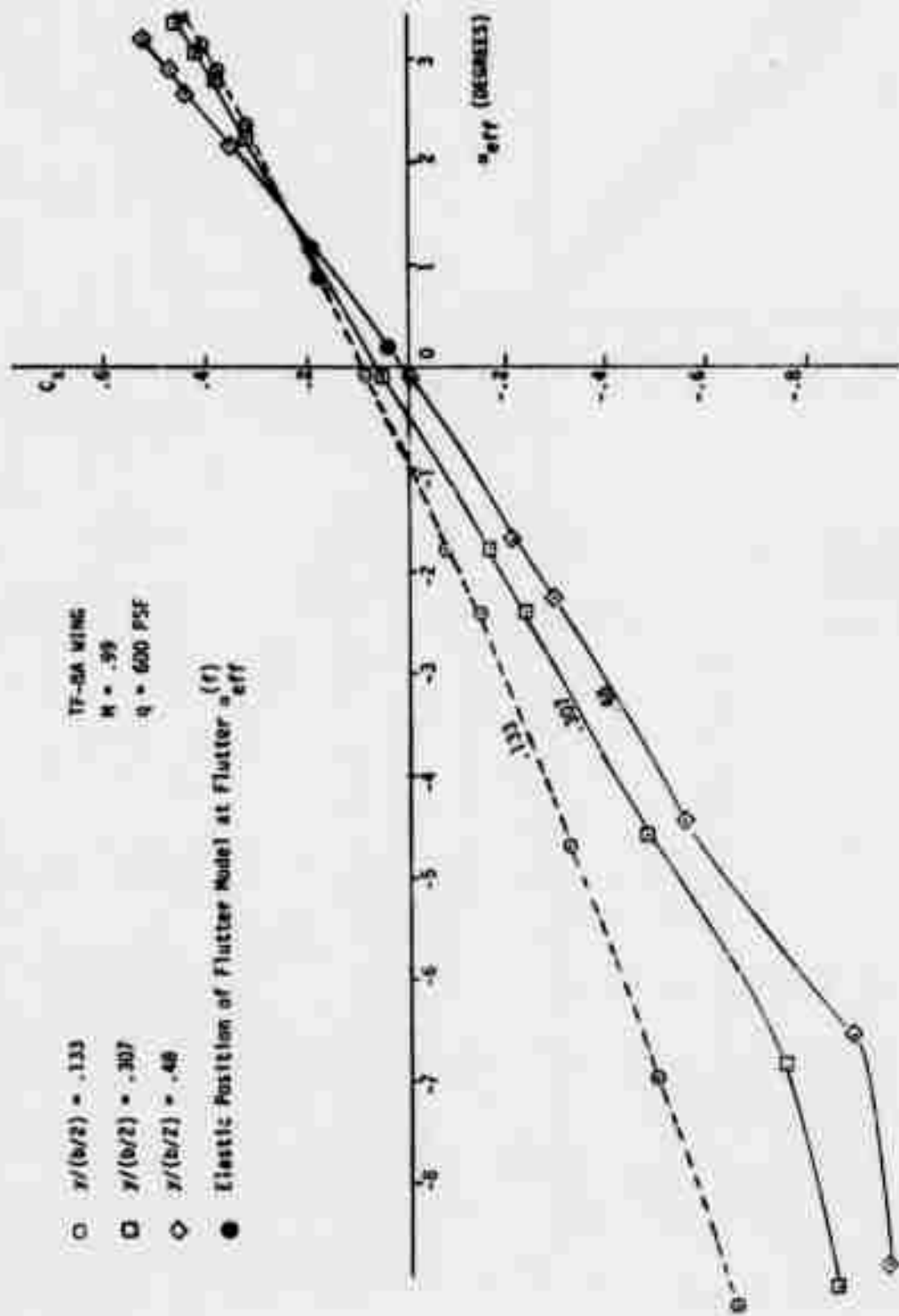


Figure 3.1-9 TF-8A C_L vs. α_{eff} ; $M_\infty = .99$; $y/(b/2) = .133, .307, .480$

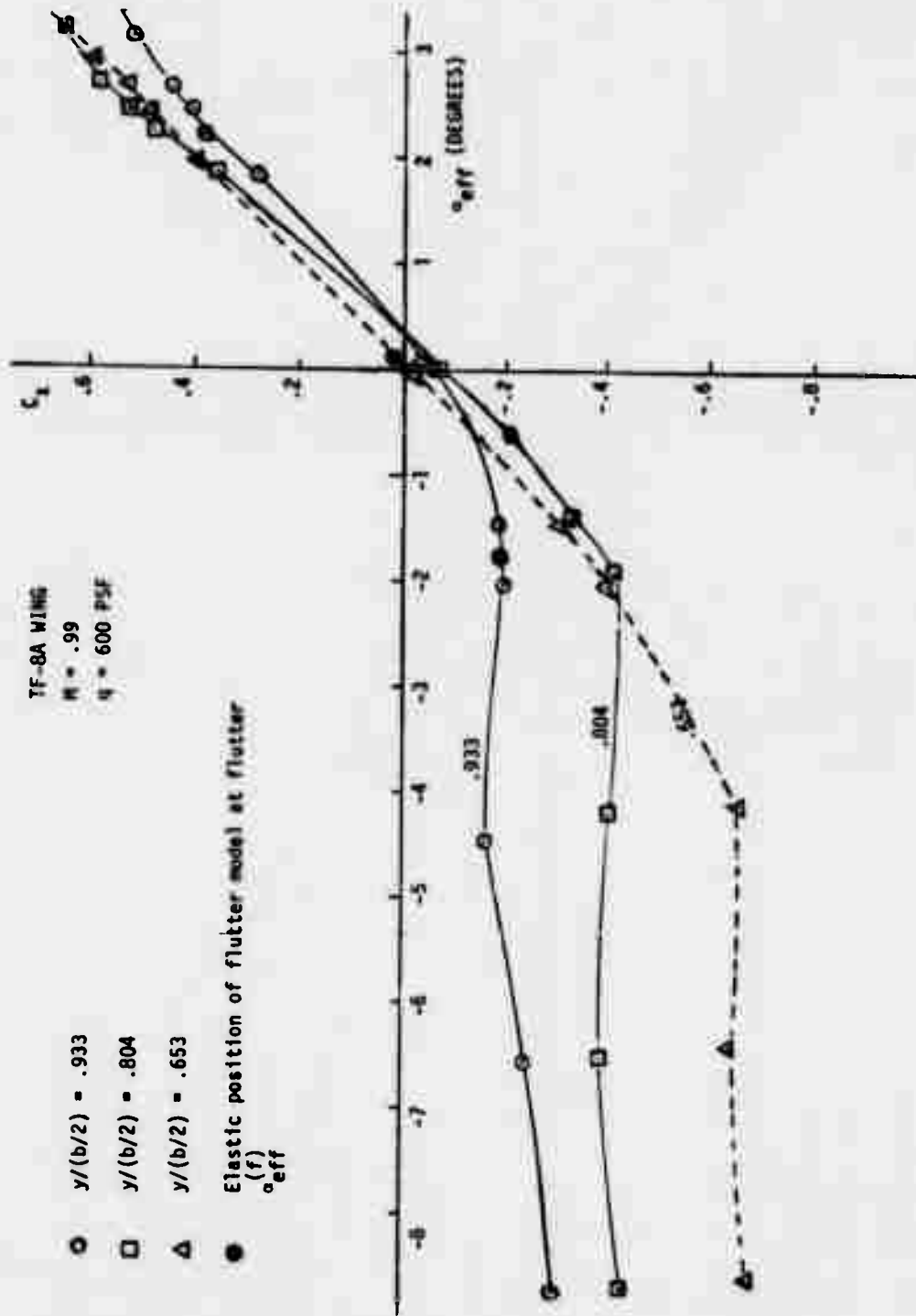


Figure 3.1-10 TF-8A C_L vs. α_{eff} ; $M_\infty = .99$; $y/(b/2) = .653, .804, .933$

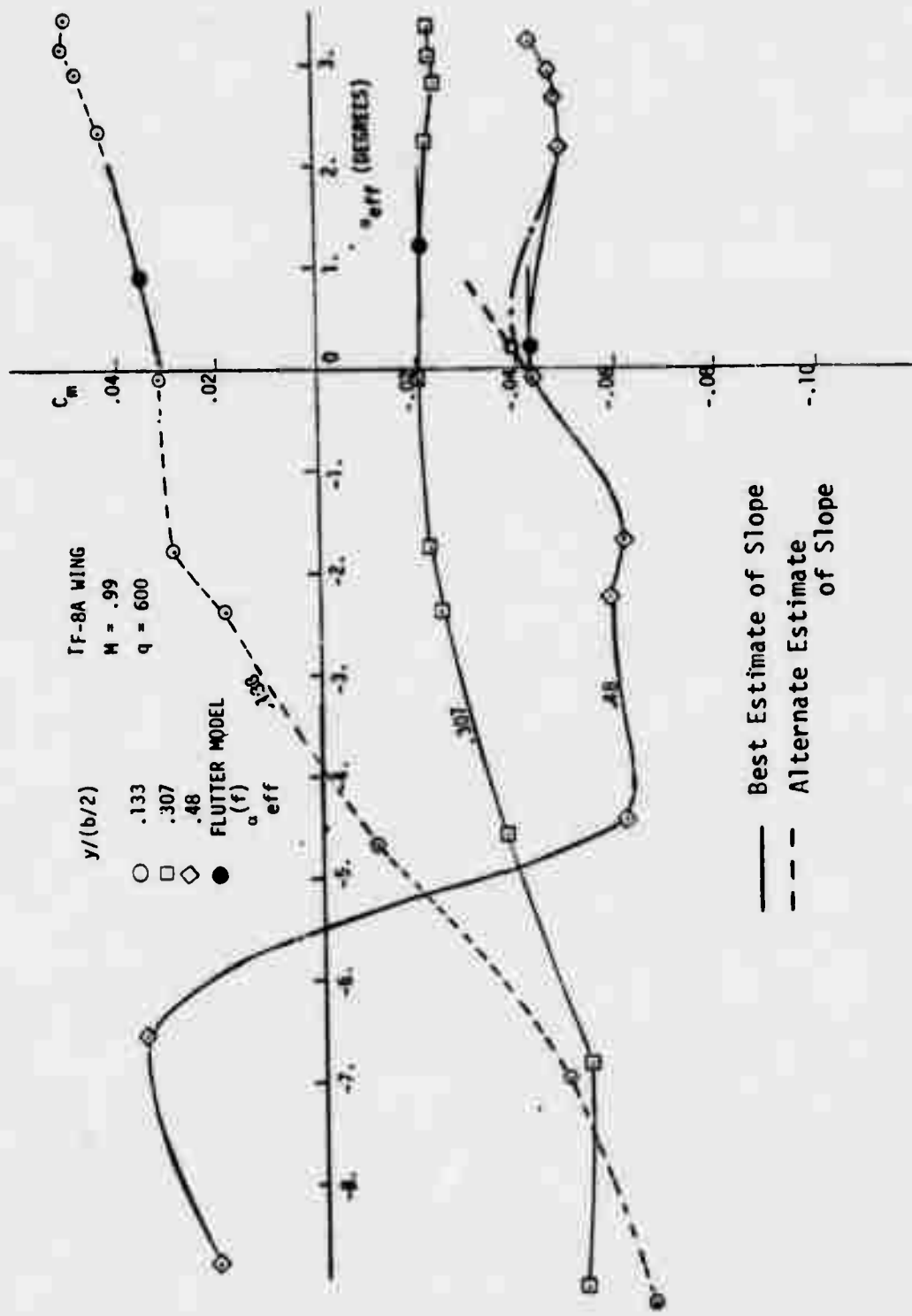


Figure 3.1-11 TF-8A C_m vs. α_{eff} ; $M_\infty = .99$; $y/(b/2) = .133, .307, .48$

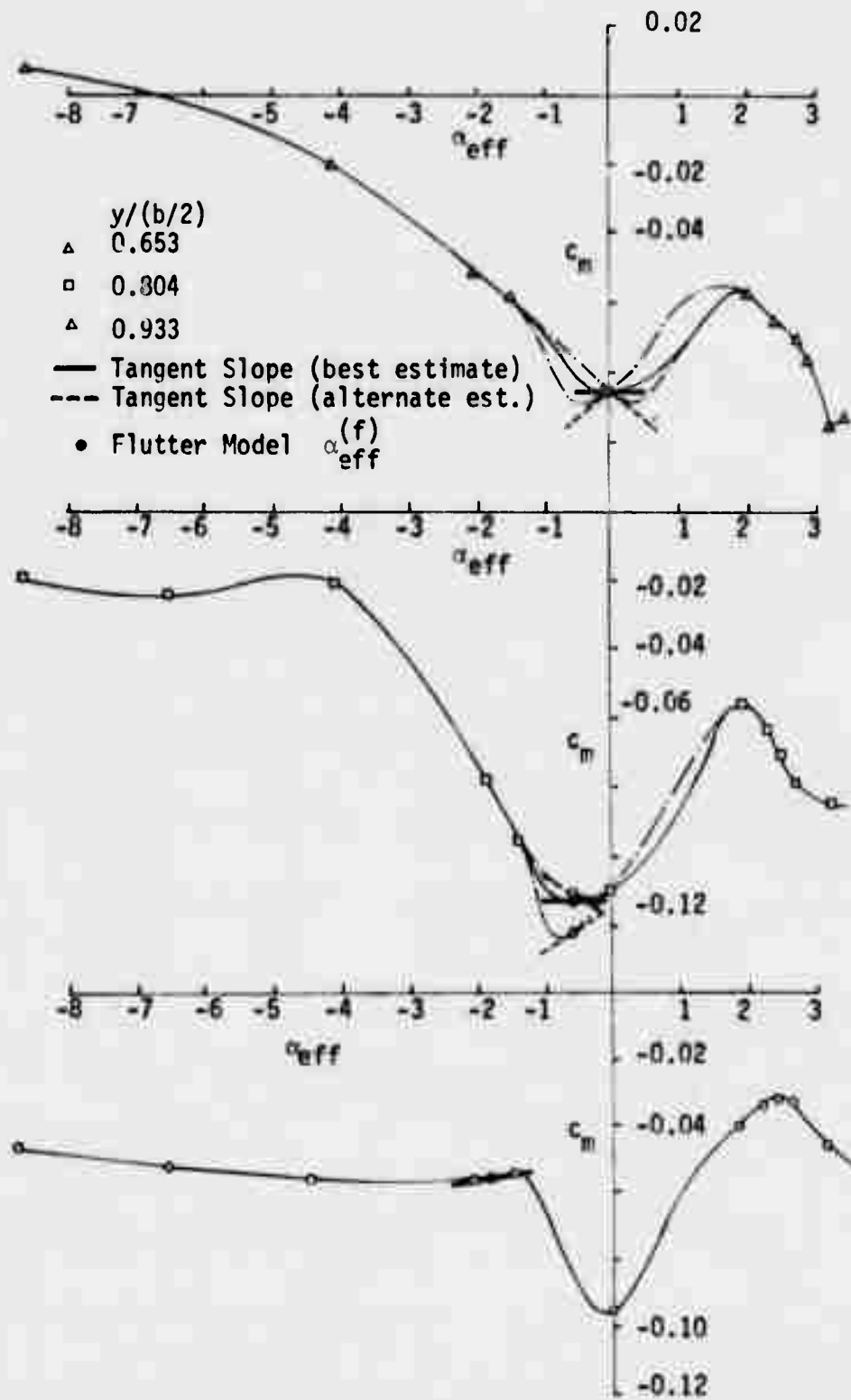


Figure 3.1-12 TF-8A c_m vs. α_{eff} : $M_\infty = .99$; $y/(b/2) = .653, .804, .933$

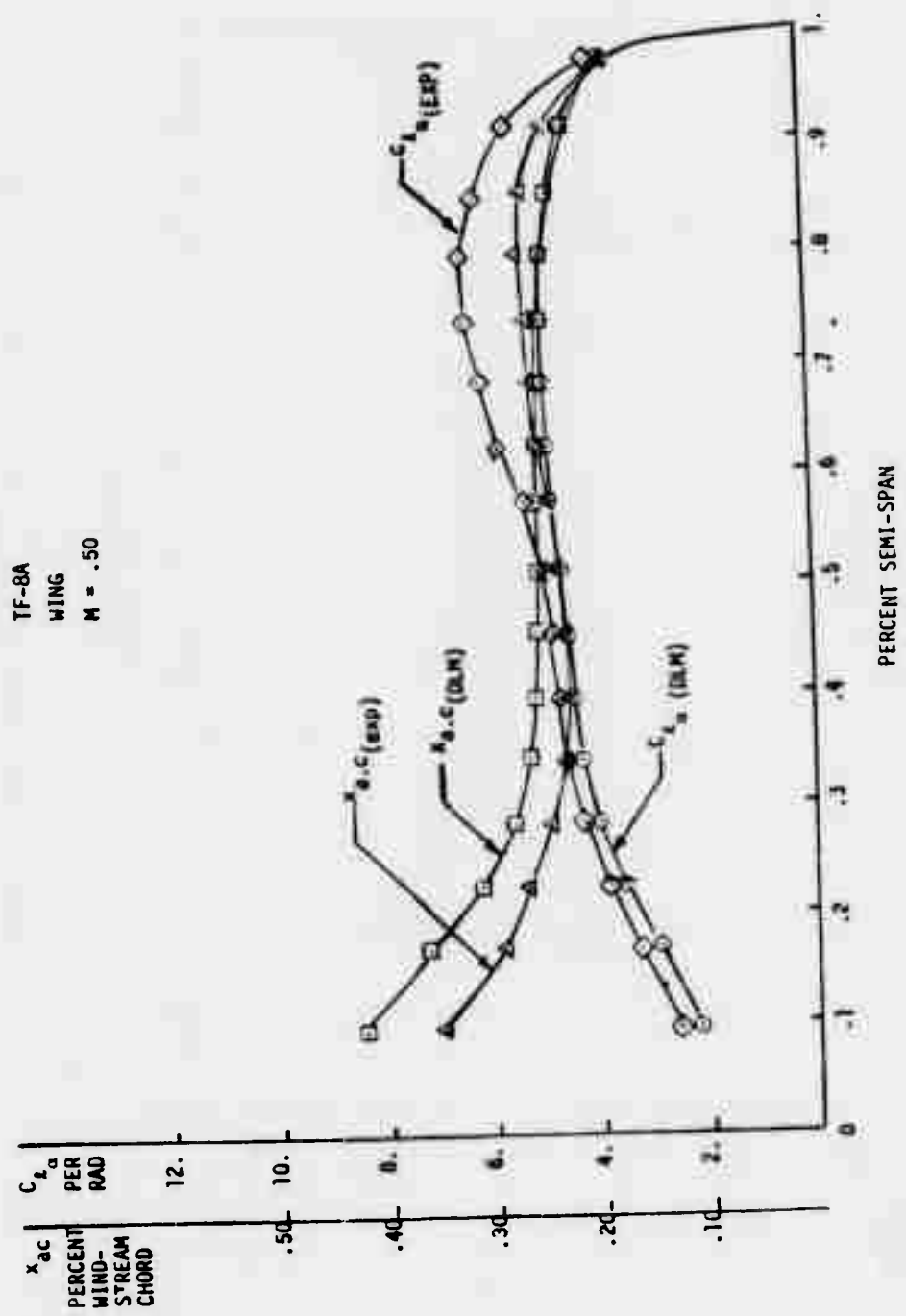


Figure 3.1-13 TF-8A C_L , $x_{a.c}$ vs. $y/(b/2)$, $M_\infty = .50$

TF-8A
WING
M = .80

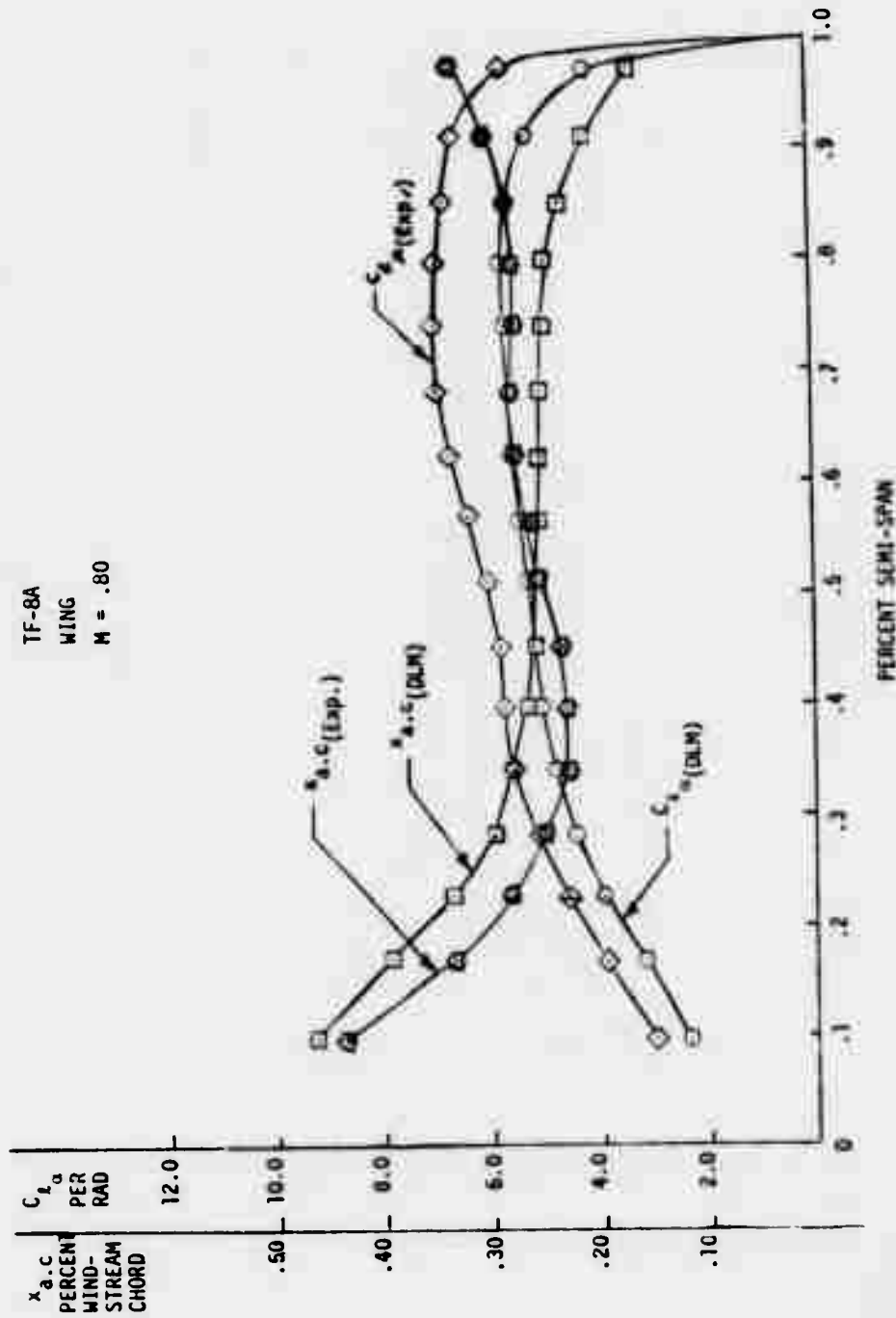


Figure 3.1-14 TF-8A C_L α, C_D α vs. y/(b/2); M_∞ = .80

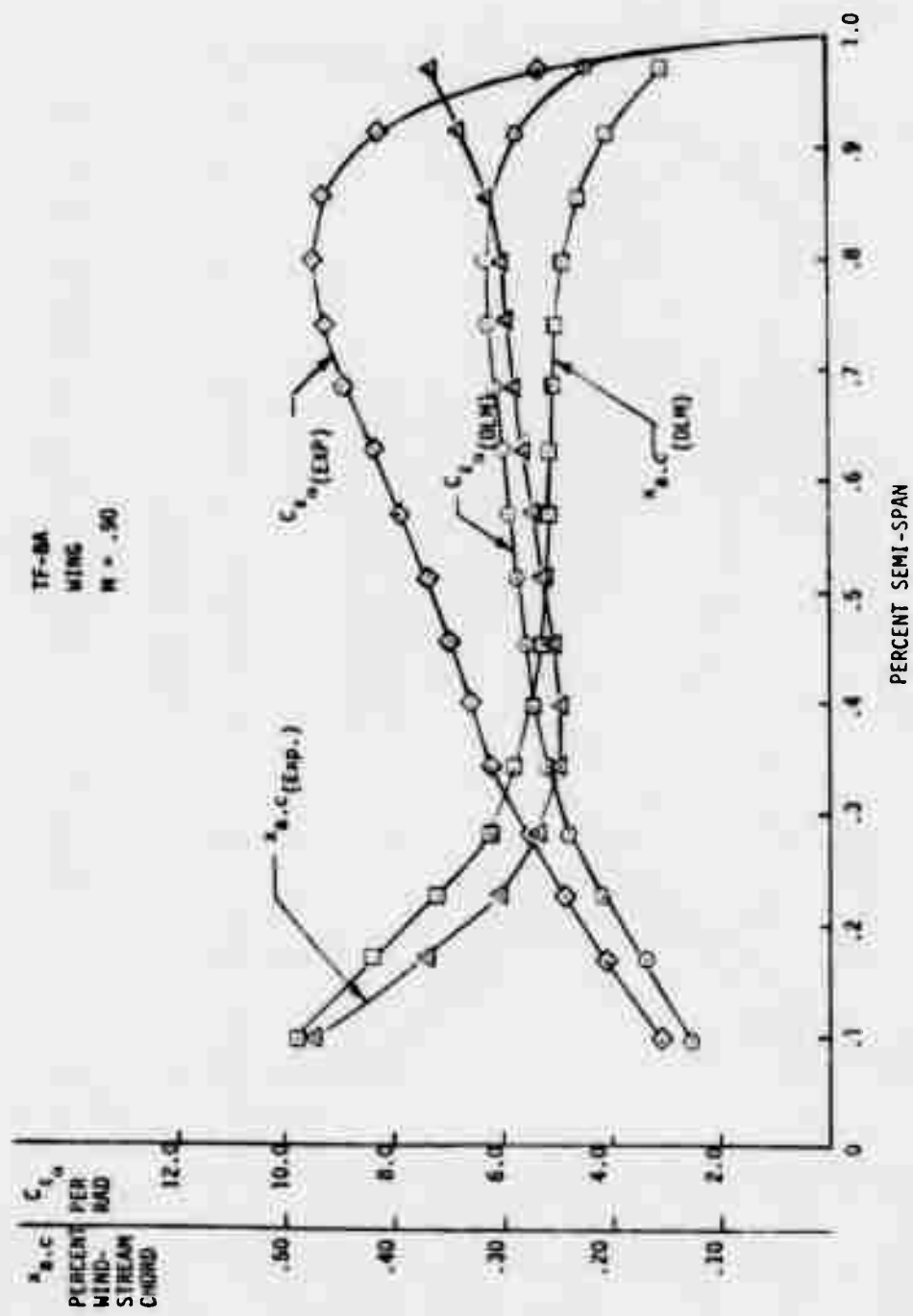


Figure 3.1-15 TF-8A $C_{L_{\alpha}}$, $x_{a.c}$ vs. $y/(b/2)$; $M_\infty = .90$

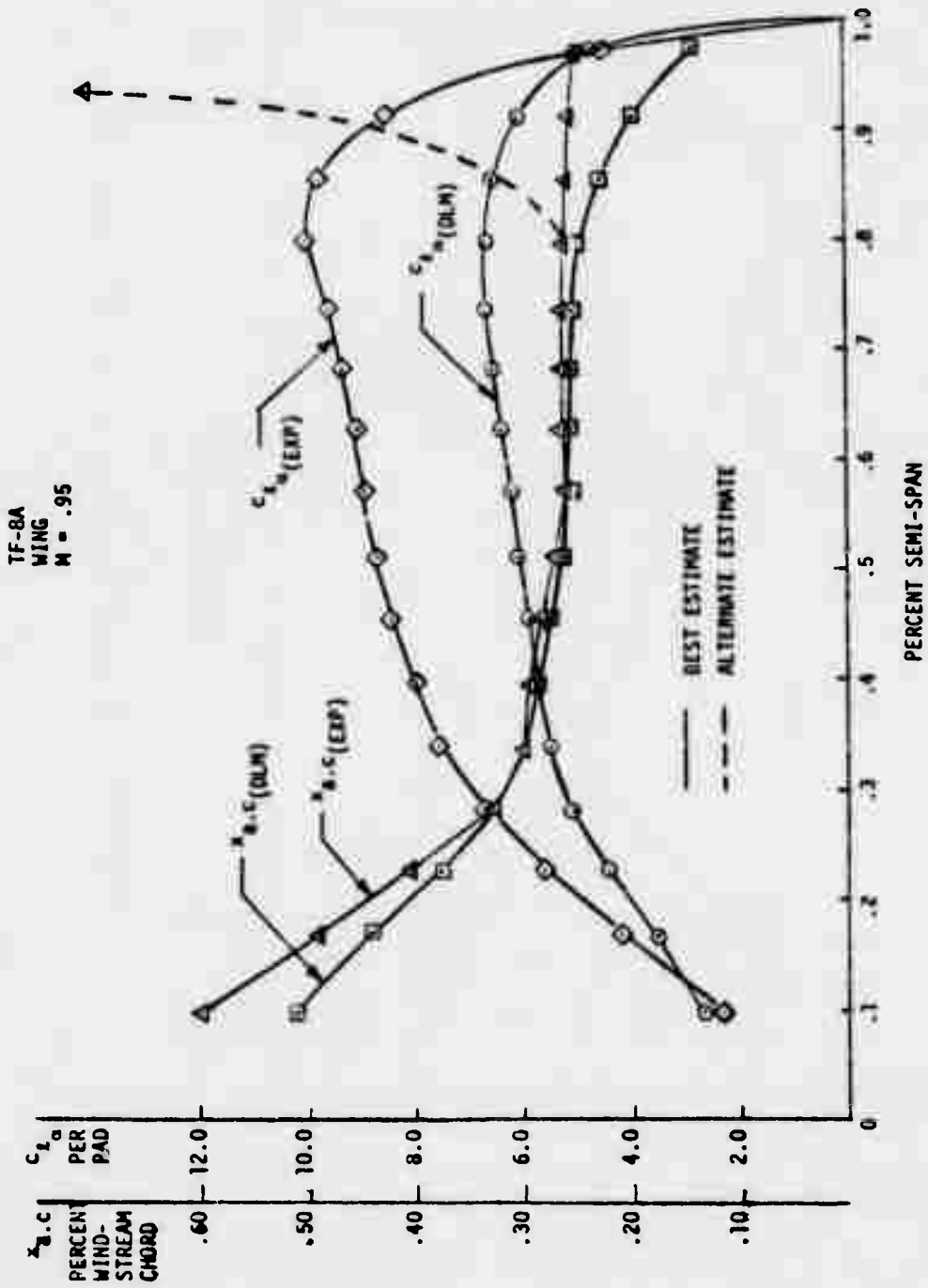


Figure 3.1-16 TF-8A $c_{l_{\alpha}}$, $x_{a,c}$ vs. $y/(b/2)$; $M_{\infty} = .95$

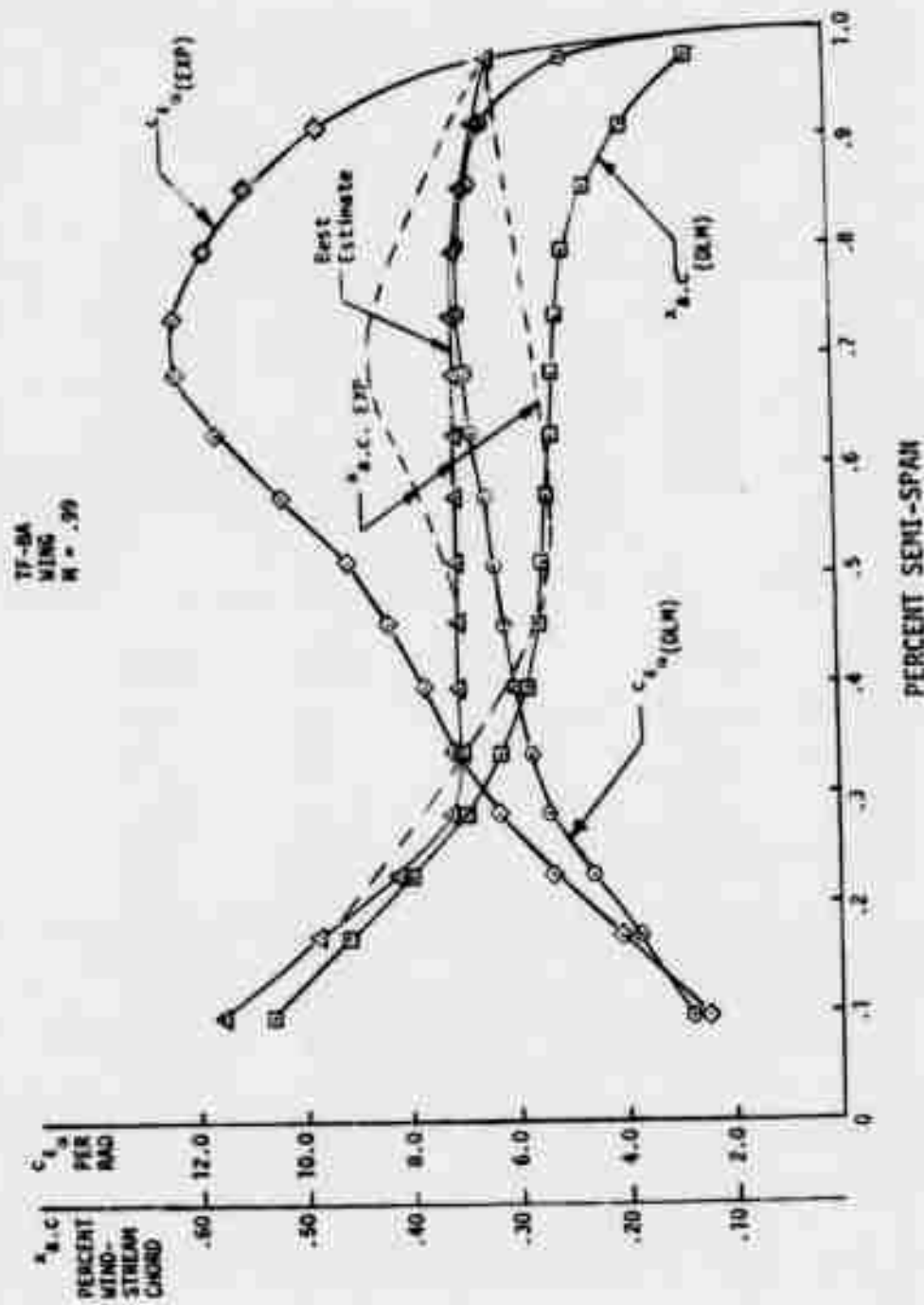


Figure 3.1-17 TF-8A c_{l_α} , $x_{a,x}$ vs. $y/(b/2)$; $M_\infty = .99$

TABLE 3.1-14

TF-8A Steady Weight Factors

$M_\infty = 0.6$			$M_\infty = 0.8$		
<u>Y/(b/2)</u>	<u>WTSCl</u>	<u>WTSCM</u>	<u>Y/(b/2)</u>	<u>WTSCl</u>	<u>WTSCM</u>
.095	1.141	1.475	.095	1.227	1.437
.167	1.107	1.440	.167	1.238	1.614
.224	1.070	1.277	.224	1.165	1.462
.280	1.075	1.224	.280	1.146	1.379
.337	1.053	1.223	.337	1.145	1.388
.394	1.033	1.162	.394	1.134	1.298
.452	1.034	1.136	.452	1.106	1.219
.509	1.057	1.133	.509	1.146	1.179
.567	1.123	1.173	.567	1.185	1.163
.624	1.119	1.205	.624	1.215	1.118
.680	1.256	1.232	.680	1.229	1.108
.737	1.285	1.228	.737	1.213	1.093
.795	1.295	1.181	.795	1.208	1.068
.852	1.266	1.162	.852	1.211	.986
.909	1.218	1.141	.909	1.262	.894
.969	1.105	1.118	.969	1.378	.689

$M_\infty = 0.90$			$M_\infty = 0.95$		
<u>Y/(b/2)</u>	<u>WTSCl</u>	<u>WTSCM</u>	<u>Y/(b/2)</u>	<u>WTSCl</u>	<u>WTSCM</u>
.095	1.216	1.336	.095	.862	.342
.167	1.213	1.552	.167	1.175	.754
.224	1.161	1.518	.224	1.271	1.051
.280	1.151	1.399	.280	1.332	1.312
.337	1.203	1.456	.337	1.383	1.389
.394	1.211	1.359	.394	1.396	1.333
.452	1.250	1.331	.452	1.433	1.373
.509	1.279	1.285	.504	1.443	1.422
.567	1.340	1.278	.567	1.436	1.442
.624	1.385	1.254	.624	1.424	1.387
.680	1.438	1.261	.68	1.430	1.397
.737	1.479	1.226	.737	1.448	1.395
.795	1.501	1.187	.795	1.496	1.413
.852	1.495	1.044	.852	1.485	1.337
.909	1.436	.808	.909	1.401	1.145
.969	1.185	.450	.969	.953	.658

TABLE 3.1-14 (Cont'd)
 TF-8A Steady Weight Factors

<u>Y/(b/2)</u>	<u>WTSCl</u>	<u>WTSCM</u>
.095	.902	.553
.167	1.104	.902
.224	1.157	1.035
.280	1.195	1.071
.387	1.256	1.045
.394	1.288	.917
.452	1.357	.913
.509	1.445	.949
.567	1.590	1.026
.624	1.729	1.107
.68	1.796	1.133
.737	1.758	1.103
.795	1.662	1.102
.852	1.576	.949
.909	1.493	.878
.969	1.279	.643

TABLE 3.1-15

TF-8A Unsteady Weight Factors

$M_{\infty} = .90$

BAY NO. 11		$y/(b/2) = .452$			
k_{r2D}	WTUSCL		WTUSCMEA		k_{r3D}
	REAL	IMAGINARY	REAL	IMAGINARY	
0	1	0	1	0	0
.095	.975	-.032	.968	-.027	.1
.190	.928	-.064	.920	-.067	.2
.314	.862	-.068	.847	-.081	.333
.950	.892	+.014	.827	+.037	1.0

BAY NO. 10		$y/(b/2) = .509$			
k_{r2D}	WTUSCL		WTUSCMEA		k_{r3D}
	REAL	IMAGINARY	REAL	IMAGINARY	
0	1	0	1	0	0
.090	.976	-.030	.970	-.025	.1
.180	.934	-.062	.926	-.064	.2
.300	.867	-.071	.854	-.082	.333
.900	.888	+.021	.817	+.035	1.0

BAY NO. 9		$y/(b/2) = .567$			
k_{r2D}	WTUSCL		WTUSCMEA		k_{r3D}
	REAL	IMAGINARY	REAL	IMAGINARY	
0	1	0	1	0	0
.085	.978	-.027	.971	-.022	.1
.170	.941	-.060	.933	-.060	.2
.280	.875	-.073	.863	-.082	.333
.857	.884	+.024	.808	+.031	1.0

TABLE 3.1-15 (Cont'd)

TF-8A Unsteady Weight Factors

$M_{\infty} = .90$

BAY NO. 8						$y/(b/2) = .624$
k_{r2D}	WTUSCL		WTUSCMEA		k_{r3D}	
	REAL	IMAGINARY	REAL	IMAGINARY		
0	1	0	1	0	0	
.080	.979	-.025	.973	-.020	.1	
.160	.947	-.057	.939	-.055	.2	
.270	.880	-.074	.869	-.083	.333	
.800	.878	+.026	.799	+.026	1.0	

BAY NO. 7						$y/(b/2) = .68$
k_{r2D}	WTUSCL		WTUSCMEA		k_{r3D}	
	REAL	IMAGINARY	REAL	IMAGINARY		
0	1	0	1	0	0	
.076	.980	-.022	.975	-.017	.1	
.152	.951	-.055	.943	-.052	.2	
.250	.889	-.073	.879	-.082	.333	
.760	.872	+.026	.792	+.020	1.0	

BAY NO. 6						$y/(b/2) = .737$
k_{r2D}	WTUSCL		WTUSCMEA		k_{r3D}	
	REAL	IMAGINARY	REAL	IMAGINARY		
0	1	0	1	0	0	
.071	.982	-.020	.976	-.014	.1	
.142	.956	-.052	.949	-.049	.2	
.240	.894	-.072	.885	-.081	.333	
.710	.864	+.023	.786	+.012	1.0	

TABLE 3.1-15 (Cont'd)
TF-8A Unsteady Weight Factors

$M_{\infty} = .90$

BAY NO. 5		$y/(b/2) = .795$			
k_{r2D}	WTUSCL		WTUSCME _{EA}		k_{r3D}
	REAL	IMAGINARY	REAL	IMAGINARY	
0	1	0	1	0	0
.067	.983	-.017	.977	-.012	.1
.133	.959	-.049	.952	-.045	.2
.220	.907	-.070	.897	-.077	.333
.670	.856	+.020	.783	+.004	1.0

BAY NO. 4		$y/(b/2) = .852$			
k_{r2D}	WTUSCL		WTUSCME _{EA}		k_{r3D}
	REAL	IMAGINARY	REAL	IMAGINARY	
0	1	0	1	0	0
.062	.970	-.014	1.046	-.008	.1
.124	.940	-.065	1.005	-.072	.2
.206	.864	-.117	.915	-.139	.333
.620	.668	-.001	.619	-.048	1.0

BAY NO. 3		$y/(b/2) = .909$			
k_{r2D}	WTUSCL		WTUSCME _{EA}		k_{r3D}
	REAL	IMAGINARY	REAL	IMAGINARY	
0	1	0	1	0	0
.057	.973	-.008	1.049	0.00	.1
.114	.946	-.057	1.012	-.062	.2
.190	.884	-.108	.935	-.129	.333
.570	.661	-.023	.626	-.077	1.0

TABLE 3.1-15 (Cont'd)

TF-8A Unsteady Weight Factors
 $M_\infty = .90$

BAY NO. 2		$y/(b/2) = .964$			
k_{r2D}	WTUSCL		WTUSCME _A		k_{r3D}
	REAL	IMAGINARY	REAL	IMAGINARY	
0	1	0	1	0	0
.052	.974	-.004	1.051	+.003	1
.105	.951	-.050	1.019	-.050	.2
.175	.900	-.098	.954	-.116	.333
.520	.661	-.046	.639	-.109	1.0

TABLE 3.1-16
TF-8A Unsteady Weight Factors

$M = .95$
 ∞

BAY NO. 11		$y/(b/2) = .452$			
k_{r2D}	WTUSCL		WTUSCMEA		k_{r3D}
	REAL	IMAGINARY	REAL	IMAGINARY	
0	1	0	1	0	0
.095	.960	-.058	.962	-.036	.1
.190	.878	-.123	.891	-.098	.2
.314	.740	-.120	.789	-.121	.333
.950	.802	+.016	.753	+.062	1.0

BAY NO. 10		$y/(b/2) = .509$			
k_{r2D}	WTUSCL		WTUSCMEA		k_{r3D}
	REAL	IMAGINARY	REAL	IMAGINARY	
0	1	0	1	0	0
.09	.962	-.053	.964	-.032	.1
.18	.891	-.118	.900	-.092	.2
.30	.750	-.126	.800	-.123	.333
.90	.796	+.031	.735	+.057	1.0

BAY NO. 9		$y/(b/2) = .567$			
k_{r2D}	WTUSCL		WTUSCMEA		k_{r3D}
	REAL	IMAGINARY	REAL	IMAGINARY	
0	1	0	1	0	0
.085	.965	-.049	.966	-.028	.1
.170	.904	-.112	.910	-.086	.2
.280	.766	-.132	.815	-.124	.333
.850	.787	+.041	.719	+.050	1.0

TABLE 3.1-16 (Cont'd)

TF-8A Unsteady Weight Factors

$M_{\infty} = .95$

BAY NO. 8		$y/(b/2) = .624$			
k_{r2D}	WTUSCL		WTUSCME _{EA}		k_{r3D}
	REAL	IMAGINARY	REAL	IMAGINARY	
0	1	0	1	0	0
.080	.967	-.044	.968	-.025	.1
.160	.914	-.105	.920	-.080	.2
.270	.774	-.134	.823	-.123	.333
.800	.776	+.049	.707	+.041	1.0

BAY NO. 7		$y/(b/2) = .68$			
k_{r2D}	WTUSCL		WTUSCME _{EA}		k_{r3D}
	REAL	IMAGINARY	REAL	IMAGINARY	
0	1	0	1	0	0
.076	.969	-.040	.970	-.021	.1
.152	.922	-.100	.927	-.074	.2
.250	.792	-.137	.840	-.122	.333
.760	.766	+.052	.699	+.033	1.0

BAY NO. 6		$y/(b/2) = .737$			
k_{r2D}	WTUSCL		WTUSCME _{EA}		k_{r3D}
	REAL	IMAGINARY	REAL	IMAGINARY	
0	1	0	1	0	0
.071	.971	-.036	.971	-.018	.1
.142	.930	-.093	.935	-.069	.2
.240	.802	-.137	.848	-.119	.333
.710	.750	+.050	.692	+.020	1.0

TABLE 3.1-16 (Cont'd)

TF-8A Unsteady Weight Factors

$M_{\infty} = .95$

BAY NO. 5					$y/(b/2) = .795$
k_{r2D}	WTUSCL		WTUSCMEA		k_{r3D}
	REAL	IMAGINARY	REAL	IMAGINARY	
0	1	0	1	0	0
.067	.973	-.030	.973	-.013	.1
.133	.936	-.088	.942	-.063	.2
.220	.824	-.136	.865	-.112	.333
.670	.734	+.044	.690	+.008	1.0

BAY NO. 4					$y/(b/2) = .852$
k_{r2D}	WTUSCL		WTUSCMEA		k_{r3D}
	REAL	IMAGINARY	REAL	IMAGINARY	
0	1	0	1	0	0
.062	.968	+.017	.980	+.021	.1
.124	.940	-.025	.969	+.009	.2
.206	.871	-.087	.954	-.017	.333
.620	.629	-.076	.836	-.054	1.0

BAY NO. 3					$y/(b/2) = .909$
k_{r2D}	WTUSCL		WTUSCMEA		k_{r3D}
	REAL	IMAGINARY	REAL	IMAGINARY	
0	1	0	1	0	0
.057	.970	+.020	.982	+.022	.1
.114	.946	-.018	.971	+.011	.2
.190	.888	-.076	.957	-.013	.333
.570	.641	-.092	.844	-.054	1.0

TABLE 3.1-16 (Cont'd)
 TF-8A Unsteady Weight Factors

$M_{\infty} = .95$

BAY NO. 2		$y/(b/2) = .969$			
k_{r2D}	WTUSCL		WTUSCMEA		k_{r3D}
	REAL	IMAGINARY	REAL	IMAGINARY	
0	1	0	1	0	0
.052	.971	+.022	.983	+.022	.1
.105	.951	-.010	.972	+.013	.2
.175	.900	-.064	.961	-.008	.333
.520	.658	-.108	.853	-.054	1.0

TABLE 3.1-17

TF-8A Unsteady Weight Factors

$M_{\infty} = .99$

BAY NO. 11		$y/(b/2) = .452$			
k_{r2D}	WTUSCL		WTUSCMEA		k_{r3D}
	REAL	IMAGINARY	REAL	IMAGINARY	
0	1	0	1	0	0
.095	.977	0.00	.992	+.010	.1
.190	.920	-.070	.978	-.006	.2
.314	.822	-.122	.959	-.021	.333
.950	.675	+.025	.892	-.024	1.0

BAY NO. 10		$y/(b/2) = .509$			
k_{r2D}	WTUSCL		WTUSCMEA		k_{r3D}
	REAL	IMAGINARY	REAL	IMAGINARY	
0	1	0	1	0	0
.090	.979	+.002	.992	+.011	.1
.180	.930	-.062	.980	-.004	.2
.300	.831	-.120	.961	-.020	.333
.900	.668	+.013	.897	-.027	1.0

BAY NO. 9		$y/(b/2) = .567$			
k_{r2D}	WTUSCL		WTUSCMEA		k_{r3D}
	REAL	IMAGINARY	REAL	IMAGINARY	
0	1	0	1	0	0
.085	.980	+.006	.993	+.011	.1
.170	.938	-.054	.982	-.002	.2
.280	.846	-.115	.964	-.019	.333
.850	.664	0.00	.903	-.030	1.0

TABLE 3.1-17 (Cont'd)
TF-8A Unsteady Weight Factors

$M_\infty = .99$

BAY NO. 8					$y/(b/2) = .624$
k_{r2D}	WTUSCL		WTUSCMEA		k_{r3D}
	REAL	IMAGINARY	REAL	IMAGINARY	
0	1	0	1	0	0
.080	.981	+.009	.993	+.012	.1
.160	.946	-.046	.984	0.00	.2
.270	.853	-.112	.965	-.018	.333
.800	.662	-.012	.908	-.031	1.0

BAY NO. 7					$y/(b/2) = .68$
k_{r2D}	WTUSCL		WTUSCMEA		k_{r3D}
	REAL	IMAGINARY	REAL	IMAGINARY	
0	1	0	1	0	0
.076	.982	+.012	.993	+.012	.1
.152	.952	-.040	.985	+.002	.2
.250	.869	-.105	.968	-.015	.333
.760	.663	-.024	.912	-.032	1.0

BAY NO. 6					$y/(b/2) = .737$
k_{r2D}	WTUSCL		WTUSCMEA		k_{r3D}
	REAL	IMAGINARY	REAL	IMAGINARY	
0	1	0	1	0	0
.071	.982	+.016	.994	+.013	.1
.142	.958	-.032	.986	+.004	.2
.240	.876	-.100	.970	-.014	.333
.710	.665	-.038	.917	-.032	1.0

TABLE 3.1-17 (Cont'd)

TF-8A Unsteady Weight Factors

$M_{\infty} = .99$

BAY NO. 5		$y/(b/2) = .795$			
k_{r2D}	WTUSCL		WTUSCMEA		k_{r3D}
	REAL	IMAGINARY	REAL	IMAGINARY	
0	1	0	1	0	0
.067	.984	+.018	.994	+.013	.1
.133	.963	-.027	.987	+.005	.2
.220	.892	-.090	.973	-.011	.333
.670	.669	-.051	.921	-.032	1.0

BAY NO. 4		$y/(b/2) = .852$			
k_{r2D}	WTUSCL		WTUSCMEA		k_{r3D}
	REAL	IMAGINARY	REAL	IMAGINARY	
0	1	0	1	0	0
.062	.972	-.014	.985	+.006	.1
.124	.940	-.086	.968	-.022	.2
.206	.832	-.160	.922	-.059	.333
.620	.574	-.001	.773	-.046	1.0

BAY NO. 3		$y/(b/2) = .909$			
k_{r2D}	WTUSCL		WTUSCMEA		k_{r3D}
	REAL	IMAGINARY	REAL	IMAGINARY	
0	1	0	1	0	0
.057	.975	-.006	.986	+.010	.1
.114	.947	-.076	.972	-.018	.2
.190	.855	-.150	.933	-.053	.333
.570	.568	-.029	.782	-.056	1.0

TABLE 3.1-17 (Cont'd)
TF-8A Unsteady Weight Factors

$M_\infty = .99$

BAY NO. 2		$y/(b/2) = .969$			
k_{r2D}	WTUSCL		WTUSCMEA		k_{r3D}
	REAL	IMAGINARY	REAL	IMAGINARY	
0	1	0	-1	0	0
.052	.976	0.00	.986	+.011	.1
.105	.952	-.064	.974	-.013	.2
.175	.876	-.140	.942	-.046	.333
.520	.569	-.058	.793	-.065	1.0

The unsteady weight factors are described in Subsection 3.3. Figures 3.3-5 through -10 present unsteady weight factors for three spanwise stations as a function of section reduced frequency, k_{r2D} where $k_{r2D} = \frac{c}{c} k_{r3D}$. The results at these three stations are applied to all wing bays as described in Subsection 3.3. Tables 3.1-15 through -17 present the unsteady correction factors for the TF-8A wing. There are no tables for $M_\infty = 0.6, 0.8$ since the unsteady weight factors for these Mach Numbers are unity (no shock wave motion). In the tables for the other Mach Numbers some inboard bays are missing. Again the reason for this is the fact that the weight factors there are unity (no shock wave motion). These data were applied at the four reduced frequencies of $k_{r3D} = 0, .1, .2, .333, \text{ and } 1.0$. The total weight factor for any bay is the product of the steady and unsteady factors:

$$WTCL = WTSCl * WTUSCL$$

$$WTCM = WTSCM * WTUSCM$$

Normally, these totals are not formed directly. The procedure followed is to: First, modify the theoretical AIC matrix with the steady weight factors, store, and use them as required; Second, modify the modified AIC matrix with the unsteady weight factors, store again, and use as required.

3.1.4 TF-8A Flutter Results - Steady Weighting

Flutter analyses were run using the "steady weighted" AIC's. The discussion of the weighting procedures, along with the unexpected difficulties experienced in connection with Reynolds Number discrepancy between the pressure and flutter models, appears above in Subsections 2.1, 2.4, and 3.1.3. In those sections it was pointed out that at high Mach numbers the static aeroelastic twist distributions and steady aerodynamic lift curve slope data seemed to indicate that the last few wing tip stations were stalled; e.g., $c_{l_\alpha} = 0$. A flutter analysis was run at $M_\infty = 0.99$ under this assumption. The flutter dynamic pressure was not reasonable ($q_F = 195$ psf).

Since the measured flutter speed trends indicated no tip stalling, flutter analysis was rerun using AIC's weighted under the assumption that the actual lift slopes at the static twist angles-of-attack are the same as shown in the pressure model data at smaller pre-stalled

values of angle-of-attack. The basis for this assumption is the Reynold's Number discrepancy between the two models (See Section 2.4 above for discussion).

Figure 3.1-18 shows a summary of computed flutter speeds under this assumption of no tip stalling for the value of $c_{l\alpha}$. Unweighted theoretical results (using subsonic Doublett Lattice Method) are shown for comparison.

As discussed above in Section 3.1.3, the available aerodynamic data was not adequate to unambiguously define the section moment slopes, $c_{m\alpha}$. At $M_\infty = 0.99$, Figure 3.1-18 shows the calculated flutter speed for three different interpretations of $c_{m\alpha}$, and illustrates the sensitivity of flutter speed to $c_{m\alpha}$. Section 3.1.3 contains a detailed discussion of this moment data and its interpretations. At $M_\infty = .95$ and 0.99 , one additional possible interpretation of $c_{m\alpha}$ (namely, using the steepest negative slope between $\alpha = 0$ and $\alpha = -1.5$) was used which resulted in an unreasonable aerodynamic center distribution (70% chord at the tip) and an unreasonable flutter speed (near 300 qsf. for both Mach numbers).

Section 5 below discusses recommended work to resolve these ambiguities. The steady weight factors (best guess for $c_{m\alpha}$) used in the TF-8A analysis are shown in Table 3.1-14.

Figure 3.1-18 shows an apparent discrepancy between the calculated and measured flutter frequencies at high Mach number. Actually, the discrepancy is not severe because the analysis shows that the flutter mode decreases in frequency very rapidly just before flutter onset. For example, the analysis shows the frequency to be dropping at a rate of 2 Hz per 3 kts at flutter.

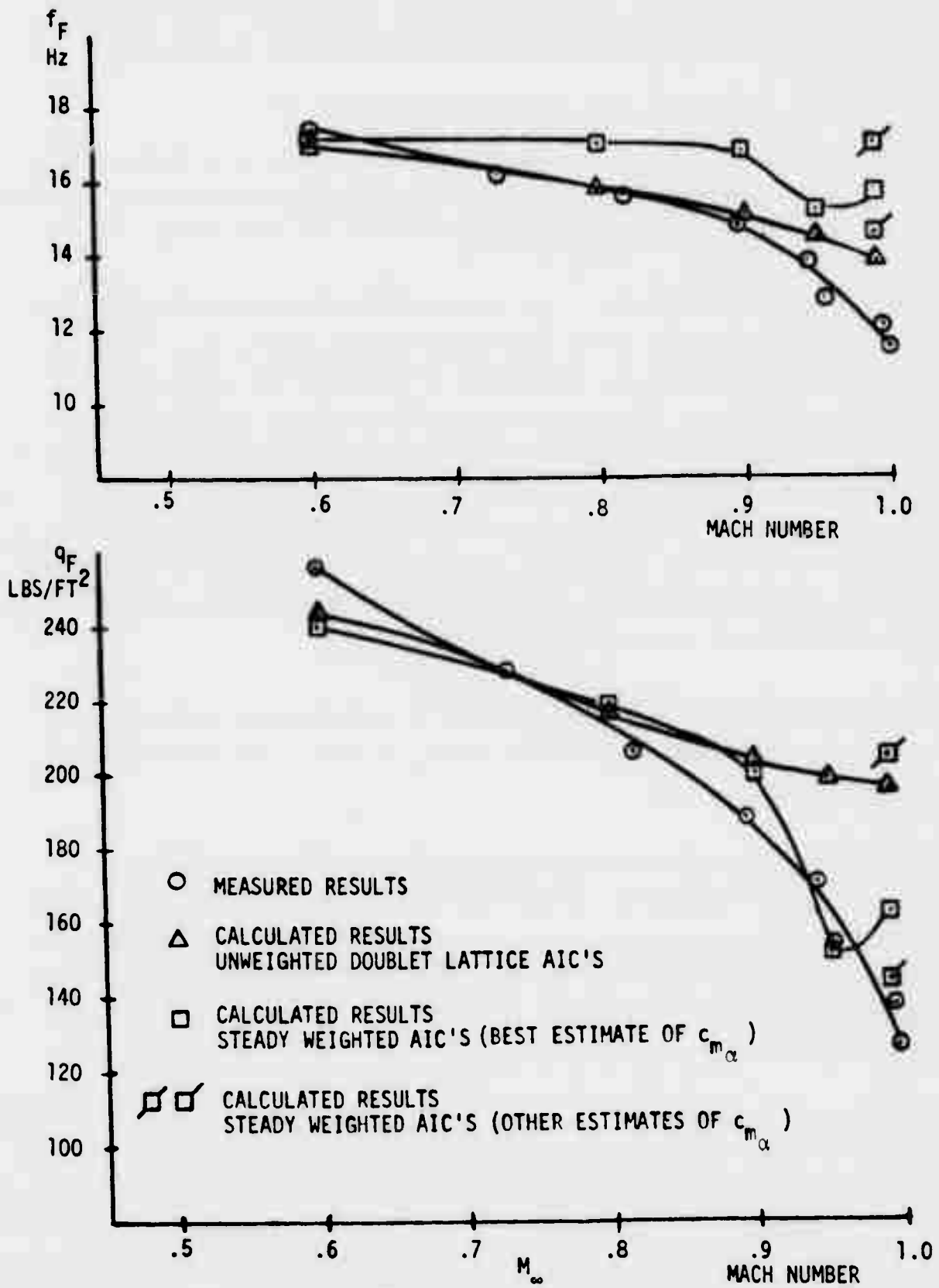


Figure 3.1-18 TF-8A Flutter Results

3.2 RESULTS OF ANALYSIS - PHASE II

3.2.1 TF-8A Flutter Analysis Results - Unsteady Corrections

Flutter analyses were also run using AIC's reflecting the "unsteady weighting factors". Section 2.5 discusses the theory and Section 3.3 discusses the application of that theory to the TF-8A wing.

Tables 3.1-15 through 3.1-17 show the unsteady weighting factors for reduced frequencies of 0, .1, .25 and 0.5. The "steady weighted" AIC's for these values of k_r were weighted by these factors and then the AIC's for the total list of reduced frequencies required by the flutter analysis was obtained by interpolation between these basic four.

The results of the flutter analyses showed that for the TF-8A the unsteady weighting factors changed the flutter speed by less than two percent at all Mach numbers.

3.3 PHASE III RESULTS

The theories developed under Phase III of the contract are presented in Subsection 2.5. It was noted there that the major transonic effect is the perturbation pressure induced by shock wave motion. The effects of shock wave motion were added to the classical lifting surface theory and the results discussed and correlated in Subsection 2.5.1.3. The correlation of this procedure using the NLR 7301 airfoil for the range of frequencies considered in the experiment is very encouraging.

The full transonic theory described in Subsection 2.5 is not entirely complete since the procedure for determining the shock wave motion for oscillatory flow has not been tried. The nondimensional shock wave motion function, $\lambda(k_r)/\lambda(k_r = 0)$ obtained experimentally for the NLR airfoil at $M_\infty = 0.7$ and $\alpha = 1.75^\circ$, can temporarily be used to obtain the shock wave motions for the TF-8A and YC-15II wings. It was felt, however, that if this approximation is to be used, then a less general theory could be used. Specifically, the method described in Subsection 2.5.1.2, as mentioned above, would be the logical choice because it contains the major transonic effect, i.e., pressures due to shock wave motion and because of its good correlation with data. A second reason for using this method is the effort involved. At its current level of development the general theory would require more time than available to run all of the conditions for the TF-8A and YC-15II wings.

The theory of Subsection 2.5.1.3 gives the incremental lift and moment due to shock wave motion as:

$$\Delta C_{l_\alpha} = \delta_1 \delta_2 (C_{p_{s_2}} - C_{p_{s_1}}) \frac{\partial \lambda_0/c}{\partial \alpha} \exp(-i2k_r \bar{\tau} A)$$

$$\delta_1 = \begin{cases} 1 & \text{upper surface} \\ -1 & \text{lower surface} \end{cases}$$

$$\delta_2 = \begin{cases} 1 & \text{shock moving aft with increasing } \alpha \\ -1 & \text{shock moving forward with increasing } \alpha \end{cases}$$

Where C_{ps_1} , C_{ps_2} are the steady pressures on either side of the shock

wave, λ_0 is the amplitude of shock motion, and $\bar{\tau}$ is the non-dimensional time ($\tau U_\infty/c$) for an acoustic wave to reach the shock wave from the trailing edge. The oscillatory value of λ_0 is approximated using the curve of $\lambda_0(k_r)/\lambda_0(k_r = 0)$ for the NLR 7301 airfoil and the value of $\lambda_0(k_r = 0)$ for the airfoil under consideration (see Figure 2.5-33). Thus, the $\lambda_0(k_r)$ for any wing is

$$\lambda_0(k_r) = \lambda_0(k_r = 0) G(k_r = 0)$$

where

$$G(k_r) = \lambda_0(k_r)/\lambda_0(k_r = 0) \text{ for NLR 7301 airfoil at } M_\infty = 0.7, \alpha = 1.75^\circ.$$

If the acoustic time $\bar{\tau}$ is computed as in Reference 4, then the constant A can be set to 1.0. To simplify the calculation, the method of Reference 4 was adopted instead of using the acoustic pulse generator (along with the estimated value for A). The approximate method of Reference 4 consists of using the following formula:

$$\tau = \frac{1}{c} \int_{x=c}^{x=x_s} \frac{dx}{(1 - M_\ell^2)/M_\ell}$$

where

$$M_\ell = 0.7 [M - M_\infty] + M_\infty$$

Where M is the local surface Mach Number

The weight factor for the lift coefficient is given in Subsection 2.4 as:

$$WTUSCL(k_r) = \frac{c_{\lambda_\alpha}^{(2DTRANS)}(k_r)/c_{\lambda_\alpha}^{(2D)}(k_r)}{c_{\lambda_\alpha}^{(2DTRANS)}(k_r = 0)/c_{\lambda_\alpha}^{(2D)}(k_r = 0)}$$

Where the transonic c_{l_α} i.e., $c_{l_\alpha}^{(2DTRANS)}$ is given as the total of the classic theory, $c_{l_\alpha}^{(2D)}$, plus the transonic increment, Δc_{l_α} .

The weight factor for the lift then becomes:

$$WTUSCL(k_r) = (1 + BCL G(k_r)LCL(k_r)) / (1 + BCL) \quad (3.3-1)$$

where

$$BCL = (C_{p_{s_2}} - C_{p_{s_1}}) \partial \lambda_0(k_r = 0) / \partial \alpha / c_{l_\alpha}^{(2D)}(k_r = 0)$$

$$LCL(k_r) = \left[c_{l_\alpha}^{(2D)}(k_r = 0) / c_{l_\alpha}^{(2D)}(k_r) \right] \exp(-12k_r \bar{\tau})$$

The derivation of the weight factors for the moment coefficient about the elastic axis follows and is similar.

$$\Delta c_{m_\alpha} = (x_s/c - x_{ea}/c) \Delta c_{l_\alpha}$$

where x_s is the shock location. The unsteady weight factors for c_{m_α} is then;

$$WTUSCM_{EA} = (1 + BCM G(k_r) LCM(k_r)) / (1 + BCM) \quad (3.3-2)$$

where

$$BCM = \frac{(x_s/c - x_{ea}/c)}{(1/4 - x_{ea}/c)} BCL$$

$$LCM(k_r) = \left[c_{m_\alpha}^{(2D)}(k_r = 0) / c_{m_\alpha}^{(2D)}(k_r) \right] \exp(-12k_r \bar{\tau})$$

The values of the steady flow classic theory are

$$c_{l_\alpha}^{(2D)}(k_r = 0) = 2\pi/\beta$$

$$c_{m_\alpha}^{(2D)}(k_r = 0) = \frac{2\pi}{\beta} (x_{ea}/c - 1/4)$$

The weight factors just described are calculated for three sections along the wing and applied to all of the aerodynamic bays. Figure 3.3-1 shows the bays that are associated with the three sections for the TF-8A wing while Figure 3.3-2 shows it for the YC-15II wing.

The elastic axis data, $x_{e.a.}/c$, to be used in the formulas for the unsteady weight factors are found in Table 3.1-1. The values of $c_{l(2D)}(k_r)$ and $c_{m(2D)}(k_r)$ are obtained from the two dimensional compressible^αsubsonic lifting surface theory.

The shock wave data to be used in these formulas could not be taken directly from steady wind tunnel data because of the elasticity of both the pressure model and the flutter model and because of the difference in built-in twist between the two models. Shock wave location and movement are highly dependent on the local section angle-of-attack and boundary layer build-up. Since both the built-in twist and elastic twist of the pressure model are different than those of the flutter model, the following procedure was followed.

The first step is to find the total section angle-of-attack, $\alpha_s^{(f)}$, of each of the three wing sections on the flutter model at an estimated dynamic pressure for flutter. The section angle-of-attack, $\alpha_s^{(f)}$, is composed of rigid body angle $\alpha^{(f)}$, elastic twist $\epsilon_e^{(f)}$, and built-in or 'jig' twist, $\epsilon_j^{(f)}$,

where 'f' indicates flutter model.

$$\alpha_s^{(f)} = \alpha^{(f)} + \epsilon_j^{(f)} + \epsilon_e^{(f)}$$

From this value of section angle-of-attack for the flutter model, is subtracted the value of $\epsilon_j^{(p)}$ for the pressure model.

$$\Delta\alpha_s^{(eff)} = \alpha_s^{(f)} - \epsilon_j^{(p)}$$

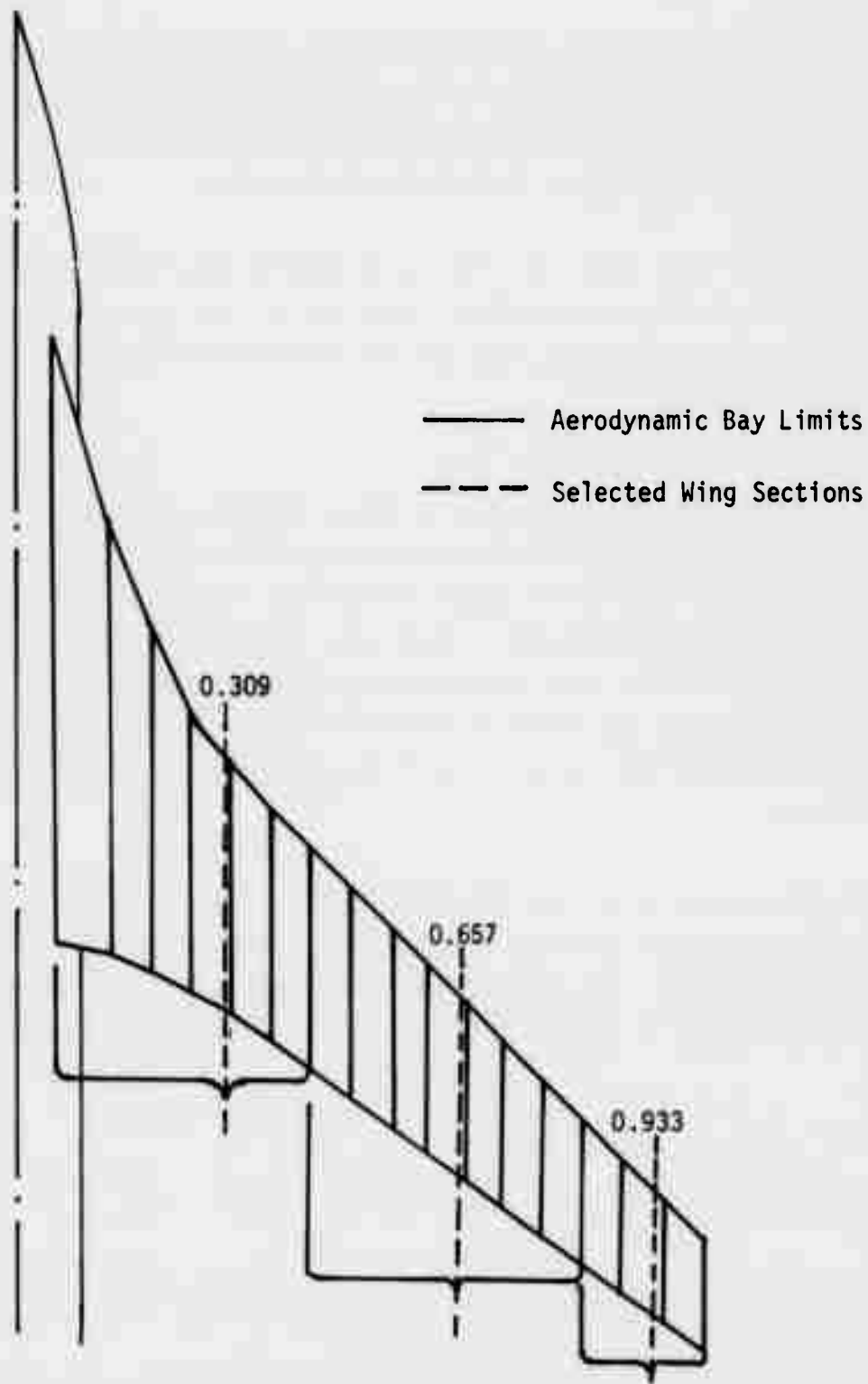


Figure 3.3-1 The Association of Aerodynamic Bays with Selected Wing Sections for the TF-8A Wing.

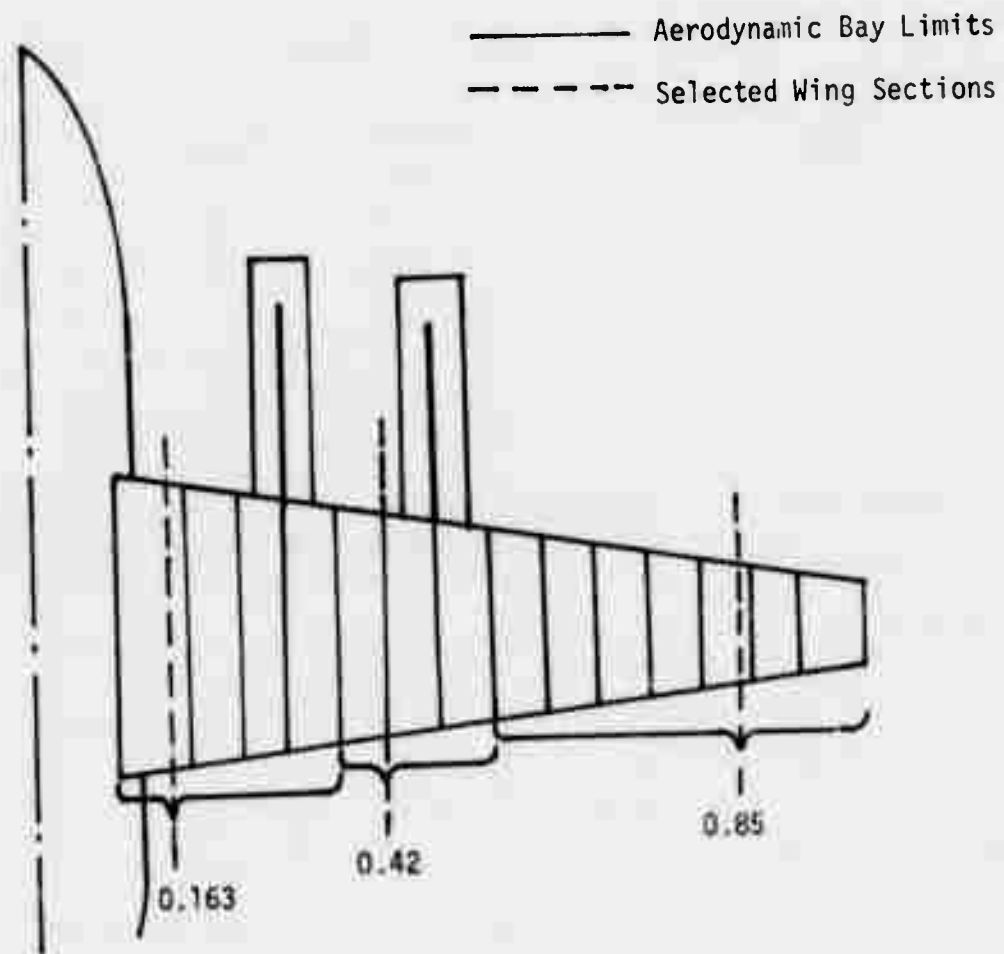


Figure 3.3-2 The Association of Aerodynamic Bays with Selected Wing Sections for the YC-15II Wing.

TABLE 3.3-1 - Elastic Axis Locations

<u>TF-8A</u>		<u>YC-15</u>	
<u>Y/(b/2)</u>	<u>x_{ea/c}</u>	<u>Y/(b/2)</u>	<u>x_{ea/c}</u>
.309	.5	.16	.38
.657	.5	.42	.43
.933	.5	.85	.5

TABLE 3.3-2 - TF-8A Incremental Angles-of-Attack Between the Elastic Flutter Model and Pressure Model

y/(b/2)	$\Delta\alpha_s$			
	M _∞ = 0.8	M _∞ = 0.9	M _∞ = 0.95	M _∞ = 0.99
.309	0.2°	0	0.6°	1.2°
.657	-0.8°	-0.4°	-0.7°	0
.933	-1.62°	-0.8°	-2.4°	-1.8°

TABLE 3.3-3 - YC-15II Incremental Angles-of-Attack Between the Elastic Aircraft and Pressure Model

y/(b/2)	$\Delta\alpha_s$ M = 0.76
.163	-0.7°
.42	-1.0°
.85	-2.0°

The incremental angle-of-attack, $\Delta\alpha_s^{(eff)}$, is the angle-of-attack on the pressure model required to match the flutter model conditions. (This angle is an effective angle and must be reduced to an actual angle by using the aeroelastic correction of the pressure model in reverse. This process was not done in the calculations; however, the resulting error is small.)

The aeroelastic calculations of $\alpha_s^{(f)}$ for the two flutter models is given in Subsection 3.1.2 for the TF-8A wing and 3.4.2 for the YC-15II wing. The value of $\epsilon_j^{(p)}$ for the pressure model is given in Figure 3.1-6. The values of $\Delta\alpha_s$ for the TF-8A wing at various Mach Numbers are presented in Table 3.3-2. The values of $\Delta\alpha_s$ for the YC-15II are given in Table 3.3-3.

The next step in the process is to find experimental pressure model data for pressure distributions that correspond as close as possible in α to the $\Delta\alpha_s$ tables above and to match this data to theoretical calculations using the Jameson and/or Garabedian methods (see Reference 16 and Appendix D for a description of the Garabedian method). The inverse process produces a modified airfoil shape when the experimental pressure distribution and Mach Number are used. The modified shape exhibits a thickening in the vicinity of the trailing edge which is typical of boundary layer growth (see Figure 3.3-3 for examples).

Early in the contract, calculations were performed using the inverse Garabedian method on TF-8A wing sections but at angles-of-attack that did not match the values of $\Delta\alpha_s$ given in Table 3.3-2. In order to take advantage of this work, the resulting modified airfoil shapes (shown in Figure 3.3-3 for $M_\infty = 0.99$) were used. Instead of revising the airfoil shape to match the data, the angle-of-attack and Mach Numbers were varied to produce a best-fit of the theory (Jameson Method) to the data. A table of these increments is given in Table 3.3-4.

Some of the section pressure distributions of the TF-8A wing could not be matched using this procedure and for these the inverse Garabedian procedure was reapplied near the correct angle of attack. For the case of

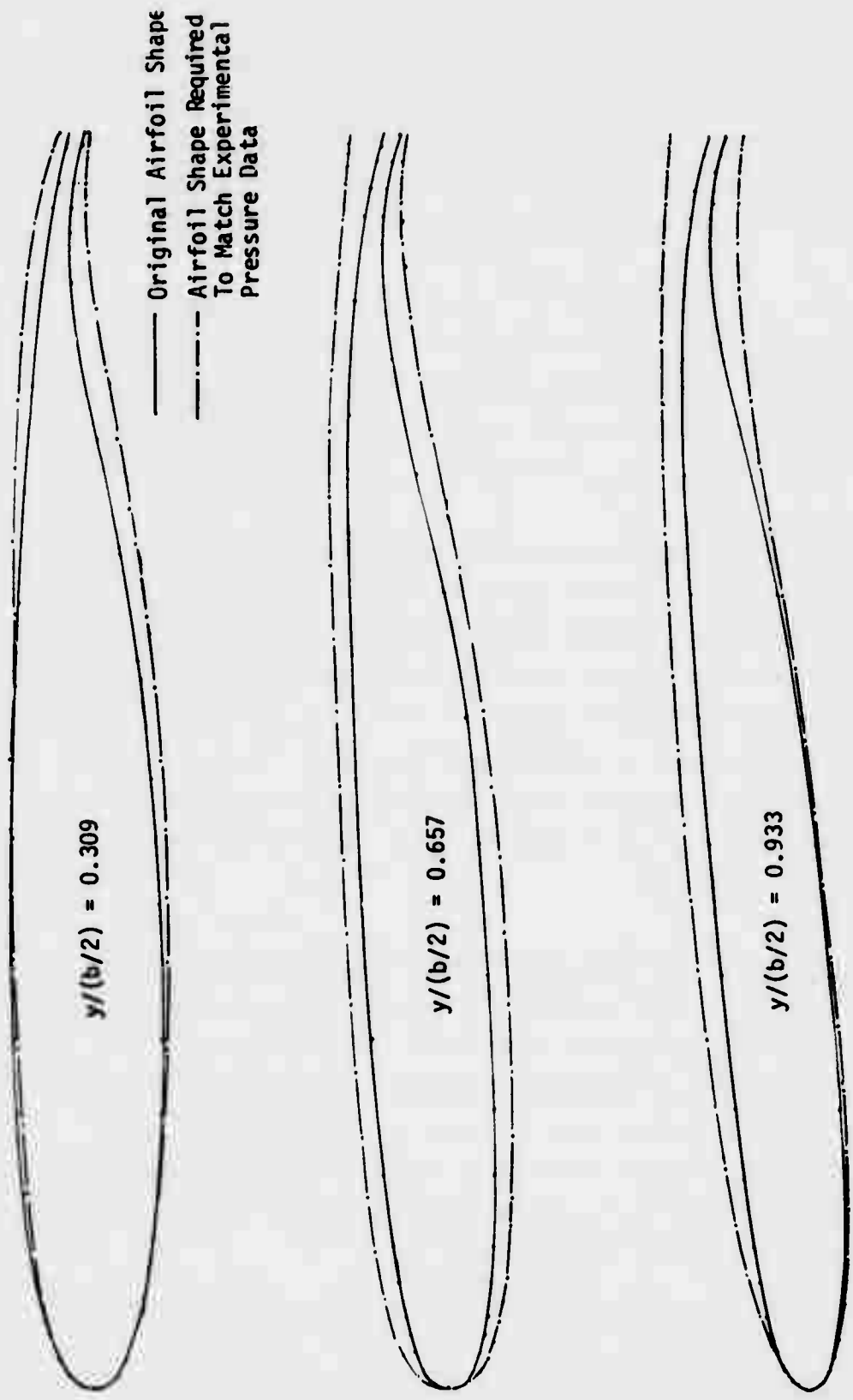


Figure 3.3-3 Comparison of Original Pressure - Model Airfoil Section Shapes With Those Required to Match Experimental Data For The TF-8A Wing. Required Airfoil Generated by Garabedian Inverse Process.

the YC-15II all of the airfoils were generated using the inverse Garabedian at angles-of-attack which were close to the desired ones given in Table 3.3-3. The output of the inverse Garabedian procedure also includes a change in angle-of-attack, $\delta\alpha$, from that which corresponds to the input experimental pressure distribution. In Tables 3.3-4 and 3.3-5, these are indicated by an asterisk (*).

The term $\delta\alpha$ is now added to the values of $\Delta\alpha_s$ and ϵ_M is added to the two-dimensional value of Mach Number ($M_{2D} = M_\infty \cos \Lambda$).

$$\overline{\Delta\alpha_s} = \Delta\alpha_s + \delta\alpha$$

$$\overline{M}_{2D} = M_{2D} + \delta M$$

The values of $\overline{\Delta\alpha_s}$ and \overline{M}_{2D} are then input into the Jameson steady transonic method and the necessary shock data calculated.

The shock data required for the calculation of the weight factors are: (1) The jump in pressure across the steady shock, $C_{p_{s_2}} - C_{p_{s_1}}$; (2) The shock location, x_s/c , (3), the local Mach Number distribution (so that $\bar{\tau}$ may be calculated); and (4) The change in shock location with respect to angle-of-attack, $\partial\lambda_0(k_r = 0)/\partial\alpha$. The last term is done in a numerical manner by varying the angle-of-attack slightly about the mean position. Thus,

$$\frac{\partial\lambda_0}{\partial\alpha} = \frac{\Delta\lambda}{\Delta\alpha}$$

An example is presented in Figure 3.3-4. The values of interest for the TF-8A and YC-15II wings are given in Tables 3.3-6 and 3.3-7.

The quantities in these tables are used to produce the desired incremental unsteady weight factors. These factors are plotted for the TF-8A wing in Figures 3.3-5 through 3.1-10. These figures are for free stream Mach Numbers, $M_\infty = 0.9, 0.95$ and 0.99 . The results for $M_\infty = .8$ are

TABLE 3.3-4 - (TF-8A) Corrections to Jameson Transonic Theory to Give Best Match to Data

$y/(b/2)$	$M_{\infty} = 0.8$		$M_{\infty} = 0.9$		$M_{\infty} = 0.95$		$M_{\infty} = 0.99$	
	$\delta\alpha$	δM	$\delta\alpha$	δM	$\delta\alpha$	δM	$\delta\alpha$	δM
0.309	No	Shock						
0.657	↓	↓	0.58°	0	0.85°	0	1.5°	0.018
0.933	↓	↓	2.08°	0.009	0.25°	0	0.5°	-0.012

TABLE 3.3-5 - (YC-15II) Differences Between Data and Garabedian Theory for α and M

$y/(b/2)$	$M_{\infty} = .76$	
	$\delta\alpha$	δM
.163	$-0.85^{\circ*}$	0^*
.42	$-1.5^{\circ*}$	0^*
.85	$-0.18^{\circ*}$	0^*

* Could not obtain good match by changing α and M in the Jameson Method and had to perform Garabedian inverse.

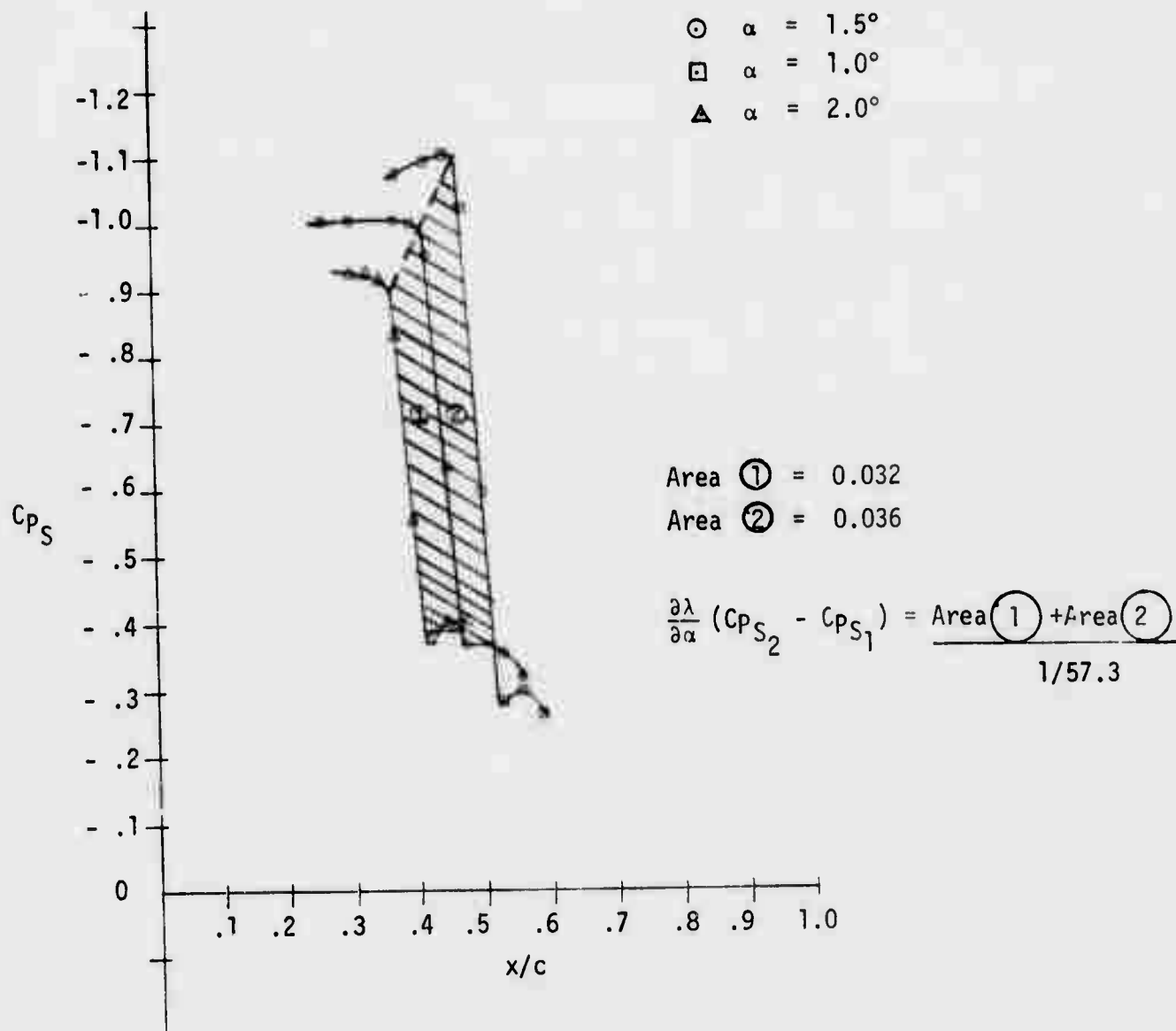


Figure 3.3-4 Steady Pressure Distribution Near the Shock Wave for Angles of Attack Near the Required Value (1.5°) for the TF-8A Wing ($y/(b/2) = 0.657$, $M_\infty = M_{3D} = 0.99$, $M_{2D} = .80$). Illustration of the Calculation $\frac{\partial \lambda}{\partial \alpha} (C_{p_{S_2}} - C_{p_{S_1}})$.

TABLE 3.3-6 - Shock Location & Motion Variables for the TF-8A Wing Section

M_{3D} (M_∞)	M_{2D}	$y/(b/2)$	δ_1	δ_2	x_s/c	$\bar{\tau}$	$(C_{ps_2} - C_{ps_1}) \delta \lambda_0 / \delta \alpha$				
.80	-	.309	(No Shocks)								
.80	-	.657									
.80	-	.933									
.90	-	.309	-	-	No Shock	-	-				
.90	.711	.657	-1	-1	0.1351	3.07	1.2900				
.90	.72	.933	-1	-1	0.2141	2.52	3.1515				
.95	-	.309	-	-	No Shock	-	-				
.95	.75	.657	-1	-1	0.2373	3.154	2.9223				
.95	.75	.933	-1	-1	0.3894	1.766	4.7413				
.99	-	.309	-	-	No Shock	-	-				
.99	.80	.657	-1	-1	0.4445	1.912	3.8964				
.99	.77	.933	-1	-1	0.3894	2.685	4.8705				

Table 3.3-7 - Shock Location & Motion Variables for the YC-15II Wing Sections

M_{3D} (M_∞)	M_{2D}	$y/(b/2)$	δ_1	δ_2	x_s/c	$\bar{\tau}$	$(C_{ps_2} - C_{ps_1}) \delta \lambda_0 / \delta \alpha$
.76	.759	.163	1	1	.3644	3.29	3.553
.76	.759	.42	1	1	.4122	3.35	1.776 Upper surface
.76	.759	.42	-1	-1	.4350	2.44	1.031 Lower surface
.76	.761	.85	-1	-1	.4644	2.07	0.974

unity because there are no shock waves at this Mach Number, and thus, are not plotted. The results for $y/(b/2) = 0.309$ for all Mach numbers are not shown for the same reasons; i.e., no distinct shock exists for this inboard wing section.

Figures 3.1-11 through 3.1-14 present the weight factors for the three sections of the YC-15II wing plotted versus reduced frequency for one Mach Number ($M = 0.76$). The section at $y/(b/2) = 0.42$ requires two plots because there are shock waves on both top and bottom surfaces.

Notice that the incremental unsteady weight factors are unity at $k_r = 0$. These factors are used to produce a weight factor correction to the steady weight factors previously discussed. As stated in Subsection 2.4, the total weight factor is the product of the steady weight factor and the unsteady weight factor.

The incremental unsteady weight factors are plotted versus a two-dimensional sectional reduced frequency. The two-dimensional sectional reduced frequency is related to the three-dimensional reduced frequency as follows (see Subsection 2.4):

$$k_{r2D} = k_{r3D} \frac{c}{C}$$

The values of k_{r3D} for the TF-8A wing are:

$$k_{r3D} \text{ (TF-8A)} = 0, 0.1, 0.333, 1.0$$

The values of k_{r3D} for the YC-15II wing are:

$$k_{r3D} \text{ (YC-15II)} = 0, 0.1, 0.25, 0.5$$

The sectional values of reduced frequency, k_{r2D} , then vary as the local chord, c , varies. The specific values of k_{r2D} and the corresponding values of weight factors for c_{l_α} and c_{m_α} are presented in Subsection 3.1.2 for the TF-8A wing and in Subsection 3.4.2 for the YC-15II wing.

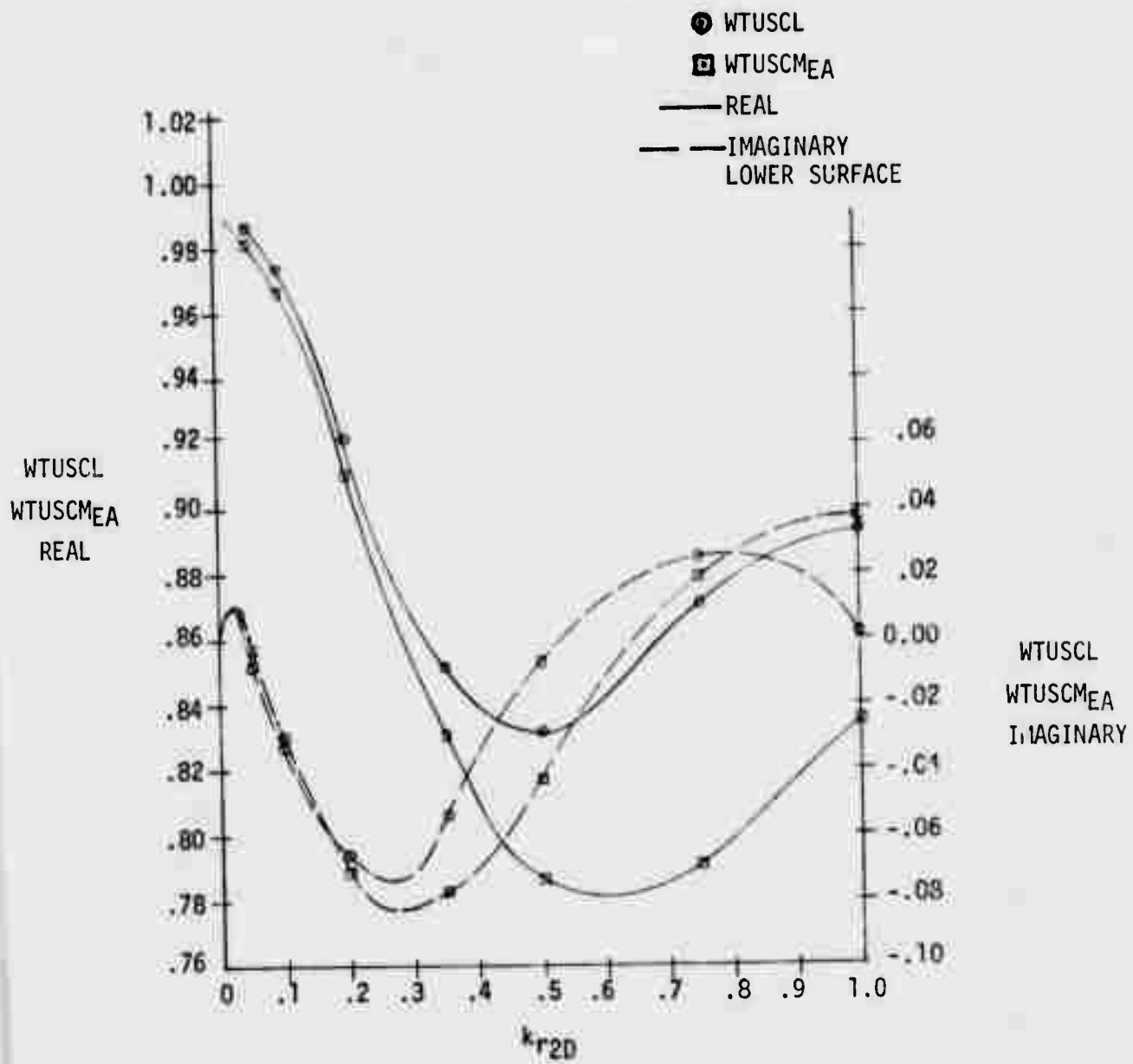


Figure 3.3-5 Unsteady Weight Factors for the TF-8A Wing
 $(y/(b/2) = 0.657, M_{3D} = 0.90, M_{2D} = 0.711)$

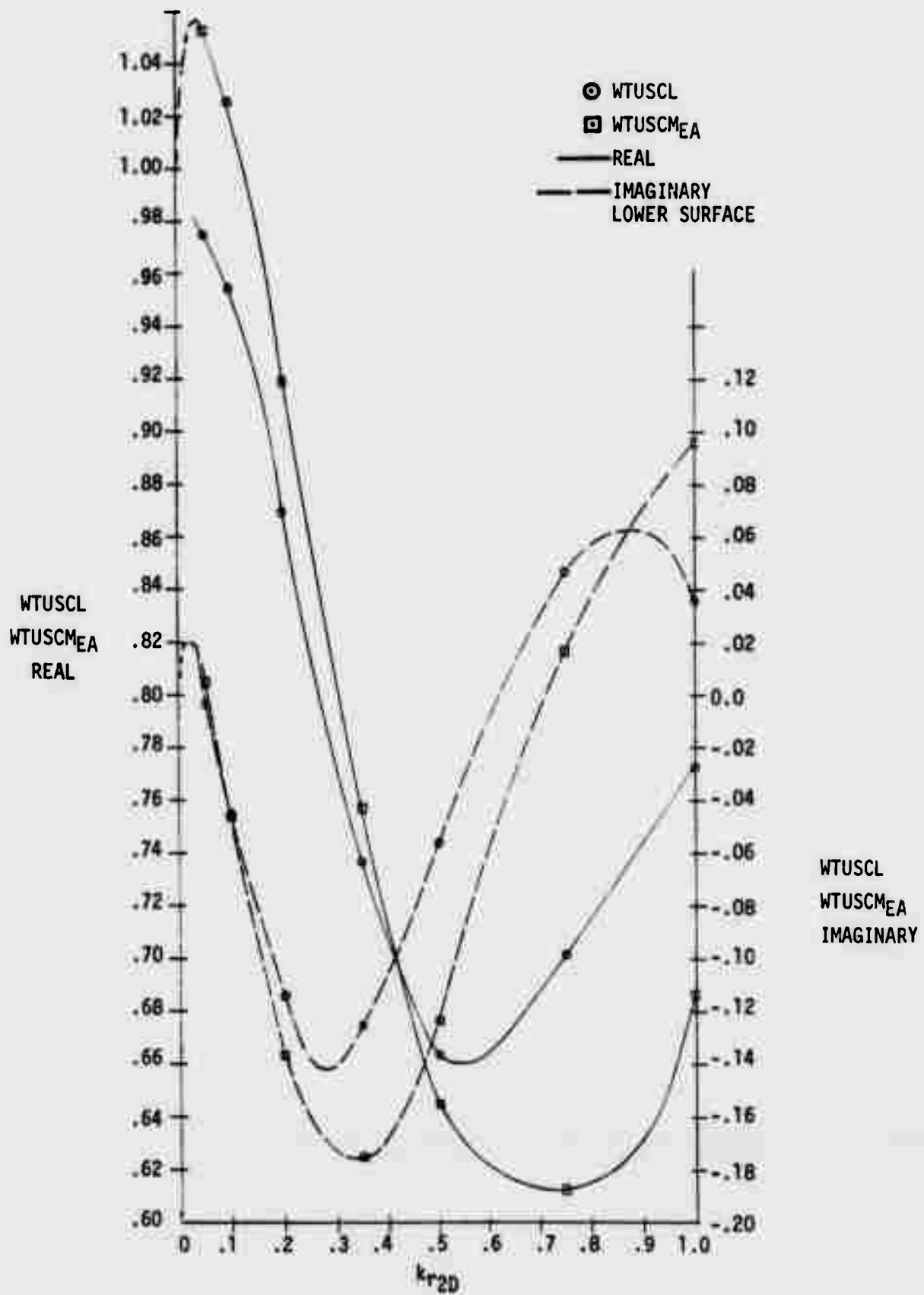


Figure 3.3-6 Unsteady Weight Factors for the TF-8A Wing
 $(y/(b/2) = 0.933, M_{3D} = 0.9, M_{2D} = 0.72)$

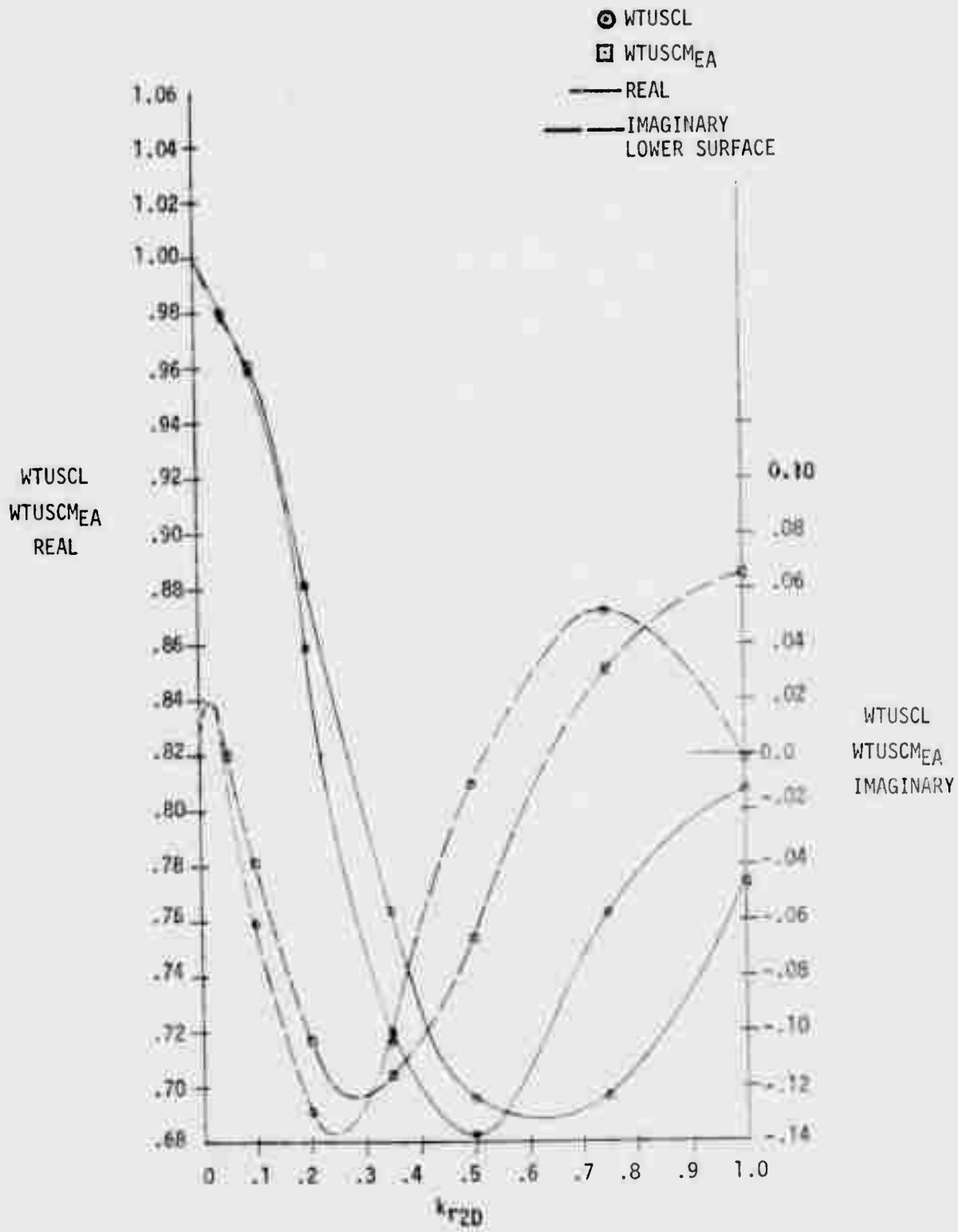


Figure 3.3-7 Unsteady Weight Factors for the TF-8A Wing
 $(y/(b/2) = 0.657, M_{3D} = 0.95, M_{2D} = 0.75)$

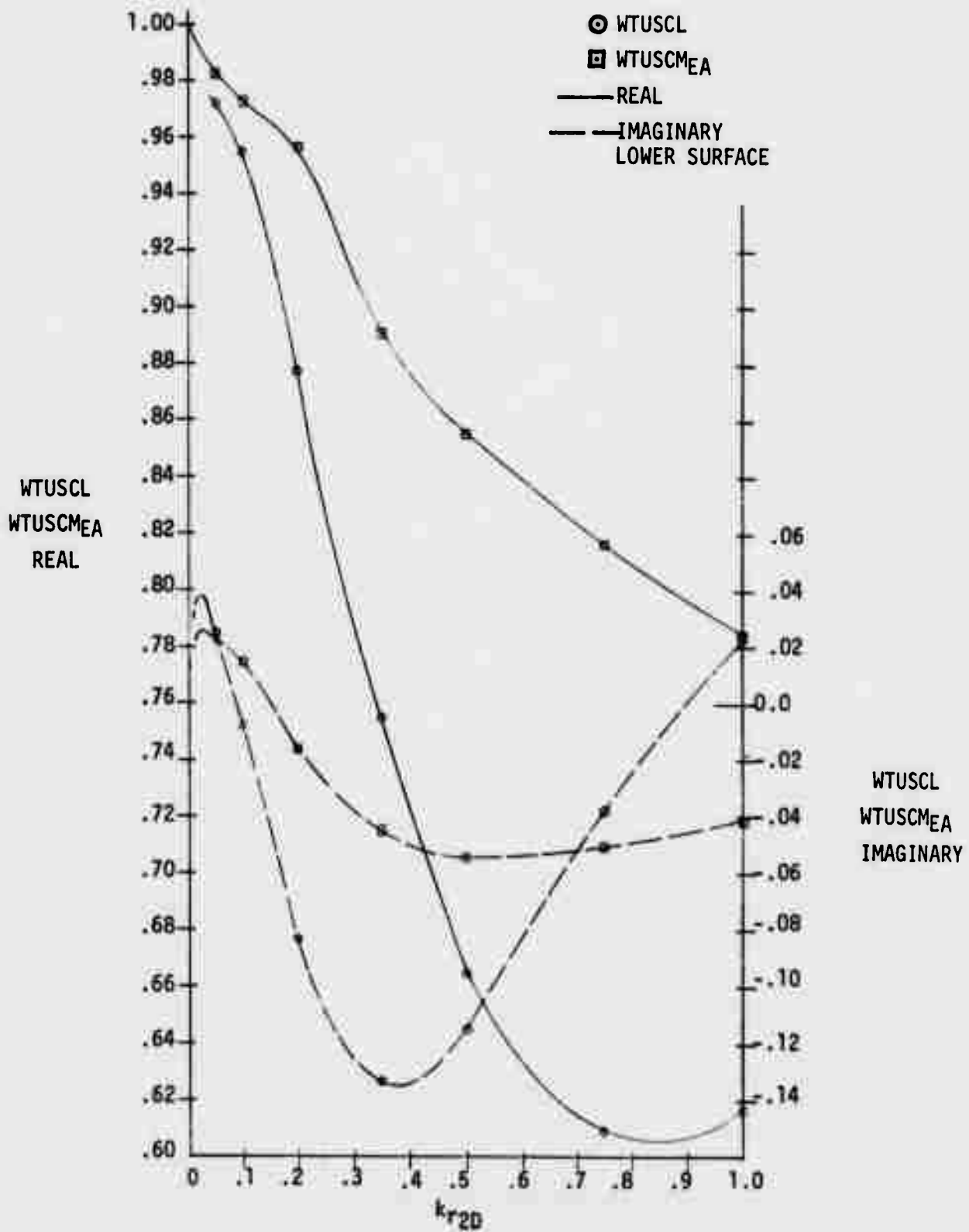


Figure 3.3-8 Unsteady Weight Factors for the TF-8A Wing
 $(y/(b/2) = 0.933, M_{3D} = 0.95, M_{2D} = 0.75)$

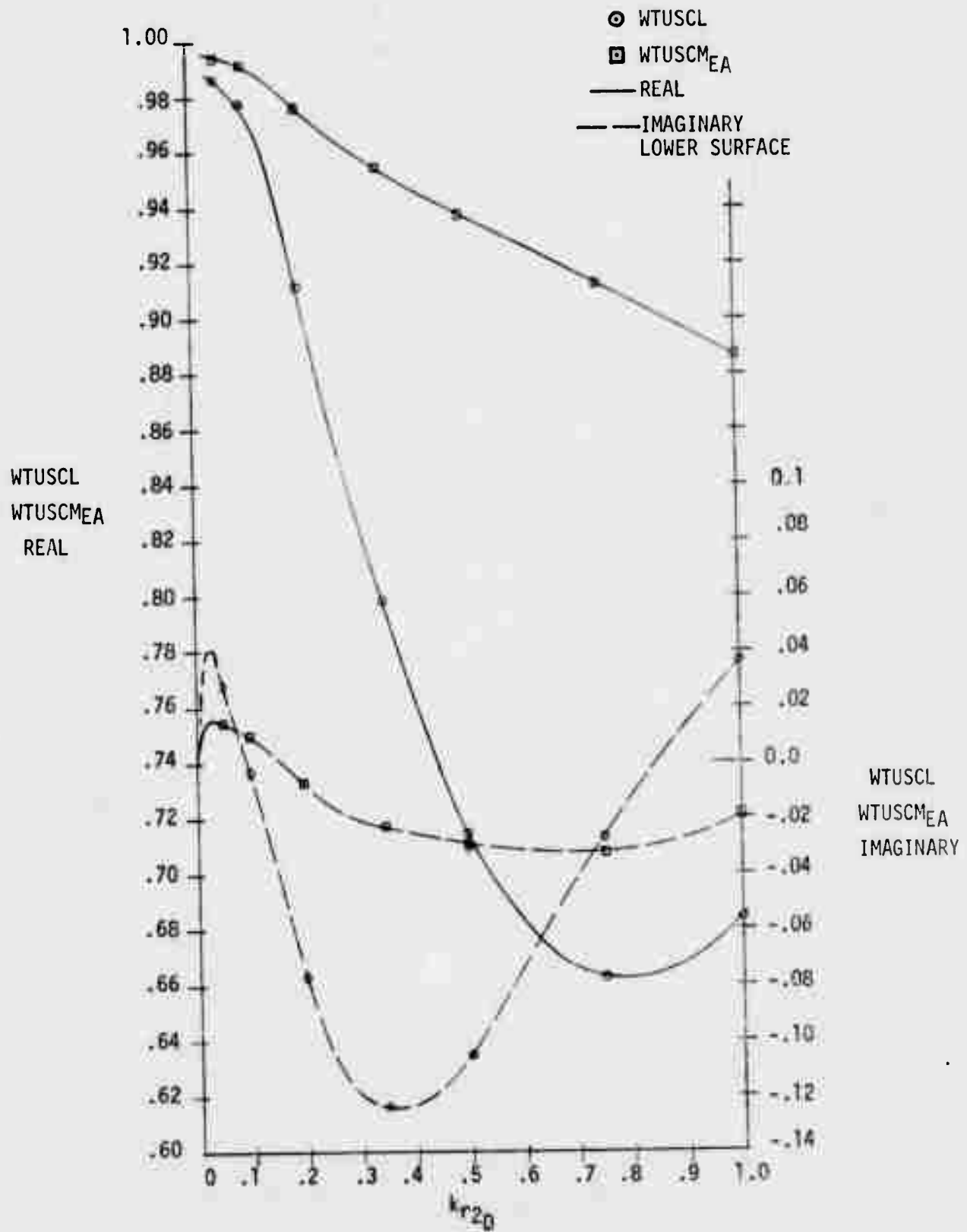


Figure 3.3-9 Unsteady Weight Factors for the TF-8A Wing
 $(y/(b/2) = 0.657, M_{3D} = 0.99, M_{2D} = 0.80)$.

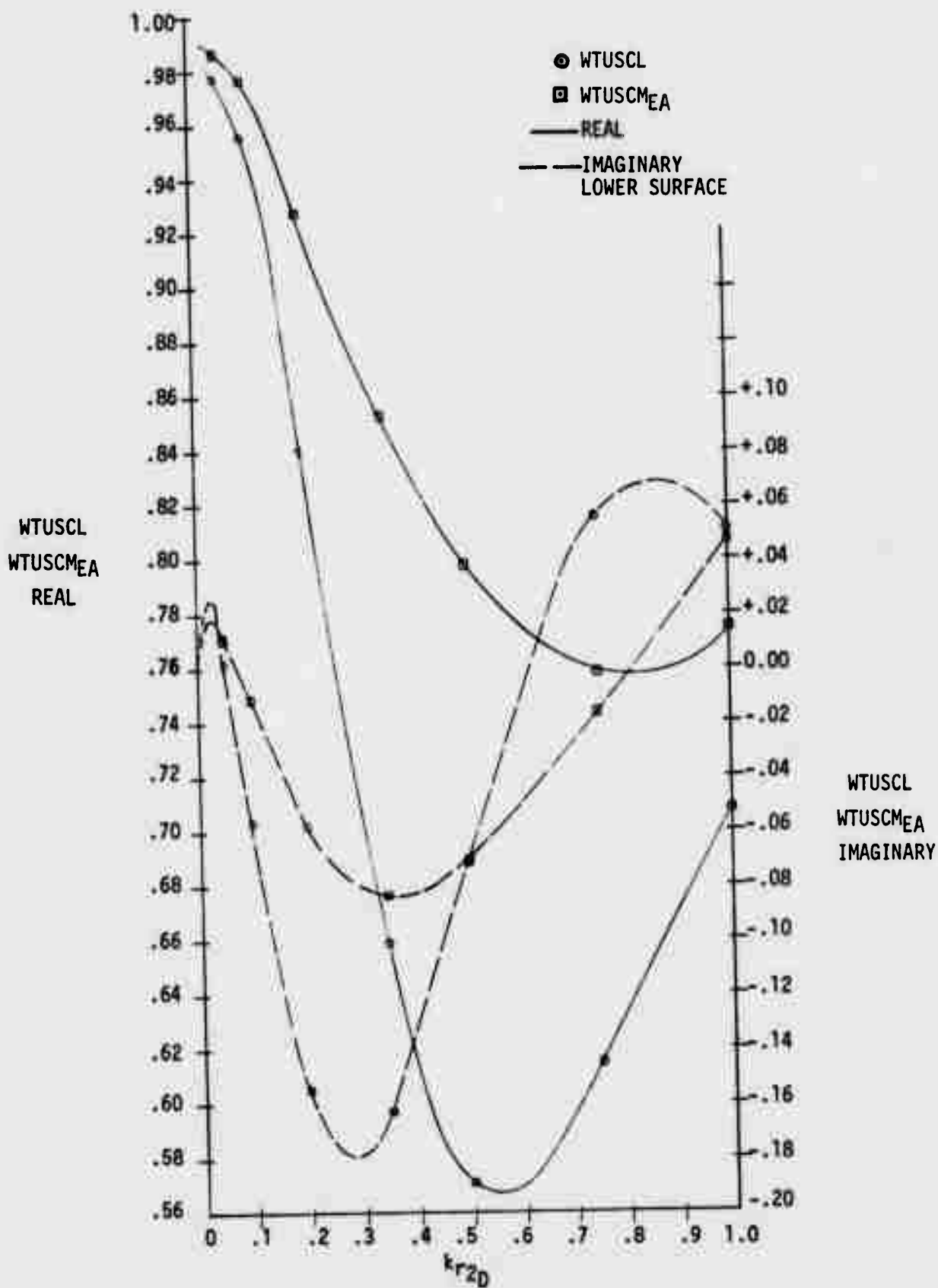


Figure 3.3-10 Unsteady Weight Factors for the TF-8A Wing ($y/(b/2) = 0.933$, $M_{3D} = 0.99$, $M_{2D} = 0.77$)

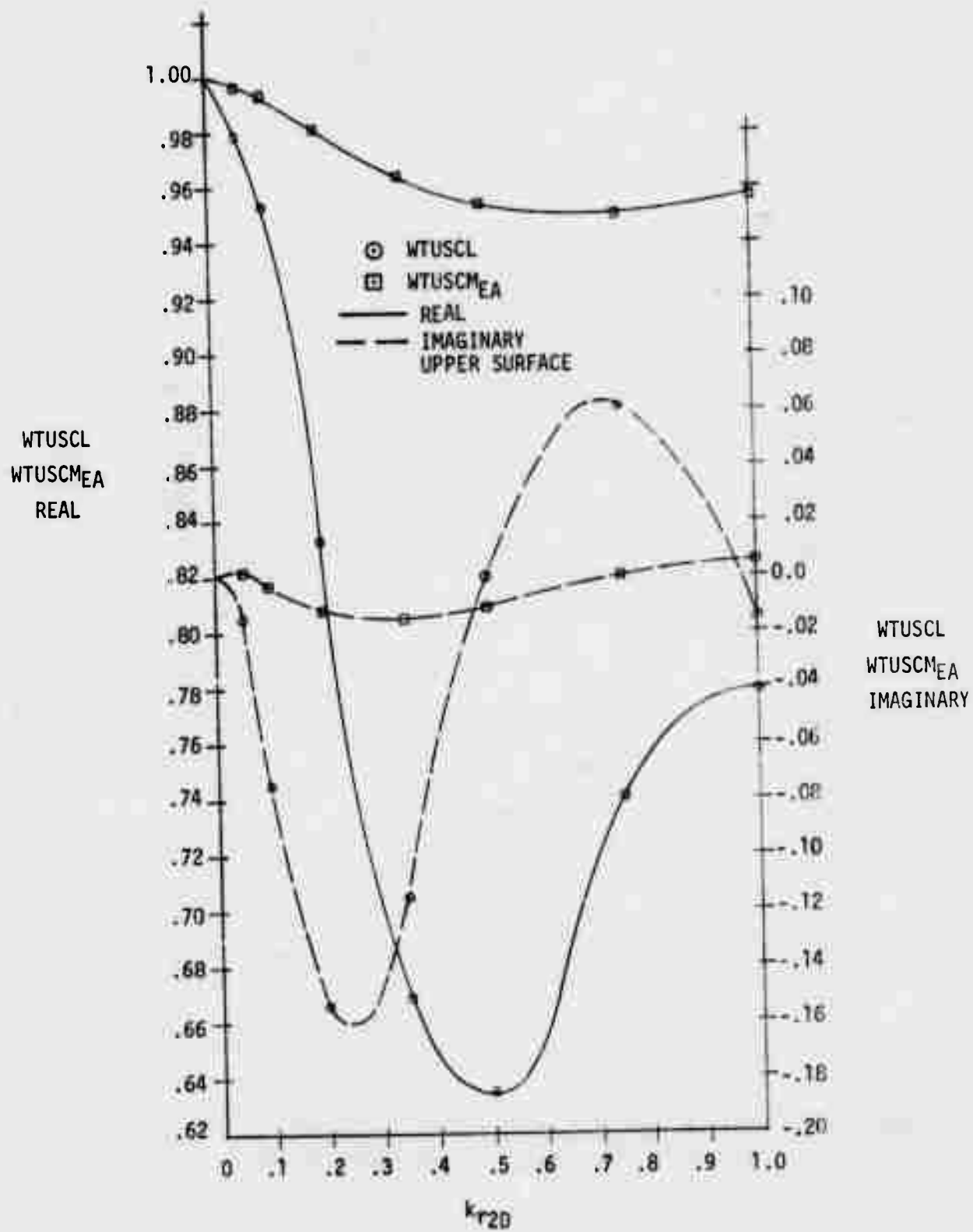


Figure 3.3-11 Unsteady Weight Factors for the YC-15II
 $(y/(b/2) = 0.16, M_{2D} = 0.759)$

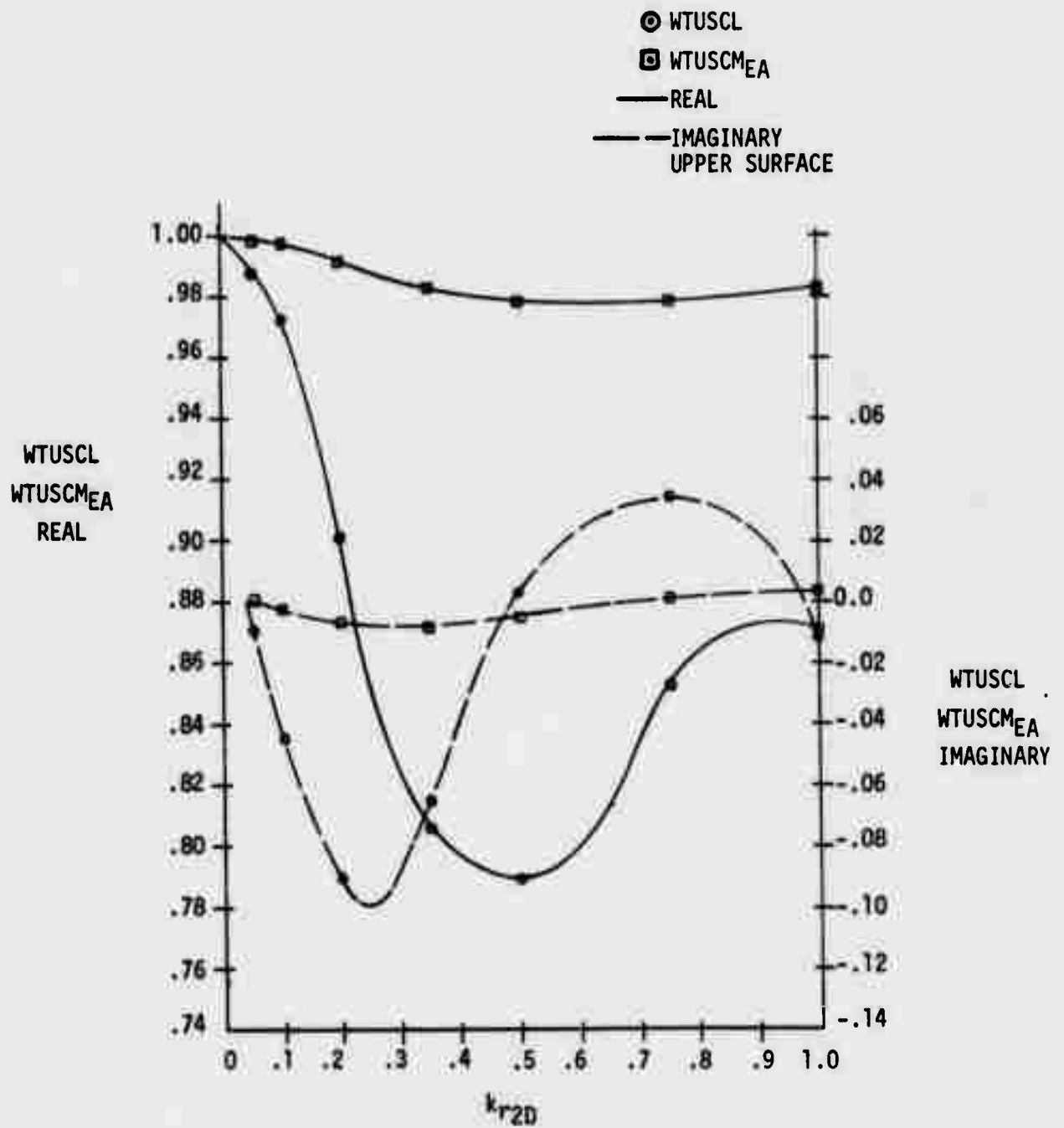


Figure 3.3-12 Unsteady Weight Factors for the YC-15II
 $(y/(b/2) = 0.42, M_{2D} = 0.759)$, Upper Surface

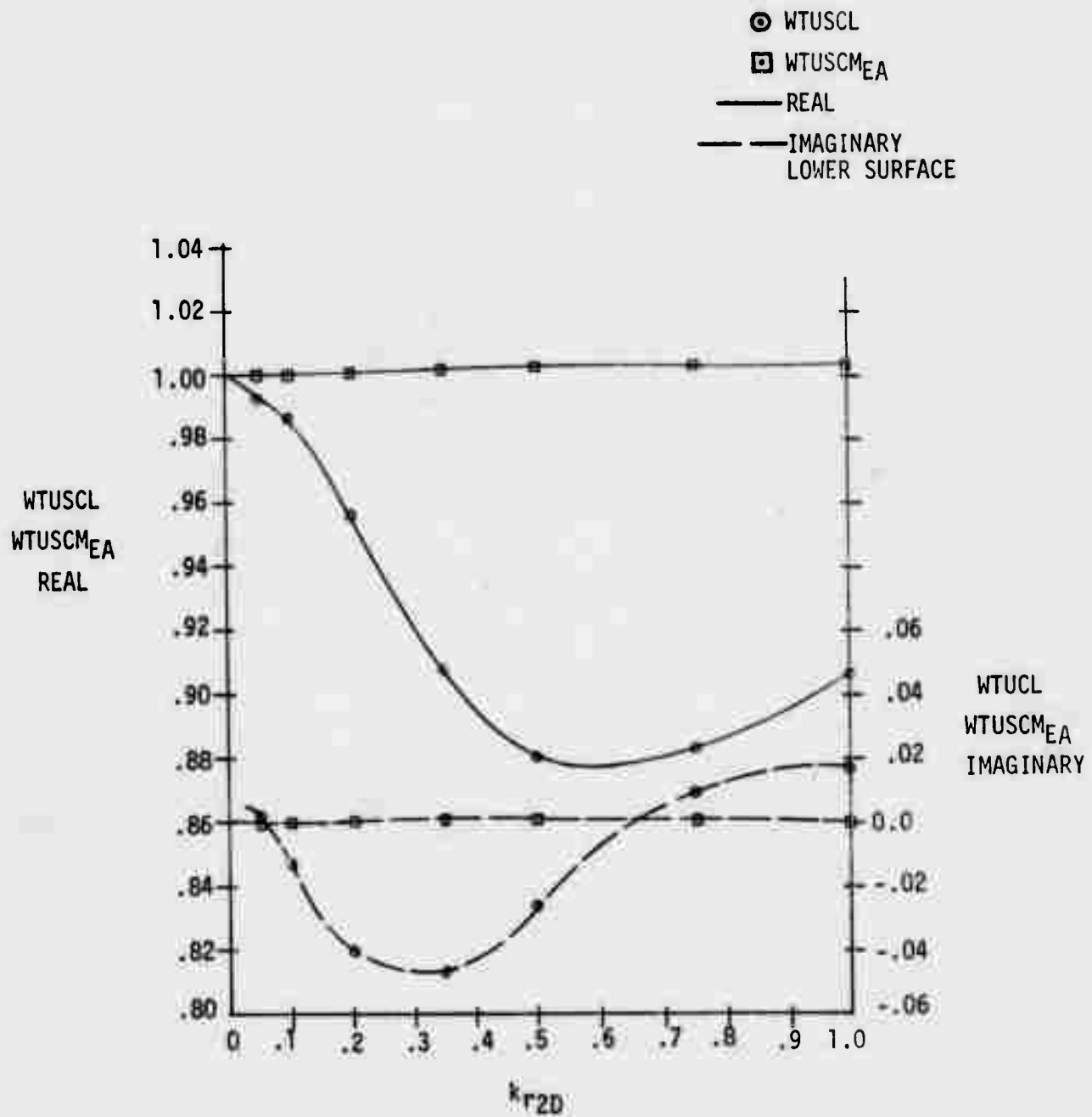


Figure 3.3-13 Unsteady Weight Factors for the YC-15II
 ($y/(b/2) = 0.42$, $M_{2D} = 0.759$), Lower Surface

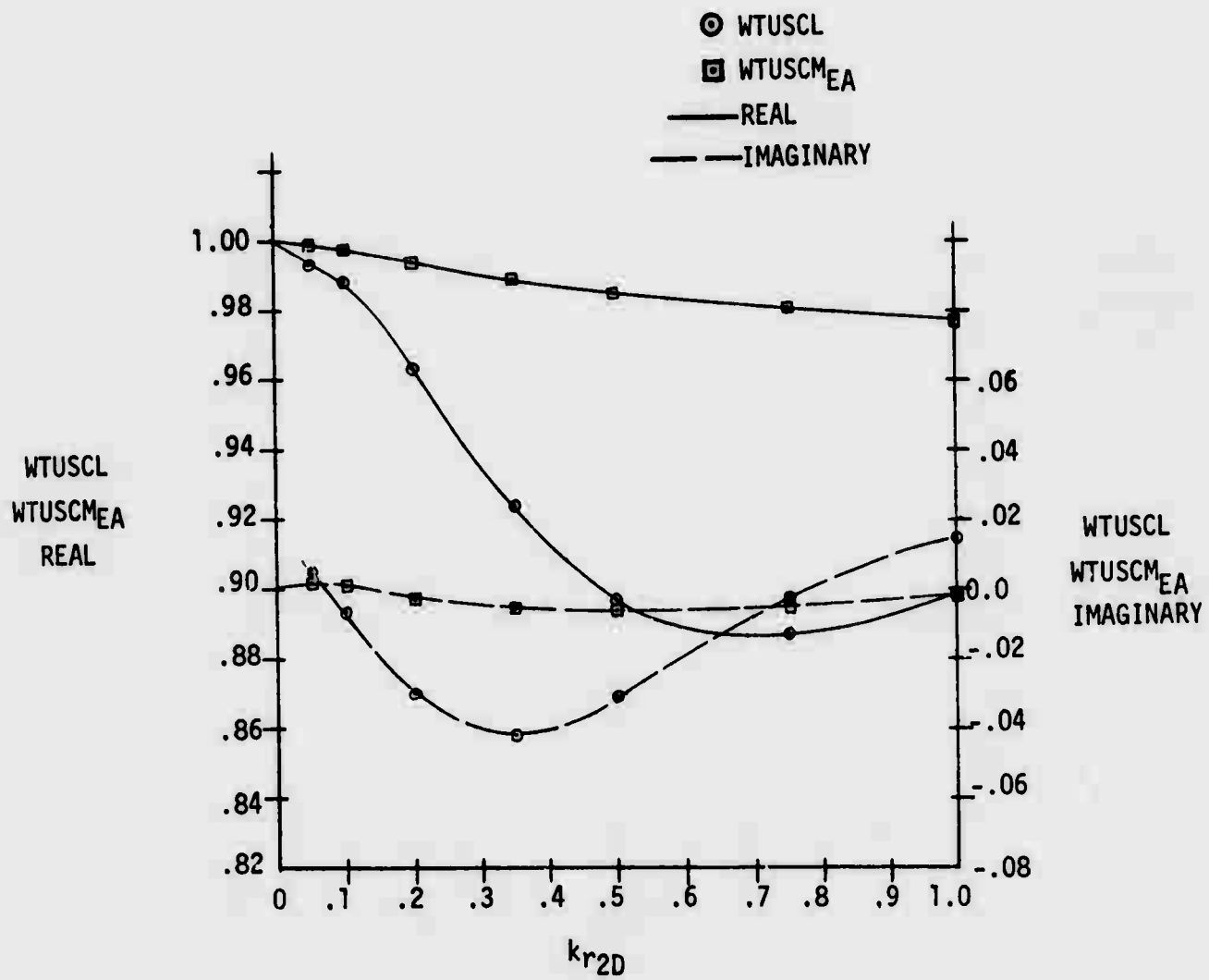


Figure 3.3-14 Unsteady Weight Factors for the YC-15II
 ($y/(b/2) = 0.85$, $M_{2D} = 0.761$)

3.4 RESULTS OF ANALYSIS - PHASE IV

The methods of Phases I - III were applied to the YC-15II aircraft.

3.4.1 YC-15II Basic Data

Reference 17 documents the YC-15II basic data.

3.4.2 YC-15II Static Aeroelastic Solutions

The methods of Section 2.3 were applied to generate the YC-15II wing static aeroelastic shape at the critical wing Mach Number, $M_\infty = 0.75$. Figure 3.4-1 shows the results for a typical payload/fuel configuration. As can be seen the unswept, relatively stiff wing undergoes quite small deflections even at this high dynamic pressure. The maximum magnitude of the wing tip angle-of-attack is about 2.5 degrees (minus).

3.4.3 Aerodynamic Data and Weighting Factors for the YC-15II Wing

The Doublet Lattice Method idealization is presented in Subsection 2.1. The resulting theoretical distribution of section lift coefficient slope and aerodynamic center are presented in Figure 3.4-4. The theoretical distributions are compared to those obtained by wind tunnel tests.

Figures 3.4-2 and 3 show that the lift and moment curve slopes are functions of the section angle-of-attack. Specifically, the angle-of-attack distribution required is one that is relative to the pressure model at zero rigid body angle-of-attack. The distribution of section angle-of-attack for the YC-15II aircraft consists of (1) the rigid body angle, $\alpha^{(a)}$, (2) the built-in twist, $\epsilon_j^{(a)}$, and (3) the elastic twist $\epsilon_e^{(a)}$ calculated at a given dynamic pressure corresponding to a flutter speed previously estimated. The superscript (a) refers to the aircraft. This curve is shown in Figure 3.4-1 of Section 3.4.2. The angle-of-attack distribution of the pressure model at zero rigid body angle-of-attack is just the pressure model built-in twist. This is also shown in Figure 3.4-1. The desired section angle-of-attack is then the difference between the aircraft and pressure model distributions, i.e.,

$$\Delta\alpha(p) = \alpha^{(a)} + \epsilon_j^{(a)} + \epsilon_e^{(a)} - \epsilon_j^{(p)} = \alpha^{(a)} + \epsilon_e^{(a)} \text{ since } \epsilon_j^{(a)} = \epsilon_j^{(p)}$$

This difference, $\Delta\alpha^{(p)}$, which is also plotted in Figure 3.4-1, is the final result. The points at which $c_{l\alpha}$ and $c_{m\alpha}$ are to be calculated are now known and are indicated in Figures 3.4-2 and -3. The resulting $c_{l\alpha}$ and $x_{a.c.}$ distributions are plotted in Figure 3.4-4. The theoretical distribution, also shown in the figure, was used as an aid in finding the experimental distribution because only three spanwise points were available.

The ratio of experimental to theoretical values of c_l and c_m at the various bay locations are the steady weight factors. Table 3.4-1 presents the results of these calculations for two estimates of $c_{m\alpha}$.

These two estimates come from the slopes on either side of the $\Delta\alpha^{(p)}$ points. These two values of $c_{m\alpha}$ are carried through the flutter calculation,

The unsteady weight factors are described in Subsection 3.3 and plots of them versus the reduced frequency k_{r2D} are given in Figures 3.3-11 through -14 for three spanwise stations. The data for these three spanwise stations are applied to all of the bays in a manner also shown in Subsection 3.3. The values of the two-dimensional reduced frequency, k_{r2D} , are related to the actual values, k_{r3D} , as shown in Subsection 2.4 as, $k_{r2D} = c/\bar{c} k_{r3D}$. The reduced frequencies considered for the generation of the AIC's are $k_{r3D} = 0, 0.1, 0.25, 0.5$. The tables of the unsteady weight factors used, WTUSCL and WTUSCME_{EA} (about elastic axis) are given in Table 3.4-2. There is a slight disparity between the tables and curves for the inboard half of the wing. Also, the shock motion on the lower surface at $y/(b/2) = 0.42$ was omitted, see Figure 3.3-13. The effects of this omission and disparity should be very small as far as flutter is concerned since the flutter speed changes due to the unsteady weight factors is itself small and due to the fact that only the inboard portion of the wing was affected.

3.4.4 YC-15II Flutter Analysis Results

Figure 3.4-2 shows the measured (high speed wind tunnel model) sectional lift curve coefficient versus angle-of-attack for three span stations. As can be seen, the statically deformed wing is still in the essentially linear range of the aerodynamics. Figure 3.4-4 shows a plot of sectional $c_{l\alpha}$ vs percent semispan using the approximately linear portion of the slopes from the previous figure (from between angles-of-attack of zero and -2.5 degrees). The AIC's were weighted to match Figure 3.4-4 for the "steady weighting" exercise. This is the same weighting that was used in the production YC-15II flutter analysis, which resulted in the previously reported minimum calculated flutter speed at $M_\infty = 0.76$. Flutter analysis results are discussed in detail in Reference 17. Thus, the static aeroelastic twist effects, which were ignored during the original YC-15II flutter analysis, are indeed negligible.

Table 3.4-2 shows the "unsteady correction" multiplicative weighting factors for the YC-15II wing. These were included in the YC-15II flutter analysis resulting in a flutter speed reduction of some 2-3 KEAS. Hence, the YC-15II results are similar to the TF-8A results in that the unsteady transonic corrections are virtually negligible in effect compared to the steady corrections. The steady corrections were of course very important on the YC-15II as they resulted in a calculated flutter speed equal to 89 percent of the flutter speed predicted by purely theoretical AIC's at $M_\infty = 0.76$. The two values of $c_{m\alpha}$ used had little influence since they are close to each other on the out-board wing. The final value of flutter speed was taken as the average of that obtained using the two values of $c_{m\alpha}$.

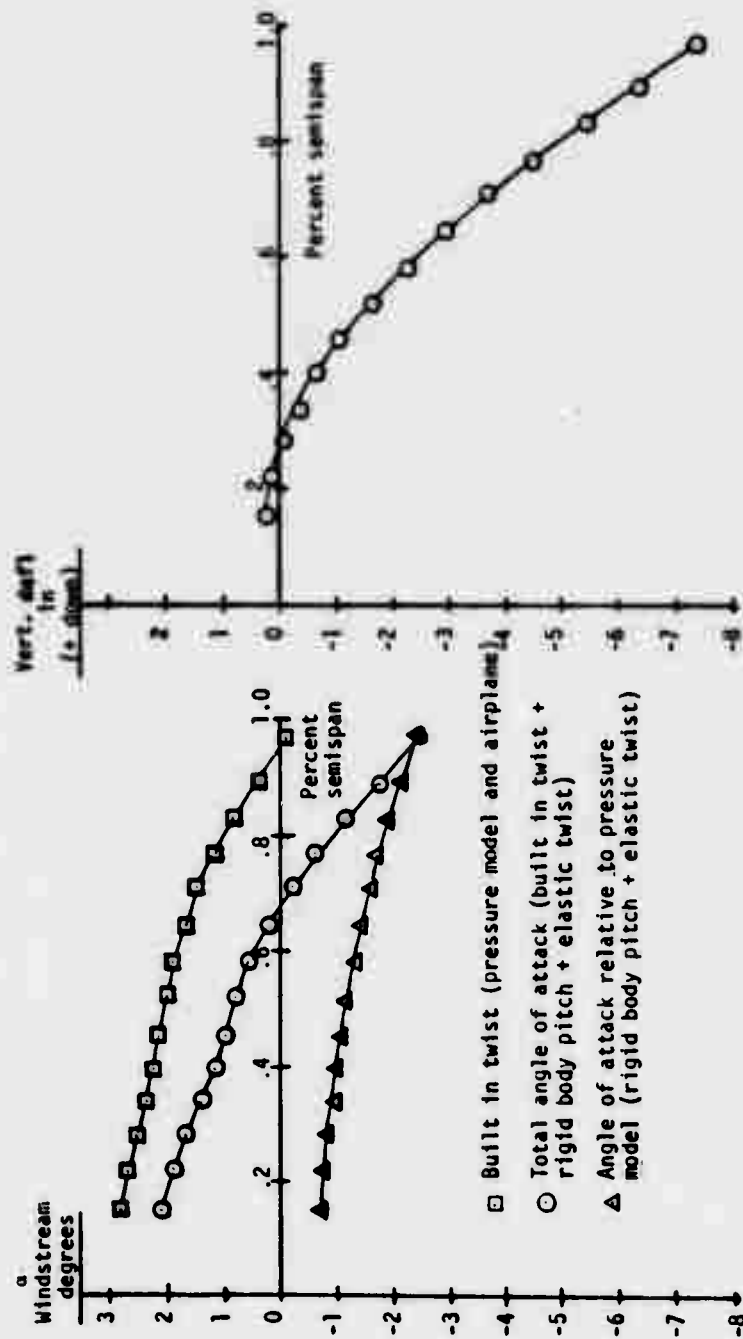


Figure 3.4-1 YC-15II Static Twist Distribution, $M_\infty = .76$

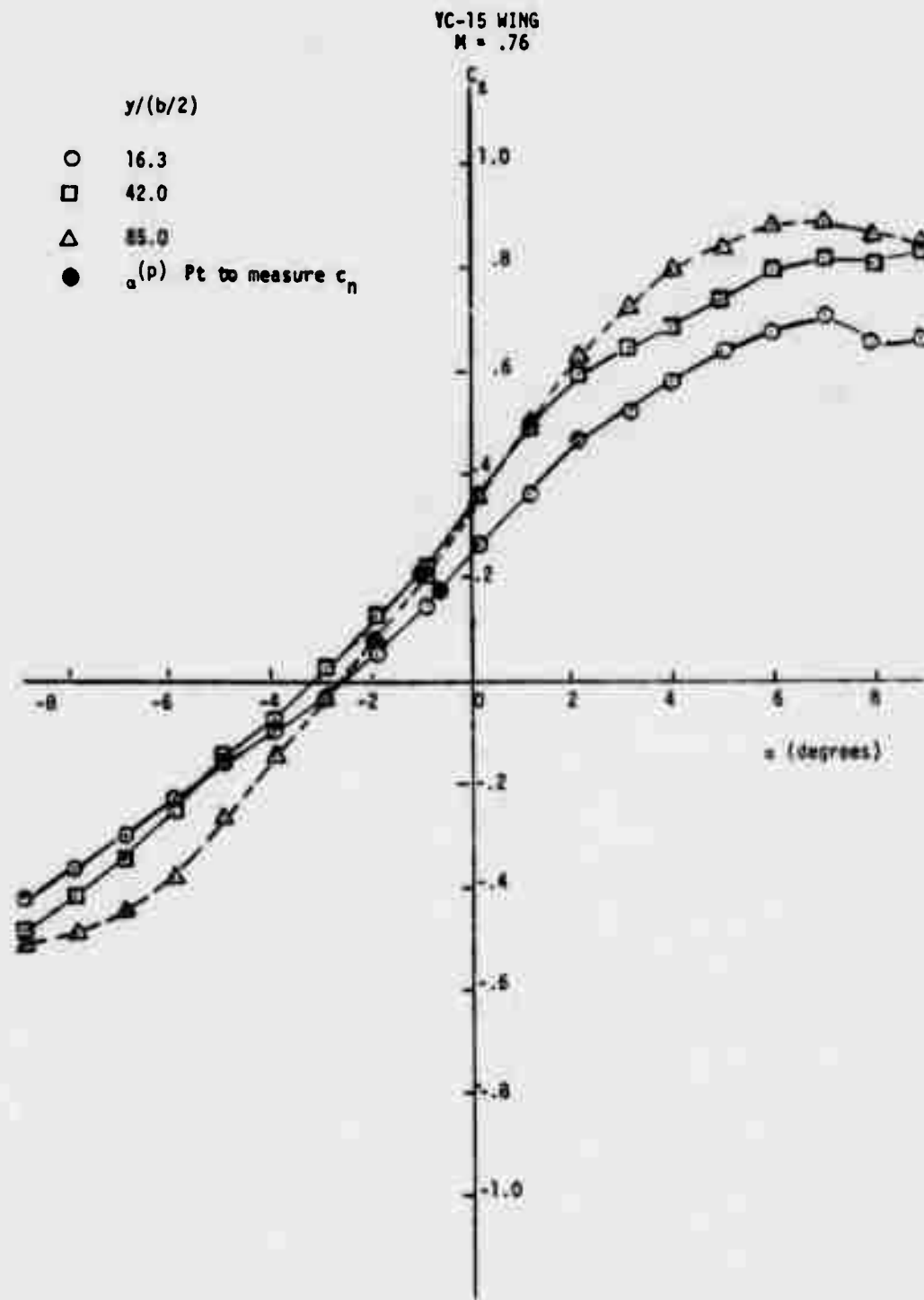


Figure 3.4-2 YC-15II c_l vs. α , $M_\infty = .76$

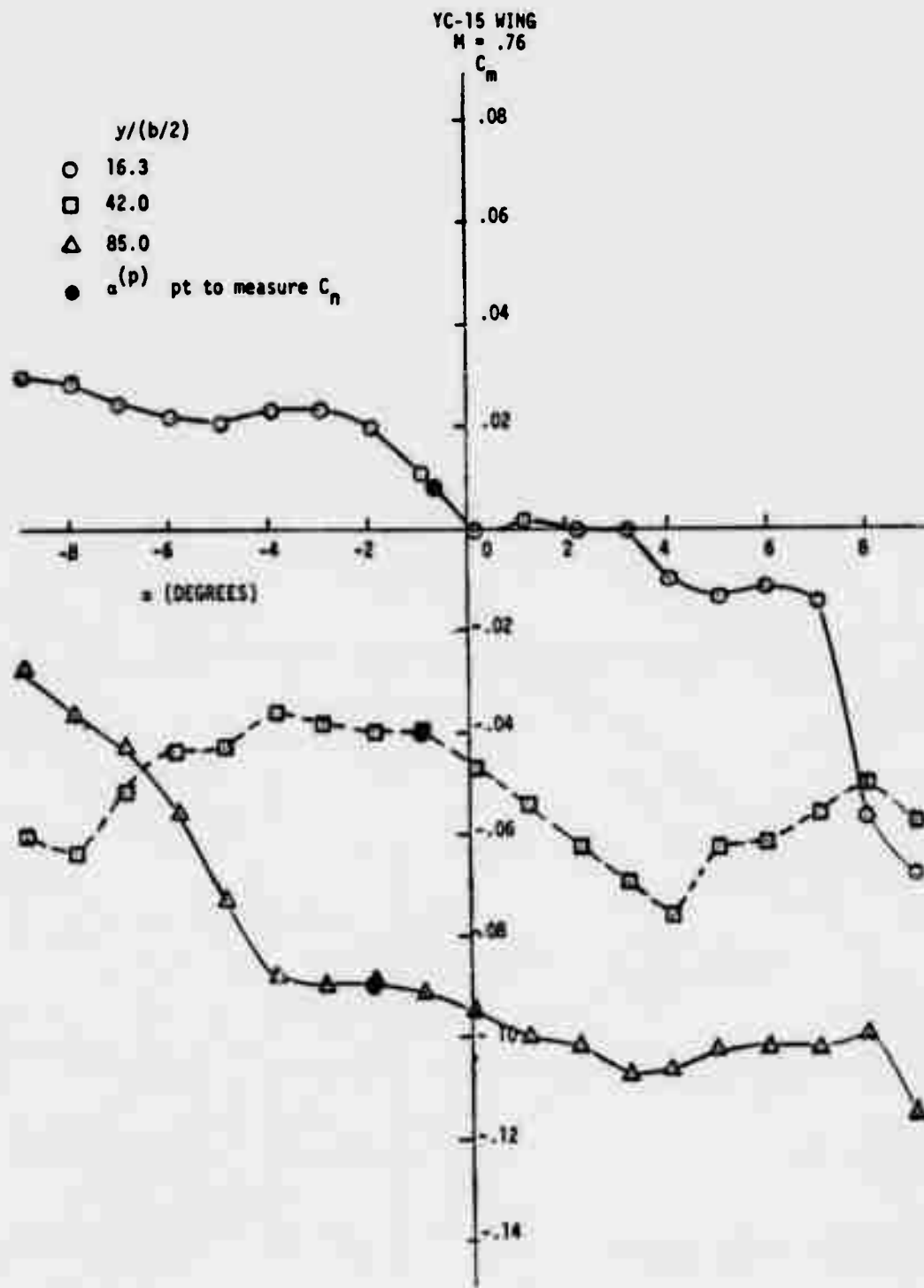


Figure 3.4-3 YC-15II C_m vs. α , $M_\infty = .76$

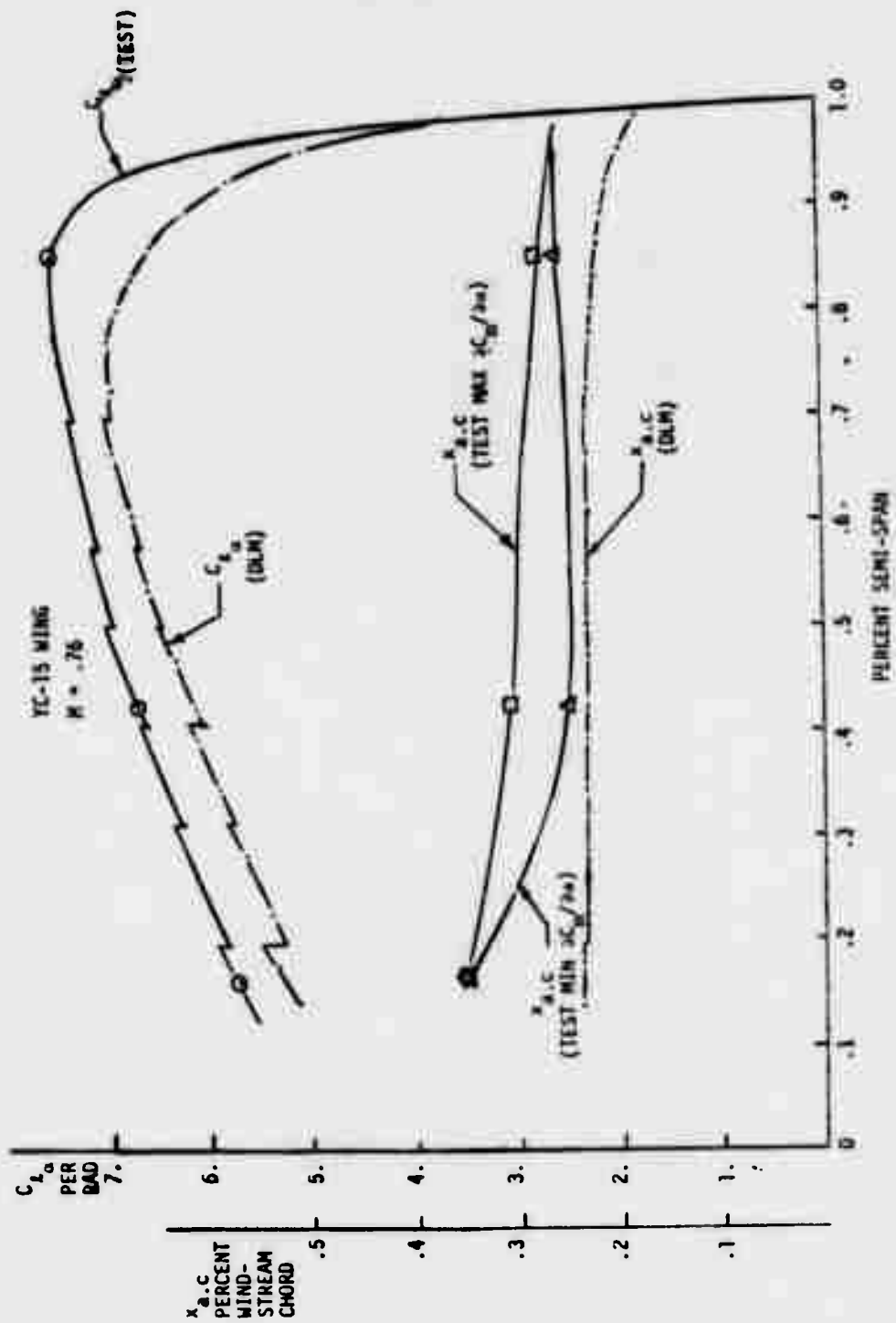


Figure 3.4-4 YC-15II $C_{L_{\alpha}}$, $x_{a.c.}$ vs. $y/(b/2)$

TABLE 3.4-1
 YC-15II Steady Weight Factors

$M_{\infty} = .76$
 (max $c_{m_{\alpha}}$)

<u>y/b/2</u>	<u>WTSCl</u>	<u>WTSCM</u>
.148	1.09434	.23618
.214	1.10185	.36447
.274	1.10035	.50098
.334	1.08813	.57113
.393	1.09421	.64771
.451	1.07981	.71515
.514	1.06818	.72542
.578	1.06074	.76112
.641	1.05491	.78418
.704	1.06475	.82415
.767	1.08538	.85471
.829	1.12782	.90167
.963	1.11765	.87788

$M_{\infty} = .76$
 (min $c_{m_{\alpha}}$)

.148	1.09434	.27415
.214	1.10185	.54004
.274	1.10035	.76158
.334	1.08813	.88133
.393	1.09421	.96664
.451	1.07981	.98728
.514	1.06818	.98121
.578	1.06074	.97858
.641	1.05491	.97690
.704	1.06475	.97725
.767	1.08538	.95956
.829	1.12782	.96335
.892	1.19167	.98948
.963	1.11765	.87788

TABLE 3.4-2

YC-15II Unsteady Weight Factors

$M_{\infty} = .759$

BAY NO. 20		$y/(b/2) = .167$			
k_{r2D}	WTUSCL		WTUSCME _{EA}		k_{r3D}
	REAL	IMAGINARY	REAL	IMAGINARY	
0	1	0	1	0	0
.184	.866	-.144	.983	-.011	.1
.459	.636	-.022	.955	-.013	.25
.918	.776	+.023	.954	+.004	.5

BAY NO. 21		$y/(b/2) = .226$			
k_{r2D}	WTUSCL		WTUSCME _{EA}		k_{r3D}
	REAL	IMAGINARY	REAL	IMAGINARY	
0	1	0	1	0	0
.175	.881	-.139	.984	-.010	.1
.437	.639	-.037	.957	-.013	.25
.875	.771	+.037	.953	+.004	.5

BAY NO. 22		$y/(b/2) = .284$			
k_{r2D}	WTUSCL		WTUSCME _{EA}		k_{r3D}
	REAL	IMAGINARY	REAL	IMAGINARY	
0	1	0	1	0	0
.167	.893	-.133	.985	-.010	.1
.417	.643	-.051	.958	-.014	.25
.833	.764	+.047	.952	+.002	.5

TABLE 3.4-2 (Cont'd)
 YC-15II Unsteady Weight Factors

$M_{\infty} = .759$

BAY NO. 23		$y/(b/2) = .344$			
k_{r2D}	WTUSCL		WTUSCMEA		k_{r3D}
	REAL	IMAGINARY	REAL	IMAGINARY	
0	1.	0	1.	0	0
.158	.903	-.128	.986	-.009	.1
.395	.650	-.069	.960	-.014	.25
.789	.753	+.056	.951	+.001	.5

BAY NO. 24		$y/(b/2) = .408$			
k_{r2D}	WTUSCL		WTUSCMEA		k_{r3D}
	REAL	IMAGINARY	REAL	IMAGINARY	
0	1.	0	1.	0	0
.149	.972	-.030	1.000	0.00	.1
.372	.902	-.045	1.002	+.001	.25
.743	.883	+.009	1.003	+.001	.5

BAY NO. 25		$y/(b/2) = .469$			
k_{r2D}	WTUSCL		WTUSCMEA		k_{r3D}
	REAL	IMAGINARY	REAL	IMAGINARY	
0	1.	0	1.	0	0
.140	.976	-.028	1.000	0.00	.1
.349	.907	-.046	1.002	.001	.25
.699	.881	+.005	1.003	.001	.5

TABLE 3.4-2 (Cont'd)
 YC-15II Unsteady Weight Factors
 $M_b = .759$

BAY NO. 26		$y/(b/2) = .537$			
k_{r2D}	WTUSCL		WTUSCMEA		k_{r3D}
	REAL	IMAGINARY	REAL	IMAGINARY	
0	1.	0	1.	0	0
.130	.979	-.025	1.000	0.00	.1
.325	.914	-.046	1.002	+.001	.25
.649	.879	0.00	1.003	+.001	.5

TABLE 3.4-2 (Cont'd)
 YC-15II Unsteady Weight Factors

$M_{\infty} = .761$

BAY NO. 27					$y/(b/2) = .604$
k_{r2D}	WTUSCL		WTUSCMEA		k_{r3D}
	REAL	IMAGINARY	REAL	IMAGINARY	
0	1	0	1	0	0
.120	.984	-.013	.996	+.001	.1
.300	.935	-.040	.990	-.004	.25
.600	.889	-.019	.983	-.006	.5

BAY NO. 28					$y/(b/2) = .664$
k_{r2D}	WTUSCL		WTUSCMEA		k_{r3D}
	REAL	IMAGINARY	REAL	IMAGINARY	
0	1	0	1	0	0
.111	.985	-.010	.997	+.001	.1
.278	.941	-.039	.991	-.004	.25
.556	.891	-.024	.984	-.006	.5

BAY NO. 29					$y/(b/2) = .725$
k_{r2D}	WTUSCL		WTUSCMEA		k_{r3D}
	REAL	IMAGINARY	REAL	IMAGINARY	
0	1	0	1	0	0
.102	.987	-.008	.997	+.001	.1
.256	.947	-.037	.992	-.004	.25
.512	.896	-.030	.985	-.006	.5

TABLE 3.4-2 (Cont'd)
 YC-15II Unsteady Weight Factors

$M_\infty = .761$

BAY NO. 30		$y/(b/2) = .785$			
k_{r2D}	WTUSCL		WTUSCMEA		k_{r3D}
	REAL	IMAGINARY	REAL	IMAGINARY	
0	1	0	1	0	0
.094	.988	-.006	.997	+.001	.1
.234	.953	-.034	.993	-.003	.25
.468	.901	-.035	.986	-.006	.5

BAY NO. 31		$y/(b/2) = .845$			
k_{r2D}	WTUSCL		WTUSCMEA		k_{r3D}
	REAL	IMAGINARY	REAL	IMAGINARY	
0	1	0	1	0	0
.085	.990	-.004	.998	+.001	.1
.212	.960	-.031	.994	-.002	.25
.424	.909	-.039	.987	-.006	.5

BAY NO. 32		$y/(b/2) = .906$			
k_{r2D}	WTUSCL		WTUSCMEA		k_{r3D}
	REAL	IMAGINARY	REAL	IMAGINARY	
0	1	0	1	0	0
.076	.991	-.001	.998	+.002	.1
.190	.967	-.028	.994	-.002	.25
.380	.917	-.041	.988	-.006	.5

TABLE 3.4-2 (Cont'd)
 YC-15II Unsteady Weight Factors

$M_o = .761$

BAY NO. 33		$y/(b/2) = .968$			
k_{r2D}	WTUSCL		WTUSCME _A		k_{r3D}
	REAL	IMAGINARY	REAL	IMAGINARY	
0	1	0	1	0	0
.067	.992	+.001	.998	+.002	.1
.168	.973	-.024	.995	-.001	.25
.335	.927	-.041	.989	-.005	.5

3.5 FLUTTER MODEL TEST PLAN

A flutter model test is presented to support the analyses in determining the effects of some of the critical parameters on flutter of supercritical wings. A brief flutter analysis of the proposed flutter model was done to verify that the desired flutter speed range could be achieved with a reasonable stiffness distribution.

3.5.1 Description of Model

Design and build a cantilevered wing flutter model representing a typical STOL transport wing. The model is to be tested in the NASA Langley Transonic Dynamics Tunnel. The model will have the following features:

1. Interchangeable airfoil segments.
 - a. Supercritical shape
 - b. Conventional shape
2. Variable angle of attack at the wing root.
3. Variable wing twist distribution.
4. Instrumented to provide spanwise internal load distribution.
5. Removable engine weights.

The model will be a single spar wing with twelve balsa segments representing the airfoil shape(s). Two dummy engines representing the important mass properties will be mounted to the wing using rigid pylons to eliminate tuning effects of the engines. These dummy engines will also be removed so as to gather data for a higher frequency flutter case. The spar will be instrumented with a series of strain gages along the span to measure bending in two directions as well as torsion. Figure 3.5-1 shows the general arrangement of the model.

The variations in angle of attack of the wing will be attainable by using either the tunnel floor turntable or the wide wall mounting fixture in the NASA Langley 16 ft TDT.

The variations of wing twist distribution will be made by shimming between the wing segments and the spar.

3.5.2 Wind Tunnel Test

The wind tunnel facility anticipated for testing the cantilevered wing is the NASA Langley 16 ft TDT which uses Freon for a test medium. Normal testing method of changing Mach No. with total pressure constant will be used. Tunnel speeds will be increased until flutter onset is obtained or some predetermined maximum is reached due to tunnel operating limit or model applicability.

3.5.3 Model Configurations

The two basic configurations will be with dummy engines and without dummy engines. The three major parameters for each configuration will be the airfoil shape, wing root angle of attack, and wing twist distribution.

3.5.4 Wind Tunnel Test Data

The model test data for any configuration will consist of the following:

1. Zero speed vibration modes and damping.
2. Wind tunnel parameters.
3. Flutter speed and frequency
4. Wing spanwise internal load distribution.
5. Wing aeroelastic deformation if measureable with optical devices.

CANTILEVERED WING FLUTTER MODEL
FOR NASA LANGLEY 16 FT. TDT

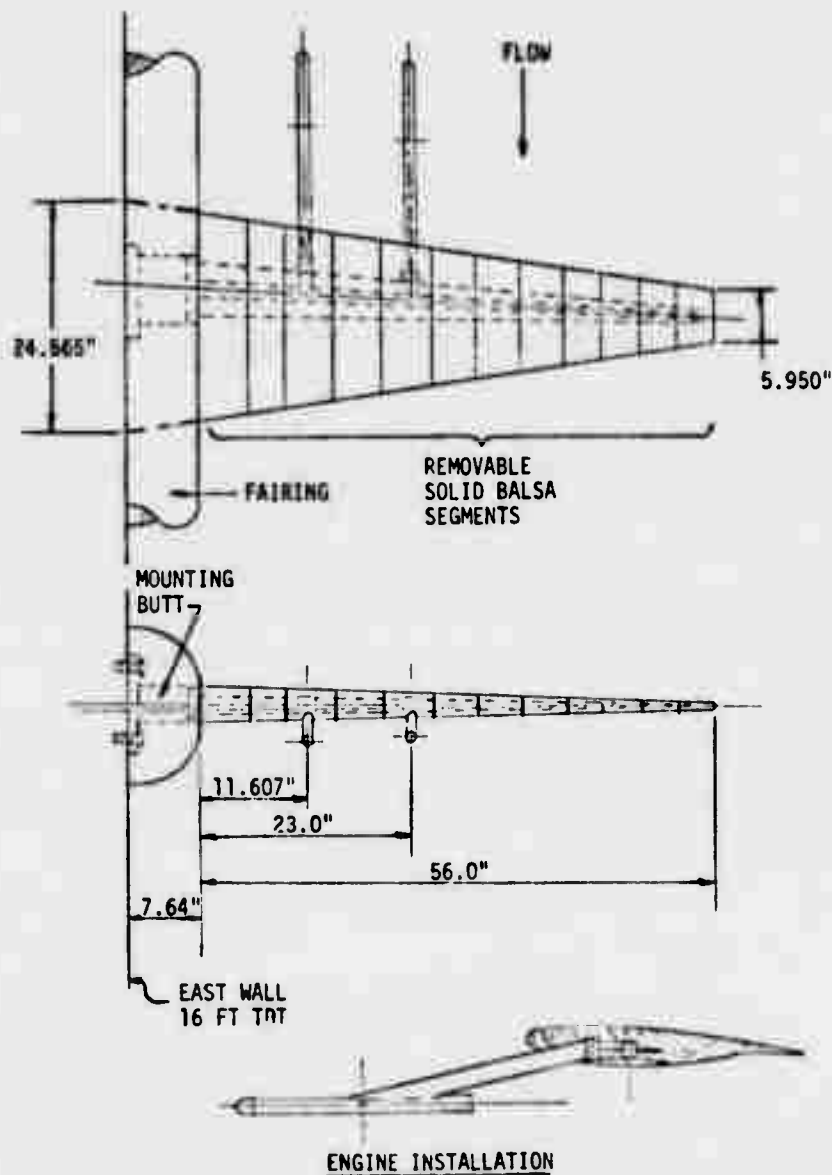


Figure 3.5-1 Proposed Cantilevered Wing Flutter Model

SECTION IV CONCLUSIONS

4.1 CONCLUSIONS RELATED TO THE FLUTTER ANALYSIS

1. The theoretical subsonic method seriously underestimates the relevant steady aerodynamic data (lift curve slopes and aerodynamic center distribution) at the critical Mach number for a wing with "supercritical" airfoil sections. This is in contrast to recent results for subsonic transport designs with conventional airfoils where the theory has been in good agreement at the critical Mach number (and overestimated the derivatives at low Mach numbers). For example, the YC-15II wing steady lift curve slope at the critical Mach number (0.76) was 17 percent higher than predicted by the Doublet Lattice Method, while for the TF-8A the wing C_L test data was approximately double the Doublet Lattice prediction (at $M = 0.99$). Figure 4.1-1 below summarizes the general trends for conventional and supercritical airfoils of recent experience.

2. The sectional lift curve slopes for a supercritical airfoil possess an inherently nonlinear character over the pre-stall range. However, it appears that the pre-stall range can be approximated by two slopes; a small slope over a small angle of attack around zero, and a steeper slope at higher angles of attack (but still before viscous effects are seen). Figure 4.1-2 shows typical data. This characteristic "dual slope" phenomenon has shown up consistently on three different supercritical designs and is more pronounced the more "supercritical" the design. The steeper slope is a transonic effect, and cannot be predicted by subsonic lattice methods.

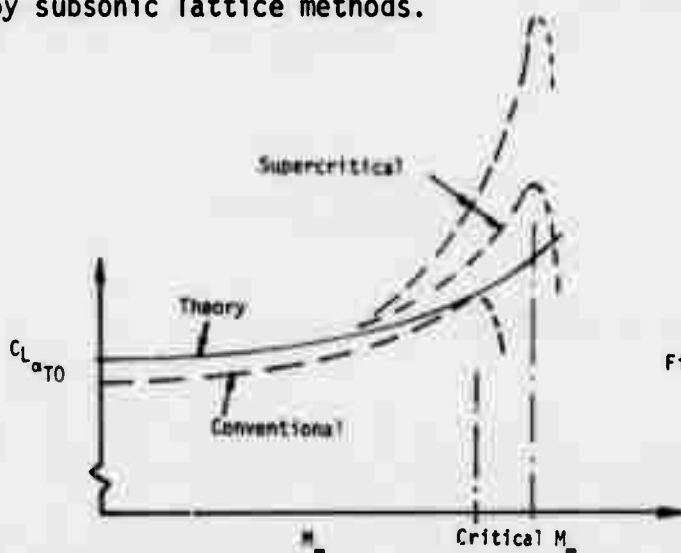


Figure 4.1-1 Comparison of Theoretical Aircraft Lift Curve Slope with Experimental Data for Conventional and Supercritical Wings.

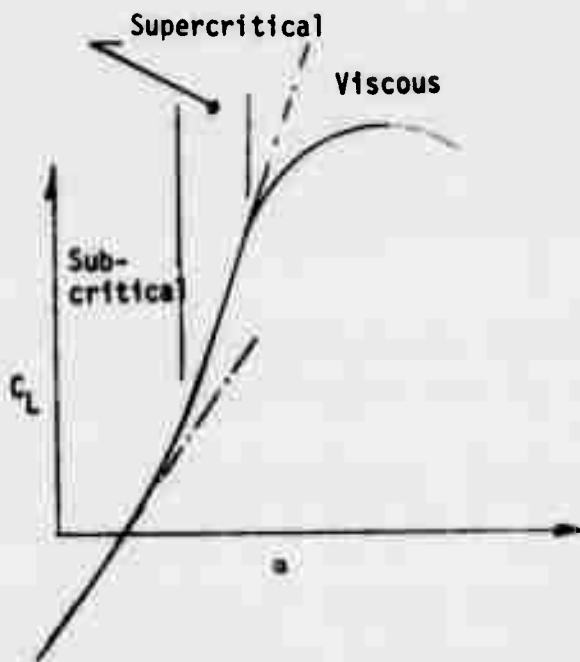


Figure 4.1-2 Nonlinear Character of The Transonic Lift-Curve

3. The "steady corrections", wherein the AIC for $k_r = 0$ was weighted to match the steady test aerodynamic data, and then these weight factors applied to all reduced frequencies, resulted in flutter speeds which were in reasonable agreement with measured flutter speeds. Analysis using purely theoretical AIC's resulted in significantly non-conservative flutter speed predictions, for both the TF-8A flutter model and the YC-15II prototype.

4. The unsteady transonic weight factors had a negligible effect on the flutter speed of both the TF-8A and YC-15II. This may be because the reduced frequency at flutter is relatively low for both aircraft; $k_{rF} = 0.15$ for the TF-8A flutter model and $k_{rF} = 0.125$ for the YC-15II. Since the direction of the effect was detrimental on both aircraft (even though negligible in magnitude), these techniques should be applied to a configuration with high flutter frequencies before any final conclusions are made.

5. For advance design configurations which use supercritical wings and for which no high speed aerodynamic data exists, application of the steady three-dimensional Jameson method (reference 11) or similar method should be made. This method has been implemented into a production status at Douglas and much correlation work done. Steady and unsteady corrections could then be based on this predicted transonic aerodynamic data in lieu of test data.

6. The effect of static twist on flutter is obviously significant since the final section angle of attack may end up in the smaller slope range, the steeper slope range, or even the viscous effect range. It seems clear, however, that the certification analysis must use the steepest slopes regardless of the 1g cruise twist distribution, so as to cover the maneuvering range of the aircraft, and other unknowns.

Accounting of static twist effects are obviously very important in a correlation analysis of a flutter model with a relatively flexible wing.

7. Incorrect Reynolds number simulation in pressure models and flutter models may lead to errors:

- a) If the high speed flutter model does not fly at a high enough Reynolds number the wing tips may stall prematurely resulting in non-conservative flutter speeds predictions or in buffet or stall flutter condition which are not realistic.
- b) If the pressure model and flutter model were flown at different Reynolds numbers (as in the TF-8A case) they will experience tip stall at different angles of attack, confusing the correlation analysis.
- c) Pressure models may not be "rigid". The TF-8A pressure model was significantly flexible. In the future, the flexibility of the pressure model should be calculated, and if significant, should either be re-designed out of the model or else the pressure data from the test should be properly modified. See Section 2.1 for a discussion of this problem and its ramifications.

8. Sufficient section lift and moment data should be available vs α to unambiguously define the curves so that accurate c_l and c_m data can be obtained at the proper twist angles. This is especially true of the moment data since it is so highly nonlinear. In practice, this means getting the data request to the relevant Aerodynamics personnel in a timely manner, since left to their own, they may not get the required pressure data at a fine enough α grid or at large enough negative angles of attack.

4.2 CONCLUSIONS RELATED TO TRANSONIC AERODYNAMICS

1. Three significant transonic effects on lifting surface aerodynamics are:

- a) Nonuniform flow fields modify the basic aerodynamics such that lifting surface elements can propagate their effects upstream through a supersonic zone. This seems to be very important for supercritical airfoils operating at their design (shock free) condition.
- b) The shock wave generates a flow field through the action of a vorticity distribution on the shock wave itself. The effects on the wing surface are especially large just aft of the shock wave.
- c) The movement of the shock wave with angle of attack creates a very large effect on the perturbation pressures and loads. This load is proportional to the shock movement times the pressure jump across the steady shock wave. For supercritical airfoils the shock movement versus angle of attack can be very large. For airfoils with shock waves this effect is probably the largest of the three effects.

2. Transonic load effects are highly dependent on the shock wave location because much of the loading is concentrated in the immediate vicinity of the shock wave. For supercritical wing sections the location of the shock wave is a sensitive function of angle of attack, boundary layer thickness, wind tunnel wall corrections etc. Thus the static aeroelastic twist distribution is very important to the flutter analysis.

SECTION V RECOMMENDATIONS

5.1 RECOMMENDATIONS: FLUTTER ASPECTS

This study confirms that supercritical wings exhibit significantly lower flutter speeds than a conventional wing of equal size and rigidity. It was demonstrated, furthermore, that these lower flutter speeds could be accurately predicted if the Doublet Lattice unsteady aerodynamics were properly weighted by the relevant test data.

The major problem encountered during this study was that the relevant aerodynamic data required to unambiguously define the important sectional lift and moment slopes were not available. A secondary complication was that the static aeroelastic twist of the TF-8A flutter model was extreme. Finally, both examples treated in this study exhibited flutter at low reduced frequencies; thus, the importance of the unsteady weight factors in general was not established.

Future studies should be planned so as to address these problems. In Section 3.5 a proposed cantilevered wing flutter model is discussed that should prove to be a useful tool to further evaluate transonic effects on flutter speed. The static twist distribution of this proposed wing will be more representative of current transport aircraft than was the TF-8A flutter model. The wing geometry is the YC-15 prototype, for which adequate definition of aerodynamic data exists. Furthermore, analysis has shown that removal of the engine weights will change the flutter frequency from a low value to a high value of k_{γ} , thus allowing a better evaluation of the unsteady weighting factors as a function of reduced frequency.

5.2 RECOMMENDATIONS FOR THE DEVELOPMENT OF TRANSONIC LIFTING SURFACE THEORY

It has been demonstrated that, for the configurations considered in this report, the steady flow transonic effects are the most important. The basic reason for this is the fact that these configurations fluttered at relatively low reduced frequencies where unsteady effects are small.

However, it is still important to obtain the unsteady effects for two reasons: 1) increased accuracy of flutter results, and 2) application to aircraft configurations that flutter at moderate to high reduced frequencies. The unsteady effects may not be important enough to develop and employ very expensive finite element methods but it does seem worth the effort to develop less expensive methods. An example of such a method is the transonic lifting surface method discussed in Subsection 2.5 of this report. Specific recommendations to further the development of this method are outlined as follows:

1. Extend the method so that the amplitude, and phase, of the unsteady shock wave motion can be determined.
2. Refine the shock motion interference flow representation. Replace the point vortex with the proper distribution along the shock.
3. Investigate the reason for poor correlation of the method in the supersonic zone and make appropriate corrections. Pertinent to this investigation is the evaluation of the impact of the various simplifying assumptions made during the analysis.
4. Extend the method to the three-dimensional case.

Transonic lifting surface theories, such as the one described in this report, and the one in References 10 and 12, require reliable production sub- and supersonic linear methods. Subsonic methods are well developed and very reliable. The same can not be said of supersonic methods, however. Thus it is recommended that supersonic methods be brought up to the same status as the subsonic ones.

APPENDIX A

SOURCE IN A NON-UNIFORM FLOW FIELD

Lifting surface theory is based on the assumption that the disturbances to the fluid caused by a surface moving through it are small. These small disturbances travel through the fluid at the speed of sound as acoustic waves. Classic lifting surface theory makes the further assumption that the medium through which the waves travel is uniform. It is felt that one of the major transonic effects arises due to the fact that acoustic waves encounter non-uniform flow fields. This is especially important for forward traveling waves in a near sonic stream. Thus, an expression is derived here for an acoustic source in a non-uniform flow field.

To start the derivation, consider a moving coordinate system xyz such that the flow at infinity is uniform and equal to U_∞ in the x direction. Consider an acoustic pulse emitted at ξ_0, η_0, ζ_0 at time $t = \tau$. If the flow is uniform near the source, then the pulse will be circular. If, in general, the flow is slightly perturbed then the wave will be deformed (see Figure A-1).

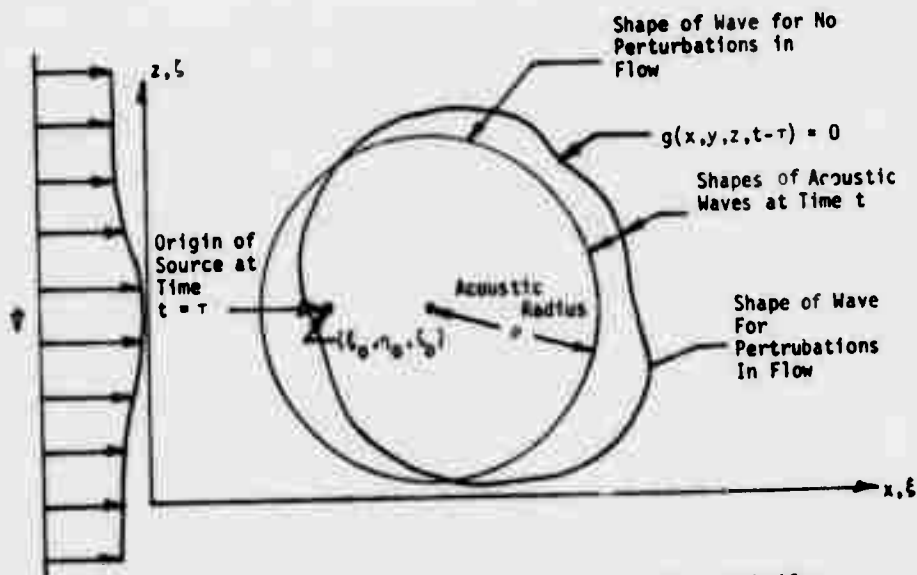


Figure A-1 Acoustic Source Pulse Surface at Time $t - \tau$ For the Uniform And Nonuniform Flow Cases

For no perturbations in the flow field, the potential is:

$$\tilde{\phi} = \frac{1}{4\pi} \sigma_0 \frac{\delta((t - \tau) - \rho/a)}{\rho}$$

where $\rho^2 = (x - \xi_0 - U_\infty (t - \tau))^2 + r^2 \equiv$ acoustic radius

$$r^2 = (y - \eta_0)^2 + (z - \zeta_0)^2$$

where a is the speed of sound and where σ_0 is the source strength. When perturbations exist, in the flow the potential is

$$\tilde{\phi} = \frac{1}{4\pi} \frac{\sigma_0 \delta(g/\bar{a})}{\bar{\rho}}$$

where $g(x, y, z, t - \tau) = 0$ is the equation of the surface of the wave, $\bar{\rho}$ is an equivalent acoustic radius such that $\sigma/\bar{\rho}$ is the wave front strength, and \bar{a} is the effective wave speed.

Now as a point on the lifting surface moves along, it creates sources of varying strength at various points along its flight path at various time (see Figure 2.5-1).

To find the total potential field due to this string of pulses simply sum or integrate them along the path as a function of time. The potential at time t is a sum of all the sources generated previously along the flight path.

$$\phi(t) = \int_0^t \tilde{\phi}(\tau) d\tau = \int_0^t \frac{\sigma(\tau)}{4\pi} \frac{\delta(t - \tau - \rho/a)}{\rho} d\tau$$

The results for perturbed flow is:

$$\phi = \int_0^t \frac{\sigma(\tau)}{4\pi} \frac{\delta(g/\bar{a})}{\bar{\rho}} d\tau$$

A theorem for the proper integration of delta functions, δ , is:

$$\int_a^b f(\tau) \delta \{g(\tau)\} d\tau = \sum_{i=1}^N \frac{f(\tau_i)}{\left| \frac{\partial g}{\partial \tau}(\tau_i) \right|}$$

where τ_i are the real roots of $g(\tau) = 0$ lying between $\tau = a$ and b and where N is the number of these roots.

The term $\partial g / \partial \tau$ is the negative of $\partial g / \partial t$ which can be shown to be

$$\frac{\partial g / \partial t}{\bar{a}} = \frac{\vec{V}_T \cdot \vec{n}}{\bar{a}}$$

where $\vec{V}_T \cdot \vec{n}$ is the velocity of the wave normal to itself. The velocity \vec{V}_T is composed of the acoustic propagation velocity, $\bar{a}\vec{n}$, and the fluid velocity \vec{V} . Thus,

$$\frac{\vec{V}_T \cdot \vec{n}}{\bar{a}} = 1 + \frac{\vec{V} \cdot \vec{n}}{\bar{a}}$$

and thus,

$$\phi = \sum_{i=1}^N \frac{\sigma(\tau_i)}{4\pi \rho(\tau_i) \left| 1 + \frac{\vec{V} \cdot \vec{n}}{\bar{a}} \right|} \quad (\text{A-1})$$

where $g(\tau_i) = 0 \quad i = 1, N$ (A-2)

The solution for $g(\tau_i) = 0 \quad i = 1, \dots, N$ amounts to finding the τ_i values for all of the waves that pass over point (x, y, z) . Figure 2.5-16 (b) presents a uniform flow supersonic case. For a point lying within the Mach cone (x_1, z_1) two waves are felt. For points lying outside the Mach cone (x_2, z_2) no waves are felt. In the uniform flow subsonic case only one wave passes a point (see Figure 2.5-16(a)). In mixed non-uniform transonic flow, the problem is complicated as figure 2.5-16(c),(d) shows. In particular Figure 2.5-16(d) shows

that point (x_1, z_1) has three waves passing over it while (x_2, z_2) has one wave passing over it even though it lies outside the Mach cone.

For uniform flow:

$$\bar{\rho}(\tau_i) = \rho(\tau_i) = a(t - \tau_i)$$

$$\vec{V} = \vec{i} U_\infty$$

$$\vec{n} \cdot \vec{i} = [x - \xi_0 - U_\infty (t - \tau_i)] / \rho(\tau_i)$$

$$g(\tau_i) = 0 = t - \tau_i - \rho(\tau_i) / a$$

$$\text{then } \bar{\rho} \left| 1 + \frac{\vec{V} \cdot \vec{n}}{a} \right| = \left| \rho + M_\infty (x - \xi_0) - U_\infty (t - \tau_i) M_\infty \right|$$

and τ_i are found solving $g(\tau_i) = 0$.

$$a^2 (t - \tau_i)^2 = \rho^2 = (x - \xi_0 - U_\infty (t - \tau_i))^2 + r^2$$

or solving for $a(t - \tau_i)$ gives:

$$a(t - \tau_i) = \pm \left\{ \frac{1}{\beta^2} [M_\infty (x - \xi_0) \pm R] \right\}$$

$$\text{where } R^2 = (x - \xi_0)^2 + \beta^2 r^2$$

Now, acoustic waves generated in the future, $(t - \tau_i) < 0$ have no effect at time t , thus,

$$(t - \tau_i) \geq 0$$

For supersonic flow ($M_\infty > 1$) both roots ($\pm R$) are admissible since $M_\infty (x - \xi_0) \geq R$. Also, for supersonic flow $(x - \xi_0) \geq 0$ since waves do not travel up stream. Finally, since β^2 is negative the negative sign outside of the braces must be used.

$$a(t - \tau_i) = \left. \begin{cases} \frac{1}{-\beta^2} [M_\infty(x - \xi_0) + R] & i = 1 \\ \frac{1}{-\beta^2} [M_\infty(x - \xi_0) - R] & i = 2 \end{cases} \right\} \text{Supersonic flow}$$

For the subsonic case $M_\infty < 1$, $M_\infty(x - \xi_0) \leq R$ and $\beta^2 \geq 0$. There are two solutions which fit the condition $(t - \tau_i) \geq 0$ but only one makes sense physically, i.e.,

$$a(t - \tau_i) = \frac{1}{\beta^2} [-M_\infty(x - \xi_0) + R] \quad i = 1 \quad \text{Subsonic flow}$$

Knowing the roots allows us to move on to find the expression for the potential as follows:

Using the equation, $\bar{\rho} = a(t - \tau_i)$ in the expression for $\bar{\rho} \left| 1 + \frac{\vec{V} \cdot \vec{n}}{a} \right|$ gives

$$\bar{\rho} \left| 1 + \frac{\vec{V} \cdot \vec{n}}{a} \right| = \left| \rho + M_\infty(x - \xi_0) - U_\infty(t - \tau_i)M_\infty \right| =$$

$$\left| (t - \tau_i) a \beta^2 + M_\infty(x - \xi_0) \right|$$

Using the expression for the roots gives:

$$\bar{\rho} \left| 1 + \frac{\vec{V} \cdot \vec{n}}{a} \right| = \left| (t - \tau_i) a \beta^2 + M_\infty(x - \xi_0) \right| = R$$

Thus, for uniform flow the expression for the potential becomes

$$\phi = \frac{\sigma \left\{ t + \frac{1}{a\beta^2} (M_\infty(x - \xi_0) + R) \right\} + \sigma \left\{ t + \frac{1}{a\beta^2} (M_\infty(x - \xi_0) - R) \right\}}{4\pi R} \quad \text{Supersonic source}$$

$$\phi = \frac{\sigma \left\{ t + \frac{1}{a\beta^2} (M_\infty(x - \xi_0) - R) \right\}}{4\pi R} \quad \text{Subsonic source}$$

These are the classic expressions for a source in a uniform flow. The evaluation of the potential ϕ for the case of non-uniform flow is dependent on the ability to numerically calculate acoustic waves propagating in a non-uniform stream. Such an acoustic wave generator can be used to determine the local normal vector \vec{n} , acoustic radius $\bar{\rho}$, and intercept time τ_i of a wave passing over the receiving point (x,y,z) that originated at the sending point (ξ_0, η_0, ζ_0) . Whether the flow is uniform or non-uniform, the acoustic wave expands at the speed of sound. The wave strength along the wave front diminishes with increased time as the wave expands. Because of non-uniform flow conditions, the wave distorts from the circular form and changes in strength along the periphery of the wave. One way to express this fact is to say that the wave dilation $\bar{\rho}$ is expressed in terms of the uniform flow acoustic wave radius ρ and a correction factor f .

$$\bar{\rho} = \rho f = a(t - \tau) f$$

The term $\rho = a(t - \tau)$ gives the increase in radius with time while f accounts for the wave strength distortion along the wave front. The expression for ϕ then becomes:

$$\phi = \sum_{i=1}^N \frac{\sigma(\tau_i)}{4\pi \rho(\tau_i) f \left| 1 + \frac{\vec{V} \cdot \vec{n}}{\bar{a}} \right|} \quad (\text{A-3})$$

where

$$g(\tau_i) = 0 \quad i = 1, N \quad (\text{A-4})$$

APPENDIX B

FLOW FIELD CALCULATIONS USING THE TWO-DIMENSIONAL, STEADY, TRANSONIC JAMESON PROCEDURE

The two-dimensional Jameson procedure transforms the space around the airfoil into a rectangle, one unit high and two units wide. This rectangle is divided up into a grid of points. The modified differential equation is solved for by finite-difference procedures in this rectangular space. The solution produces a value of potential at each point in the rectangular plane. The procedure in finding the velocity at a particular point in physical space is to:

1. Find the location of the point of interest in the transformed space.
2. Find the derivative of ϕ in this space at the point of interest.
3. Find the velocity transformation to be applied to the differentials of ϕ to produce the velocity vector in the physical plane.

The following equations and sketches describe the process of transforming from the physical to the computational plane.

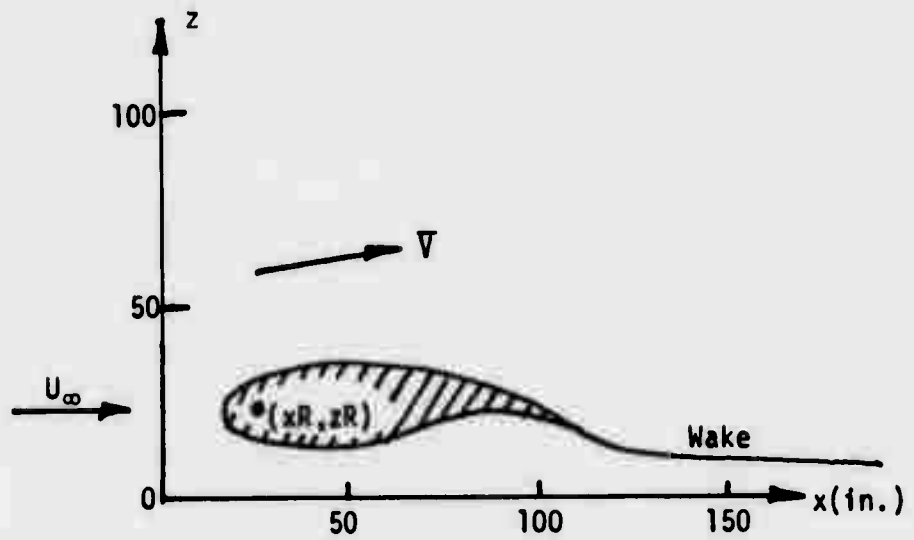


Figure B-1 Physical Plane

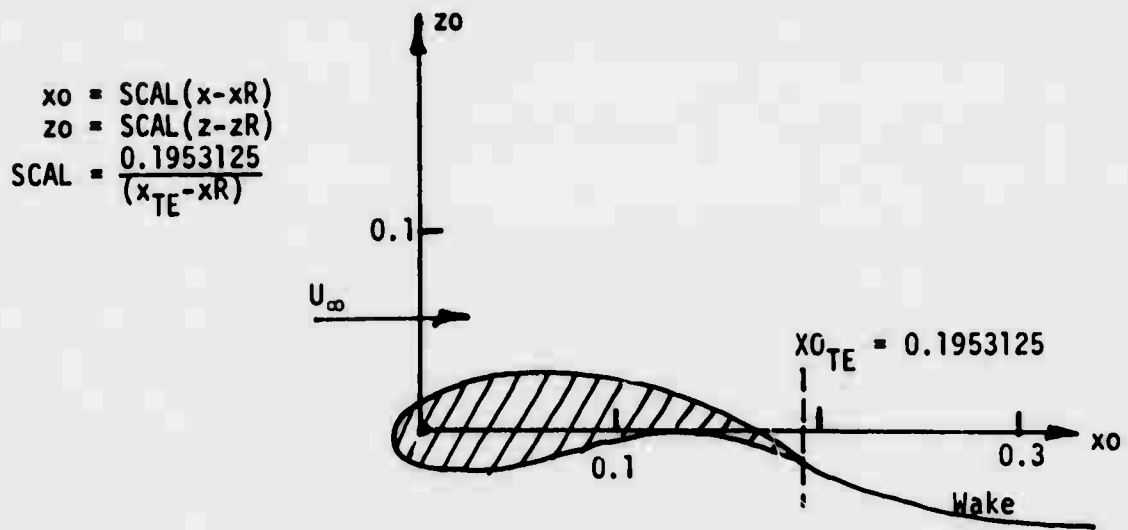


Figure B-2 Scaled and Shifted Plane

$$x_p = \rho \cos \theta, \quad \rho = \sqrt{2} (x_0^2 + z_0^2)^{1/4}$$

$$z_p = \rho \sin \theta, \quad \theta = \frac{1}{2} \text{Atan}(z_0/x_0)$$

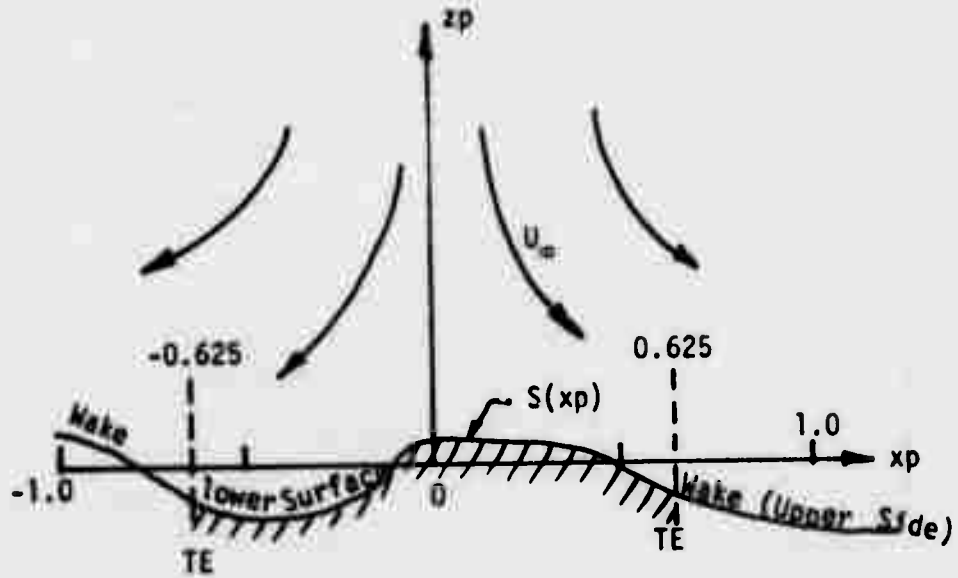


Figure B-3 Unwrapped Plane.

$$\bar{x}_p = x_p$$

$$\bar{z}_p = z_p - S(x_p)$$

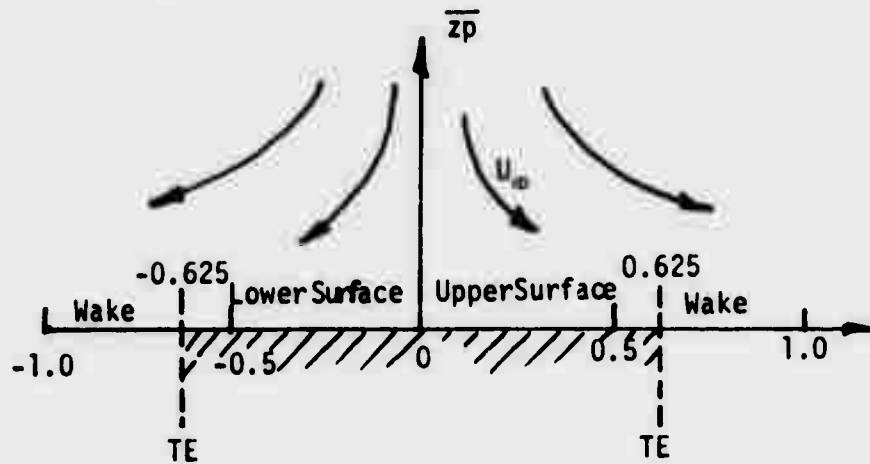


Figure B-4 Vertical Shear Plane

$$z_c = \bar{z}_p / \sqrt{\frac{1}{4} + \bar{z}_p^2}$$

$$x_c = \begin{cases} A & \text{if } |\bar{x}_p| \leq 0.625 \\ B & \text{if } |\bar{x}_p| > 0.625 \end{cases}$$

$$A = \bar{x}_p$$

$$B = 0.625 \delta + C$$

$$C = \bar{x}_p - 0.625 \delta$$

$$D = \frac{\sqrt{1 + D^2}}{0.375}$$

$$\delta = \text{sign}(\bar{x}_p)$$

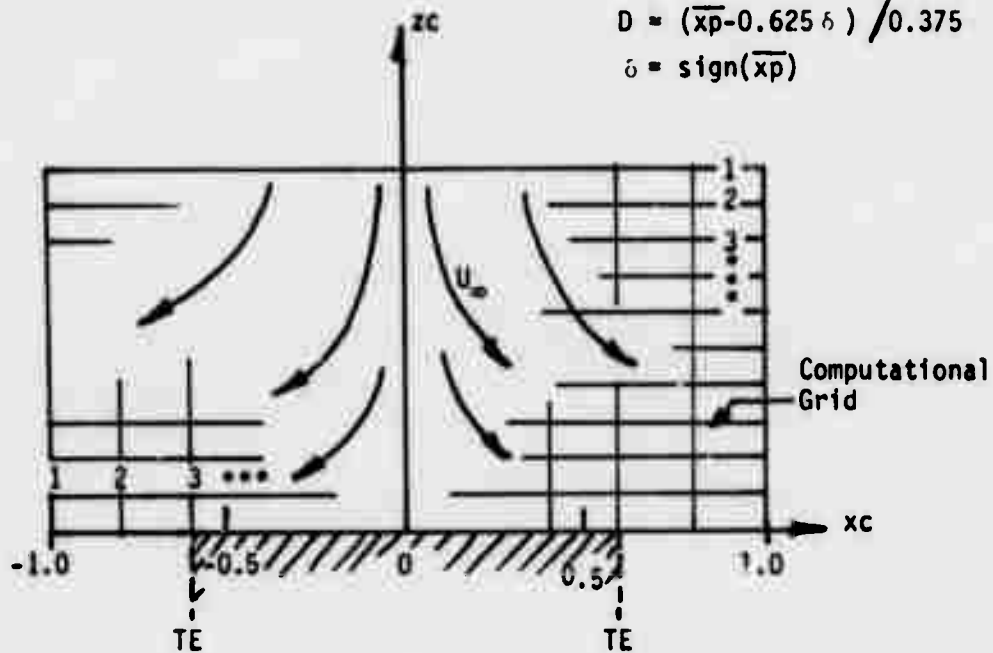


Figure B-5 Computational Plane

Once the desired points are transformed into the computational plane the desired derivatives $\partial\phi/\partial z_c$ can be numerically obtained from the tabulated values of ϕ vs. z_c and x_c . The following procedure is required to transform these derivatives in the computational plane into velocity components, V_x V_z in the physical plane.

$$V_x = \partial\Delta\phi/\partial x_0 + \cos\alpha$$

$$V_z = \partial\Delta\phi/\partial z_0 + \sin\alpha$$

where $\partial\Delta\phi/\partial x_0$ and $\partial\Delta\phi/\partial z_0$ are:

$$\partial\Delta\phi/\partial x_0 = \partial\Delta\phi/\partial xp \left(\frac{xp}{\rho}\right) - \partial\Delta\phi/\partial zp \left(\frac{zp}{\rho}\right)$$

$$\partial\Delta\phi/\partial z_0 = \partial\Delta\phi/\partial xp \left(\frac{zp}{\rho}\right) + \partial\Delta\phi/\partial zp \left(\frac{xp}{\rho}\right)$$

$$\text{where } \rho = xp^2 + zp^2$$

and where $\partial\Delta\phi/\partial xp$ and $\partial\Delta\phi/\partial zp$ are:

$$\partial\Delta\phi/\partial xp = \partial\Delta\phi/\partial \bar{xp} - \partial\Delta\phi/\partial \bar{zp} \text{ as}(xp)/\partial xp$$

$$\partial\Delta\phi/\partial zp = \partial\Delta\phi/\partial \bar{zp}$$

The quantities $\partial\Delta\phi/\partial \bar{xp}$ and $\partial\Delta\phi/\partial \bar{zp}$ are found as follows:

$$\partial\Delta\phi/\partial \bar{xp} = \partial\Delta\phi/\partial xc A$$

$$\partial\Delta\phi/\partial \bar{zp} = \partial\Delta\phi/\partial zc \frac{1}{4} / \left(\frac{1}{4} + \bar{zp}\right)^{3/2}$$

$$\text{where } A = \begin{cases} 1, & |xc| \leq .625 \\ 1 / \left[1 + \left(\frac{xp}{.375}\right)^2\right]^{3/2}, & |xc| > .625 \end{cases}$$

A finally the terms $\partial\Delta\phi/\partial xc$, $\partial\Delta\phi/\partial zc$ are determined numerically from the grid of $\Delta\phi$ vs. xc and zc .

APPENDIX C

SUPERSONIC TWO-DIMENSIONAL DOUBLET LATTICE METHOD

For supersonic flow the following integral equation holds:

$$w = \frac{\partial}{\partial z} \frac{\partial}{\partial \zeta} I$$

$$\text{where } I = \int_{\xi}^{x-B(z-\zeta)} \Delta\phi(\xi) \phi_{2D} d\xi$$

i.e.

and where $\Delta\phi(\xi)$ is the potential jump across the airfoil and ϕ_{2D} is the potential due to a source of unit strength, i.e.,

$$\phi_{2D} = J_0(\lambda R) \exp(-i\lambda M_\infty(x-\xi))/2B$$

$$\text{where } R^2 = (x-\xi)^2 - B^2(z-\zeta)^2$$

$$B^2 = M_\infty^2 - 1$$

$$\lambda = \omega M_\infty / U_\infty B^2$$

where w is the downwash boundary condition applied to the lifting surface and $J_0(\lambda R)$ is a Bessel Function of the first kind.

The first step in the derivation of a Doublet Lattice Method for supersonic flow is the evaluation of the double differential of the integral, i.e., $\partial^2 I / \partial z \partial \zeta$.

Performing the first differential gives:

$$\frac{\partial I}{\partial \zeta} = B \Delta\phi(\xi=x-B(z-\zeta)) \Delta\phi_{2D}(\xi=x-B(z-\zeta))$$

$$\int_{\xi}^{x-B(z-\zeta)} \Delta\phi(\xi) \frac{\partial \phi_{2D}}{\partial \zeta} d\xi$$

i.e.

Now

$$\Delta\phi_{2D}(\xi=x-B(z-\zeta)) = \frac{1}{2B} \exp(-i\lambda M_{\infty} B(z-\zeta))$$

since $J_0(0) = 1.0$

Taking the second derivative of I gives

$$\begin{aligned} \partial^2 I / \partial z \partial \zeta &= B \partial \Delta\phi(\xi=x-B(z-\zeta)) / \partial z \quad \Delta\phi_{2D}(\xi=x-B(z-\zeta)) \\ &+ B \Delta\phi(\xi=x-B(z-\zeta)) \quad \partial \Delta\phi_{2D}(\xi=x-B(z-\zeta)) / \partial z \\ &- B \Delta\phi(\xi=x-B(z-\zeta)) \quad \partial \Delta\phi_{2D} / \partial \zeta \Big|_{\xi=x-R(z-\zeta)} \\ &+ \int_{\xi}^{x-B(z-\zeta)} \Delta\phi(\xi) \partial^2 \phi_{2D} / \partial z \partial \zeta \, d\xi \\ &\text{l.e.} \end{aligned}$$

The terms of this expression are evaluated as follows: (use

$$\bar{\Delta}\phi = \Delta\phi(\xi=x-B(z-\zeta)), \quad \bar{\phi}_{2D} = \phi_{2D}(\xi=x-B(z-\zeta))$$

$$\partial \bar{\Delta}\phi / \partial z = \frac{\partial \Delta\phi}{\partial \xi} \frac{\partial \xi}{\partial z} = \Delta\phi'(-B)$$

$$\partial \bar{\phi}_{2D} / \partial \zeta = -i(\lambda M_{\infty} / 2) \exp(-i\lambda M_{\infty} B(z-\zeta))$$

$$\partial \Delta\phi_{2D} / \partial \zeta = \frac{-J_1(\lambda R)}{2B} \frac{\lambda \partial R}{\partial \zeta} \exp(-i\lambda M_{\infty} B(z-\zeta))$$

$$\partial \Delta\phi_{2D} / \partial \zeta \Big|_{\xi=x-B(z-\zeta)} = \frac{-B\lambda^2(z-\zeta)}{4} \exp(-i\lambda M_{\infty} B(z-\zeta))$$

since $\lim J_1(\lambda R) / \lambda R \rightarrow 1/2$ as $\lambda R \rightarrow 0$

$$\partial^2 \phi_{2D} / \partial z \partial \zeta = \tilde{F}(\exp(-i\lambda M_{\infty} B(z-\zeta))) / 2B$$

where

$$\tilde{F} = -J_1' \lambda^2 \frac{\partial R}{\partial z} \frac{\partial R}{\partial \zeta} - J_1 \lambda \frac{\partial^2 R}{\partial z \partial \zeta}$$

$$\text{and } \frac{\partial R}{\partial \zeta} = \frac{B^2(z-\zeta)}{R} = \frac{-\partial R}{\partial \bar{z}}$$

$$\frac{\partial^2 R}{\partial \zeta \partial \bar{z}} = \frac{B^2}{R} + \frac{B^4(z-\zeta)^2}{R^3}$$

Before these terms are substituted into the expression for $\partial^2 I / \partial z \partial \bar{z}$ the limit $z \rightarrow \zeta$ must be applied since the receiving points (x, z) must range over the airfoil surface (which is $z = \zeta$). In the limit as $z \rightarrow \zeta$;

$$R \rightarrow |x - \xi|$$

$$\partial \bar{\phi}_{2D} / \partial z \rightarrow -i\lambda M_\infty / 2$$

$$\partial \Delta \phi_{2D} / \partial \zeta \Big|_{\xi=x-B(z-\zeta)} \rightarrow 0$$

$$\tilde{F} \rightarrow -J_1(\lambda|x-\xi|) \lambda B^2 / |x-\xi|$$

$$\Delta \phi(\xi=x-B(z-\zeta)) \rightarrow \Delta \phi(x)$$

$$\Delta \phi'(\xi=x-B(z-\zeta)) \rightarrow \Delta \phi'(x)$$

$$\Delta \phi_{2D}(\xi=x-B(z-\zeta)) \rightarrow \frac{1}{2B}$$

The final expression for $\partial^2 I / \partial z \partial \bar{z}$, line $z \rightarrow \zeta$ is:

$$\lim_{z \rightarrow \zeta} \partial^2 I / \partial z \partial \bar{z} = \frac{-B}{2} \left\{ \Delta \phi'(x) + i\lambda M_\infty \Delta \phi(x) + \lambda^2 \int_{\xi}^x \Delta \phi(\xi) F(\lambda|x-\xi|) \exp(-i\lambda M_\infty(x-\xi)) d\xi \right\} \quad (C-1)$$

l.e.

where $F = J_1(\lambda|x-\xi|) / \lambda|x-\xi|$

Notice that ξ is always less than or equal to x thus $x - \xi$ is always positive and the absolute value sign can be dropped. For simplicity of notation introduce

$$p = \lambda(x - \xi) \text{ then}$$

$$w = \frac{-B}{2} \left\{ \Delta\phi'(x) + i\lambda M_\infty \Delta\phi(x) + \lambda \int_0^x \Delta\phi(\xi) F(p) \exp(-iM p) dp \right. \quad \text{l.e.} \quad \text{(C-2)}$$

where

$$F(p) = J_1(p)/p, \text{ and } \xi = x - p/\lambda \text{ and } \Delta\phi'(x) = \partial\Delta\phi/\partial x$$

Equations (C-1) or (C-2) are the final results for the downwash due to a distribution of potential jump $\Delta\phi(x)$, on a lifting surface (and wake). Lifting surface theories, such as the Doublet Lattice Method (DLM) do not use a distribution of potential jump but use a distribution of pressure jump,

$C_p(x)$. This distribution of pressure jump is simulated in the DLM by a series of point pressure doublets. The point pressure doublet (shown in Figure C-1) possesses the following properties: (1) the pressure jump and potential jump are zero for points forward of the doublet; (2) the pressure is a delta function at the location of the doublet; and (3) the pressure jump is zero downstream of the doublet but the potential jump is not (wake). Mathematically, this is expressed as follows:

$$\Delta C_p = \begin{cases} 0 & x < x_0 \\ 2\Delta\phi_p \delta(x - x_0) & x = x_0 \\ -2(\Delta\phi_x + i \frac{\omega}{U_\infty} \Delta\phi) = 0 & x > x_0 \end{cases}$$

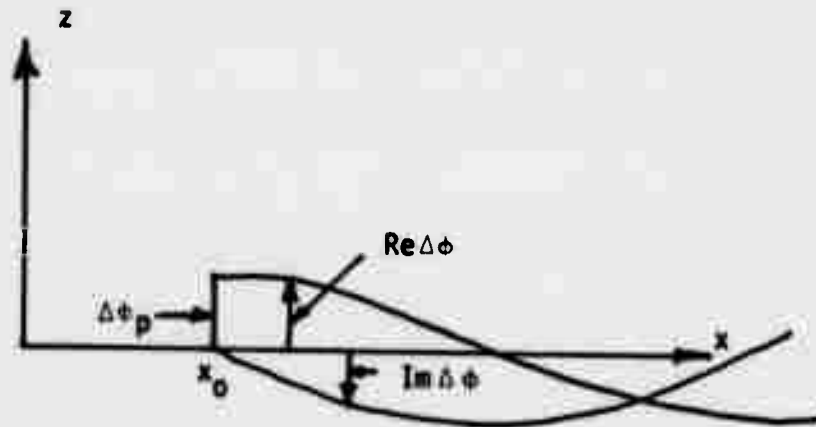


Figure C-1 Potential Jump Due to a Point Pressure Doublet

Solving the differential equation for $\Delta\phi$ downstream of x_0 and taking into account the properties at and ahead of x_0 gives:

$$\Delta\phi = \Delta\phi_p H(x - x_0) \exp(-i\omega(x - x_0)/U_\infty) \quad (C-3)$$

Placing (C-3) into the first two terms of (C-2) gives:

$$\Delta\phi' + i\lambda M_\infty \Delta\phi = \Delta\phi_p \left\{ \delta(x - x_0) + \frac{i\omega}{U_\infty \beta^2 z} H(x - x_0) \exp(-i\omega(x - x_0)/U_\infty) \right\} \quad (C-4)$$

when it is noted that $\partial H/\partial x = \delta$. The expression for $\Delta\phi(\xi)$ given in terms of (C-3) and the variable p is:

$$\begin{aligned} \Delta\phi(\xi) + \Delta\phi_p H(\xi - x_0) \exp(-i\omega(\xi - x_0)/U_\infty) = \\ \Delta\phi_p H(\xi - x_0) \exp(-i\omega(\xi - x_0)/U_\infty) \exp\left(+\frac{i\omega}{\lambda U_\infty} p\right) \end{aligned}$$

Combining the last part of this term with the term $\exp(-iM_\infty p)$ in (C-2) gives:

$$\exp(i\omega p/\lambda U_\infty) \exp(-iM_\infty p) = \exp(-ip/M_\infty)$$

Placing this term and (C-4) into (C-2) gives the downwash, w_p , for a point pressure doublet.

$$w_p = \frac{-B}{2} \Delta\phi_p \left\{ \delta(x-x_0) + \frac{i\omega}{U_\infty \beta^2} H(x-x_0) \exp(-i\omega(x-x_0) / U_\infty) \right. \\ \left. + \lambda \exp(-i\omega(x-x_0) / U_\infty) \int_0^{p_{l.e.}} H(\xi-x_0) e^{-ip/M_\infty} F(p) dp \right\}$$

The step function in the integral eliminates that part of the integral lying in front of x_0

$$H(\xi-x_0) = \begin{cases} 0 & \xi < x_0 \text{ or } p > \lambda(x-x_0) = p_0 \\ 1 & \xi \geq x_0 \text{ or } p \leq p_0 \end{cases}$$

Thus, the upper limit becomes p_0 , thus

$$p_{l.e.} \rightarrow p_0 = \lambda(x - x_0)$$

and the term $H(\xi-x_0)$ can be eliminated.

Let

$$E(p_0, M_\infty) = \int_0^{p_0} e^{-ip/M_\infty} F(p) dp \quad (C-5)$$

where $F(p) = J_1(p)/p$

Then the expression for w becomes

$$w_p = -\frac{B}{2} \Delta\phi_p \left\{ \delta(x-x_0) + \lambda \left[\frac{i}{M_\infty} + \frac{1}{2} E(p_0, M_\infty) \right] \exp(+i\omega(x-x_0) / U_\infty) \right\} \quad (C-6)$$

The force f generated by the point doublet in the uniform flow U_∞ is

$$f = \int \Delta C_p d\xi = - \int 2 (\Delta\phi' + i \frac{\omega}{U_\infty} \Delta\phi) d\xi$$

Introducing equation (C-3) gives

$$f = -2\Delta\phi_p \int \delta(\xi-x_0) d\xi = -2\Delta\phi_p$$

In the Doublet Lattice Method a point doublet is placed on each element. The resulting force generated by this doublet is averaged over the element to produce an average pressure, $\overline{\Delta C_p}$. Thus,

$$\overline{\Delta C_p} = f/\Delta X = - \frac{2}{\Delta X} \Delta\phi_p$$

Solving this for $\Delta\phi_p$ and introducing the result into (C-6) gives the result for the local downwash w due to a point pressure doublet of average pressure $\overline{\Delta C_p}$. If we also average the downwash over the element, \overline{w}_p , then the result is

$$\overline{w}_p = \frac{B}{4} \overline{\Delta C_p} \Delta X \left\{ \overline{\delta} + \lambda [1/M_\infty + E/2] \exp(-i\omega(x-x_0)/U_\infty) \right\} \quad (C-7)$$

Since the average of the delta function is

$$\overline{\delta} = \frac{1}{\Delta X} \int_0^{\Delta X} \delta(x-x_0) dx = \begin{cases} \frac{1}{\Delta X} & \text{on the element} \\ 0 & \text{off of the element} \end{cases}$$

Equation (C-7) then, along with the expressions for E and δ are the final results for the downwash due to a pressure element in supersonic flow. The expression for E , i.e.,

$$E(p_0, M_\infty) = \int_0^{p_0} e^{-ip/M_\infty} F(p) dp$$

$$p_0 = \lambda(x-x_0)$$

$$F(p) = J_1(p)/P$$

is evaluated numerically.

The steady case, $\omega = 0$, reduces to the classic results

$$\bar{w}_p = \frac{B\Delta C p}{4}$$

APPENDIX D

THE GARABEDIAN TRANSONIC AIRFOIL INVERSE PROCEDURE

The program method of analysis is based on the work of Korn, Garabedian and Jameson and utilizes a Poisson fast solver differencing scheme. Because viscous effects are not considered in the 2-D Jameson flow solution, the analytical pressure distribution obtained was often an unacceptable match with pressures obtained experimentally. The effect of the viscous boundary layer can be seen in Figure 2.4-5 where the pressures on both the upper and lower airfoil surfaces are seen to deviate from the experimental data. In order to account for the effects of viscosity, it was decided to alter the geometry of the airfoil used in the 2-D inviscid analysis. To do this, use was made of a transonic airfoil design computer program (A5BE) containing an inverse Garabedian design option. Although basically inviscid, the program accounts for viscosity by adding a displacement thickness to the original airfoil geometry.

To decrease computational time and lower cost, a Poisson fast solver differencing scheme was incorporated into the program. The advantage of the fast solver lies in the fact that convergence occurs in fewer cycles through the flow field than with other methods. Because the governing compressible flow equation is unstable for transonic flows when written in the form used with the fast solver, fast solver cycles are alternated with successive line over-relaxation cycles. The SLOR cycles handle the supersonic regions, and the fast solver cycles propagate information quickly through the flow field and satisfy the Kutta condition. A restriction to using the fast Poisson solver is that the equations must be solved in a closed area with Neuman, Dirichlet or periodic boundary conditions. This restriction is satisfied by using a circle as the computational plane. The circumference, which corresponds to the airfoil surface, has Neumann conditions, the center of the circle, infinity in the physical plane, has Dirichlet conditions, and periodic conditions are established along a line from the tail to infinity.

To aid in the analysis, the program was set up to run from the IBM 2250 graphics terminal. The original airfoil geometry, 2-D Mach number and desired

2-D lift coefficient are input and a 20 cycle flow solution is performed first on a coarse grid and then on a grid refined by halving the crude grid mesh spacing. The resulting pressure distribution is then displayed on the tube and is changed using a light pen to correspond to the experimental data. Twenty cycle inverse flow solutions are then performed on both the coarse and refined grids to obtain a revised airfoil geometry. The updated geometry can then be run forward through a flow solution and the resulting pressure distribution again compared and updated if necessary. This process is repeated until the revised geometry produces the desired pressure distribution.

Examples of airfoil geometries revised using the inverse Garabedian program are shown in Figure 3.3-3. The revision to the station .309 geometry is a typical boundary layer displacement correction for attached flows in that the trailing edge thickness and camber are altered.

The station .657 revision is untypical due to a thickening of the entire airfoil section. Because the two-dimensional airfoil geometry is scaled from the 3-D coordinates as $Z_{2D}/c = Z_{3D}/c / \cos \Lambda_{EFF}$, the thickness correction indicates the use of an incorrect (too small) effective sweep angle in the initial scaling operation. Because the 2-D Mach number is scaled down as $M_{2D} = M_{\infty} \cos \Lambda_{EFF}$, the thickness displacement can also be seen to indicate that too large a 2-D Mach number was used in the inverse calculation. This uniform thickening would be eliminated if the 2-D Mach number were lowered an appropriate amount and the case rerun in the Garabedian inverse.

REFERENCES

1. Giesing, J. P., Kalman, T. P., Rodden, W. P., "Subsonic Unsteady Aerodynamics for General Configurations, Part II, Application of the Doublet-Lattice Method and the Method of Images to Lifting-Surface/Body Interference" AFFDL-TR-71-5 Part II, Dec. 1971.
2. Harris, D., Wind-Tunnel Measurements of Aerodynamic Load Distribution on an NASA Supercritical-Wing Research Airplane Configuration, NASA TMX-2469, Feb. 1972.
3. Giesing, J. P., Kalman, T. P., Rodden, W. P., "Correction Factor Techniques for Improving Aerodynamic Prediction Methods", NASA CR-144967, May 1976.
4. Tijdeman, H., Schippers, P., Persoon, A. J., "Unsteady Airloads on an Oscillating Supercritical Airfoil", NLR MP 77008U, April 1977.
5. Ballhaus, W. F., Magnus, R. J., Yoshihara, H., "Unsteady Transonic Flows Over Airfoils", CASD-NSC-75-005, Sept. 1975.
6. Magnus, R. J., Yoshihara, H., "Calculations of Transonic Flow Over an Oscillating Airfoil", AIAA Paper 75-98, Jan. 1975.
7. Ehlers, F. E., "A Finite Difference Method for the Solution of the Transonic Flow Around Harmonically Oscillating Wings", NASA CR-2257, July 1974.
8. Traci, R. M., Farr, J. L., Albano, E., "Perturbation Method for Transonic Flows about Oscillating Airfoils", AIAA Paper No. 75-877, June 1975.
9. Chan, S. T. K., Brashears, M. R., "Finite Element Analysis of Transonic Flow", AFFDL-TR-74-11, March 1974.

10. Cunningham, A. M., "An Oscillatory Kernel Function Method for Lifting Surfaces in Mixed Transonic Flow", AIAA Paper No. 74-359, April 1974.
11. Jameson, A., Gaughey, D. A., "Numerical Calculation of the Transonic Flow Past a Swept Wing", NYU ERDA Rept. C00 3077-140, May 1977.
12. Cunningham, A. M., "Further Developments in the Prediction of Oscillatory Aerodynamics in Mixed Transonic Flow", AIAA Paper 75-99, Jan. 1975.
13. Hafez, M. M., Rizk, M. H., Murman, E. M., Wellford, L. C., "Numerical Solution of the Unsteady Transonic Small-Disturbance Equation", Flow Research Report No. 83, Aug. 1977.
14. Liepmann, H. W., Roshko, A., "Elements of Gasdynamics", John Wiley & Sons, Inc., New York, N.Y. 1957.
15. Landahl, M. T., "Unsteady Transonic Flow", Pergamon Press, Long Island City, N.Y. 1961.
16. Tranen, T. L., "Analysis and Design of Transonic Airfoils", MDC-A3760, Dec. 1975.
17. Pearson, R. M., Galligher, J. L., Zuhuruddin, K., "YC-15II Flutter Analysis, MDC-J7198, Feb. 1977.